ABSTRACT

HENDRIX, SERENA ELAINE. Shear Performance of High-Strength Lightweight Concrete Columns under Seismic Loads. (Under the direction of Dr. Mervyn Kowalsky.)

The objective of this research is to evaluate the shear performance of high-strength lightweight concrete square columns. Lightweight concrete is used in order to reduce the inertial mass of buildings and bridges, thus reducing the levels of seismic response. Unfortunately past performance of lightweight concrete in seismic regions has been questionable with regard to shear.

The research includes both an experimental and analytical component. For the experimental portion, eight tests were conducted on half-sized square columns in which the variables were transverse reinforcement detail and aggregate type (shale, slate, clay, and normal weight conventional rock). Another set of eight tests was performed by Pablo Robalino, whose research involved the cyclic loading tests of lightweight normal-strength concrete in shear (Robalino 2006). All columns were subjected to reverse cyclic loading applied by a hydraulic actuator. The analytical model used to predict shear capacities was the Revised UCSD model for lightweight concrete (Kowalsky et al. 2000). This research examines the shear strength of lightweight concrete compared to normal weight concrete at different levels of deformation.

The results of these experiments show that in terms of displacement capacity and energy absorption there is no significant difference between normal weight and lightweight concrete. The strength of the concrete shear resisting mechanism degraded at a somewhat faster rate at higher levels of ductility (μ_7 or greater), for lightweight specimens compared to normal weight specimens. This was the case for both normal- and high-strength concrete, although high-strength showed a slower rate of degradation.

The high-strength lightweight specimens showed lower shear strength than normal weight specimens, but higher than the predicted normal-strength lightweight specimens. It is recommended that the low ductility plateau of the γ factor for lightweight concrete be raised from 0.25 to 0.27 when using high-strength concrete, and the high ductility plateau remain the same at 0.035 for the Revised UCSD model.

Shear Performance of High-Strength Lightweight Concrete Columns under Seismic Loads

by
Serena Elaine Hendrix

A thesis submitted to the Graduate Faculty of
North Carolina State University
in partial fulfillment of the
requirements for the Degree of
Master of Science

Civil Engineering

Raleigh, North Carolina

2008

APPROVED BY:

_____	_____
Dr. Vernon C. Matzen	Dr. James M. Nau

_____
Dr. Mervyn J. Kowalsky
Chair of Advisory Committee

BIOGRAPHY

Serena Elaine Hendrix was born in Decatur, Georgia in 1984. She was raised in Columbus, GA, then moved to Raleigh, North Carolina where she obtained her Bachelor of Science at North Carolina State University in 2006. While working at the university as an undergraduate researcher, she decided to pursue a Master of Science degree at NCSU, completed in 2008. She plans to work for an engineering firm and become a licensed engineer.

ACKNOWLEDGEMENTS

There are many people that made this project a success, first and foremost my academic advisor and chair of my advisory committee Dr. Mervyn Kowalsky. He is a faculty member at NCSU and specializes in earthquake engineering. He has been instrumental in my growth as a student these past two years. I wish to thank Dr. Nau and Dr. Matzen for being a part of my committee and for the guidance throughout my years at NCSU. This project would not have been possible without funding provided by the Expanded Shale, Clay, and Slate Institute (ESCSI) for which I am extremely grateful.

For the laboratory portion of my research, I extend my gratitude to Greg Lucier, Bill Dunleavy, and in particular Jerry Atkinson at Constructed Facilities Laboratory for their expertise. I thank Ready Mixed Concrete Company, in particular Ken Vickers for providing all of the concrete for this research project, as well as Mike Robinson (ESCSI) for designing the concrete mixes and conducting several concrete tests. Others I wish to thank include Courtney Shepard, Jacob Griffin, and Kurtis Kennedy for their assistance.

TABLE OF CONTENTS

LIST OF TABLES vi
LIST OF FIGURES viii

CHAPTER 1 – INTRODUCTION 1
Previous Research 2
Motivation 5

CHAPTER 2 – TEST DESIGN, SETUP, AND PROCEDURE 9
Modeling 9
Column Design 16
Casting 19
Test Setup 23
Instrumentation 27
General Loading Schedule 29

CHAPTER 3 – BRITTLE SHEAR FAILURE SPECIMENS 31
3.1 - Normal Weight Brittle Shear Failure Specimen (NWB) 33
Force-controlled Cycles 33
Displacement-controlled Cycles 35
Force-Displacement Response / Damping 41
3.2 – Lightweight Clay Brittle Shear Failure Specimen (CLB) 43
Force-controlled Cycles 43
Displacement-controlled Cycles 45
Force-Displacement Response / Damping 49
Curvature Profiles 50
Strain Gage Histories and Profiles 51
3.3 – Lightweight Shale Brittle Shear Failure Specimen (SHB) 54
Force-controlled Cycles 54
Displacement-controlled Cycles 56
Force-Displacement Response / Damping 62
Curvature Profiles 63
Strain Gage Histories and Profiles 64
3.4 – Lightweight Slate Brittle Shear Failure Specimen (SLB) 66
Force-controlled Cycles 66
Displacement-controlled Cycles 68
Force-Displacement Response / Damping 73
Curvature Profiles 74
Strain Gage Histories 75

CHAPTER 4 – DUCTILE SHEAR FAILURE SPECIMENS 77
4.1 - Normal Weight Ductile Shear Failure Specimen (NWD) 79
Force-controlled Cycles 79
Displacement-controlled Cycles 80
Force-Displacement Response / Damping 89
Curvature Profiles 90
Strain Gage Histories and Profiles 91
4.2 – Lightweight Clay Ductile Shear Failure Specimen (CLD) 95
Force-controlled Cycles 95
Displacement-controlled Cycles 97
Force-Displacement Response / Damping 103
Curvature Profiles 104
Strain Gage Histories and Profiles 106
4.3 – Lightweight Shale Ductile Shear Failure Specimen (SHD) 109
Force-controlled Cycles 109
Displacement-controlled Cycles 110
Force-Displacement Response / Damping 115
Curvature Profiles 115
Strain Gage Histories and Profiles 117
4.4 – Lightweight Slate Ductile Shear Failure Specimen (SLD) 120
Force-controlled Cycles 120
Displacement-controlled Cycles 121
Force-Displacement Response / Damping 124
Curvature Profiles 125
Strain Gage Histories 127

CHAPTER 5 – TEST COMPARISONS 128
5.1 – Displacement Capacity 129
Brittle Failure Test Specimens: 129
Ductile Failure Test Specimens: 131
5.2 – Strength Degradation 135
Brittle Failure Test Specimens: 135
Ductile Failure Test Specimens: 138
5.3 – Energy Absorption 141
5.4 – Shear Strength 146
5.5 – Miscellaneous Data 152

CHAPTER 6 – CONCLUSIONS AND RECOMMENDATIONS 154

REFERENCES 156

APPENDIX 160
Curvature Calculations 161
Strain Gage Method for Calculating the Steel Truss Component for Shear Resistance 161
Shear Deformation Calculations and Graphs 162
Damping Calculations Using Jacobsen's Approach 170
Strain Penetration Length Calculations 171
Equipment Specification 171
Force-Displacement Responses 172
Working Strain Gage Histories 174
Linear Potentiometer Histories 181

LIST OF TABLES

CHAPTER 2 – TEST DESIGN, SETUP, AND PROCEDURE

Table 2.1 – Testing matrix 19
Table 2.2 – Concrete data 22

CHAPTER 5 – TEST COMPARISONS

Table 5.1 – High-strength brittle specimens, displacement capacities for specific loads 131
Table 5.2 – High-strength ductile specimens, displacement capacities for specific loads 133
Table 5.3 – NWB: Strength degradation 136
Table 5.4 – CLB: Strength degradation 136
Table 5.5 – SHB: Strength degradation 137
Table 5.6 – SLB: Strength degradation 137
Table 5.7 – NWD: Strength degradation after maximum load 139
Table 5.8 – CLD: Strength degradation after maximum load 139
Table 5.9 – SHD: Strength degradation after maximum load 139
Table 5.10 – SLD: Strength degradation after maximum load 140
Table 5.11 – Hysteretic damping calculations for high-strength brittle specimens 141
Table 5.12 – Hysteretic damping calculations for high-strength ductile specimens 141
Table 5.13 – Miscellaneous data for high-strength specimens 152

LIST OF FIGURES

CHAPTER 1 – INTRODUCTION

Figure 1.1 – Second floor of the Olive View Hospital Psychiatric Ward after the San Fernando earthquake 5
Figure 1.2 – A portion of the Cypress Viaduct after the Loma Prieta earthquake 6
Figure 1.3 – Normal weight (left) and lightweight (right) concrete surfaces 8

CHAPTER 2 – TEST DESIGN, SETUP, AND PROCEDURE

Figure 2.1 – α factor for V_c equation 10
Figure 2.2 – β factor for V_c equation 11
Figure 2.3 – γ factor for V_c equation 12
Figure 2.4 – Shear strength contribution due to compressive axial load (Robalino 2006) 13
Figure 2.5 – Illustration of variables in V_s equation 15
Figure 2.6 – Predictions of brittle shear failure for normal-strength specimens (Robalino 2006) 17
Figure 2.7 – Predictions of ductile shear failure for normal-strength specimens (Robalino 2006) 17
Figure 2.8 – Column section and steel reinforcement details, brittle (left) and ductile (right) (Robalino 2006) 18
Figure 2.9 – In the foreground, formwork setup before concrete pour (left) and after (right) 20
Figure 2.10 – Brittle failure (left) and ductile failure (right) steel cages inside formwork 20
Figure 2.11 – Two specimens after the removal of formwork (left) and concrete cylinders (right) 21
Figure 2.12 – Illustration of T-shape member 22
Figure 2.13 – Test setup, specimen only 23
Figure 2.14 – Central (left) and side (right) footing cross sections (Robalino 2006) 24
Figure 2.15 – Hydrocal® White poured under (left) and between (right) footing pieces 25
Figure 2.16 – Complete test setup 26
Figure 2.17 – Linear potentiometers on north face (left) and east face (right) of column 27
Figure 2.18 – Strain gage placements on transverse steel 28
Figure 2.19 – String pot locations on south face of column 29
Figure 2.20 – General loading schedule 30

CHAPTER 3 – BRITTLE SHEAR FAILURE SPECIMENS

Figure 3.1 – Predicted Force-Displacement Response for Brittle Failure Mode 32
Figure 3.2 – NWB: Actual loading protocol 33
Figure 3.3 – NWB: North face (left) and south face (right) at $\pm F_y^{'}/2$ 34
Figure 3.4 – NWB: East (left) and west (right) faces at $\pm F_y^{'}$ 35
Figure 3.5 – NWB: East (left) and west (right) faces at $\pm\mu_{1,1}$ 36
Figure 3.6 – NWB: Concrete crushing on south face at $\pm\mu_{1.5,1}$ 37
Figure 3.7 – NWB: East (left) and west (right) faces at maximum load ($\pm\mu_{2,1}$) 37
Figure 3.8 – NWB: West face crushing at + $\mu_{2,1}$ (left) and south face spalling at - $\mu_{2,3}$ (right) 38
Figure 3.9 – NWB: West face at - $\mu_{2.9,1}$ (left), + $\mu_{2.9,2}$ (center), and - $\mu_{2.9,3}$ (right) 39
Figure 3.10 – NWB: East face at + $\mu_{2.9,1}$ (left), + $\mu_{2.9,2}$ (center), and - $\mu_{2.9,3}$ (right) 39
Figure 3.11 – NWB: North face at - $\mu_{2.9,1}$ (left) and - $\mu_{2.9,3}$ (right) 40
Figure 3.12 – NWB: South face at- $\mu_{2.9,1}$ (left) and - $\mu_{2.9,3}$ (right) 40
Figure 3.13 – NWB: Approximate Force-Displacement Response 41
Figure 3.14 – CLB: Actual loading protocol 43
Figure 3.15 – CLB: North face (left) and south face (right) at $\pm 3F_y^{'}/4$ 44
Figure 3.16 – CLB: North face (left) and south face (right) at $\pm F_y^{'}$ 44
Figure 3.17 – CLB: East face (left) and west face (right) at $\pm F_y^{'}$ 45
Figure 3.18 – CLB: Concrete spalling on south face at $\pm\mu_{1.5,1}$ (left) and $\pm\mu_{1.5,3}$ (right) 46
Figure 3.19 – CLB: East face at - $\mu_{1.9,1}$ (left), - $\mu_{1.9,3}$ (center), and - $\mu_{3,1}$ (right) 47
Figure 3.20 – CLB: West face at - $\mu_{1.9,1}$ (left), - $\mu_{1.9,3}$ (center), and - $\mu_{3,1}$ (right) 48
Figure 3.21 – CLB: North (left) and south (right) faces at $\pm\mu_{1.9,3}$ 48
Figure 3.22 – CLB: North (left) and south (right) faces at $\pm\mu_{3,1}$ 49
Figure 3.23 – CLB: Actual Force-Displacement Response 49
Figure 3.24 – CLB: Curvature profiles for force-controlled (left) and displacement-controlled (right) cycles 50
Figure 3.25 – CLB: BS1 strain gage history 52
Figure 3.26 – CLB: East face strain profile 53
Figure 3.27 – SHB: Actual loading protocol 54
Figure 3.28 – SHB: West (left) and south (right) faces at $\pm F_y^{'}/2$ 55
Figure 3.29 – SHB: East (left) and west (right) faces at $\pm F_y^{'}$ 55
Figure 3.30 – SHB: North (left) and south (right) faces at $\pm F_y^{'}$ 56
Figure 3.31 – SHB: East (left) and west (right) faces at $\pm\mu_{1.5,1}$ 57

Figure 3.32 – SHB: Concrete crushing and spalling on east (left) and south (right) faces at $\pm\mu_{1.5,1}$ 57
Figure 3.33 – SHB: East (left) and west (right) faces at $\pm\mu_{2.2,1}$ 58
Figure 3.34 – SHB: Concrete crushing and spalling on east (left) and north (right) faces at $\pm\mu_{2.2,1}$ 59
Figure 3.35 – SHB: East face at $-\mu_{2.2,2}$ (left) and $-\mu_{3,1}$ (right) 60
Figure 3.36 – SHB: West face at $-\mu_{2.2,2}$ (left) and $-\mu_{3,1}$ (right) 60
Figure 3.37 – SHB: North (left) and south (right) faces at $-\mu_{3,1}$ 61
Figure 3.38 – SHB: East (left) and west (right) face instruments 61
Figure 3.39 – SHB: Actual Force-Displacement Response 62
Figure 3.40 – SHB: Curvature profiles for force-controlled (left) and displacement-controlled (right) cycles 63
Figure 3.41 – SHB: BS2 strain gage history 64
Figure 3.42 – SHB: West face strain profile 65
Figure 3.43 – SLB: Actual loading procedure 66
Figure 3.44 – SLB: West (left) and south (right) faces at $\pm F_y^{'}/2$ 67
Figure 3.45 – SLB: East (left) and west (right) faces at $\pm F_y^{'}$ 67
Figure 3.46 – SLB: North (left) and south (right) faces at $\pm F_y^{'}$ 68
Figure 3.47 – SLB: Spalling of concrete on south face at $\pm\mu_{1.3,3}$ (left) and north face at $\pm\mu_{1.7,3}$ (right) 69
Figure 3.48 – SLB: East (left) and west (right) faces at $\pm\mu_{1.7,3}$ 70
Figure 3.49 – SLB: East face at $-\mu_{2.5,1}$ (left), $-\mu_{2.5,3}$ (center), and $+\mu_{3.6,1}$ (right) 71
Figure 3.50 – SLB: West face at $-\mu_{2.5,1}$ (left), $-\mu_{2.5,3}$ (center), and $+\mu_{3.6,1}$ (right) 71
Figure 3.51 – SLB: North face at $-\mu_{2.5,1}$ (left), $-\mu_{2.5,3}$ (center), and $+\mu_{3.6,1}$ (right) 72
Figure 3.52 – SLB: South face at $-\mu_{2.5,1}$ (left), $-\mu_{2.5,3}$ (center), and $+\mu_{3.6,1}$ (right) 72
Figure 3.53 – SLB: East face instrument 73
Figure 3.54 – SLB: Actual Force-Displacement Response 73
Figure 3.55 – SLB: Curvature profiles for force-controlled (left) and displacement-controlled (right) cycles 74
Figure 3.56 – SLB: East face strain gage history 75

CHAPTER 4 – DUCTILE SHEAR FAILURE SPECIMENS

Figure 4.1 – Predicted Force-Displacement Response for Ductile Failure Mode 77
Figure 4.2 – NWD: Actual loading protocol 79
Figure 4.3 – NWD: West (left) and south (right) faces at $\pm F_y^{'}$ 80
Figure 4.4 – NWD: North face at $-\mu_{1.7,3}$ 81

Figure 4.5 – NWD: East (left) and west (right) faces at $-\mu_{2.6,1}$ 81
Figure 4.6 – NWD: North (left) and south (right) spalling at $-\mu_{2.6,1}$ 82
Figure 4.7 – NWD: East face at $-\mu_{5.2,1}$ and $-\mu_{5.2,3}$ 83
Figure 4.8 – NWD: West face at $-\mu_{5.2,1}$ and $-\mu_{5.2,3}$ 83
Figure 4.9 – NWD: North face spalling at $-\mu_{5.2,1}$ and $-\mu_{5.2,3}$ 84
Figure 4.10 – NWD: North face at $-\mu_{7.2,1}$ (left), $-\mu_{7.2,3}$ (center), and $-\mu_{9.3,1}$ (right) 85
Figure 4.11 – NWD: South face at $-\mu_{7.2,1}$ (left), $-\mu_{7.2,3}$ (center), and $-\mu_{9.3,1}$ (right) 85
Figure 4.12 – NWD: Concrete spalling at $-\mu_{7.2,1}$ (left) and $-\mu_{7.2,3}$ (right) 86
Figure 4.13 – NWD: East face at $-\mu_{7.2,1}$ (left), $-\mu_{7.2,3}$ (center), and $-\mu_{9.3,1}$ (right) 86
Figure 4.14 – NWD: West face at $-\mu_{7.2,1}$ (left), $-\mu_{7.2,3}$ (center), and $-\mu_{9.3,1}$ (right) 87
Figure 4.15 – NWD: West face long. bar buckling and stirrup detachment at $-\mu_{9.3,1}$ 88
Figure 4.16 – NWD: North (left) and east (right) face long. bar buckling at $-\mu_{9.3,1}$ 88
Figure 4.17 – NWD: Actual Force-Displacement Response 89
Figure 4.18 – NWD: Curvature profile for force-controlled cycles 90
Figure 4.19 – NWD: Curvature profile for displacement-controlled cycles 91
Figure 4.20 – NWD: BS3 strain gage history 92
Figure 4.21 – NWD: West face strain profile for force-controlled cycles 93
Figure 4.22 – NWD: West face strain profile for displacement-controlled cycles 93
Figure 4.23 – CLD: Actual loading protocol 95
Figure 4.24 – CLD: North face (left) and west face (right) at $\pm F_y^{'}/2$ 96
Figure 4.25 – CLD: East (left) and west (right) faces at $\pm F_y^{'}$ 96
Figure 4.26 – CLD: North face at $-\mu_{1.3,1}$ (left) and south face at $-\mu_{1.3,3}$ 97
Figure 4.27 – CLD: North face (left) and south face (right) at $-\mu_{1.8,3}$ 98
Figure 4.28 – CLD: East (left) and west (right) faces at $-\mu_{2.7,3}$ 99
Figure 4.29 – CLD: East (left) and west (right) faces at $-\mu_{5.4,1}$ 100
Figure 4.30 – CLD: East face at $-\mu_{5.4,3}$ (left), $-\mu_{7.8,1}$ (center), and $-\mu_{7.8,3}$ (right) 101
Figure 4.31 – CLD: West face at $-\mu_{5.4,3}$ (left), $-\mu_{7.8,1}$ (center), and $-\mu_{7.8,3}$ (right) 101
Figure 4.32 – CLD: West face long. bar buckling and stirrup detachment at $-\mu_{7.8,3}$ 102
Figure 4.33 – CLD: North face at $-\mu_{5.4,3}$ (left), $-\mu_{7.8,1}$ (center), and $-\mu_{7.8,3}$ (right) 102
Figure 4.34 – CLD: South face at $-\mu_{5.4,3}$ (left), $-\mu_{7.8,1}$ (center), and $-\mu_{7.8,3}$ (right) 103
Figure 4.35 – CLD: Actual Force-Displacement Response 104
Figure 4.36 – CLD: Curvature profile for force-controlled cycles 105

Figure 4.37 – CLD: Curvature profile for displacement-controlled cycles 105
Figure 4.38 – CLD: TS2 strain gage history 107
Figure 4.39 – CLD: East face strain profile for force-controlled cycles 108
Figure 4.40 – CLD: East face strain profile for displacement-controlled cycles 108
Figure 4.41 – SHD: Actual loading protocol 109
Figure 4.42 – SHD: South face (left) and west face (right) at $\pm 3F_y^{'}/4$ 110
Figure 4.43 – SHD: South face (left) and west face (right) at - $\mu_{1.8,3}$ 111
Figure 4.44 – SHD: East (left) and west (right) faces at - $\mu_{3.6,3}$ 112
Figure 4.45 – SHD: West face at - $\mu_{5.4,1}$ (left), - $\mu_{5.4,3}$ (center), and - $\mu_{7.6,1}$ (right) 112
Figure 4.46 – SHD: North face at - $\mu_{5.4,1}$ (left), - $\mu_{5.4,3}$ (center), and - $\mu_{7.6,1}$ (right) 113
Figure 4.47 – SHD: South face at - $\mu_{5.4,1}$ (left), - $\mu_{5.4,3}$ (center), and - $\mu_{7.6,1}$ (right) 113
Figure 4.48 – SHD: West face long. bar buckling (left) and stirrup detachment (right) at - $\mu_{7.6,1}$ 114
Figure 4.49 – SHD: Actual Force-Displacement Response 115
Figure 4.50 – SHD: Curvature profile for force-controlled cycles 116
Figure 4.51 – SHD: Curvature profile for displacement-controlled cycles 116
Figure 4.52 – SHD: BS3 strain gage history 117
Figure 4.53 – SHD: West face strain profile for force-controlled cycles 118
Figure 4.54 – SHD: West face strain profile for displacement-controlled cycles 119
Figure 4.55 – SLD: Actual loading protocol 120
Figure 4.56 – SLD: West (left) and south faces (right) at $\pm F_y^{'}$ 121
Figure 4.57 – SLD: North (left) and south faces (right) at - $\mu_{1.7,3}$ 122
Figure 4.58 – SLD: West face at - $\mu_{5.1,3}$ (left), - $\mu_{6.9,1}$ (center), and + $\mu_{6.9,3}$ (right) 123
Figure 4.59 – SLD: North face at - $\mu_{5.1,3}$ (left), - $\mu_{6.9,1}$ (center), and + $\mu_{6.9,3}$ (right) 123
Figure 4.60 – SLD: West face long. bar buckling (left) and stirrup detachment (right) after + $\mu_{6.9,3}$ 124
Figure 4.61 – SLD: Actual Force-Displacement Response 125
Figure 4.62 – SLD: Curvature profile for force-controlled cycles 126
Figure 4.63 – SLD: Curvature profile for displacement-controlled cycles 126
Figure 4.64 – SLD: West face strain gage history 127

CHAPTER 5 – TEST COMPARISONS

Figure 5.1 – Force-displacement envelopes for normal-strength (left, Robalino 2006) and high-strength (right) brittle test specimens, for first cycle of loading (a and d), second cycle (b and e), and third cycle (c and f) ... 129
Figure 5.2 – Force-displacement envelopes for normal-strength (left, Robalino 2006) and high-strength (right) ductile test specimens, for first cycle of loading (a and d), second cycle (b and e), and third cycle (c and f) ... 132

Figure 5.3 – Damping values for high-strength brittle (left) and ductile (right) test specimens 142
Figure 5.4 – Correction factors applied to Jacobsen Damping (Priestley et al. 2007) 143
Figure 5.5 – Corrected damping values plotted with Dwairi model for a) brittle and b) ductile tests 144
Figure 5.6 – V_n vs. ductility for high-strength brittle tests 146
Figure 5.7 – V_n vs. ductility for high-strength ductile tests 147
Figure 5.8 – Actual and predicted γ values for high-strength shale lightweight brittle test specimens 148
Figure 5.9 – Actual and predicted γ values for high-strength normal weight and shale lightweight 149
Figure 5.10 – Max strain vs. shear deformation for tests with working strain gages 150
Figure 5.11 – Revised strength degradation analytical models for normal-strength concrete shear resisting mechanism (Robalino 2006) 151

CHAPTER 6 – CONCLUSIONS AND RECOMMENDATIONS

Figure 6.1 – Strength degradation analytical models for normal-strength and high-strength concrete shear resisting mechanisms 155

APPENDIX

Figure 7.1 – Shear deformation by components (left) and shear deformation envelopes (right) for clay brittle specimen 164
Figure 7.2 – Shear deformation by components (left) and shear deformation envelopes (right) for shale brittle specimen 164
Figure 7.3 – Shear deformation by components (left) and shear deformation envelopes (right) for slate brittle specimen 164
Figure 7.4 – Shear deformation by components (left) and shear deformation envelopes (right) for normal weight ductile specimen 165
Figure 7.5 – Shear deformation by components (left) and shear deformation envelopes (right) for clay ductile specimen 165
Figure 7.6 – Shear deformation by components (left) and shear deformation envelopes (right) for shale ductile specimen 166
Figure 7.7 – Shear deformation by components (left) and shear deformation envelopes (right) for slate ductile specimen 166
Figure 7.8 – Shear Deformation envelopes for all brittle tests 167
Figure 7.9 – Shear Deformation envelopes for all ductile tests 167
Figure 7.10 – Deformation components for clay (left) and shale (right) brittle specimens 168
Figure 7.11 – Deformation components for slate brittle specimen 169

Figure 7.12 – Deformation components for normal weight (left) and clay (right) ductile specimens 169
Figure 7.13 – Deformation components for shale (left) and slate (right) ductile specimens..... 169
Figure 7.14 – Areas for use with Jacobsen's approach 170
Figure 7.15 – Brittle test force-displacement responses – a) NWB, b) CLB, c) SHB, d) SLB 172
Figure 7.16 – Ductile test force-displacement responses – a) NWB, b) CLB, c) SHB, d) SLB 173
Figure 7.17 – CLB: Strain gage histories – a) TS2, b) TS3, c) BS1 174
Figure 7.18 – SHB: East face strain gage histories – a) TS1, b) TS2, c) TS3..... 175
Figure 7.19 – SHB: West face strain gage histories – a) BS1), b) BS2, c) BS4 and d) BS5..... 176
Figure 7.20 – SLB: East face strain gage histories 176
Figure 7.21 – NWD: East face strain gage histories – a) TS1, b) TS2, c) TS3 177
Figure 7.22 – NWD: West face strain gage histories – top left (BS1), top right (BS2), bottom left (BS3) and bottom right (BS4)..... 178
Figure 7.23 – CLD: Strain gage histories – a) TS1, b) TS2, c) BS2..... 179
Figure 7.24 – SHD: East face strain gage histories – left (TS2), right (TS3)..... 179
Figure 7.25 – SHD: West face strain gage histories – a) BS1, b) BS2, c) BS3, d) BS4, e) BS5..... 180
Figure 7.26 – SLD: Strain gage histories for east (left) and west (right) faces..... 181
Figure 7.27 – CLB: North face linear potentiometer histories – a) N1, b) N2, c) N3, d) N4, e) N5..... 182
Figure 7.28 – CLB: South face linear potentiometer histories – a) S1, b) S2, c) S3, d) S4, e) S5 183
Figure 7.29 – CLB: East face linear potentiometer histories – a) E1, b) E2, c) E3, d) E4..... 184
Figure 7.30 – CLB: West face linear potentiometer histories – a) W1, b) W2, c) W3, d) W4..... 185
Figure 7.31 – SHB: North face linear potentiometer histories – a) N1, b) N2, c) N3, d) N4, e) N5..... 186
Figure 7.32 – SHB: South face linear potentiometer histories – a) S1, b) S2, c) S3, d) S4, e) S5 187
Figure 7.33 – SHB: East face linear potentiometer histories – a) E1, b) E2, c) E3, d) E4..... 188
Figure 7.34 – SHB: West face linear potentiometer histories – a) W1, b) W2, c) W3, d) W4..... 189
Figure 7.35 – SLB: North face linear potentiometer histories – a) N1, b) N2, c) N3, d) N4, e) N5..... 190
Figure 7.36 – SLB: South face linear potentiometer histories – a) S1, b) S2, c) S3, d) S4, e) S5 191
Figure 7.37 – SLB: East face linear potentiometer histories – a) E1, b) E2, c) E3, d) E4..... 192

Figure 7.38 – SLB: West face linear potentiometer histories – a) W1, b) W2, c) W3, d) W4 193
Figure 7.39 – NWD: North face linear potentiometer histories – a) N1, b) N2, c) N3, d) N4, e) N5 194
Figure 7.40 – NWD: South face linear potentiometer histories – a) S1, b) S2, c) S3, d) S4, e) S5 195
Figure 7.41 – NWD: East face linear potentiometer histories – a) E1, b) E2, c) E3, d) E4 196
Figure 7.42 – NWD: West face linear potentiometer histories – a) W1, b) W2, c) W3, d) W4 197
Figure 7.43 – CLD: North face linear potentiometer histories – a) N1, b) N2, c) N3, d) N4, e) N5 198
Figure 7.44 – CLD: South face linear potentiometer histories – a) S1, b) S2, c) S3, d) S4, e) S5 199
Figure 7.45 – CLD: East face linear potentiometer histories – a) E1, b) E2, c) E3, d) E4 200
Figure 7.46 – CLD: West face linear potentiometer histories – a) W1, b) W2, c) W3, d) W4 201
Figure 7.47 – SHD: North face linear potentiometer histories – a) N1, b) N2, c) N3, d) N4, e) N5 202
Figure 7.48 – SHD: South face linear potentiometer histories – a) S1, b) S2, c) S3, d) S4, e) S5 203
Figure 7.49 – SHD: East face linear potentiometer histories – a) E1, b) E2, c) E3, d) E4 204
Figure 7.50 – SHD: West face linear potentiometer histories – a) W1, b) W2, c) W3, d) W4 205
Figure 7.51 – SLD: North face linear potentiometer histories – a) N1, b) N2, c) N3, d) N4, e) N5 206
Figure 7.52 – SLD: South face linear potentiometer histories – a) S1, b) S2, c) S3, d) S4, e) S5 207
Figure 7.53 – SLD: East face linear potentiometer histories – a) E1, b) E2, c) E3, d) E4 208
Figure 7.54 – SLD: West face linear potentiometer histories – a) W1, b) W2, c) W3, d) W4 209

CHAPTER 1 – INTRODUCTION

This chapter covers the general definition of lightweight concrete, objectives, and motivation for the research. Also included is a brief section covering previous research directly related to high-strength concrete and shear strength of lightweight concrete from January 2006 to May 2008. The reader is referred to Robalino, 2006 for a more detailed literature review with regards to the shear performance of lightweight concrete members preceding 2006.

Instrumental to the understanding of lightweight concrete behavior is the concrete's defining characteristics and the process of creating it. The definition of lightweight concrete varies depending on the source, but is generally any concrete with a density around 115 to 125 pounds per cubit feet (pcf) in comparison to normal weight concrete, which is about 150 pcf. Typically this represents about a twenty percent reduction in mass, which is desirable for the design of buildings in seismic areas. A reduction in mass leads to a reduction in lateral forces, so the required sizes of members and foundations are smaller, thus reducing cost as well as construction time.

Lightweight concrete is typically composed of either lightweight sand or lightweight aggregate. This research focuses on lightweight aggregate, consisting of select minerals expanded in a rotary kiln. These minerals become porous, reducing their unit weight while keeping other important properties such as durability intact (ESCSI 2006). The three aggregates used for this project are representative of

those readily available within the U.S., namely shale from the Midwest, slate from the Southeast, and clay minerals from the West Coast.

The objective is to determine the shear strength of high-strength lightweight rectangular columns and compare different lightweight test specimens with one another as well as with normal weight specimens. Other factors of interest are also compared, including displacement capacity, strength degradation, and energy absorption. Recommendations are made for the Revised UCSD shear model (Kowalsky and Priestley, 2000) when using high-strength lightweight concrete.

Previous Research

There has been very little research in the area of shear performance of lightweight concrete columns under reversed cyclic loading. However there has been a significant amount of research in the separate categories of high-strength concrete in seismic regions, shear strength of columns, columns in seismic regions, and shear strength of concrete members in seismic regions. This section provides some examples of the research in these areas over the past two years.

"Seismic Testing of Bridge Columns Incorporating High-Performance Materials" Restrepo et. al., 2006.

This paper appearing in the ACI Structural Journal investigates the performance of two bridge column units with respect to drift capacity and the formation of plastic hinges. The columns were constructed of 8 ksi concrete and

reinforced with high-performance reinforcing steel. The main conclusion from this research was that columns of this type are able to “form flexural plastic hinges and can sustain drift levels of approximately 4% without failure,” (Restrepo et. al. 2006).

“Shear Strength of Reinforced Concrete Members Subjected to Monotonic Loads”
Ramin and Matamoros, 2006.

This paper describes the development of a model for calculating the shear strength of concrete members, considering components related to arch action, truss action, friction, and the contribution of the un-cracked compression zone. The model was found to be reasonably accurate in providing shear strength predictions for members of a wide range of geometries, compressive strengths, and with variable amounts of transverse steel.

“Seismic Performance of Full-Scale Reinforced Concrete Columns”
Bae and Bayrak, 2008.

Simulated seismic tests were conducted on five columns, and the results are presented in this research paper. The paper finds that the member performance of columns is significantly affected by the shear span to depth ratio at high axial load levels, and also that “the axial load applied on a column plays an important role in determining the plastic hinge length,” (Bae and Bayrak 2008).

“Seismic Behavior of RC Columns with Circular, Square, and Diamond Sections” Xiao and Zhang, 2008.

Fourteen large-scale columns of different sectional geometries were tested for this project. The results compared well with the numerical solution procedure developed in the paper. The paper concludes with recommendations on limiting values of the axial compressive stress ratio for the three different geometric shapes tested.

“Deformation Capacity and Shear Strength of Reinforced Concrete Members Under Cyclic Loading” ACI Committee 445 and ACI Committee 441, 2006.

This is a symposium publication, and serves as a compilation of several papers on the subject. This publication includes some of the recent research on this topic with the goal of leading to an improved model for performance-based engineering.

“Shear Performance of Reinforced Lightweight Concrete Square Columns in Seismic Regions” Robalino, 2006.

As stated in the abstract, the research presented in the current work involves a second set of tests, the first of which was conducted by Pablo Robalino at North Carolina State University. Robalino used reversed cyclic loading to investigate the shear performance of normal-strength (4ksi) concrete, and will be discussed further throughout this document.

Motivation

Two well-documented cases involving the failure of lightweight concrete in earthquakes are summarized in this section.

In 1971, San Fernando, CA experienced an earthquake of magnitude 6.6. The Olive View Hospital complex in San Fernando included several buildings composed of lightweight concrete, constructed between 1964 and 1970. Many of these structures were badly damaged. The Psychiatric Unit was the most severely damaged (Figure 1.1). The first story columns completely collapsed due to a shear failure. Initially, lightweight concrete was thought to have been the cause.

Figure 1.1 – Second floor of the Olive View Hospital Psychiatric Ward after the San Fernando earthquake

Upon further examination, the failure was actually attributed to the complex's pre-1971 non-ductile design rather than the lightweight concrete itself. The columns of this particular building were detailed with an insufficient amount of transverse reinforcement (Jennings 1971). Another lightweight concrete building that was

damaged in this complex was the auditorium. This one-story building suffered large displacements resulting in a complete loss of the structure. The failure is suggested to have been caused by an insufficient amount of lateral displacement resistance (Jennings 1971).

A 6.9 magnitude earthquake occurred in Loma Prieta, CA in 1989. This caused significant damage to the Cypress Viaduct, a two level 1.2 mile long freeway built in the 1950's (Figure 1.2). Several sections of the second level collapsed onto the first.

Figure 1.2 – A portion of the Cypress Viaduct after the Loma Prieta earthquake

Only one section of this bridge (one bent and two columns) was made of lightweight concrete. However this section on the first level was the most heavily damaged of all the first level columns. This failure was eventually attributed to insufficient transverse reinforcement (USGS 1989).

The American Concrete Institute (ACI) requires a reduction in the calculation of the concrete component of shear capacity of lightweight concrete. When using lightweight sand this reduction is 15%, and is 25% when using other lightweight concrete mixtures, including those with lightweight aggregate (ACI 11.2.1.2). ACI also limits the use of high-strength lightweight concrete to a compressive strength of 5 ksi in seismic design, “unless demonstrated by experimental evidence that structural members made with that lightweight concrete provide strength and toughness equal to or exceeding those of comparable members made with normal weight concrete of the same strength,” (ACI 21.2.4.2).

The physical properties of lightweight concrete contribute to its potentially lower shear strength. Because lightweight aggregate is porous, it is weaker in tension than normal weight aggregate and thus more susceptible to cracking. The shear cracks that develop in the member travel through the aggregate rather than around the aggregate as in normal weight concrete. This creates a smoother concrete surface (Figure 1.3), reducing the aggregate interlock (friction between surfaces) and thus the shear capacity.

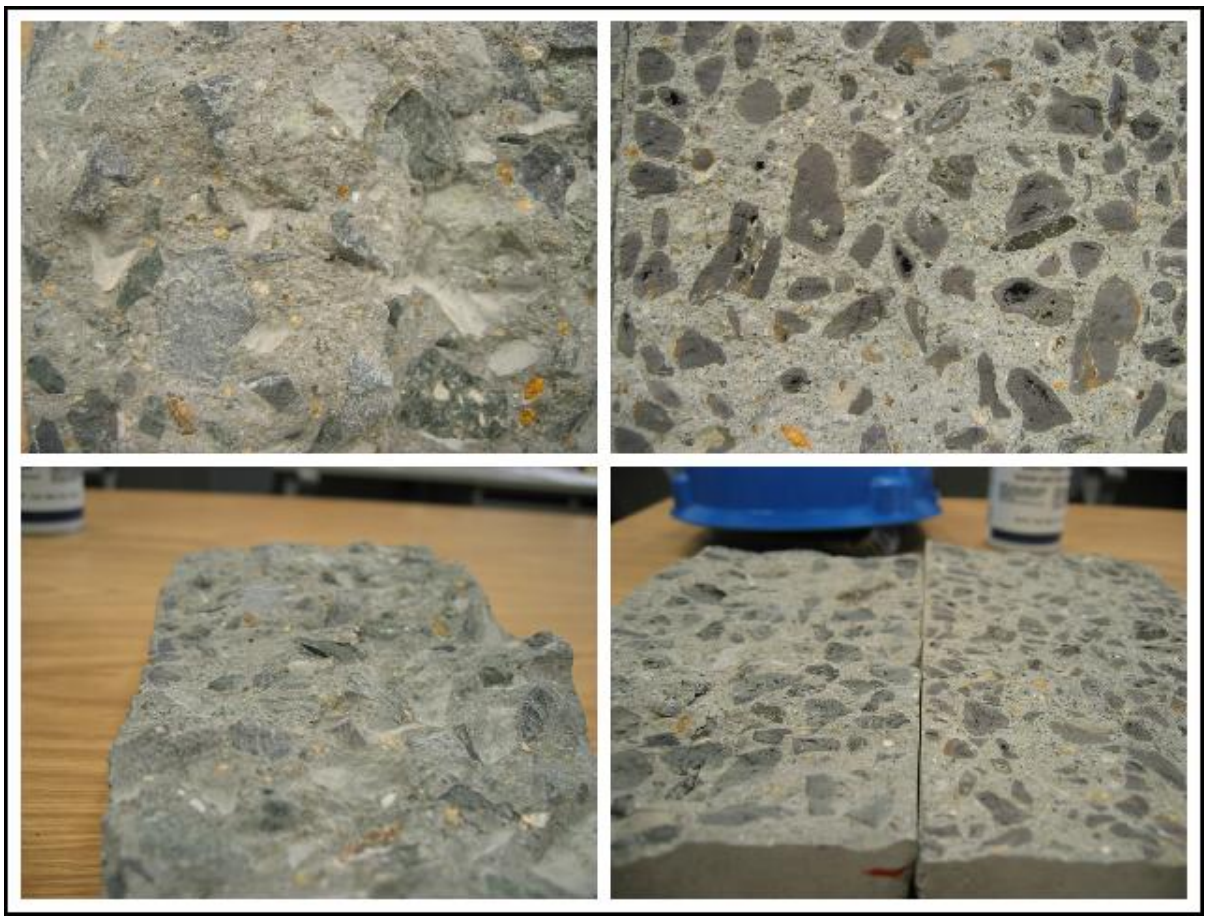

Figure 1.3 – Normal weight (left) and lightweight (right) concrete surfaces

This introduction chapter explained the objectives and motivation behind this research. It is the past performance of lightweight concrete, the significant reductions in shear strength required by ACI, the nature of lightweight aggregate, and a lack of previous research that shows the needed for this research project. The topics of test design, setup, analysis, results, and conclusions will be addressed in the following chapters.

CHAPTER 2 – TEST DESIGN, SETUP, AND PROCEDURE

This portion covers the technical aspects involving the test specimens. The shear model used for this research is discussed in the first section. This leads into the design of the test specimens, followed by the casting procedure and the setup for testing in the laboratory. The instrumentation is listed and the chapter concludes with a general loading schedule that was used as the testing procedure.

Modeling

This research project utilizes the Revised UCSD shear model developed at the University of California at San Diego (Kowalsky and Priestley 2000). The model consists of three separate components of the shear capacity of a column shown below in equation 2.1, where V_n is the nominal shear capacity, V_c is the concrete shear resisting mechanism, V_p is the contribution of axial load to shear capacity, and V_s is the shear capacity of the steel truss mechanism. Each component is described below in detail.

$$V_n = V_c + V_p + V_s \qquad \text{Eq. 2.1}$$

V_c, the shear capacity of concrete includes several variables for this model (Equation 2.2). Two of these variables are f_c' and A_g, which are the concrete strength and gross cross-sectional area of the member, respectively. The α factor accounts for the inverse relationship of the strength of the concrete shear resisting mechanism and the aspect ratio, as observed in tests. In other words, shorter columns experience a confining effect from the nearby footing or other connection,

more so than a taller column. α is given in equation form (Eq. 2.3) as well as graphical form (Fig. 2.1), where L is the length and D is the depth of the member.

$$V_c = \alpha\beta\gamma\sqrt{f_c'}(0.8A_g) \qquad \text{(MPa)} \qquad \text{Eq. 2.2}$$

$$1 \le \alpha = 3 - \frac{L}{D} \le 1.5 \qquad \text{Eq. 2.3}$$

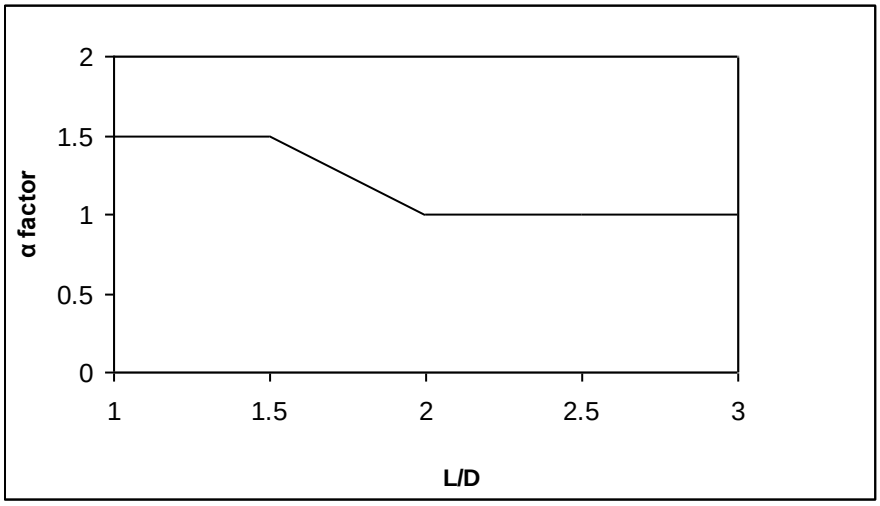

Figure 2.1 – α factor for V_c equation

Another factor in the calculation of V_c is β, which is proportional to the longitudinal steel ratio of the column (Eq. 2.4, Fig. 2.2). A section with a higher longitudinal steel ratio (ρ_l) will tend to have smaller cracks. This means the aggregate interlock is higher, which increases the concrete shear capacity.

$$\beta = 0.5 + 20\rho_l \le 1 \qquad \text{Eq. 2.4}$$

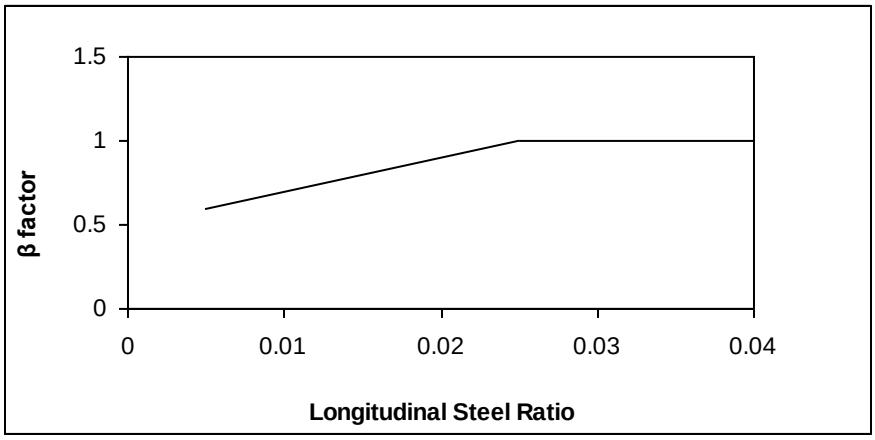

Figure 2.2 – β factor for V_c equation

Perhaps the most important variable in the V_c formula is γ (Fig. 2.3). This variable represents the observed effect of decreasing shear capacity with increasing ductility. As ductility increases, cracks widen, and aggregate interlock is lost, decreasing the shear resistance of the concrete. Note that when using the lightweight portion of this model, there is a 15% reduction for ductility levels below 2 (0.29 to 0.25), a 30% reduction for levels above 8 (0.050 to 0.035) and a linear transition between.

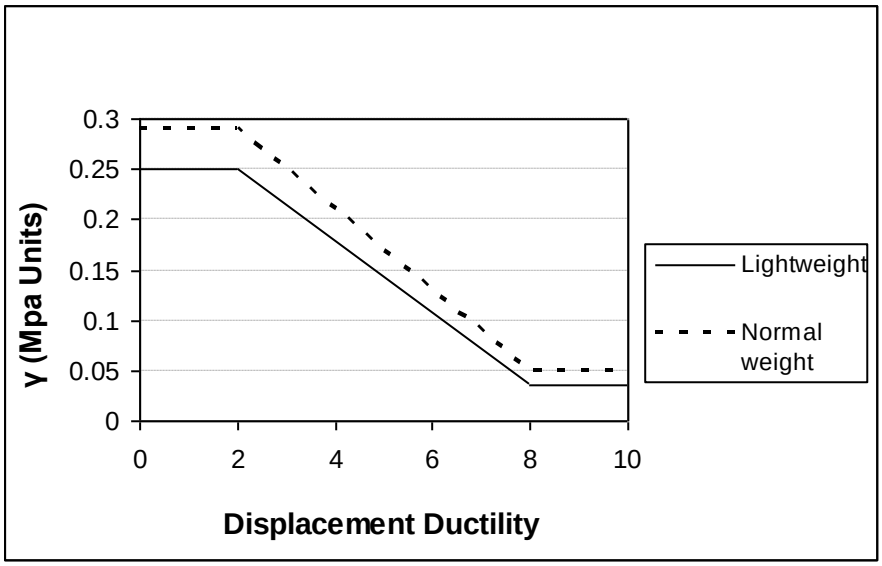

Figure 2.3 – γ factor for V_c equation

V_p is the contribution of the axial load to shear capacity (Eq. 2.5, 2.6). It is taken as the horizontal component of the compressive axial load that is transferred through the inclined strut along the member as shown in Figure 2.4.

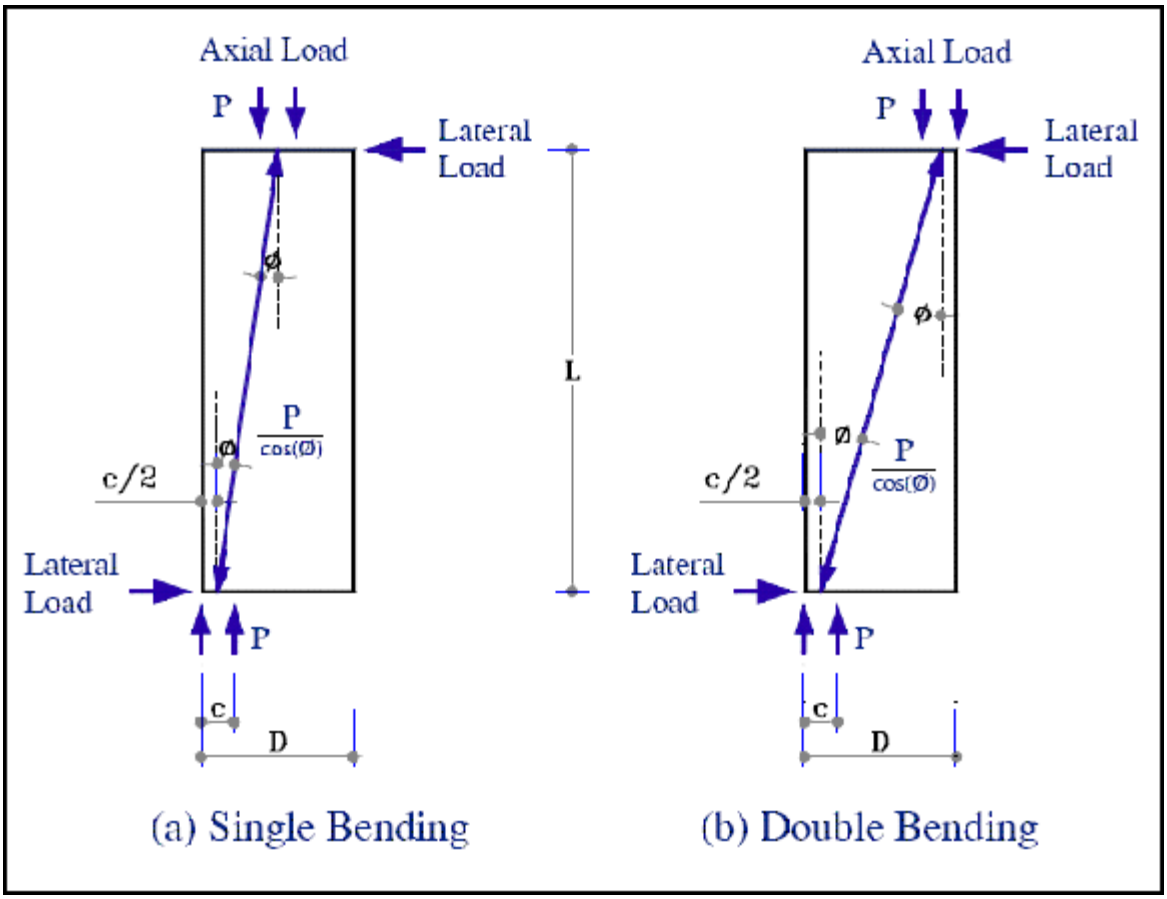

Figure 2.4 – Shear strength contribution due to compressive axial load (Robalino 2006)

The compressive load enters and exits through the center of the compressive section of the columns. For a column experiencing single bending, which is the case for this project, the load enters through the center of the applied load at the top of the column and exits through the center of the compression zone at the bottom of the column. For columns in double bending, the load enters and exits through the center of the compression zones at the top and bottom of the column.

$$V_p = P\frac{(D-c)}{2L} \quad \text{for P > 0} \qquad \text{Eq. 2.5}$$

$$V_p = 0 \quad \text{for P} \leq 0 \qquad \text{Eq. 2.6}$$

P is the axial load where compression is positive, and c is the distance to the neutral axis.

V_s is the shear capacity of the steel truss mechanism, shown in Equation 2.7.

$$V_s = A_s f_y \frac{(D - c - \mathrm{cov})}{s} \cot(\theta) \qquad \text{Eq. 2.7}$$

A_s is the area of steel that is contributing to shear resistance, which is the steel that crosses the shear cracks that are formed. For square sections with symmetric stirrup layouts, this value is the area of one stirrup multiplied by the number of stirrup legs in the direction of loading. f_y is the yield stress of the steel, cov is the cover to the outside of the longitudinal reinforcement, s is the spacing, and θ is the average inclination of the shear cracks as illustrated in Figure 2.5, which is assumed to be 30° for this model.

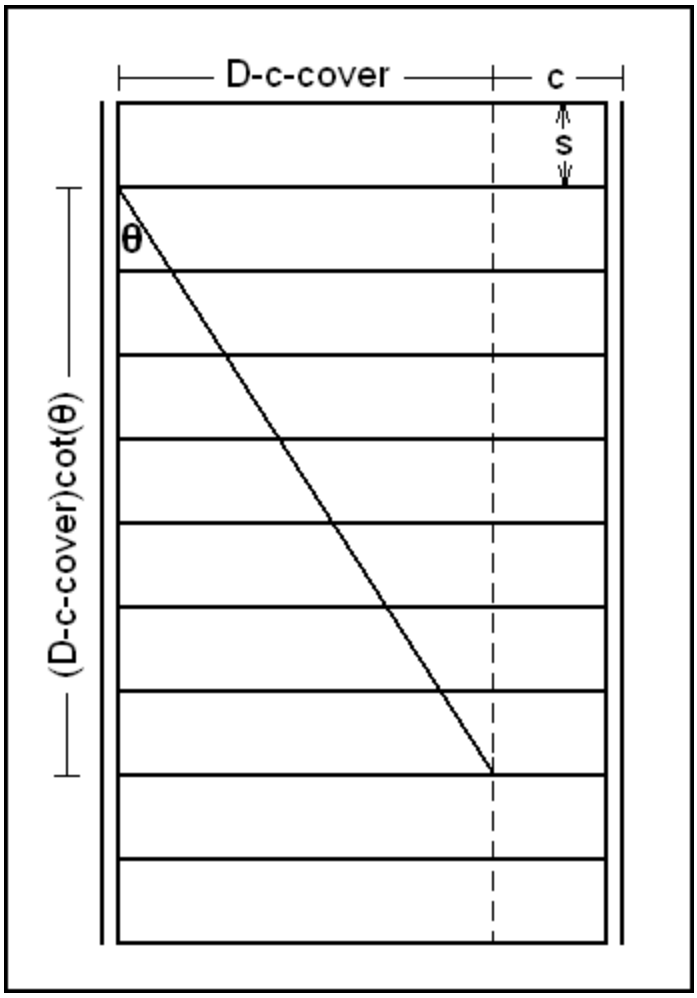

Figure 2.5 – Illustration of variables in V_s equation

This model recognizes that it is not the entire stirrup that is effective in resisting shear forces in the member, but only the steel that is in the tension zone of the member. Because the cracks are closed in the compression zone, the steel in this region does not contribute to the shear capacity.

The total shear capacity of a member is the sum of concrete, axial load, and steel truss contributions. V_p and V_s are constants assuming a single value of the

neutral axis depth, which can be predicted. Therefore the shape of V_n is controlled by the shape of V_c.

Column Design

In order to design the specimens for this research, the force-displacement response was needed. This can be obtained from a moment-curvature analysis of a section. A MATLAB computer program called CUMBIA (Montejo and Kowalsky 2007) was used for this purpose. This program generates moment-curvature plots using a sectional approach, and also generates force-displacement graphs. Sections of various sizes and steel configurations were used to create different force-displacement graphs for the purpose of obtaining specific types of failure. Also considered in this design was the limitation of the laboratory facility, such as capacity of the loading actuator and other equipment available for use.

A shear failure occurs at the intersection of the shear capacity envelope and the force-displacement envelope of a member. If a brittle shear failure is desired, the force-displacement graph intersects the low ductility plateau of the shear capacity graph (Figure 2.6). If a ductile shear failure is desired, the intersection occurs in the high ductility plateau (Figure 2.7). Note it is much more difficult to obtain a ductile shear failure than a brittle shear failure. If the two curves intersect at a displacement lower than where the ductile plateau begins, then a non-ductile shear failure occurs. If the two curves do not intersect, then a shear failure does not occur.

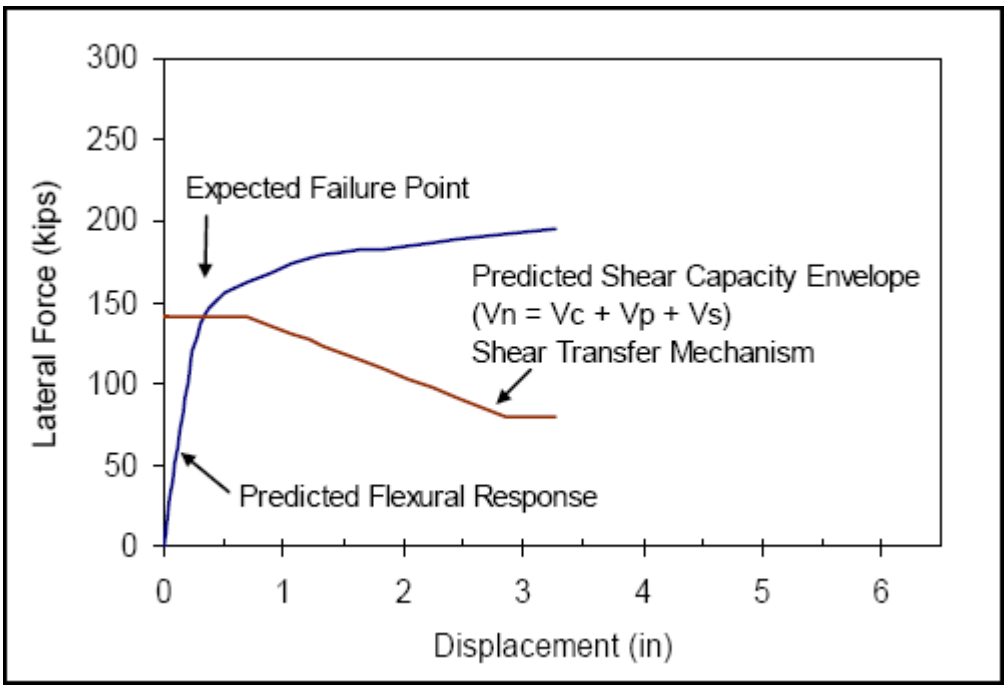

Figure 2.6 – Predictions of brittle shear failure for normal-strength specimens (Robalino 2006)

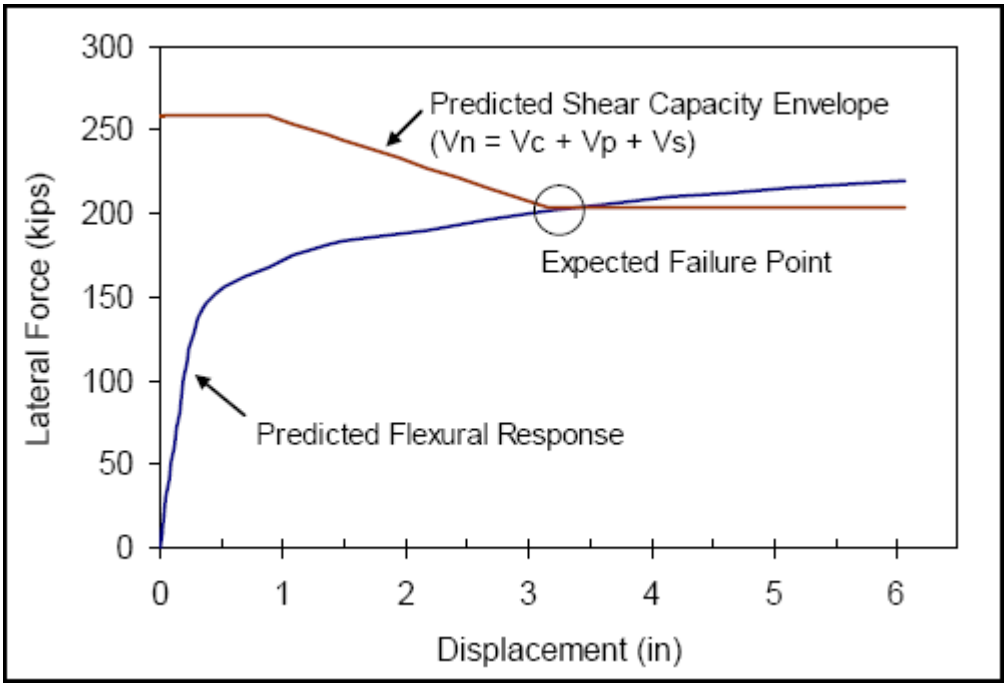

Figure 2.7 – Predictions of ductile shear failure for normal-strength specimens (Robalino 2006)

Robalino designed a section size with two configurations of steel for the two desired types of failure using this method (Figure 2.8). Each column was 5'6" tall. These same layouts were used for this research.

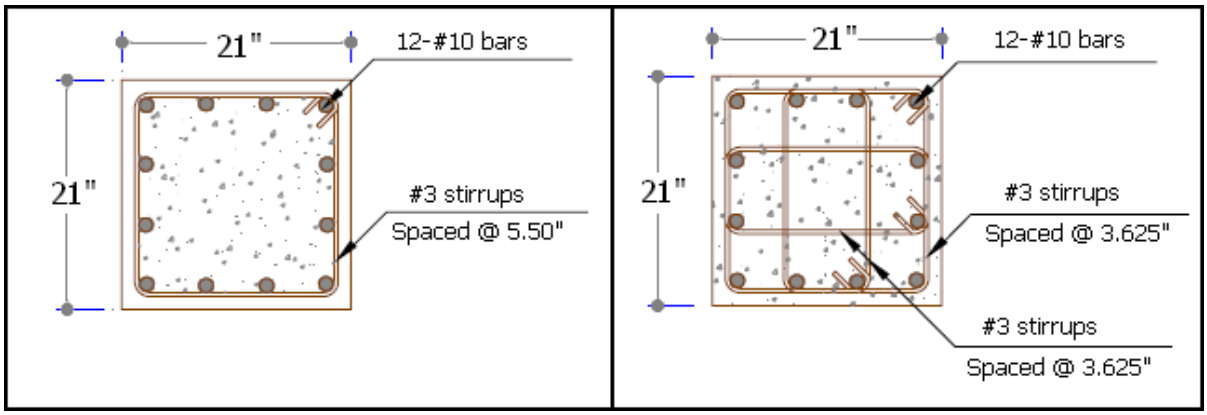

Figure 2.8 – Column section and steel reinforcement details, brittle (left) and ductile (right) (Robalino 2006)

The word 'ductility' when used in this document refers to displacement ductility. Δ_y is the equivalent first yield point on the moment curvature diagram and is defined as the first yield displacement (Δ_y') multiplied by a ratio of the nominal moment to the first yield moment as shown in Equation 2.8.

$$\Delta_y = \Delta_y' \frac{M_n}{M_y'} \qquad \text{Eq. 2.8}$$

$$\mu = \frac{\Delta}{\Delta_y} \qquad \text{Eq. 2.9}$$

The ductility is then computed using Equation 2.9, where the current displacement is divided by the displacement at equivalent first yield. Ductility one (μ_1) occurs when the displacement is equal to the first yield displacement. μ_2 is twice this number, μ_4 four times this number, and so on.

The testing matrix for this research is shown in Table 2.1. Note tests one through eight were identical except for concrete strength (4 ksi instead of 8 ksi) and were conducted by Robalino.

Table 2.1 – Testing matrix

All columns: f'_c = 8 ksi				
Test	Column I.D.	Aggregate Source and Type	Supplier	Shear Failure Mode
9	NWB	Normal Weight Aggregate	Ready Mixed	Brittle
10	NWD			Ductile
11	CLB	West Coast (Clay)	Fraiser Park	Brittle
12	CLD			Ductile
13	SHB	Midwest (Shale)	Buildex	Brittle
14	SHD			Ductile
15	SLB	Southeast (Slate)	Stalite	Brittle
16	SLD			Ductile

The first two letters of the Column I.D. represent the type of aggregate, while the last letter distinguishes between a brittle and a ductile desired failure mode. Three lightweight aggregates were used (clay, shale, and slate), and normal weight aggregate was used for comparison. There were two specimens of each aggregate type for the two different failure modes.

Casting

The casting of all specimens used for testing took place in May and June of 2007 outdoors at Constructed Facilities Laboratory on the NCSU campus in Raleigh, NC. Wooden formwork was used to cast the T-shape sections, two at a time (Figure 2.9).

Figure 2.9 – In the foreground, formwork setup before concrete pour (left) and after (right)

PVC pipes were used to create holes in the concrete for column attachment to the actuator, and for post-tensioning in the footing, which will be illustrated in the next section.

Each concrete pour involved one type of concrete with the two different configurations of steel (Figure 2.10). A closer spacing of stirrups was used towards the top part of the column to insure minimal damage in this area where the load would be applied.

Figure 2.10 – Brittle failure (left) and ductile failure (right) steel cages inside formwork

A vibrator was used during concrete pours and very few voids were found in the concrete upon curing. Moist burlap was applied to the concrete surface after each concrete pour to enhance the curing process, and each specimen was covered with plastic. The formwork was removed three to four days after the concrete pour.

Two final specimens are shown in Figure 2.11. This figure also shows cylinders that were made during a concrete pour, that were later used to conduct compression and tensile tests. These cylinders were kept with the specimens at all times. This is not an ASTM standard, however obtaining the accurate strength of each specimen was important for this research, so this seemed most appropriate.

Figure 2.11 – Two specimens after the removal of formwork (left) and concrete cylinders (right)

Figure 2.12 shows how the T-shape section represents a half column in a building. This research used half-sized columns in single bending, as opposed to full-sized columns in double bending, which would have been a much more difficult and complicated lab setup, but results were expected to be similar.

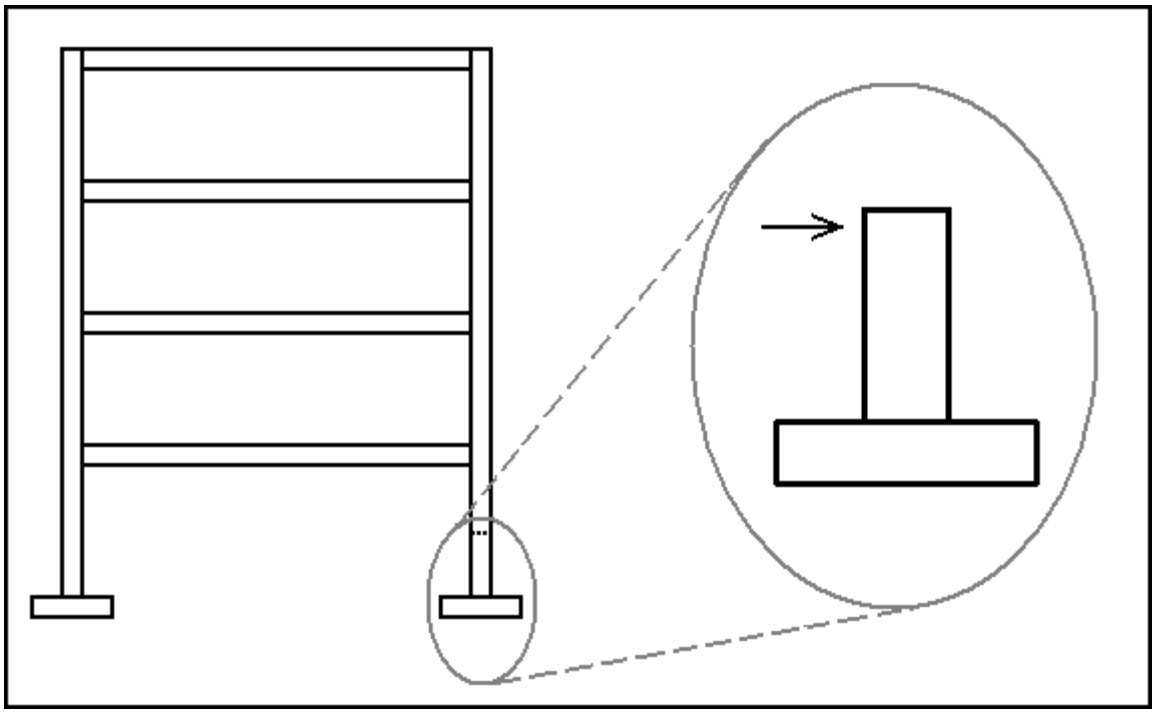

Figure 2.12 – Illustration of T-shape member

Concrete data is shown in Table 2.2. The unit weights were obtained using the standard ASTM C138 test, the tensile strengths were obtained from ASTM C496, and the compressive strength tests followed ASTM C39, with the exception of the curing method of the cylinders stated previously.

Table 2.2 – Concrete data

Column ID	Unit weight (lbs/ft^3)	28-day compressive strength (ksi)	Test Day strength (ksi)	28-day split tension strength (psi)
NWB	151	7.8	9.5	690
NWD			9.5	
CLB	124	7.6	8.4	551
CLD			8.4	
SHB	121	7.4	8.9	660
SHD			8.9	
SLB	120	7.8	8.5	611
SLD			8.5	

Test Setup

All tests took place indoors at Constructed Facilities Laboratory. Figure 2.13 shows one specimen at the beginning of setup. Three separate footing pieces can be seen.

Figure 2.13 – Test setup, specimen only

The central piece was cast with the column, while the other two pieces were post-tensioned to the central footing. A large footing was desired, so in order to prevent the entire footing from being cast each time, the two side footing pieces were created to be used with each of eight tests. A 50 kip load on each of two bars was used to post-tension the footing pieces together in order for the entire footing to act as one unit. The footing section details are shown in Figure 2.14. Each footing

piece was approximately 8’8” and was designed to be a fixed support for the column. The reaction wall and a large steel plate can be seen in the background on the right side of Figure 2.13. This plate was used to connect the actuator to the wall, which acted as a fixed support for the actuator.

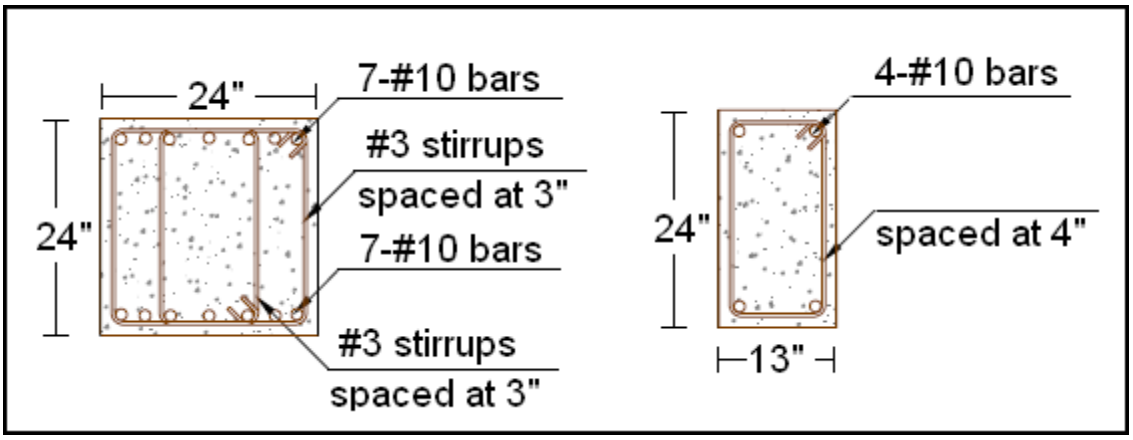

Figure 2.14 – Central (left) and side (right) footing cross sections (Robalino 2006)

Because concrete does not have a smooth surface, voids existed between the side footing pieces and the central footing, as well as between the footing pieces and the floor. A gypsum cement called Hydrocal® White was combined with water to form a mixture that could be poured into these locations, that would harden to 2000~3000 psi. This allowed forces to be transferred between the two rough surfaces. Examples are shown in Figure 2.15.

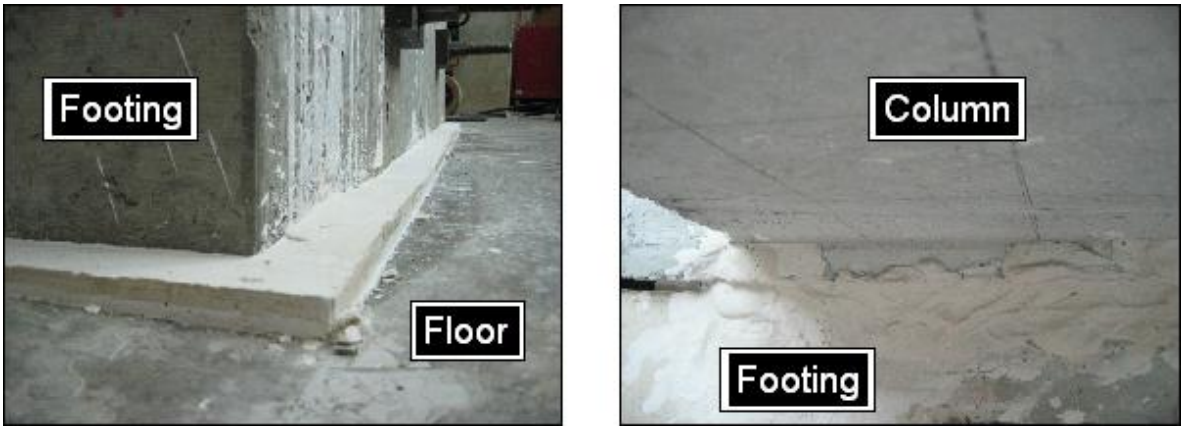

Figure 2.15 – Hydrocal® White poured under (left) and between (right) footing pieces

The footing pieces were placed on enough insulating board to hold the specimen off the ground before pouring the cement.

Figure 2.16 shows the completed setup of a test specimen. Each column was painted white for ease in the identification and marking of cracks. The 440 kip actuator was attached to the column using four threaded rods. The center of this actuator-to column connection is 4’6” above the footing, making this the effective column height.

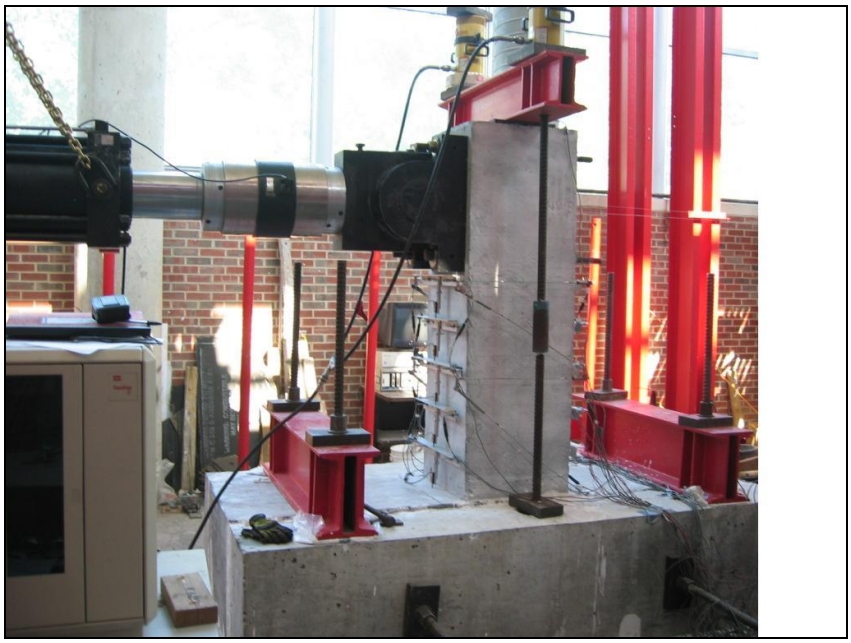

Figure 2.16 – Complete test setup

An axial load of approximately 176 kips, corresponding to a 5% axial load ratio, was applied to the column for the duration of the test. Although columns may experience higher axial loads, this number was felt to be reasonable for this test setup and was limited by the maximum capacity of the two 60-ton jacks that were used. Two crossbeams can be seen on each side of the footing. Two bars run through each crossbeam, the footing, and a 30” thick concrete floor. A post-tensioning force of 100 kips was applied to each of these bars to prevent overturning of the specimen due to the predicted maximum lateral load.

Instrumentation

From here on, the faces of the column will be referred to with cardinal directions, where north is the face where the actuator is attached, south is the face opposite of north, and east and west are the corresponding faces perpendicular to the direction of loading.

Several forms of instrumentation were used to collect data during tests. Five linear potentiometers were used on both the north and south faces of each column. They were bolted to metal angles which were anchored into the column, as shown in Figure 2.17 (left). They measured vertical displacement that could be used to calculate curvature and shear deformation.

Four larger linear potentiometers were also used on both the east and west faces in order to measure shear deformation. The configuration is shown in Figure 2.17 (right). Threaded rods were used to extend the gage lengths.

Figure 2.17 – Linear potentiometers on north face (left) and east face (right) of column

Ten strain gages were placed throughout the effective height of the column on transverse steel stirrups, so that strain in the steel at different loads and different locations could be determined (Figure 2.18). This information was used in calculating the actual steel truss contribution to shear capacity.

The specifications of the strain gages, loading actuator, and the data acquisition system can be found in the Appendix.

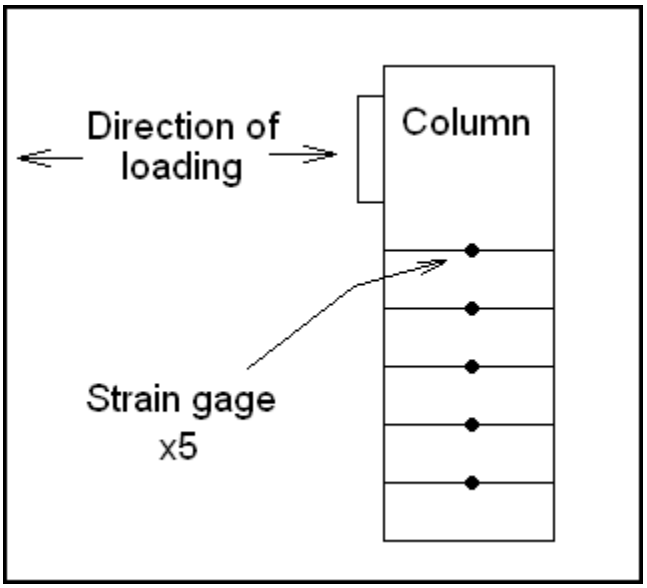

Figure 2.18 – Strain gage placements on transverse steel

In order to determine the displacement at the center of loading, two string potentiometers were placed at a fixed location and connected to the column at two points shown in Figure 2.19. Two string pots were used for accuracy, and also to determine if any twisting occurred in the column.

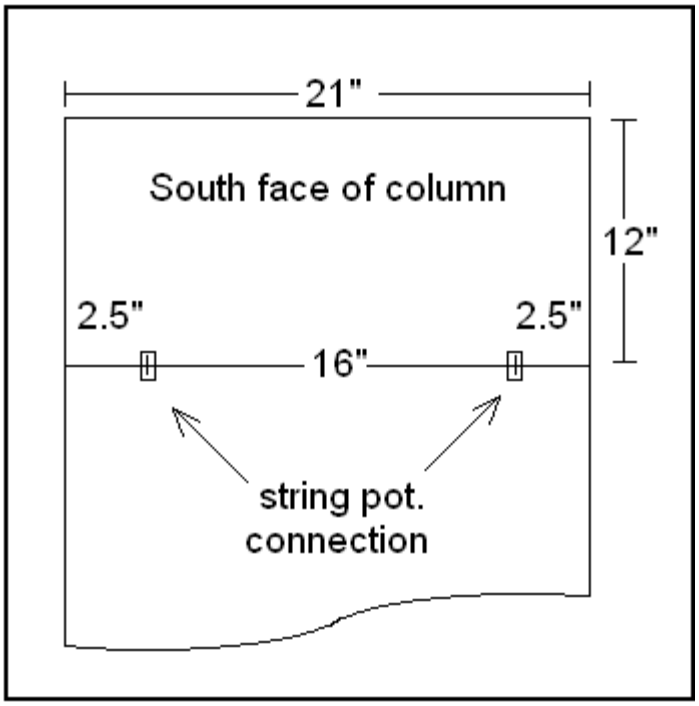

Figure 2.19 – String pot locations on south face of column

Additionally, one load cell was used to measure the axial load throughout the test. It was placed under one of the two loading jacks at the top of the column. Because the jacks were connected and each jack applied the same load, one load cell was sufficient.

General Loading Schedule

A general loading schedule that was used for all tests is shown in Figure 2.20. It consists of loading to quarter-points of predicted longitudinal steel yielding, then conducting three cycles of loading for each ductility level (μ_1, $\mu_{1.5}$, μ_2, μ_3, μ_4, μ_6, μ_8, μ_{10}). It should be noted that the brittle failure tests were not expected to exceed μ_3, while ductile failure tests were predicted to fail around μ_8. Tests were stopped at a

load that was approximately one half of the maximum load, indicating that a failure had most certainly occurred before that point.

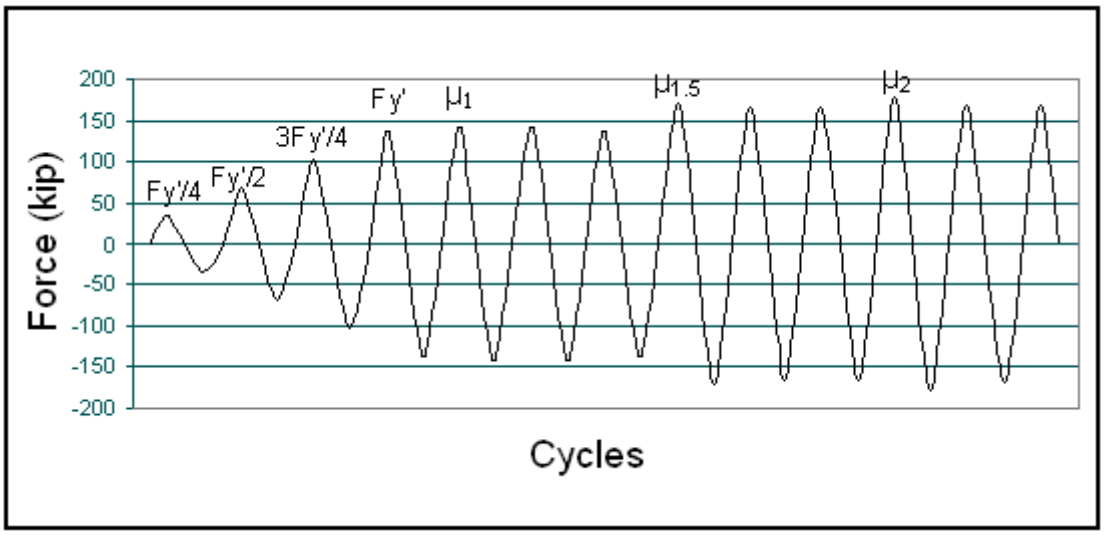

Figure 2.20 – General loading schedule

The ductility levels were calculated using Equations 2.8 and 2.9. The CUMBIA program described previously predicts M_n and M_y' for a given section, and Δ_y' may be found directly during testing.

Test descriptions, analyses, and conclusions are discussed in the following chapters.

CHAPTER 3 – BRITTLE SHEAR FAILURE SPECIMENS

This chapter will cover specific observations of the four brittle shear failure mode specimens, including pictures and descriptions. The force-displacement responses are shown for each test, followed by hysteretic damping calculations. The curvature and strain profiles are given as well. Final comparisons between the eight tests for this research and the eight normal-strength tests will be made in Chapter 5.

In Chapter 2, Figure 2.6 shows the predictions of the brittle shear failure mode by Robalino, 2006. This graph was used in the design of the test specimens. Since the same cross-section geometries and steel reinforcement were used for this research, but with an increase in concrete strength, the shear capacity changed. Recall that V_c is dependent upon concrete strength (Eq. 2.2). Comparing Figure 2.6 with Figure 3.1 shown below, note that the V_n graph has increased, and the intersection of both the lightweight and normal weight V_n graphs with the predicted force-displacement response has shifted. This indicates that the predicted failure is slightly more ductile for these higher strength concrete specimens compared to the normal-strength concrete specimens.

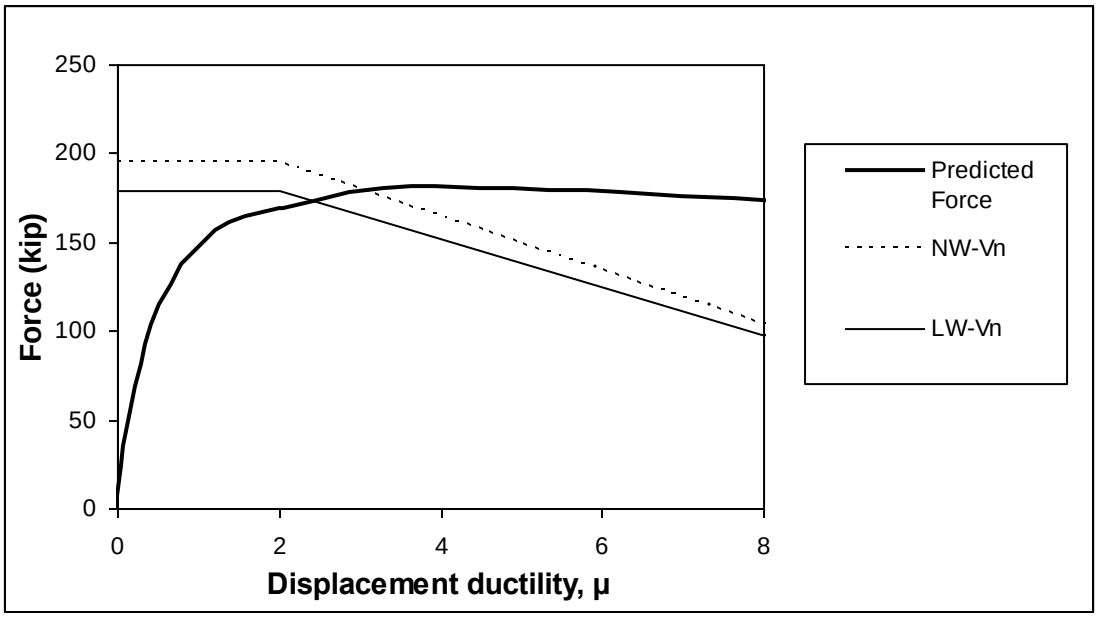

Figure 3.1 – Predicted Force-Displacement Response for Brittle Failure Mode

The first half of the loading protocol was force-controlled, since specific forces were desired. This included all loading up until the first yield point ($F_y^{'}$), which was predicted to be 136 kips. The second portion was displacement-controlled. The value of the μ_1 displacement for the first test was 0.41 inches, calculated from Equation 2.9. A new value for μ_1 was computed for the first four tests, upon finding the actual displacement at first yield ($F_y^{'}$). For the last four tests, the decision was made to assume a value of 0.41 inches for μ_1, so these tests would have the same load histories. In both cases, the actual ductility levels computed for each test individually are shown.

The test observations discussed here are presented in tabular form in Chapter 5, for easy comparison.

3.1 - Normal Weight Brittle Shear Failure Specimen (NWB)

Unfortunately, no raw data was obtained from the data acquisition system for this test. The only data obtained includes approximate force and displacement points and the ends of each cycle, axial load measurements, and pictures of the test.

The approximate loading procedure for this test is shown in Figure 3.2. The designation + $\mu_{1,1}$ corresponds to the push direction of the first cycle of μ_1. Other cycles are labeled in a similar manner.

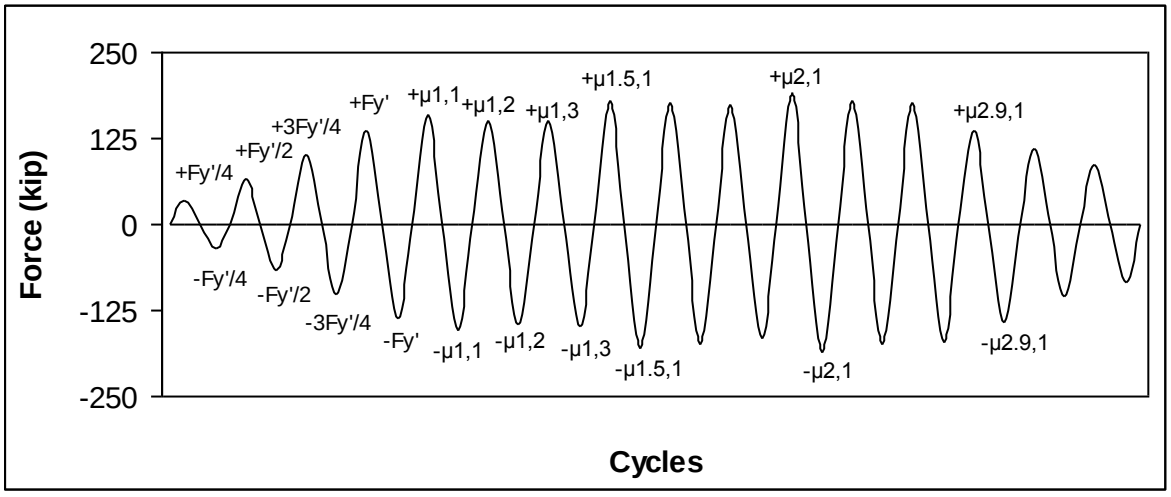

Figure 3.2 – NWB: Actual loading protocol

Force-controlled Cycles

The first flexural cracks appeared on the north and south faces during the push cycle of half of the predicted yield force (+ $F_y^{'}/2$ = 68 kips). These cracks developed in the lower half of the column, spaced about five to six inches apart,

consistent with the 5.5” spacing of the transverse reinforcement (Figure 3.3). The same observations were made during the pull cycle (- $F_y^{'}/2$).

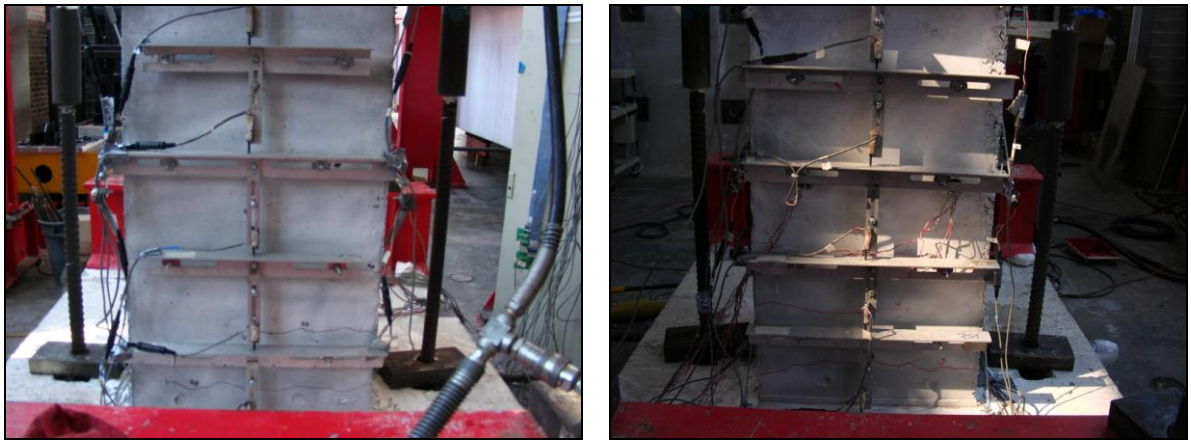

Figure 3.3 – NWB: North face (left) and south face (right) at $\pm F_y^{'}/2$

During the $\pm 3F_y^{'}/4$ cycle, the top half of the column began to show flexural cracking. Also, flexural cracks began to spread to the east and west faces. At this time, the cracks were generally horizontal. By the $\pm F_y^{'}$ cycle, the first flexure-shear cracks appear. These cracks on the east and west faces began as horizontal flexure cracks, but then begin to slope downwards to form shear cracks as shown in Figure 3.4.

Figure 3.4 – NWB: East (left) and west (right) faces at $\pm F_y^{'}$

Three more flexural cracks formed on the north and south faces, and one small vertical crack could be seen on the north face. The top displacement reached during the $+F_y^{'}$ cycle was 0.30 inches, and for $-F_y^{'}$ was -0.33 inches. The maximum measured flexural crack width was 0.012 in.

Displacement-controlled Cycles

The first μ_1 cycle (0.41 in. top displacement) produced the first shear-only cracks (shear cracks not originating from flexural cracks), as shown in Figure 3.5. On the north and south faces, a few vertical cracks formed, corresponding to the location of longitudinal steel due to the lateral expansion of the member. Examples of these cracks are shown for a later cycle (Figures 3.11 and 3.12). The largest crack width during this cycle was 0.03 in.

Figure 3.5 – NWB: East (left) and west (right) faces at $\pm\mu_{1,1}$

Because of degradation of the specimens, the second and third cycles achieve lower lateral forces. This generally means very few new cracks are produced, so these cycles will not be referenced throughout this document unless significant changes are recorded with regards to the first cycle.

The $\pm\mu_{1.5,1}$ cycle brought on more extensions of the flexure-shear and the shear-only cracks, with few new cracks. The maximum crack width was measured at 0.05 inches. The first evidence of minor concrete crushing and spalling occurred during this cycle on the south face (Figure 3.6). No other changes were recorded for the north and south faces until the second and third cycles, where more vertical cracks formed. The second and third cycles also caused an increase in the crack widths, obtaining values as high as 0.06 in.

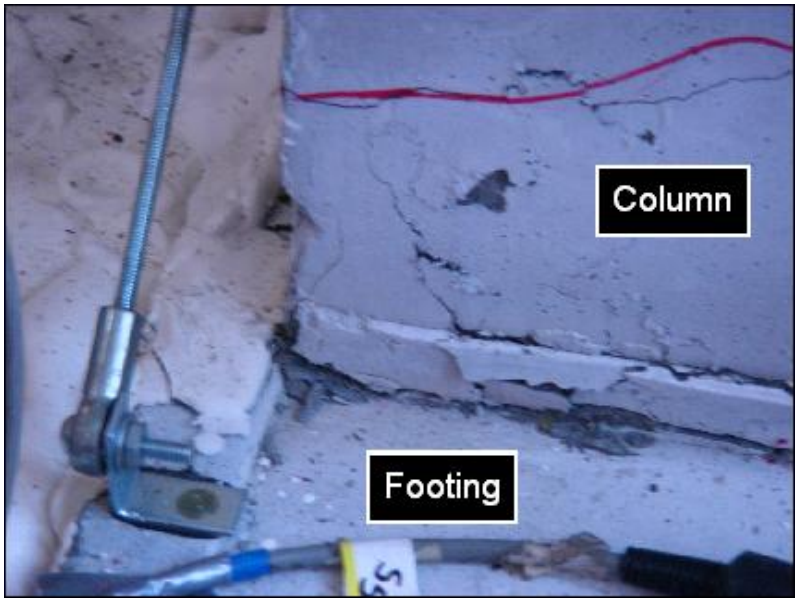

Figure 3.6 – NWB: Concrete crushing on south face at $\pm \mu_{1.5,1}$

The maximum lateral loads of +191 kips and -187 kips were achieved in the $\pm \mu_{2,1}$ cycle, and the displacement was ±0.82 inches. Cracks propagated on the east and west faces (Figure 3.7), and only one new crack was found on the north and south faces.

Figure 3.7 – NWB: East (left) and west (right) faces at maximum load ($\pm \mu_{2,1}$)

Crushing and spalling of the concrete became more prominent in the three cycles of $\pm \mu_2$ as seen in Figure 3.8. Several extensions of cracks appeared on the east and west faces in the second cycle, and cracks widened to a maximum of 0.08 inches. Only a few extensions occurred during the third cycle. No changes occurred on the north and south faces excluding progressive crushing at the bottom of each face.

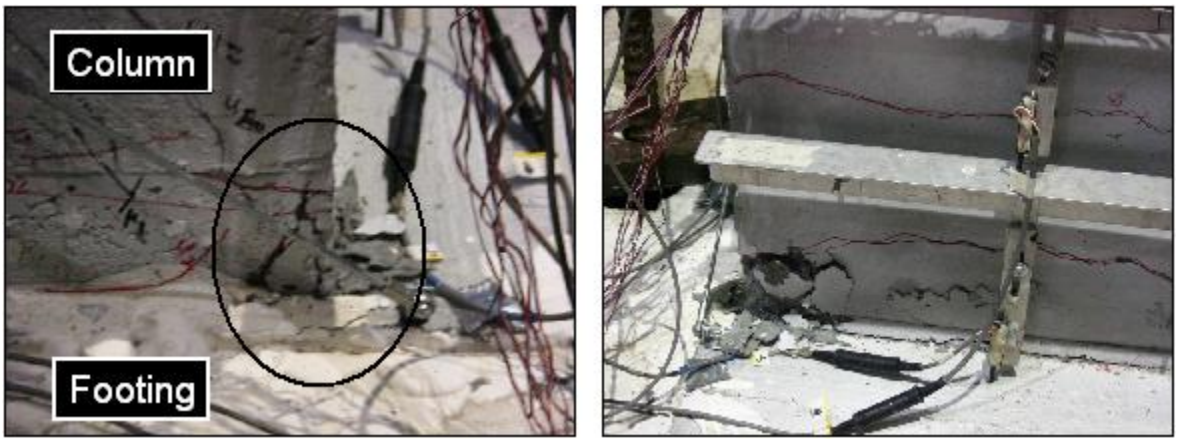

Figure 3.8 – NWB: West face crushing at + $\mu_{2,1}$ (left) and south face spalling at - $\mu_{2,3}$ (right)

During the first cycle of $\pm \mu_{2.9}$, cracks dramatically increased in width up to 0.19 inches. The second and third cycles widened these flexure and shear cracks up to 0.56 inches. The progressive damage including the widening of the cracks are shown in Figures 3.9 and 3.10. The increasing crushing of the concrete can be seen at the base of the column, as well as spalling of the concrete cover mainly on the west face. Note also the large 'X-shape' shear cracks that can be seen clearly on the east face. The average inclination of these shear cracks was approximately 28° from the vertical axis of the column.

Figure 3.9 – NWB: West face at - $\mu_{2.9,1}$ (left), + $\mu_{2.9,2}$ (center), and - $\mu_{2.9,3}$ (right)

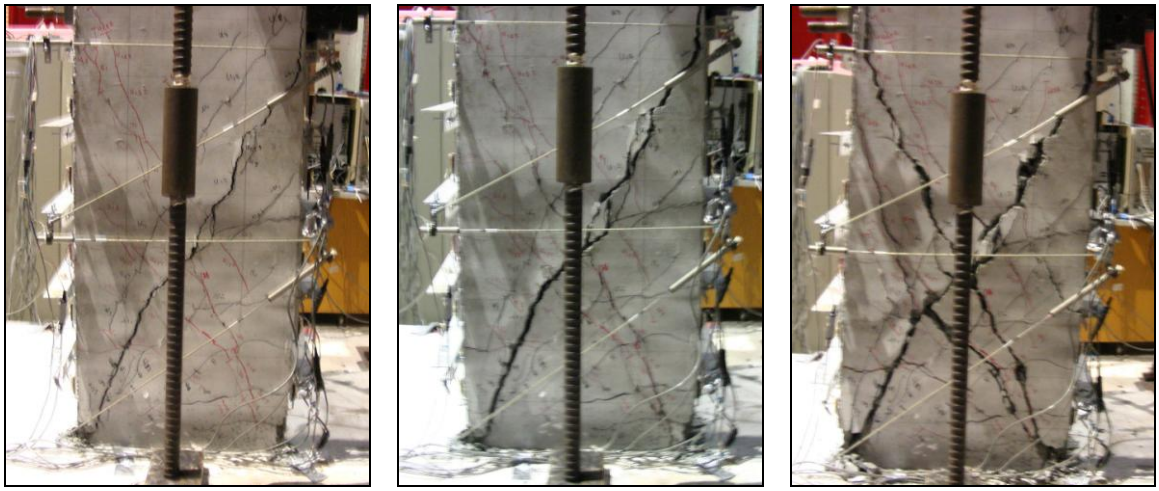

Figure 3.10 – NWB: East face at + $\mu_{2.9,1}$ (left), + $\mu_{2.9,2}$ (center), and - $\mu_{2.9,3}$ (right)

The amount and size of vertical cracks increased greatly for the first cycle, and continued to increase until the third and final cycle of $\mu_{2.9}$ (Figures 3.11 and 3.12). These figures show four lines of vertical cracking, propagating on the majority of the face of the column, at the location of the four longitudinal bars on each face. Also,

some concrete spalling can be seen at the bottom of the south face of the column in Figure 3.12.

Figure 3.11 – NWB: North face at - $\mu_{2.9,1}$ (left) and - $\mu_{2.9,3}$ (right)

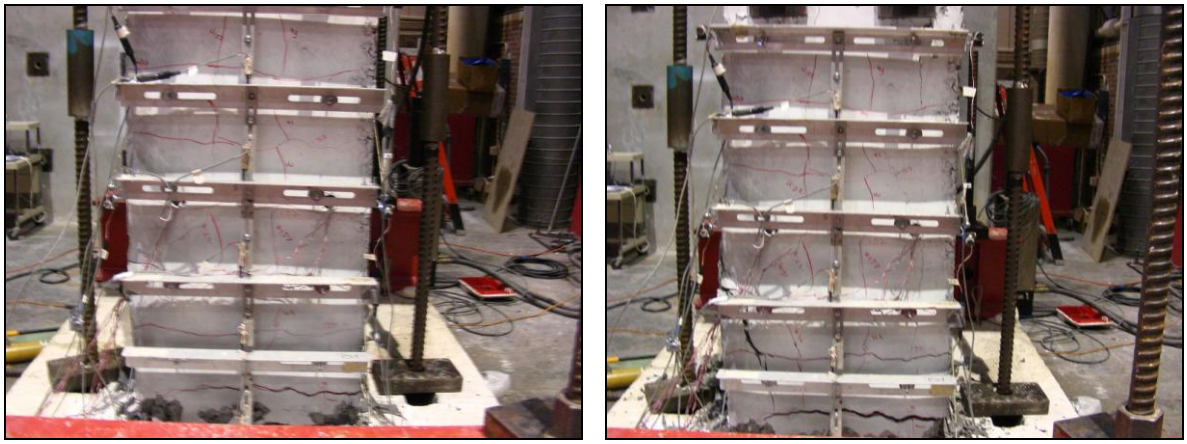

Figure 3.12 – NWB: South face at- $\mu_{2.9,1}$ (left) and - $\mu_{2.9,3}$ (right)

The top displacement for this specimen was 1.23 inches. Corresponding lateral loads declined significantly for each cycle of $\mu_{2.9}$. The $+\mu_{2.9,1}$ cycle reached a load of 136 kips, while the second and third cycles obtained loads of only 111 and 88 kips,

respectively. The test was stopped upon completion of these three cycles since the third cycle maximum load was less than half of the test maximum (191 kips).

Force-Displacement Response / Damping

The actual force-displacement response was not obtained for this test. However, a physical drawing of this response was created during the test using an X-Y recorder. Several points of this drawing were then digitized as accurately as possible. The results are shown in Figure 3.13.

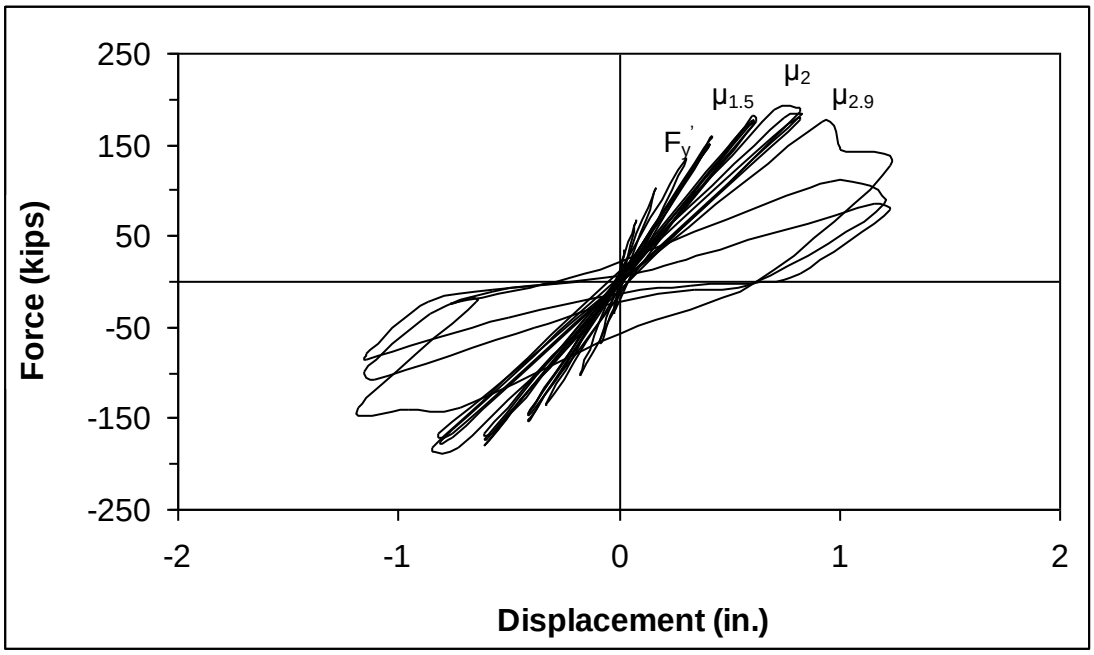

Figure 3.13 – NWB: Approximate Force-Displacement Response

Hysteretic damping calculations were made for the fist cycle of every ductility level for every test. These calculations used Jacobsen's approach (Jacobsen 1960), and the description and equation are listed in the Appendix. However, because the

force-displacement response was not exact for this test, accurate calculations could not be made. The most accurate hysteretic damping calculation was made for the first cycle of $\mu_{2.9}$, where a value of 14% was obtained.

3.2 – Lightweight Clay Brittle Shear Failure Specimen (CLB)

The actual loading procedure for the first lightweight specimen is shown in Figure 3.14.

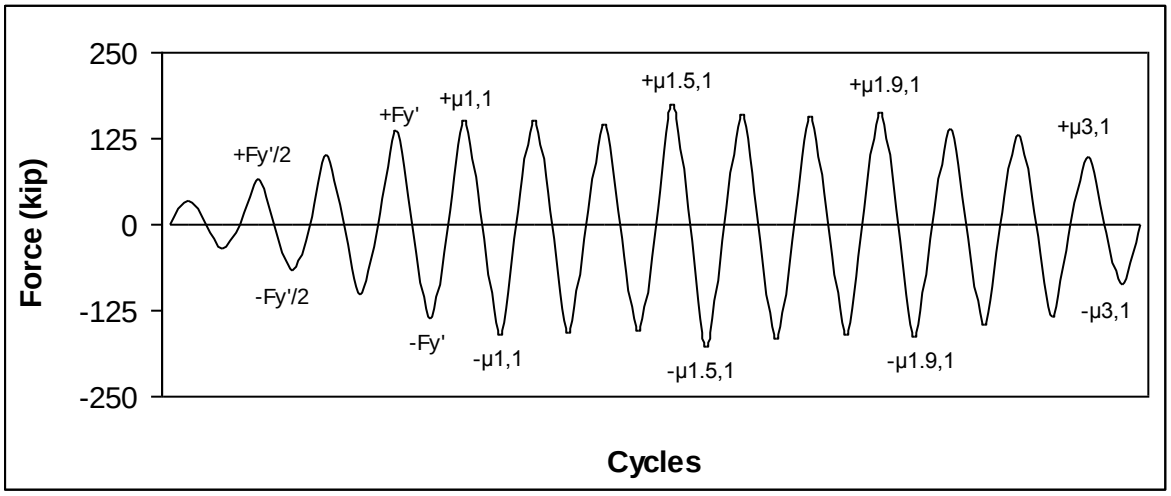

Figure 3.14 – CLB: Actual loading protocol

Force-controlled Cycles

The first flexural cracks appeared on the north and south faces during the $+F_y^{'}/2$ cycle. Unlike the normal weight specimen, these cracks propagated to the east and west faces during this cycle, but no longer than four inches. These cracks developed throughout the height of the column, spaced about four to six inches apart. The north face also showed some vertical cracking during this early cycle, and more flexural cracks appeared during the $\pm 3F_y^{'}/4$ cycle (Figure 3.15).

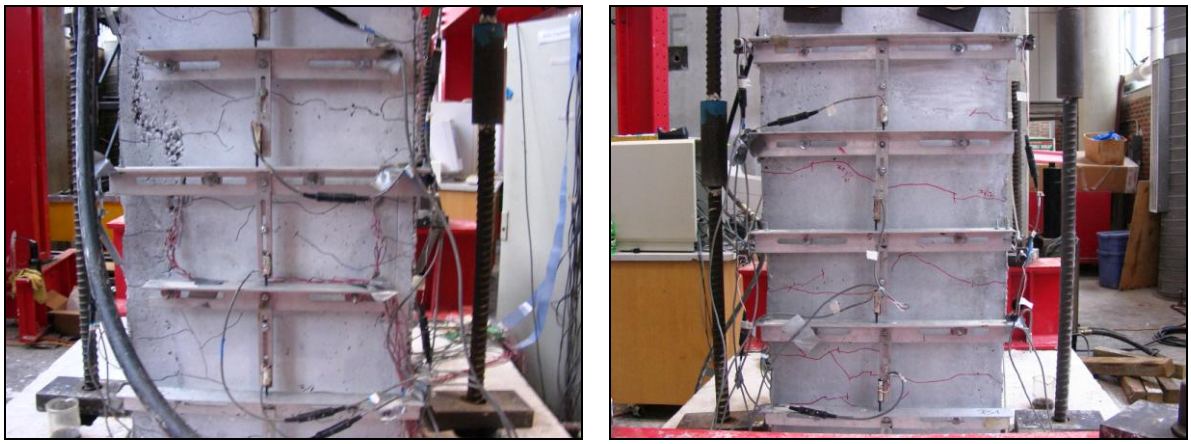

Figure 3.15 – CLB: North face (left) and south face (right) at $\pm 3F_y^{'}/4$

During the $\pm 3F_y^{'}/4$ cycle, the flexural cracks spread further into the east and west faces and became flexure-shear cracks. By the $\pm F_y^{'}$ cycle, extensive cracking was evident on all faces (Figure 3.16, 3.17). A few shear-only cracks were formed during this cycle. The north and south faces showed more vertical cracks, while cracks on the east and west faces propagated downwards.

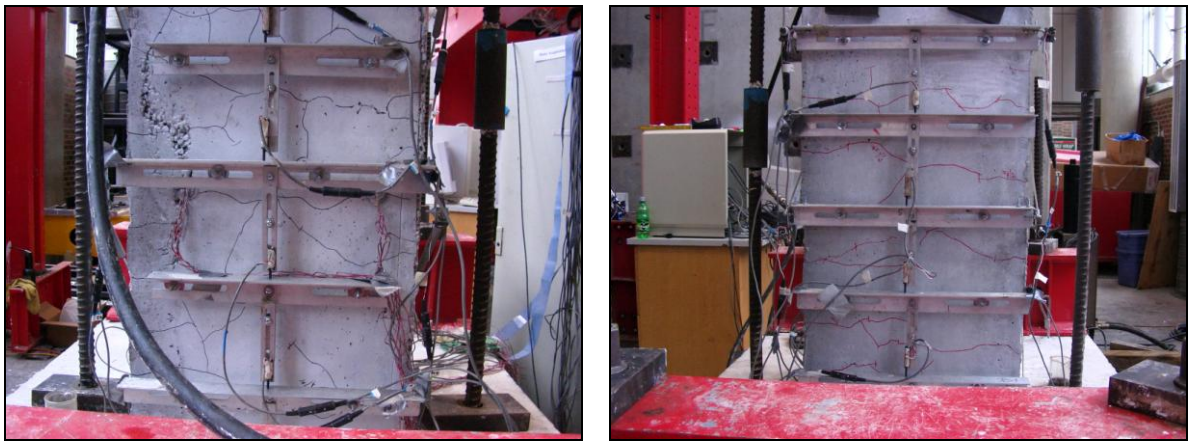

Figure 3.16 – CLB: North face (left) and south face (right) at $\pm F_y^{'}$

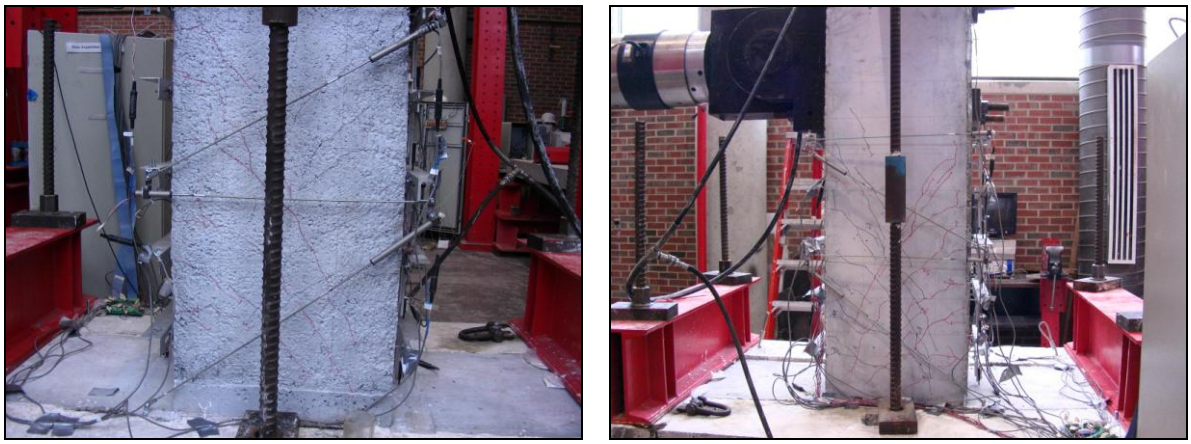

Figure 3.17 – CLB: East face (left) and west face (right) at $\pm F_y^{'}$

Because of the rough finished surface of the east face, the cracks were more difficult to identify. This led to some cracks remaining unmarked until they widened significantly. Also, the cracks that were marked are less distinguishable than the west face cracks.

Overall, the cracking was more severe for this specimen than for the normal weight specimen, as more cracking appeared for the same amount of load. The top displacement reached during the $+F_y^{'}$ cycle was 0.42 inches, and was -0.38 inches for $-F_y^{'}$. Note these values are higher than the normal weight specimen. The maximum measured flexural crack width was 0.016 in.

Displacement-controlled Cycles

With this higher yield displacement, a higher first ductility level was calculated as μ_1 = 0.52 inches. More shear-only cracks formed on the east and west faces, and flexure-shear cracks were extended. The north and south faces remained relatively

unchanged, with the addition of only two vertical cracks on each face. The largest crack width during this cycle was 0.025 in. The corresponding second and third cycles resulted in very few short extensions and no new cracks.

The maximum lateral loads of +174 kips and -178 kips were achieved in the $\pm\mu_{1.5,1}$ cycle, and the corresponding displacement was ±0.79 inches. This cycle brought on more extensions of the flexure-shear and the shear-only cracks, with few new cracks. The cracks became visibly wider, as the maximum shear crack width recorded was 0.04 inches. The concrete began to crush and spall off during this cycle (Figure 3.18). No changes were recorded during the second and third cycles for the north and south faces except the widening of existing cracks. By the third cycle, shear cracks widened to 0.06 in.

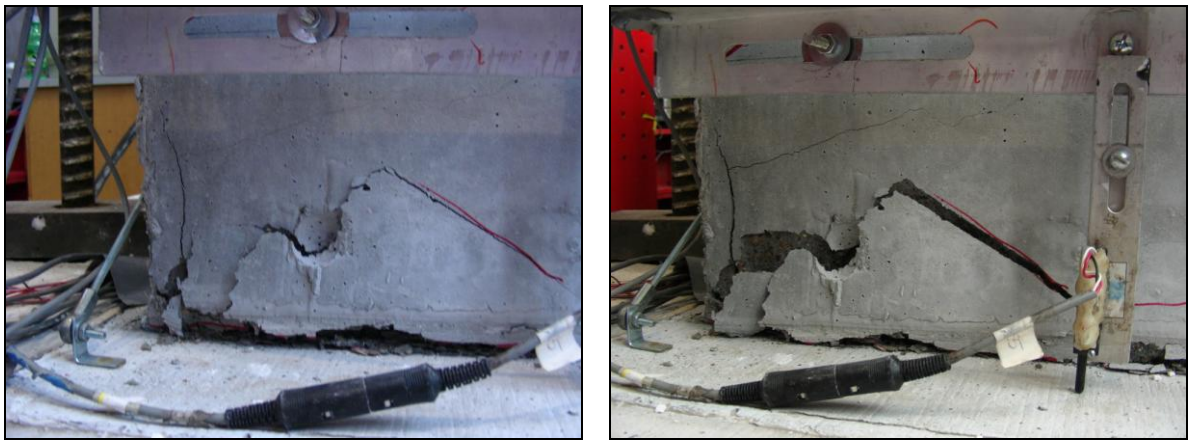

Figure 3.18 – CLB: Concrete spalling on south face at $\pm\mu_{1.5,1}$ (left) and $\pm\mu_{1.5,3}$ (right)

Crushing and spalling of the concrete continued for the three cycles of $\pm\mu_{1.9}$. Several extensions of cracks and a few new shear cracks appeared on the east and west faces in the second cycle.

Cracks widened significantly until the test was stopped on the first cycle of μ_3 (Figure 3.19, 3.20). The average inclination of these shear cracks from the vertical axis of the column was approximately 26°. Note the crushing in the bottom corners. The $-\mu_{3,1}$ cycle picture shows dilation of the column. A 36% load drop occurred between $-\mu_{1.9,3}$ (135 kips) and $-\mu_{3,1}$ (86 kips), and the maximum top displacement of 1.56 inches occurred during the $\pm\mu_{3,1}$ cycle.

Figure 3.19 – CLB: East face at $-\mu_{1.9,1}$ (left), $-\mu_{1.9,3}$ (center), and $-\mu_{3,1}$ (right)

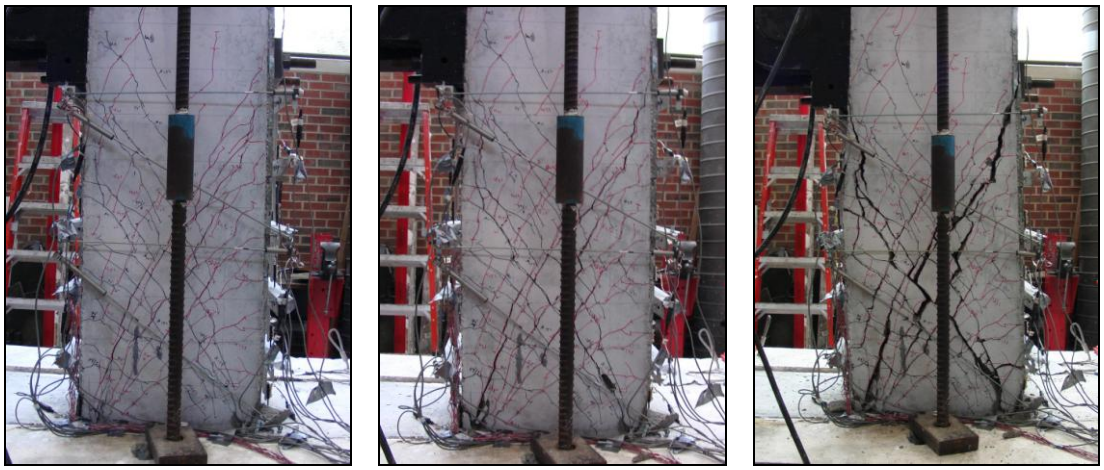

Figure 3.20 – CLB: West face at - $\mu_{1.9,1}$ (left), - $\mu_{1.9,3}$ (center), and - $\mu_{3,1}$ (right)

Several vertical cracks formed on the north and south faces during the $\pm\mu_{1.9,3}$ cycle (Figure 3.21). No new cracks were formed, but existing cracks widened significantly through the $\pm\mu_{3,1}$ loading cycle (Figure 3.22).

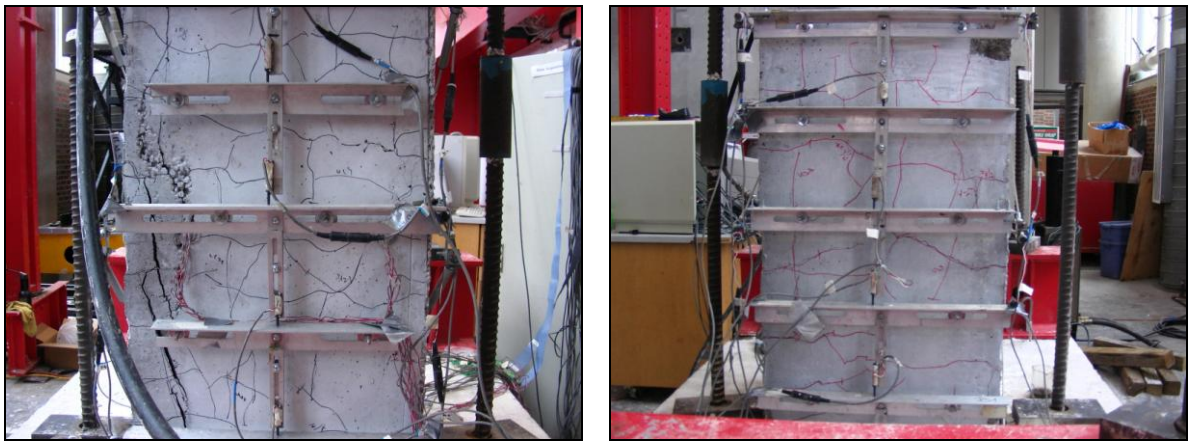

Figure 3.21 – CLB: North (left) and south (right) faces at $\pm\mu_{1.9,3}$

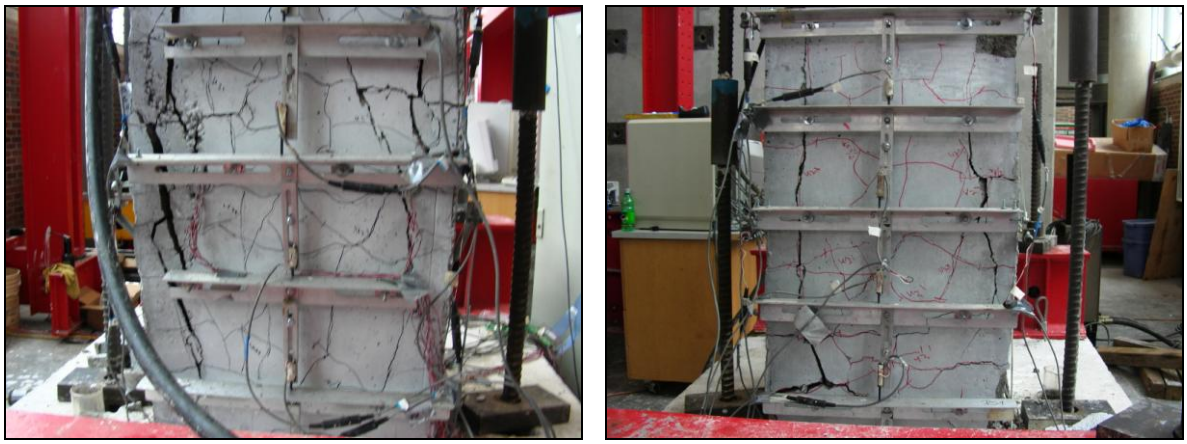

Figure 3.22 – CLB: North (left) and south (right) faces at $\pm \mu_{3,1}$

Force-Displacement Response / Damping

The actual force-displacement response is shown below (Figure 3.23).

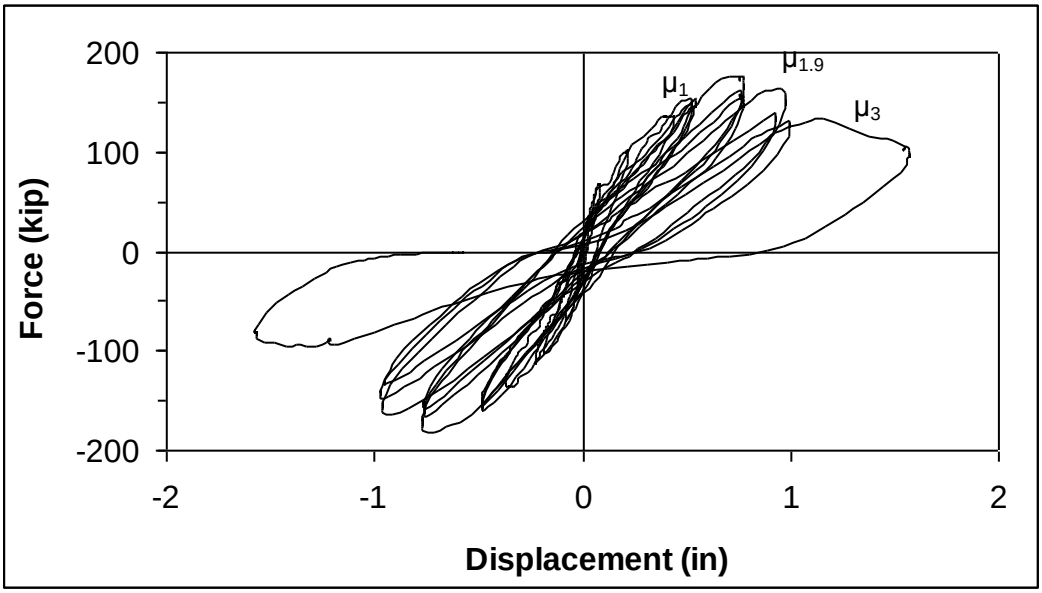

Figure 3.23 – CLB: Actual Force-Displacement Response

A well-defined pinched shape is apparent in all cycles after yield. This is due to plastic and shear deformations which were expected. This effect was observed in all brittle failure specimens.

For this test, hysteretic damping was calculated for the first cycle of each ductility level. The $\mu_{1.9,1}$ cycle achieved a damping value of 10.8%. This value increased to a maximum of 14.7% for the $\mu_{3,1}$ cycle.

Curvature Profiles

Curvature profiles were generated for this test. The average curvature was calculated at the center of each of five cells on the north and south faces. The equations involved in the calculation are discussed in the Appendix. Two plots are shown in Figure 3.24. The predicted yield curvature, an output from the CUMBIA program, is plotted on each graph.

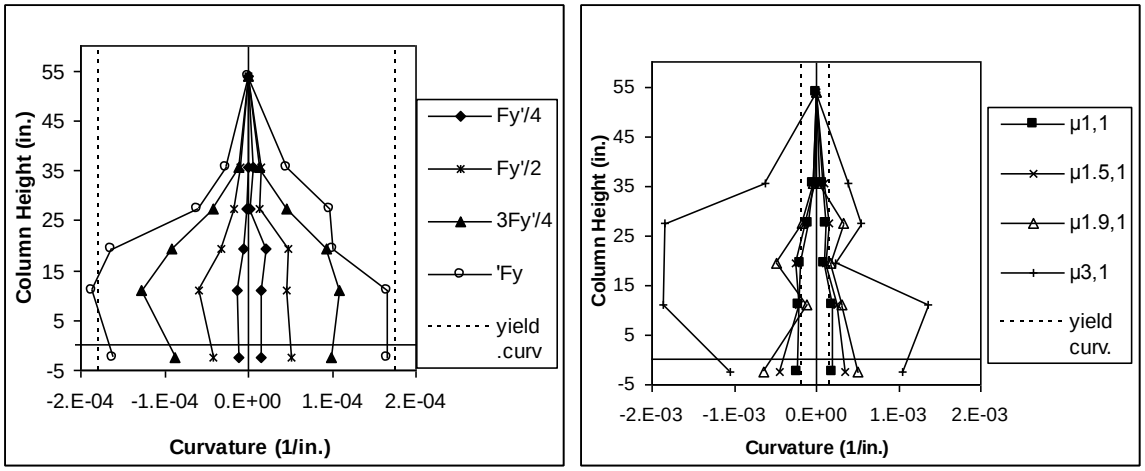

Figure 3.24 – CLB: Curvature profiles for force-controlled (left) and displacement-controlled (right) cycles

Note that the bottom cell includes a strain penetration length because the rotation extends into the footing, and the center of this cell lies inside the footing. The strain penetration calculations are shown in the Appendix.

For the displacement-controlled cycles, the curvature generally increased with distance from the load, as expected. The curvature was measured as a slightly lower value within the footing, in most cases. The maximum calculated curvature values for the F_y' (-1.66e-4 and +1.87e-4) matched well with the predicted yield curvature value (±1.78e-4 in^{-1}.). By the end of the test, the entire instrumented section of the column exceeded the yield curvature.

Each cycle of displacement control brought on increasing levels of curvature. A large increase in curvature occurred during the $\mu_{3,1}$ cycle, and the maximum values reached were +1.36e-3 and -1.87e-3 in^{-1}.

Strain Gage Histories and Profiles

An example strain gage history is shown in Figure 3.25. A small diagram in the top right corner shows the location of the BS1 strain gage, which is on the west face, 38 inches from the base of the column. All strain gage histories are given in the Appendix.

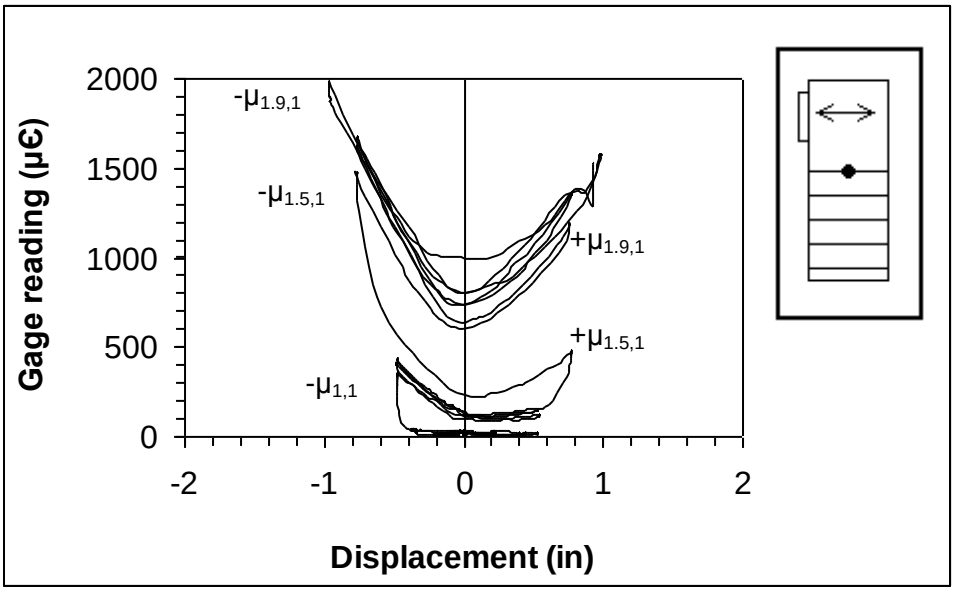

Figure 3.25 – CLB: BS1 strain gage history

According to this gage history, the transverse stirrup to which the strain gage was attached never reached yield strain (2069 μЄ). This particular gage became inactive during the $+\mu_{1.9,2}$ cycle. The first activation of this particular stirrup occurs on the pull cycle of $\mu_{1,1}$, as shown. During this cycle some shear-only cracks were formed, indicating that load is being transferred to the stirrups. Throughout the test, the steel strains were higher during the pull cycles. Upon careful examination of photographs, it has been determined that cracks formed during the pull cycles up to $\mu_{1.9,1}$ were wider than cracks formed during the push cycles.

The strain gage profiles were generally unreliable for this test. Four out of the ten strain gages produced no data, and another two gages yielded incorrect results. Nevertheless, a partial profile is shown below in Figure 3.26.

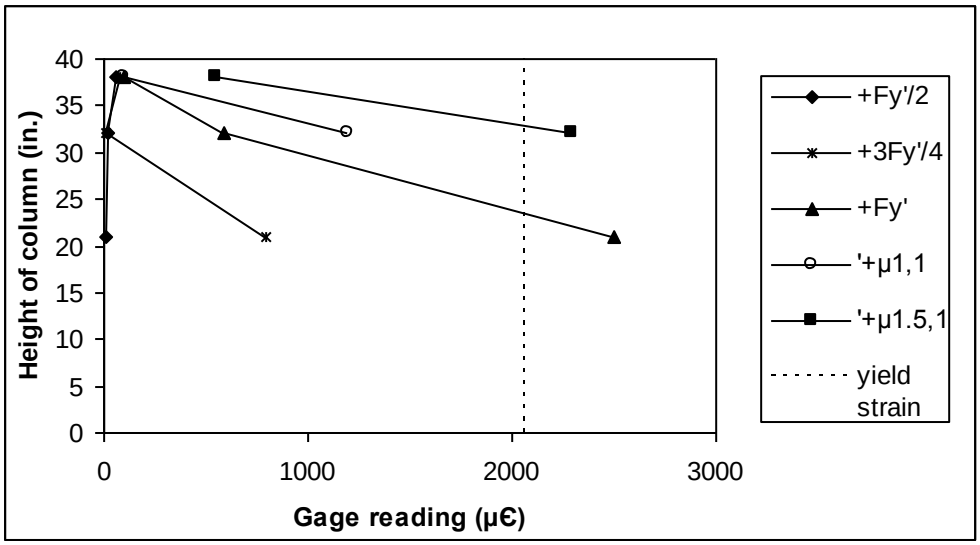

Figure 3.26 – CLB: East face strain profile

Data was not collected for the bottom two gages on this face. Additionally, the third gage stopped working after the force-controlled cycles. These profiles were expected be generally symmetric about the middle gage, with the maximum strain occurring at the around 21" (depth of the section) above the footing.

3.3 – Lightweight Shale Brittle Shear Failure Specimen (SHB)

The actual loading procedure for this specimen is shown in Figure 3.27.

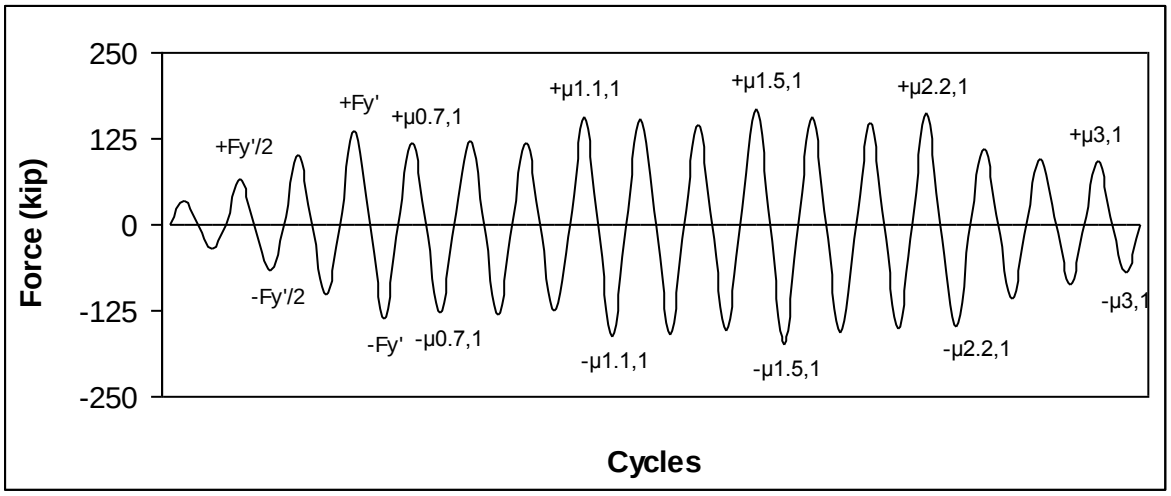

Figure 3.27 – SHB: Actual loading protocol

Force-controlled Cycles

The $\pm F_y^{'}/2$ cycle caused the first flexure cracks to form on the north and south faces. These cracks also spread to the east and west faces during this cycle. Most cracks appeared in the bottom half of the column, and were spaced at about four to six inches (Figure 3.28).

Figure 3.28 – SHB: West (left) and south (right) faces at $\pm F_y^{'}/2$

During the $\pm 3F_y^{'}/4$ cycle, the cracks spread on all faces, and several new flexural cracks were formed. Most of the cracks on the east and west faces became flexure-shear cracks. The largest crack width measured was 0.01 inches. By the $\pm F_y^{'}$ cycle, several new cracks had formed, and many were shear-only cracks (Figure 3.29). Also, the north and south faces exhibited some vertical cracking and additional flexure cracks (Figure 3.30).

Figure 3.29 – SHB: East (left) and west (right) faces at $\pm F_y^{'}$

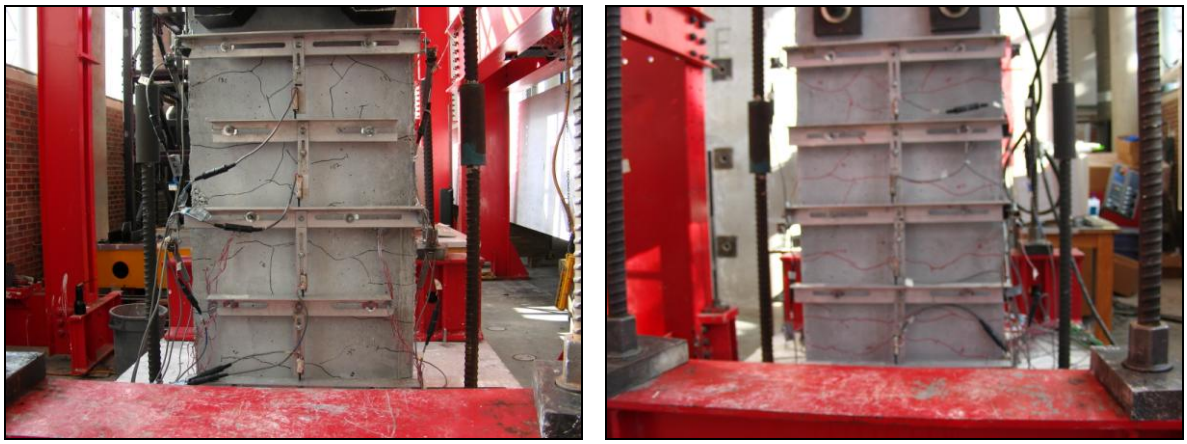

Figure 3.30 – SHB: North (left) and south (right) faces at $\pm F_y^{'}$

The top displacement reached during the + $F_y^{'}$ cycle was 0.48 inches, and for - $F_y^{'}$ was -0.41 inches. The maximum flexural crack width measured was 0.013 in.

Displacement-controlled Cycles

The value of μ_1 for this test was 0.57 inches, but the first ductility level that the specimen was loaded to was $\mu_{0.7}$ at 0.41 inches. Because the loads for all $\mu_{0.7}$ cycles were lower than the $F_y^{'}$ cycle, no new cracks were expected. No new cracks were found, and there were very few extensions found by the end of the third cycle.

The $\pm \mu_{1.1,1}$ cycle brought on a few more extensions of the flexure-shear and the shear-only cracks. Three new vertical cracks formed on the south face, but there were no changes to the north face of the column. During the second and third

cycles, a few small extensions were recorded on the east and west faces, and the north and south faces remained unchanged.

The maximum lateral loads of +169 kips and -175 kips were achieved in the $\pm \mu_{1.5,1}$ cycle, and the corresponding displacements were +0.82 and -0.85 inches (Figure 3.31). Maximum crack widths on the east and west faces were 0.05 inches. These faces also showed the first evidence of minor concrete spalling (Figure 3.32).

Figure 3.31 – SHB: East (left) and west (right) faces at $\pm \mu_{1.5,1}$

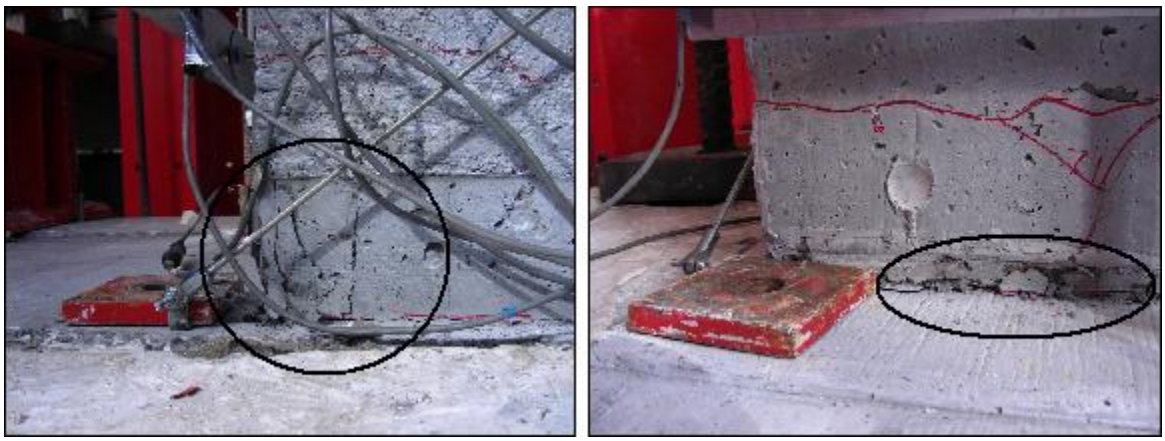

Figure 3.32 – SHB: Concrete crushing and spalling on east (left) and south (right) faces at $\pm \mu_{1.5,1}$

A few new vertical cracks formed on the north and south faces. The second and third cycles caused progressive crushing, and a few shear cracks extended on the east and west faces.

A few very large shear cracks opened up during the $\pm\mu_{2.2,1}$ cycle (Figure 3.33). The largest of these was measured at 0.25 inches. A load drop coincided with the formation of these shear cracks, indicating a shear failure. Several new vertical cracks formed on the north and south faces, which corresponded the location of the longitudinal bars. Crushing became more severe on all faces of the specimen (Figure 3.34).

Figure 3.33 – SHB: East (left) and west (right) faces at $\pm\mu_{2.2,1}$

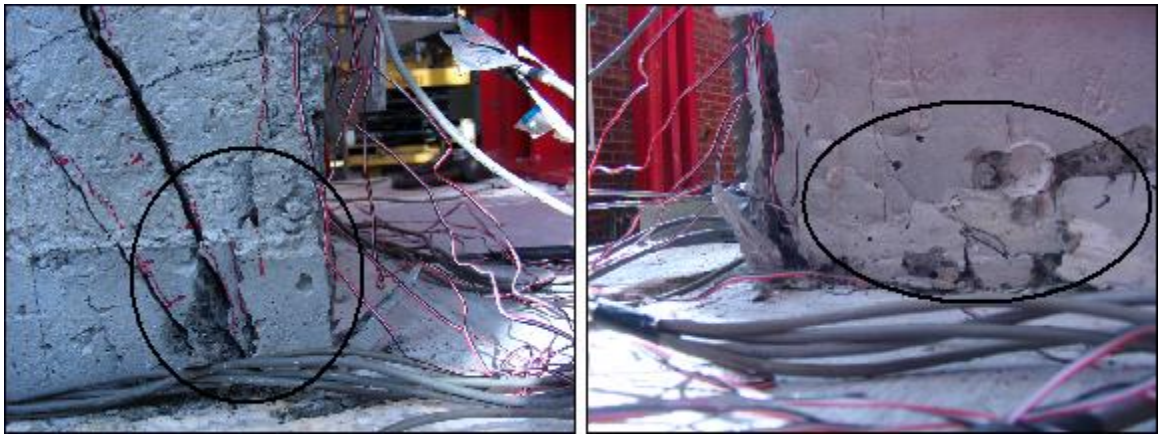

Figure 3.34 – SHB: Concrete crushing and spalling on east (left) and north (right) faces at $\pm\mu_{2.2,1}$

The second cycle worsened the condition of the structure as a whole, causing cracks to widen, and spalling to increase. The third cycle however caused very little damage. The greatest strength degradation for this test occurred in the three cycles of $\mu_{2.2}$. In the push direction, the maximum lateral force decreased from 164 kips to 96 kips over the three cycles.

The progressive damage of the $\pm\mu_{2.2.2}$ and $\pm\mu_{3,1}$ cycles are shown in Figures 3.35 and 3.36. The largest crack width in the $\pm\mu_{3,1}$ cycle was 0.75 inches. The increasing crushing of the concrete can be seen at the bottom corners of the column, as well as spalling of the concrete cover. The average inclination of these shear cracks from the vertical axis of the column was about 28°.

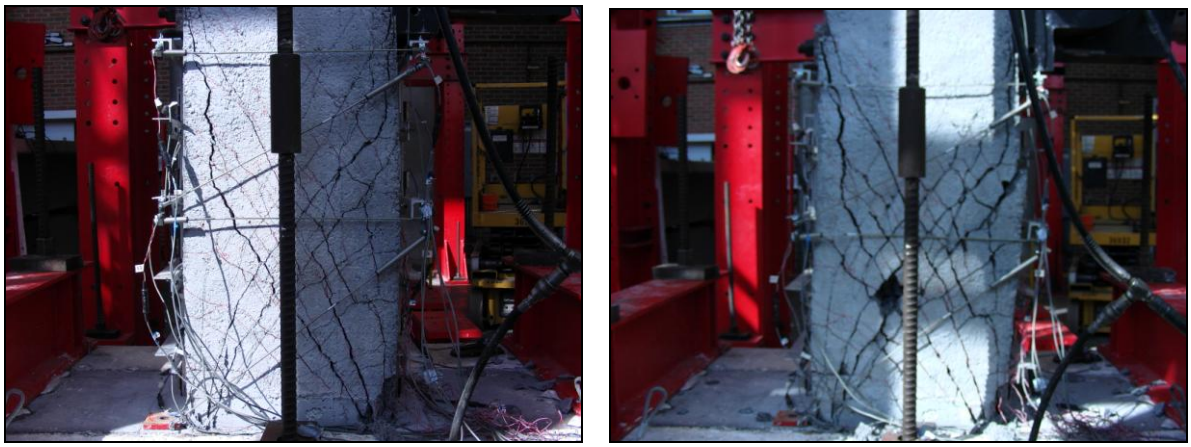

Figure 3.35 – SHB: East face at - $\mu_{2.2,2}$ (left) and - $\mu_{3,1}$ (right)

Figure 3.36 – SHB: West face at - $\mu_{2.2,2}$ (left) and - $\mu_{3,1}$ (right)

By the final cycle, the north and south faces were completely covered with flexure and vertical cracks (Figure 3.37). In the case of the north face, a large section of concrete cover on the left side broke away from the specimen.

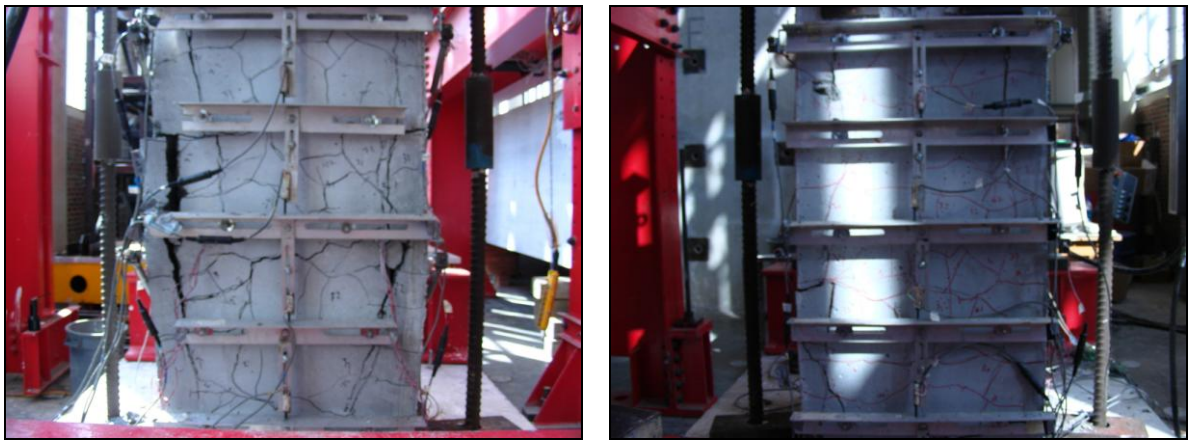

Figure 3.37 – SHB: North (left) and south (right) faces at - $\mu_{3,1}$

The large crack widths caused several instruments to reach their stroke limit. As seen in Figure 3.38, when the instruments reached their limit, they began to bend the aluminum angles they were attached to. Therefore, the data collected from the last few cycles ($\mu_{2.2,2}$, $\mu_{2.2,3}$, and $\mu_{3,1}$) is inaccurate.

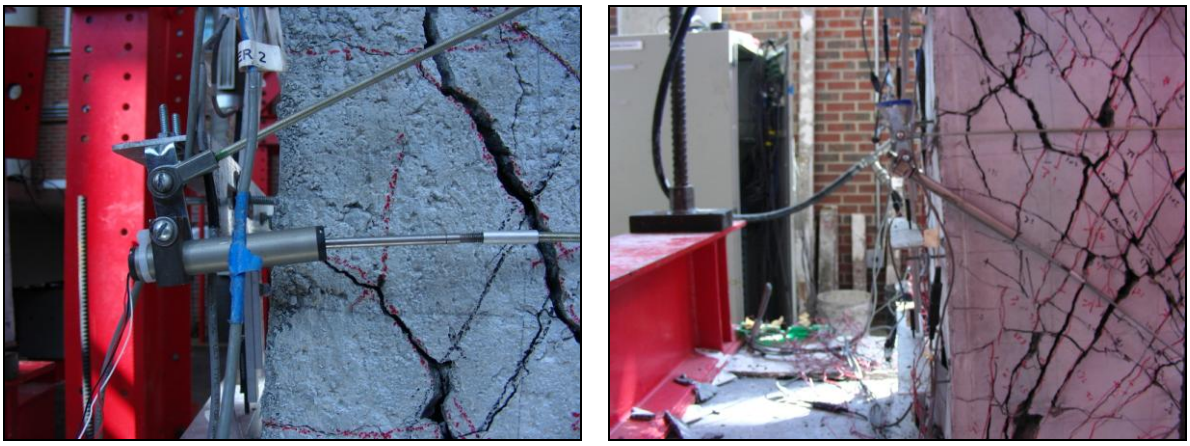

Figure 3.38 – SHB: East (left) and west (right) face instruments

The left picture shows a linear potentiometer on the east face being bent due to the large crack widths. This instrument caused the attached angle to bend downward.

This angle movement led to the shortening of the south face potentiometer below the angle, and the elongation of the one above the angle. The right picture in Figure 3.38 shows a similar effect on the west face of the column. The long diagonal potentiometer is bent slightly upwards.

Only one cycle of μ_3 was conducted for this test due to the significant load drop. The top displacement reached was 1.70 inches.

Force-Displacement Response / Damping

The force-displacement response for this test is shown below (Figure 3.39). The rapid strength degradation can be seen in the $\mu_{2.2}$ cycles.

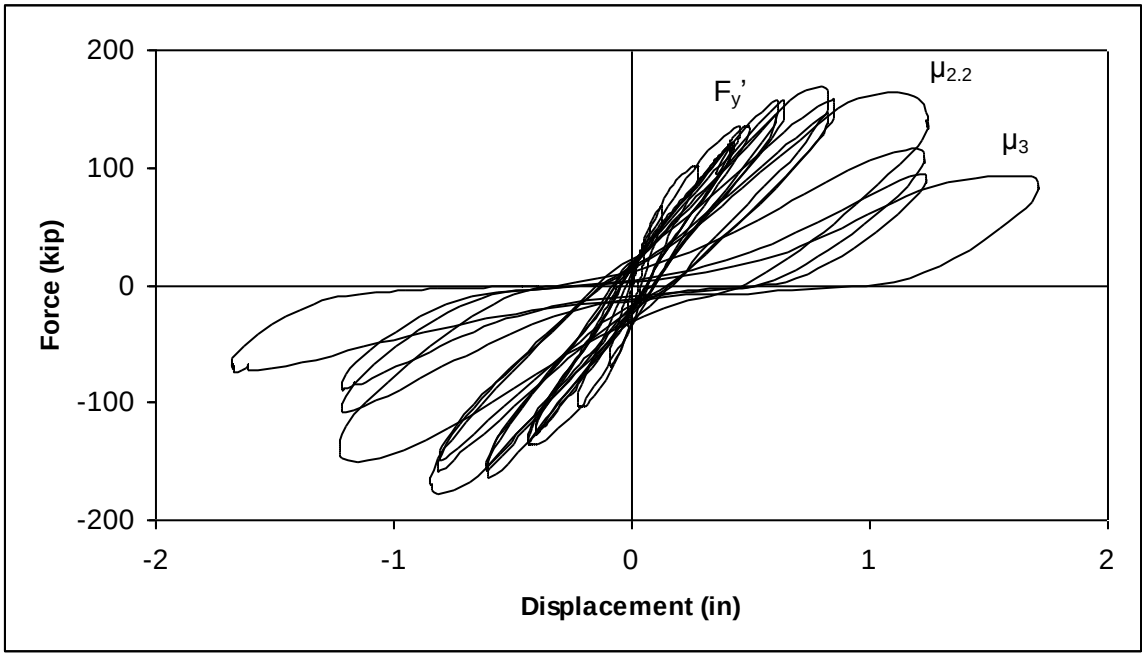

Figure 3.39 – SHB: Actual Force-Displacement Response

The maximum damping value of 13.3% was reached during the $\mu_{2.2,1}$ cycle. Additionally, the damping during the maximum load cycle ($\mu_{1.5,1}$) was 8.8%.

Curvature Profiles

The two curvature profiles are shown in Figure 3.40.

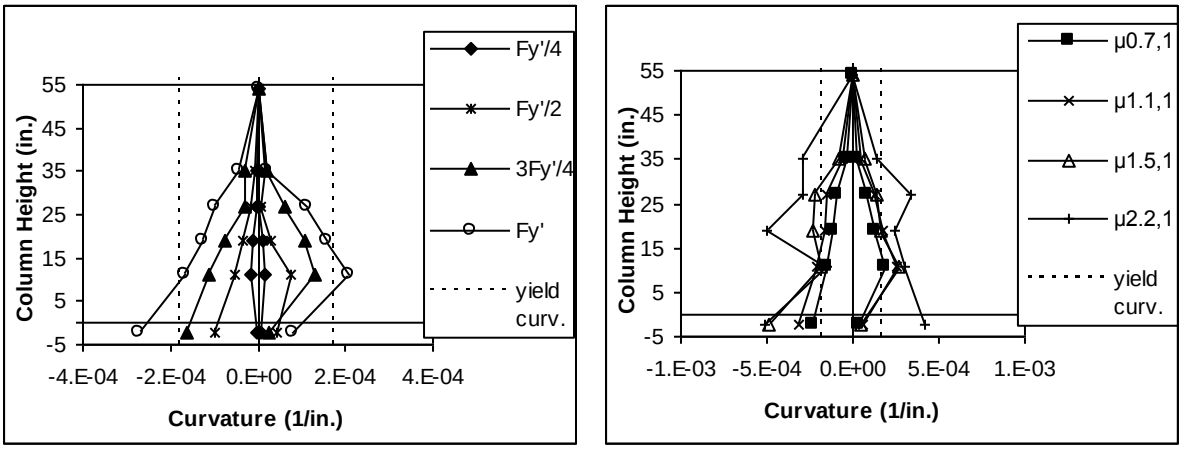

Figure 3.40 – SHB: Curvature profiles for force-controlled (left) and displacement-controlled (right) cycles

The first cycle of μ_3 is not shown because the instruments became unreliable after $\mu_{2.2,1}$, as discussed before. The profiles are not symmetric, as they show larger values in the pull (negative) direction of loading in most cases. Note the significant increase in value at several points for the $\mu_{2.2,1}$ cycle. This corresponds with a load drop, extensive crushing, a large increase in crack width, and a significant increase in top displacement and damping.

The maximum calculated curvature for the $F_y^{'}$ cycle matched reasonably well with the predicted value for the push cycle (2.08e-4 in^{-1}) but poorly for the pull cycle (-2.73e-4 in^{-1}). The maximum values calculated were +4.17e-4 and -5.07e-4 in^{-1} during the $\mu_{2.2,1}$ cycle.

Strain Gage Histories and Profiles

One strain gage history is shown in Figure 3.41.

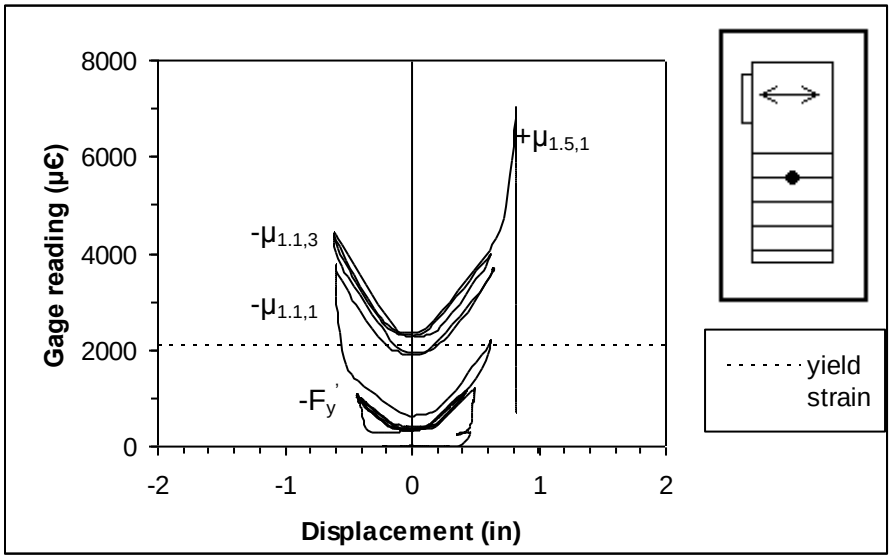

Figure 3.41 – SHB: BS2 strain gage history

The first activity in this stirrup occurred during the + $F_y^{'}$ loading cycle, where a value of 1210 με was reached. This corresponds to the formation of the first shear-only cracks. The strain continued to increase during the $\mu_{1.1}$ cycles, as cracks widened and spread. The gage reached a maximum value of 7040 με while loading to

$+\mu_{1.5,1}$, then began reading incorrect values, most likely due to detachment from the steel surface. Since loads were typically higher for the pull cycles, the steel strains were expected to be higher in the pull direction (negative), which was the case.

The strain gage profile was reliable up until and including the $\mu_{1.1,1}$ cycle. Eight out of the ten gages collected data. The profile is shown below in Figure 3.42.

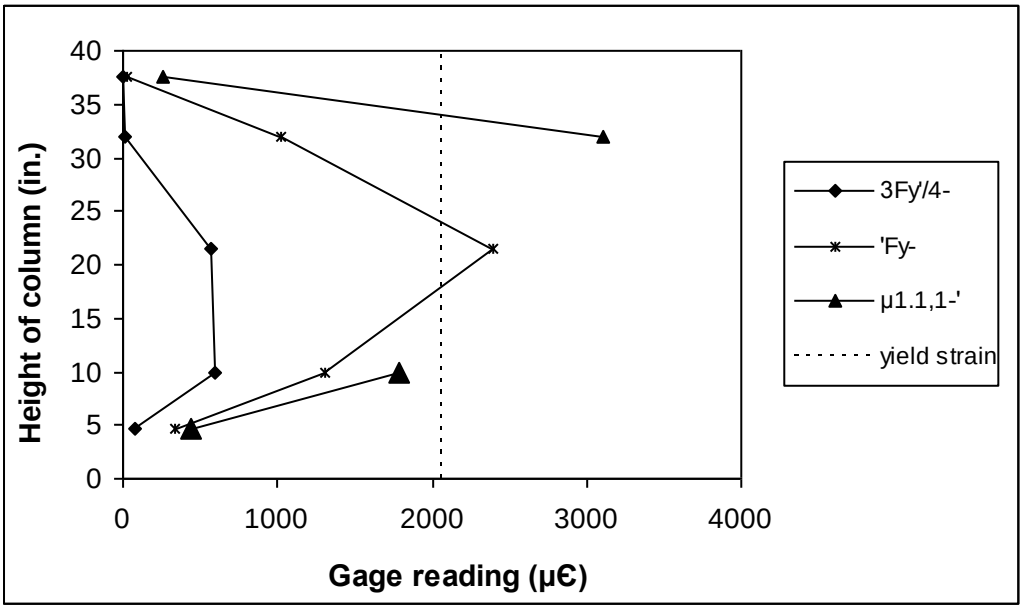

Figure 3.42 – SHB: West face strain profile

This profile shows that the middle gage (21" above the column base) was the only stirrup of the five shown that yielded during the $F_y^{'}$ cycle. The maximum strain value location shifted as the test progressed, but most likely occurred at the middle gage, which did not read correctly for the $\mu_{1.1,1}$ cycle.

3.4 – Lightweight Slate Brittle Shear Failure Specimen (SLB)

The actual loading procedure is shown in Figure 3.43.

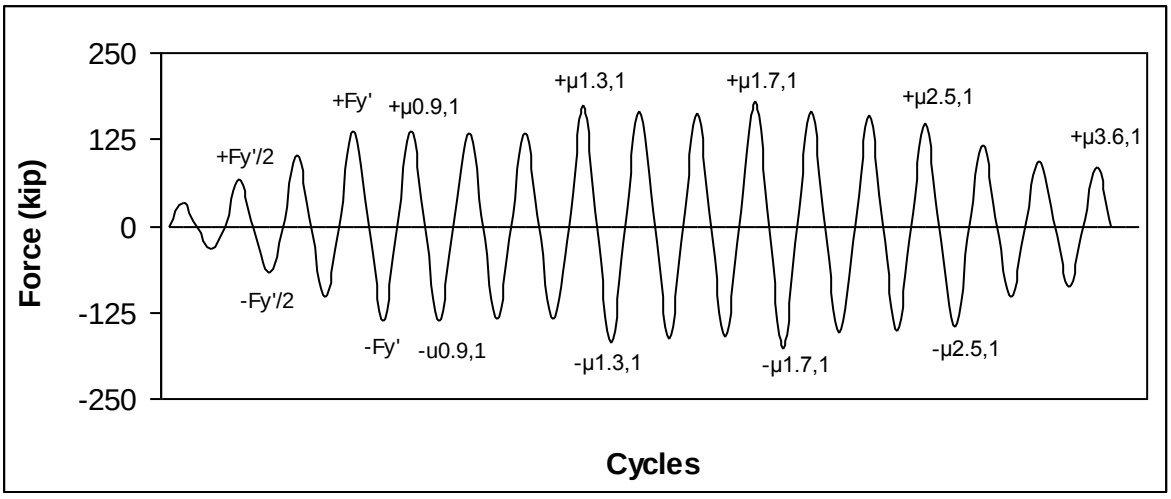

Figure 3.43 – SLB: Actual loading procedure

Force-controlled Cycles

The $\pm F_y^{'}/2$ cycle caused the first flexure cracks to form on all faces of the specimen. The cracks were spaced at four to seven inches apart and occurred in the bottom half of the column (Figure 3.44).

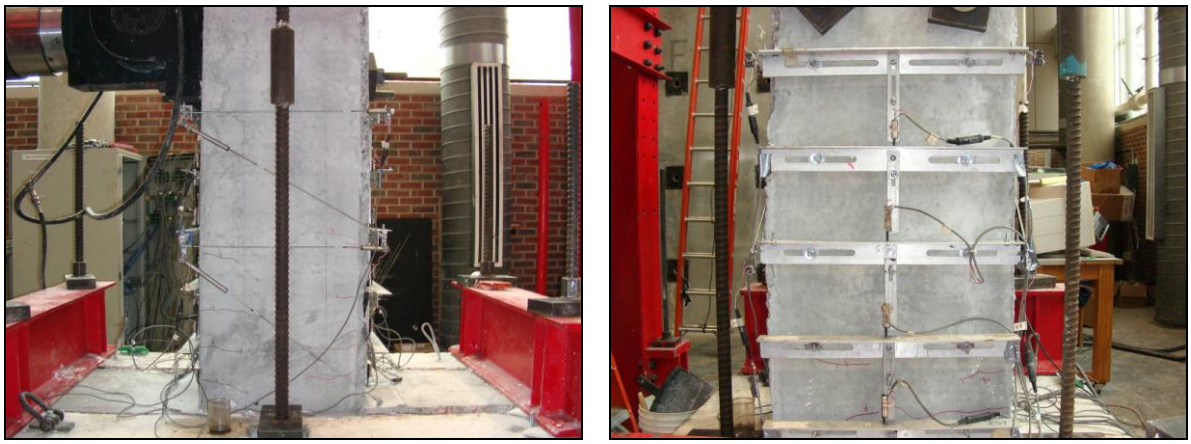

Figure 3.44 – SLB: West (left) and south (right) faces at $\pm F_y^{'}/2$

The flexural cracks progressed and became flexure-shear cracks during the $\pm 3F_y^{'}/4$ cycle. Several new cracks formed and continued to spread throughout the height of the column. During the $\pm F_y^{'}$ cycle, the first shear-only cracks appeared and spanned the entire height of the column (Figure 3.45). The first vertical cracks were formed on the north and south faces (Figure 3.46).

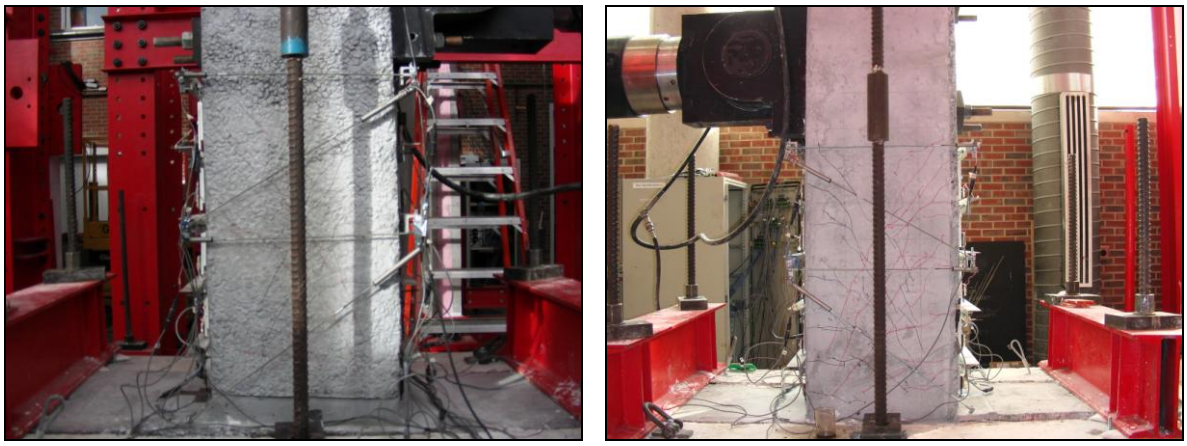

Figure 3.45 – SLB: East (left) and west (right) faces at $\pm F_y^{'}$

Figure 3.46 – SLB: North (left) and south (right) faces at $\pm F_y^{'}$

The top displacement reached during the $\pm F_y^{'}$ cycle was 0.38 inches, and for -$F_y^{'}$ was -0.37 inches. The maximum measured flexural crack width was 0.013 in.

Displacement-controlled Cycles

This test was one of the five tests that used the same value for μ_1 (0.41”), and ductility levels have been scaled to μ_1 = 0.48 inches. Since this was only slightly higher than the $\pm F_y^{'}$ displacements, some new cracks were expected. Only a few cracks were found on each face, and the second and third cycles caused some additional cracking.

The $\pm \mu_{1.3,1}$ cycle caused only a few more extensions of the flexure-shear and the shear-only cracks. There were no changes to the north face of the column, but the south face showed two new cracks. The second and third cycles brought few

changes with respect to cracks. However some spalling of the concrete began, which progressed throughout the rest of the test (Figure 3.47).

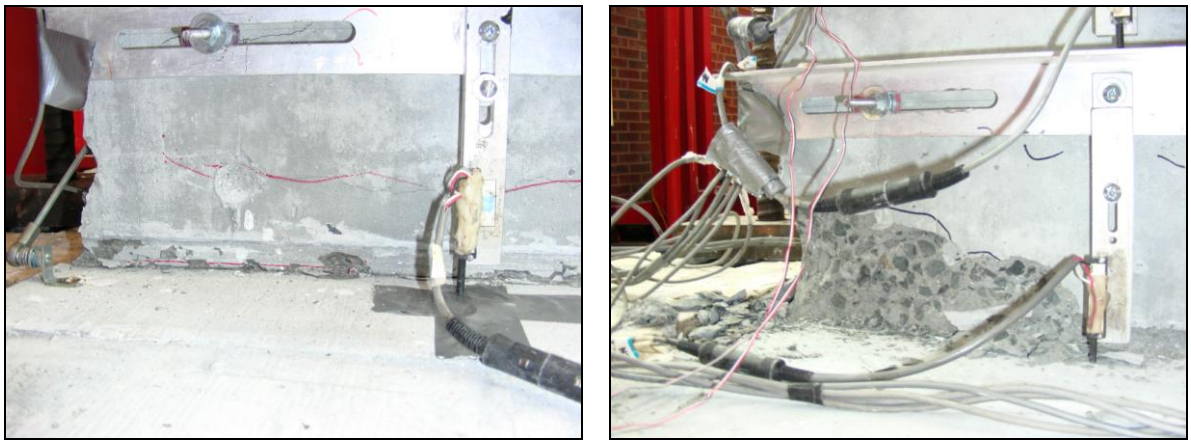

Figure 3.47 – SLB: Spalling of concrete on south face at $\pm \mu_{1.3,3}$ (left) and north face at $\pm \mu_{1.7,3}$ (right)

The maximum lateral loads of +180 kips and -177 kips were achieved in the $\pm \mu_{1.7,1}$ cycle, and the corresponding displacements were ±0.82. The maximum crack widths measured during this cycle were 0.05 inches. There were no new cracks and very few extensions of existing cracks for the three cycles of $\mu_{1.7}$ (Figure 3.48).

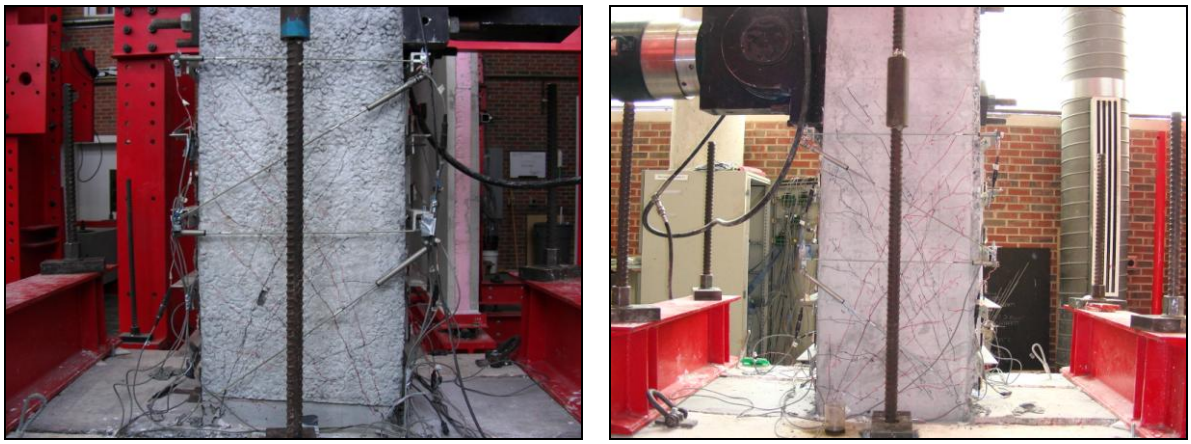

Figure 3.48 – SLB: East (left) and west (right) faces at $\pm\mu_{1.7,3}$

The crack widths increased significantly during the $\pm\mu_{2.5,1}$ cycle, as the maximum recorded shear crack was 0.19 inches. These cracks became as wide as 0.38 inches by the third cycle of $\mu_{2.5}$ (Figure 3.49, and 3.50). The average inclination of the shear cracks from the vertical axis of the column was about 27°. Crushing worsened in the corners of the columns, and some spalling occurred on the east and west faces.

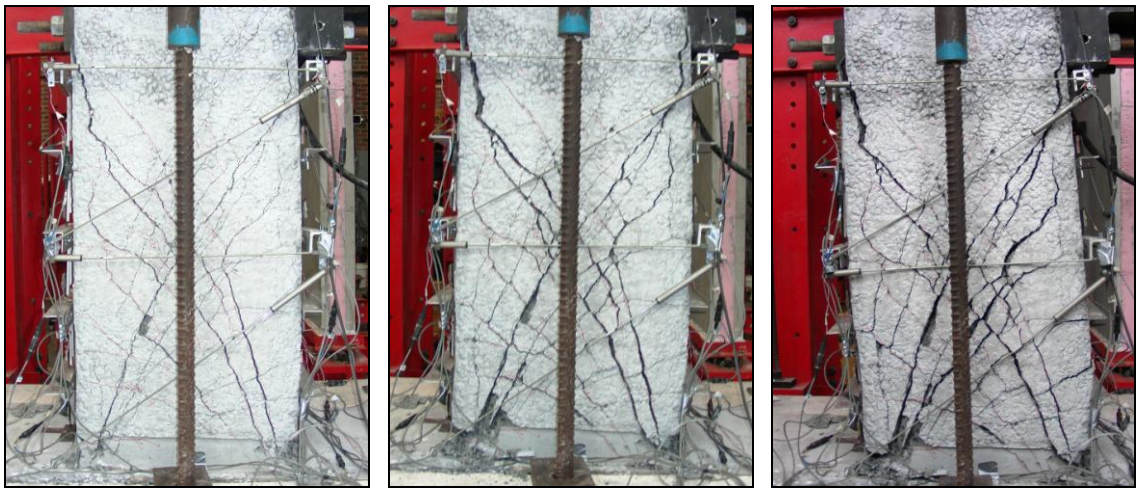

Figure 3.49 – SLB: East face at - $\mu_{2.5,1}$ (left), - $\mu_{2.5,3}$ (center), and + $\mu_{3.6,1}$ (right)

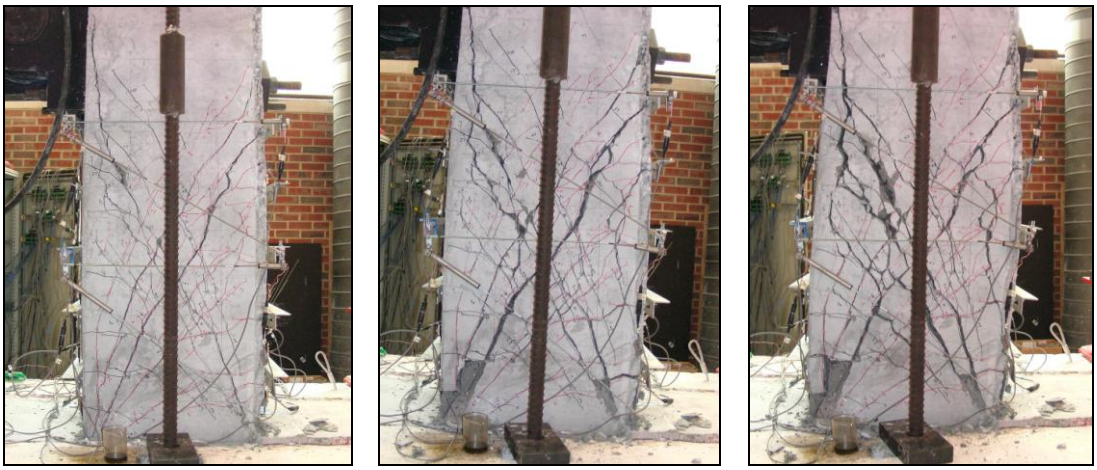

Figure 3.50 – SLB: West face at - $\mu_{2.5,1}$ (left), - $\mu_{2.5,3}$ (center), and + $\mu_{3.6,1}$ (right)

The progression of vertical cracking is shown for the east and west faces during the final cycles (Figures 3.51 and 3.52).

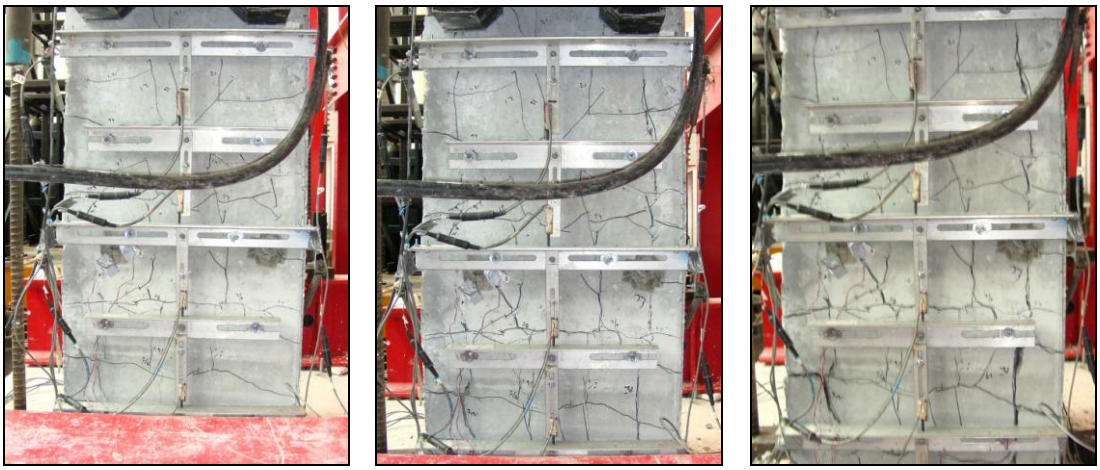

Figure 3.51 – SLB: North face at - $\mu_{2.5,1}$ (left), - $\mu_{2.5,3}$ (center), and + $\mu_{3.6,1}$ (right)

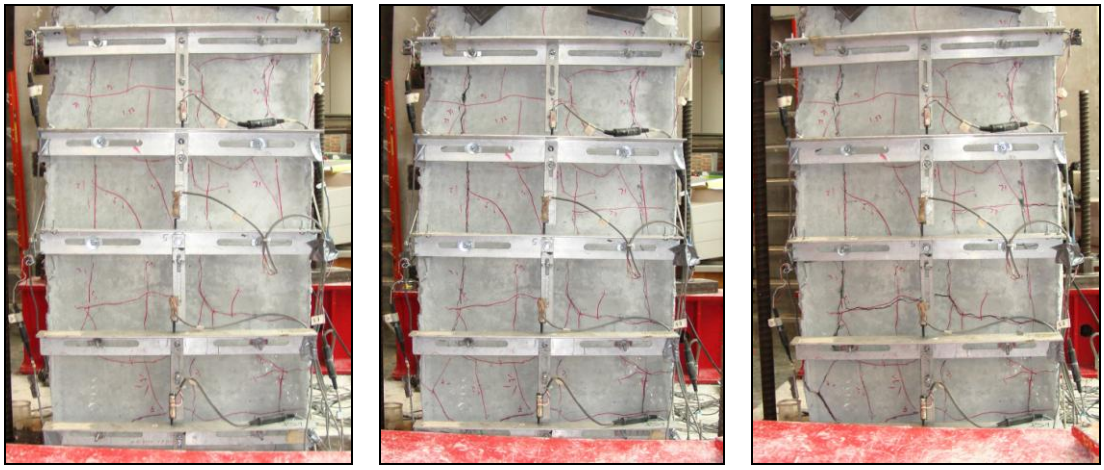

Figure 3.52 – SLB: South face at - $\mu_{2.5,1}$ (left), - $\mu_{2.5,3}$ (center), and + $\mu_{3.6,1}$ (right)

The large amount of dilation of the specimen caused the concrete to bear against the east and west face instruments, causing them to yield incorrect measurements. Figure 3.53 shows one instrument rod on the east face bowing outwards, although it was straight at the beginning of the test. This effect was noticed at the end of the - $\mu_{2.5,3}$ cycle.

Figure 3.53 – SLB: East face instrument

Because of the large strength drop occurring during the + $\mu_{3.6,1}$ cycle, the test was stopped, and the pull cycle of $\mu_{3.6,1}$ was not completed.

Force-Displacement Response / Damping

The force-displacement response for this test is shown below (Figure 3.54).

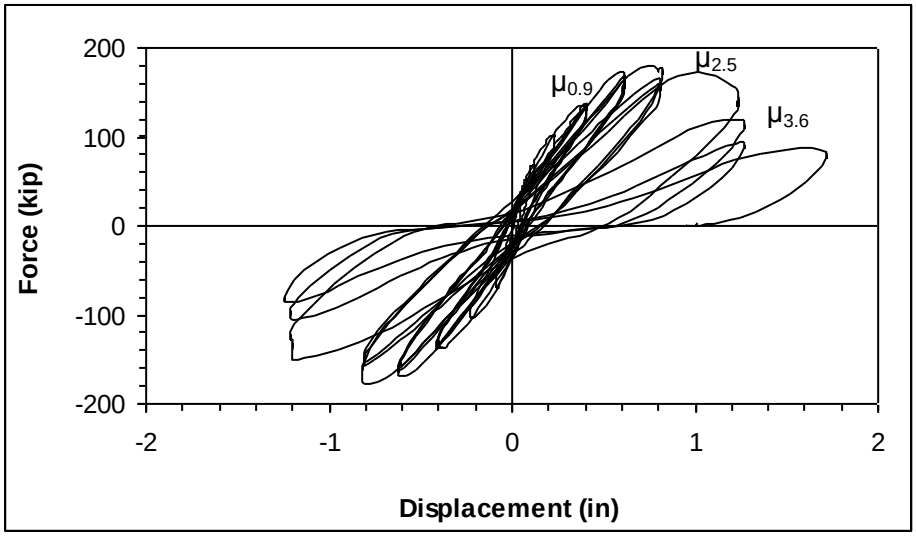

Figure 3.54 – SLB: Actual Force-Displacement Response

A large amount of strength degradation occurred during the $\mu_{2.5}$ cycles, where the load decreased from 172 kips to 94 kips in the positive loading direction. The hysteretic damping for the maximum loading cycle ($\mu_{1.7,1}$) was 9.8%, while the $\mu_{2.5,1}$ cycle reached a value of 14.7%.

Curvature Profiles

The curvature profiles for force and displacement-controlled segments of the test are shown in Figure 3.55.

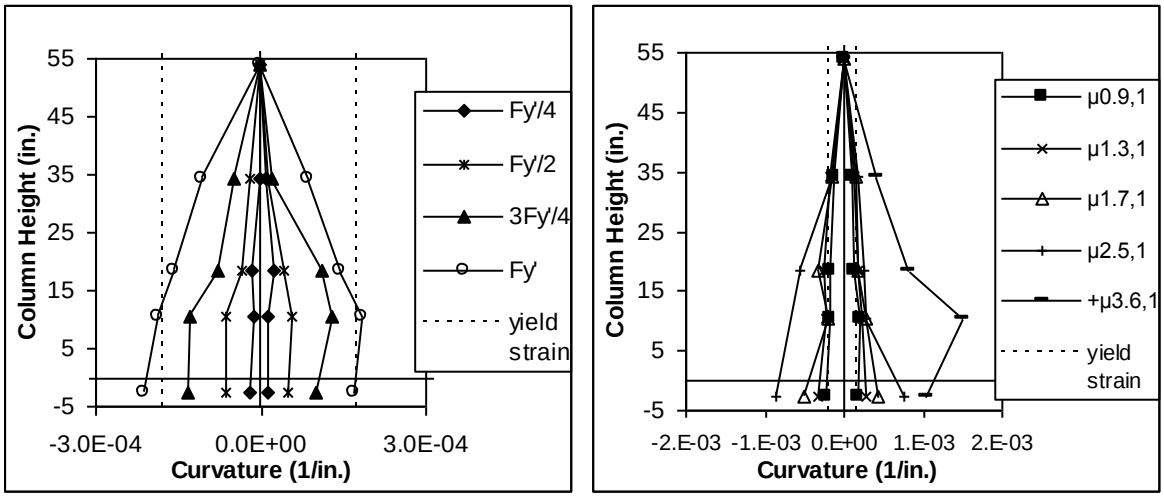

Figure 3.55 – SLB: Curvature profiles for force-controlled (left) and displacement-controlled (right) cycles

The second gage from the top (26 inches from the column base) has been removed from each graph because of inaccurate results. The instruments used to calculate curvature showed reasonable results throughout the test. The profiles are fairly symmetric as expected.

The predicted value for the yield curvature (±1.78e-4) was quite accurate, since the measured maximum curvatures for the $F_y^{'}$ cycle were +1.85e-4 and -2.11e-4 in^{-1}. The maximum curvatures for the test were +1.49e-3 for the $+\mu_{3.6,1}$ cycle and -8.73e-4 for the $-\mu_{2.2,1}$ cycle.

Strain Gage Histories

Only two strain gages collected data during this test. Additionally, the location of these strain gages is unknown, except that they were both located on the east face. One of the strain gage histories is shown below in Figure 3.56.

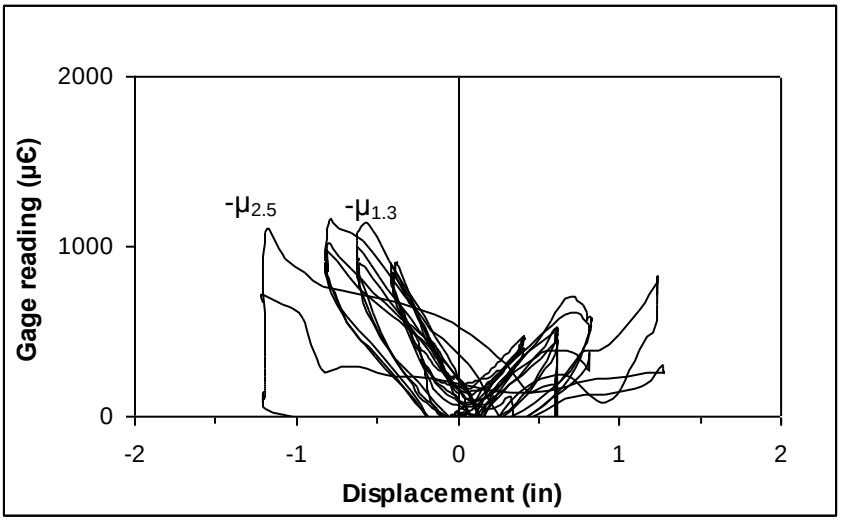

Figure 3.56 – SLB: East face strain gage history

The general 'V-shape' can be seen, however this gage recorded negative values throughout the cycles, and is thus generally unreliable. According to this gage history, the maximum recorded value was lower than 2069 με, meaning this

particular stirrup did not yield. Since only two of ten gages recorded data, a strain profile could not be generated for this test.

CHAPTER 4 – DUCTILE SHEAR FAILURE SPECIMENS

This chapter will cover test observations, force-displacement responses, damping, curvature profiles, and strain profiles of the four ductile shear failure mode specimens. All tests will be compared in Chapter 5.

Figure 4.1 shows the predicted response and expected failure point. As with the brittle specimens, the V_n for the ductile specimens has increased. Compared to Figure 2.7, the intersection of the two graphs is not as clear. The predicted shear capacity for the normal weight specimens does not intersect with the force-displacement graph until a ductility level which cannot be reached, so a flexural failure is predicted.

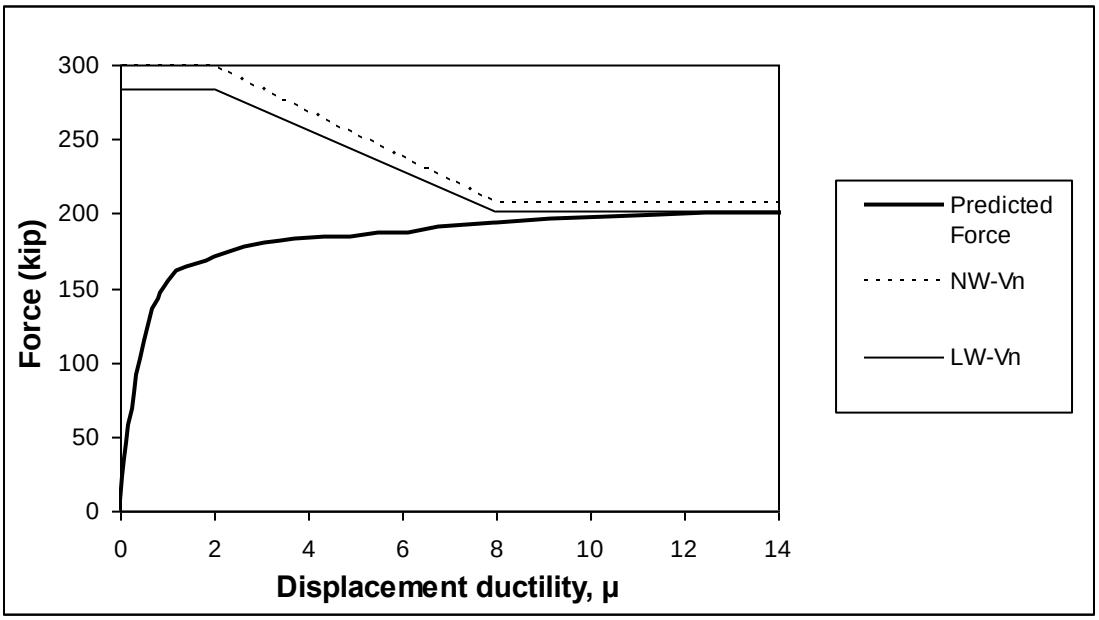

Figure 4.1 – Predicted Force-Displacement Response for Ductile Failure Mode

The first half of the loading protocol was force-controlled, where the specimens were loaded up to the first yield point ($F_y^{'}$ = 136 kips). The second portion was displacement-controlled, where the specimens were loaded up to ductility level 10.

The test observations discussed here are presented in tabular form in Chapter 5, for easy comparison.

4.1 - Normal Weight Ductile Shear Failure Specimen (NWD)

The experimental loading procedure for this test is shown in Figure 4.2.

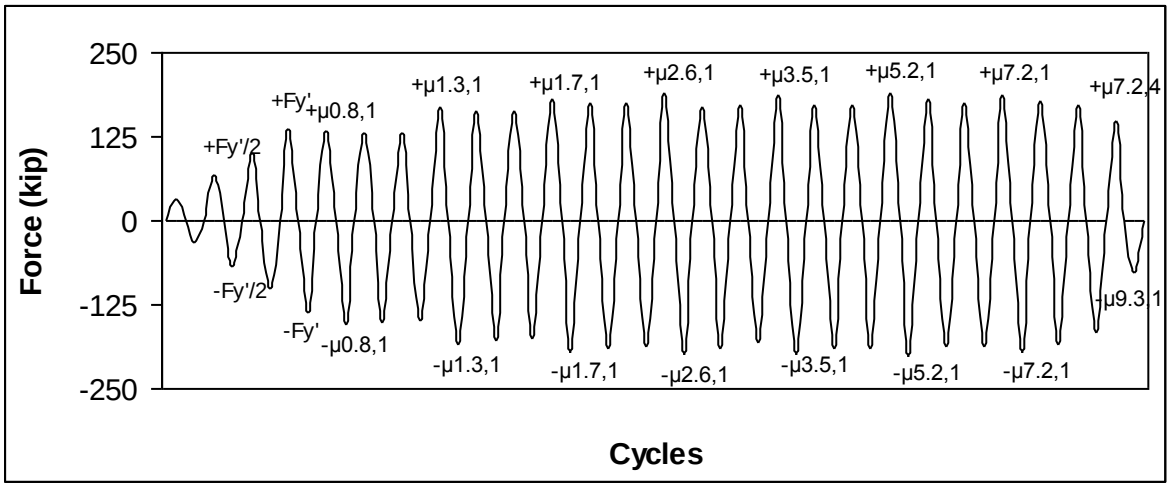

Figure 4.2 – NWD: Actual loading protocol

Force-controlled Cycles

The first flexural cracks appeared near the bottom of the column on the north and south faces during the $F_y^{'}/2$ cycle. Only two cracks were found on each face. The $\pm 3F_y^{'}/4$ cycle caused the first cracks on the east and west faces, which were spaced three to seven inches apart. A few of these cracks started to become flexure-shear cracks. Some new flexural cracks were also formed in the middle area of the column.

During the $\pm F_y^{'}$ cycle, several flexure cracks propagated downwards to form flexure-shear cracks. Some shear-only cracks also formed during this cycle (Figure

4.3, left). Only one new crack was found on the north face, while no changes were recorded for the south face (Figure 4.3, right).

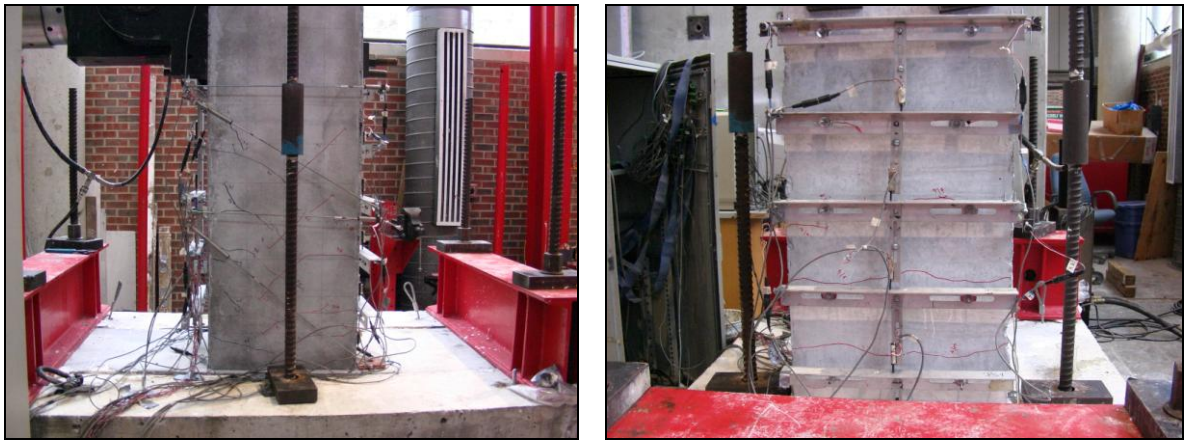

Figure 4.3 – NWD: West (left) and south (right) faces at $\pm F_y^{'}$

The top displacement reached during the + $F_y^{'}$ cycle was +0.37 inches, and for - $F_y^{'}$ was -0.28 inches.

Displacement-controlled Cycles

Very few new cracks appeared on all faces for the first cycle of $\mu_{0.8}$. Only a few cracks were extended during the second and third cycles. A few more extensions and new cracks were formed during the $\pm \mu_{1.3}$ cycles, but there were no changes for the north and south faces. Similar results were recorded for the $\mu_{1.7}$ cycles, with the exception of some spalling that began on the north and south faces (Figure 4.4).

Figure 4.4 – NWD: North face at - $\mu_{1.7,3}$

Several extensions occurred on the east and west faces during the $\pm \mu_{2.6,1}$ cycle, and the first signs of crushing can seen at the corners of the column (Figure 4.5). The largest shear crack measured was 0.016 inches for the push cycle, and 0.035 inches for the pull cycle, although the maximum loads were similar (+191 kips and -199 kips).

Figure 4.5 – NWD: East (left) and west (right) faces at - $\mu_{2.6,1}$

Also, the north and south faces exhibited a large increase in spalling compared to previous cycles (Figure 4.6). A single new crack formed on the bottom of the north face.

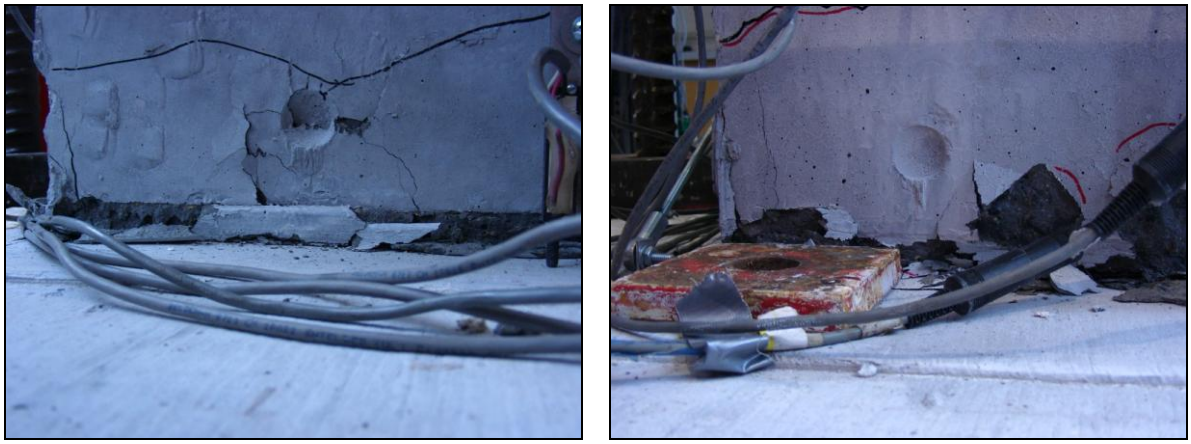

Figure 4.6 – NWD: North (left) and south (right) spalling at - $\mu_{2.6,1}$

The second and third cycles caused the formation of one new flexure crack on the north face and one new vertical crack on the south face. Spalling continued, and the maximum flexure crack width was measured at 0.06 inches. Several extensions occurred on the east and west faces.

The $\pm\mu_{3.5,1}$ cycle caused new shear cracks and extensions of shear cracks to form on the east and west faces. Crushing and spalling continued on all faces. One new flexure crack was found on both the north and south faces. By the third cycle, many cracks were extended on the east and west faces.

Some extensions were found during the $\pm\mu_{5.2,1}$ cycle, but the most damage occurring on the east and west faces was the crushing of the bottom corners as a

plastic hinge began to form. The condition of the specimen as a whole deteriorated throughout the three cycles of $\pm \mu_{5.2}$, as cracks widened (Figures 4.7 and 4.8).

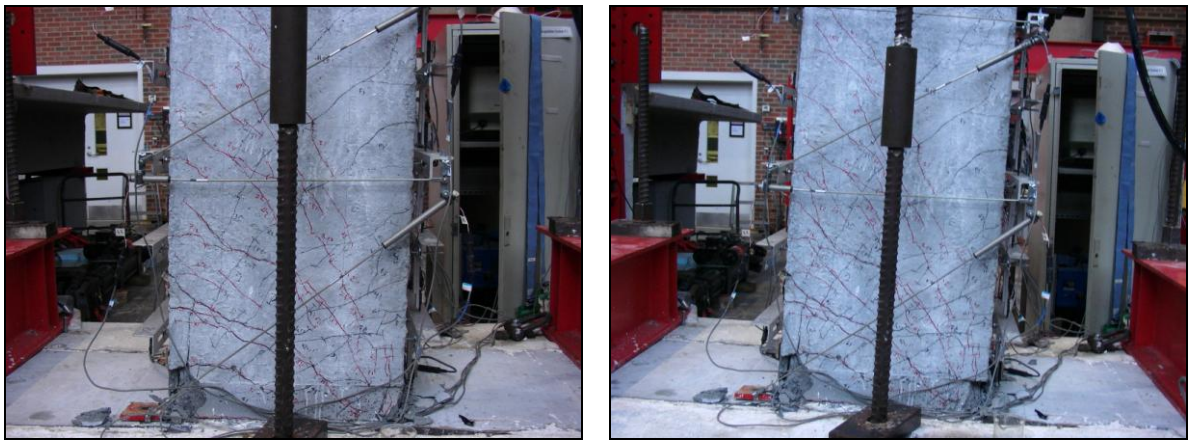

Figure 4.7 – NWD: East face at $-\mu_{5.2,1}$ and $-\mu_{5.2,3}$

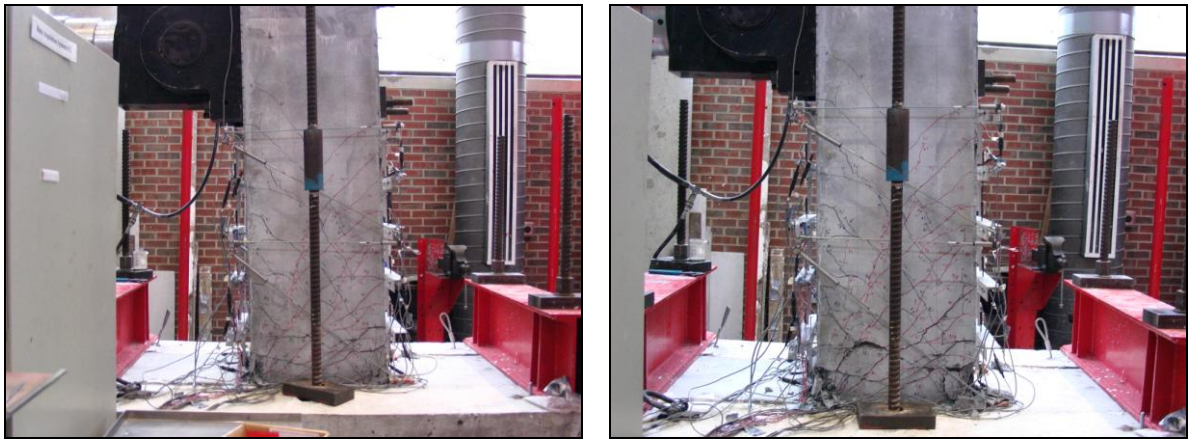

Figure 4.8 – NWD: West face at $-\mu_{5.2,1}$ and $-\mu_{5.2,3}$

A few vertical cracks formed on the north and south faces throughout the $\mu_{5.2}$ cycles, and crushing and spalling continued (Figure 4.9).

Figure 4.9 – NWD: North face spalling at $-\mu_{5.2,1}$ and $-\mu_{5.2,3}$

The maximum loads of +191 and -202 kips occurred during the $\pm\mu_{5.2,1}$, at respective displacements of +2.27 and -2.28 inches. It should be noted that although the $\mu_{5.2}$ cycle achieved the highest loads, ductility levels from two to eight achieved similarly high load levels, as seen in the force-displacement response (Figure 4.17). Also, the strengths degraded at similar rates throughout the three cycles.

Because of a limited horizontal displacement allowance of the axial stressing bars, the $+\mu_{9.3,1}$ portion of the cycle could not be completed. Therefore the specimen was loaded to $+\mu_{7.2,4}$ in the push direction, and $-\mu_{9.3,1}$ in the pull direction. This caused a larger tension force, leading to greater damage on the south face.

The north and south faces showed significant degradation throughout the last four cycles of the test (Figure 4.10, 4.11). These faces showed almost no new cracking until the second and third cycles. Note the increase in vertical cracking on the north face for the $-\mu_{9.3,1}$ cycle. The south face exhibited excessive spalling of

concrete cover for a majority of the column height. Note also that some instruments were removed from the north, south, and east faces in order to avoid damage.

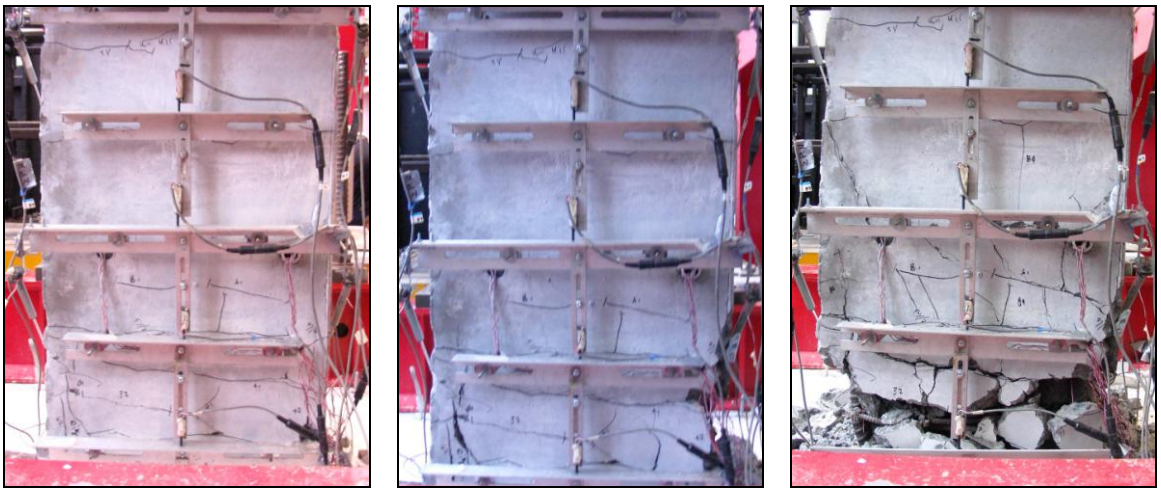

Figure 4.10 – NWD: North face at - $\mu_{7.2,1}$ (left), - $\mu_{7.2,3}$ (center), and - $\mu_{9.3,1}$ (right)

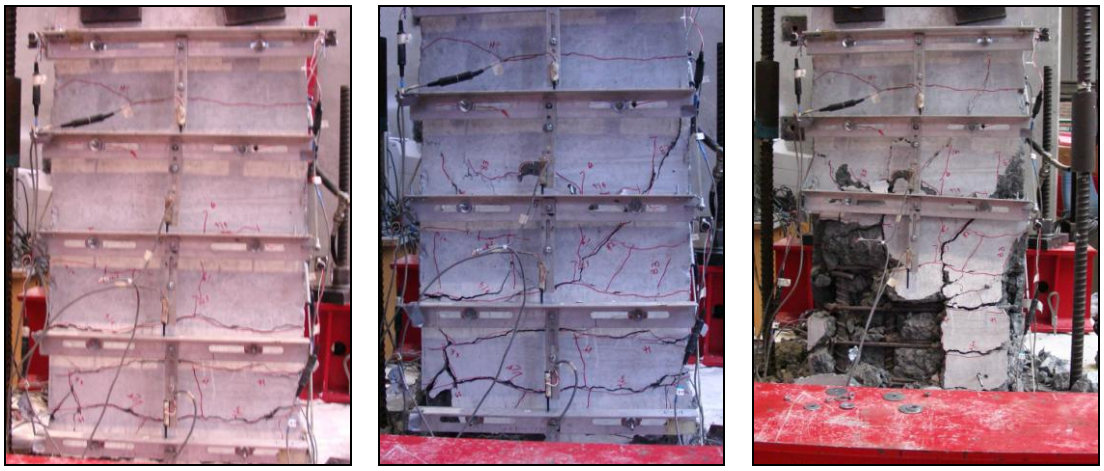

Figure 4.11 – NWD: South face at - $\mu_{7.2,1}$ (left), - $\mu_{7.2,3}$ (center), and - $\mu_{9.3,1}$ (right)

Figure 4.11 shows a large diagonal crack forming on the south face for the - $\mu_{7.2,3}$. This figure also clearly shows how the flexure cracks align with the stirrups, and the

vertical cracks align with the longitudinal bars. The north and south faces broke away completely from the bottom of the column. The north face is shown in Figure 4.12.

Figure 4.12 – NWD: Concrete spalling at - $\mu_{7.2,1}$ (left) and - $\mu_{7.2,3}$ (right)

The east and west faces also showed large amounts of damage during the last four cycles of loading (Figures 4.13 and 4.14).

Figure 4.13 – NWD: East face at - $\mu_{7.2,1}$ (left), - $\mu_{7.2,3}$ (center), and - $\mu_{9.3,1}$ (right)

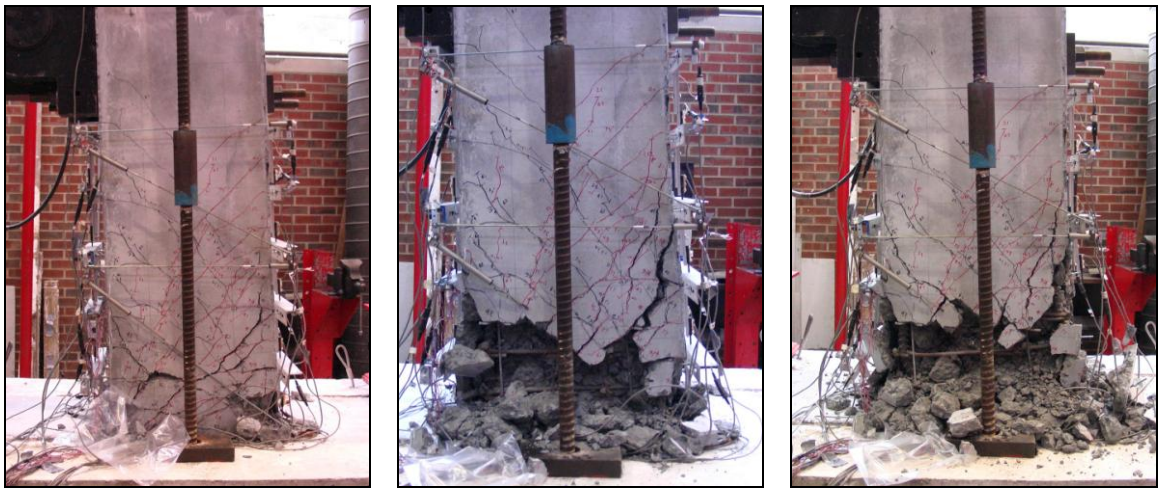

Figure 4.14 – NWD: West face at $-\mu_{7.2,1}$ (left), $-\mu_{7.2,3}$ (center), and $-\mu_{9.3,1}$ (right)

Although the column showed significant deterioration, the maximum load reached during the $\mu_{7.2,1}$ cycle was high (+188 kips and -195 kips) and degradation throughout the three cycles was only slightly greater for $\mu_{7.2}$ when compare to $\mu_{1.7}$ or $\mu_{2.6}$. However the $-\mu_{9.3,1}$ loading dropped significantly to 78 kips from the 149 kips obtained for $+\mu_{7.2,4}$.

During the $-\mu_{9.3,1}$ loading, the hook ends of one stirrup at the bottom of the column began to straighten out and unhook from a longitudinal bar due to dilation of the column (Figure 4.15). The buckling of the corner longitudinal can also be seen here, as well as in for other bars in Figure 4.16.

Figure 4.15 – NWD: West face long. bar buckling and stirrup detachment at - $\mu_{9.3,1}$

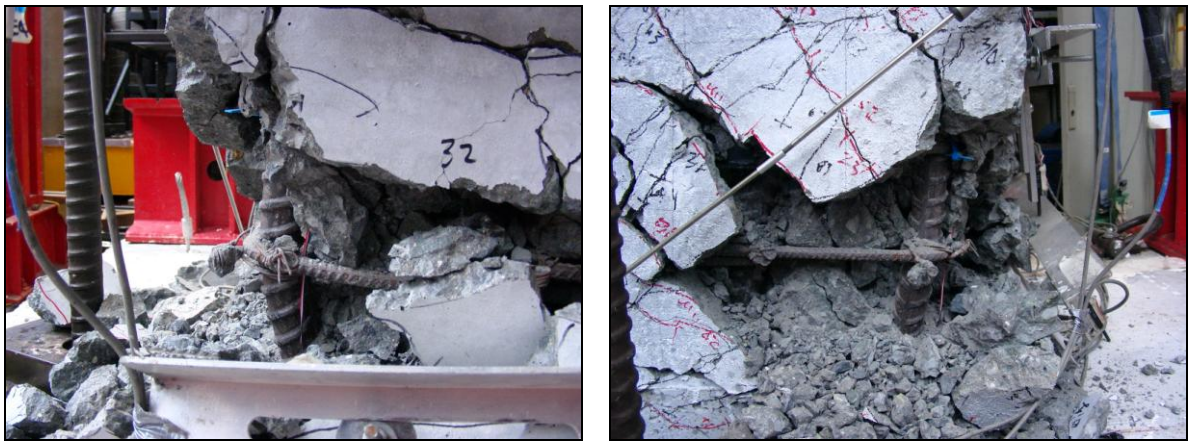

Figure 4.16 – NWD: North (left) and east (right) face long. bar buckling at - $\mu_{9.3,1}$

The average inclination of the east and west face shear cracks was 32°. The top displacement for this specimen was 3.37 inches for + $\mu_{7.2,4}$ and -4.08 inches for - $\mu_{9.3,1}$. These numbers were averages recorded from the two string potentiometers attached at the top of the column. The two instruments read different values for the last three cycles of the test, indicating that the column experienced some twisting.

For the $\pm \mu_{7.2,2}$ cycle, this twisting was calculated to be 0.44° in a counterclockwise direction. The angle of twisting became 1.8° by the $-\mu_{9.3,1}$ loading. This was likely caused by the column's initial imperfect alignment with the loading actuator. The twisting probably affected the readings of the east and west face potentiometers, so these cycles were not considered in the calculation of shear deformation.

Force-Displacement Response / Damping

The actual force-displacement response is shown below (Figure 4.17).

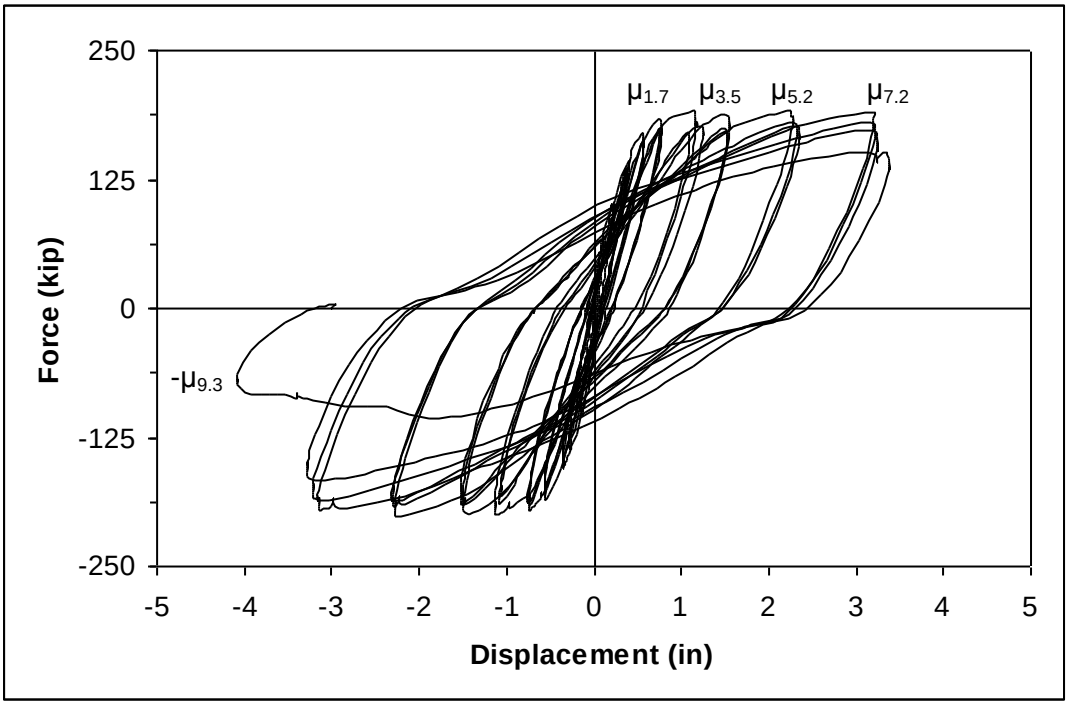

Figure 4.17 – NWD: Actual Force-Displacement Response

Note how the load stays almost constant from $\pm\mu_{1,7}$ to $\pm\mu_{7.2}$ for each set of cycles (first through third). Damping was calculated for this test, where the $\mu_{5.2,1}$ cycle achieved a level of 22.2%, and the maximum damping was 25.8%, occurring during the $\mu_{7.2,1}$ cycle.

Curvature Profiles

Curvature profiles are shown for this test (Figures 4.18 and 4.19). The predicted yield curvature is also plotted on each graph.

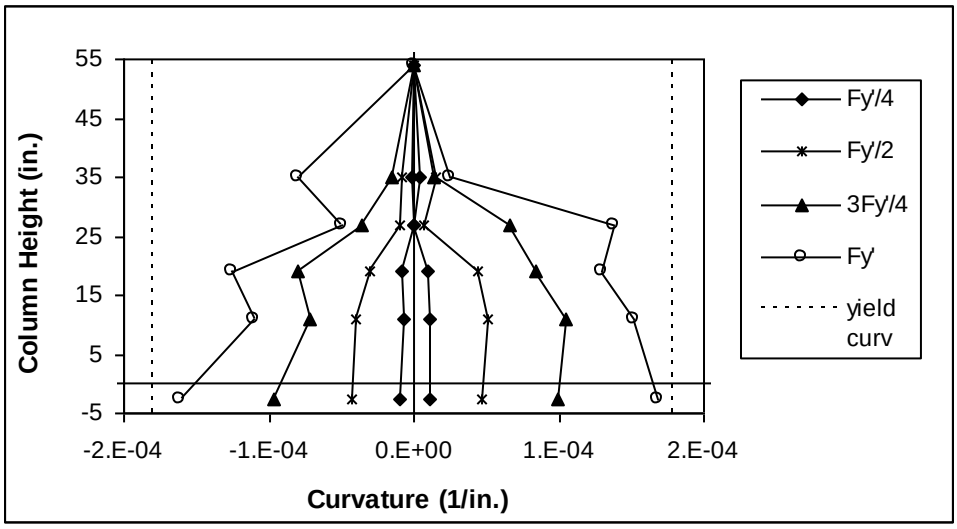

Figure 4.18 – NWD: Curvature profile for force-controlled cycles

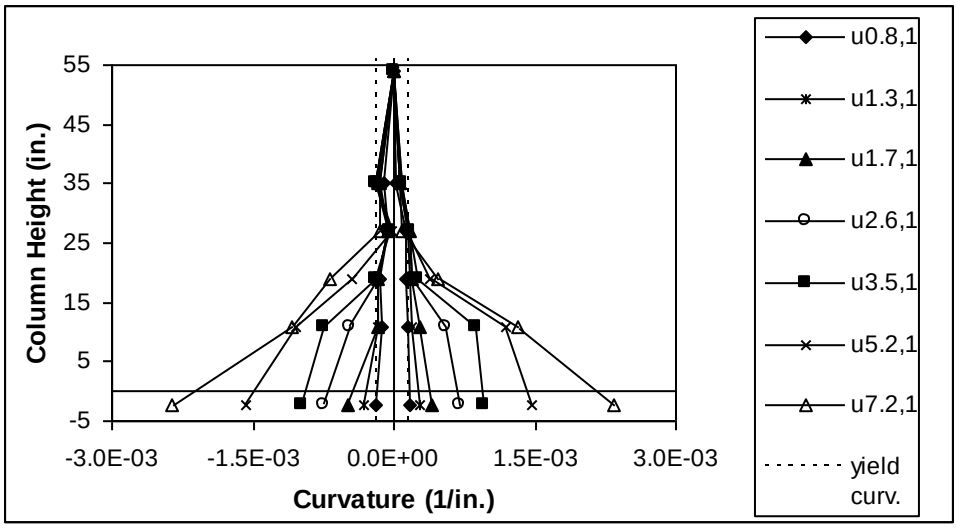

Figure 4.19 – NWD: Curvature profile for displacement-controlled cycles

For both graphs, the curvature generally increased with distance from the load, and also with the amount of load. The calculated curvature values at the center of the bottom cell for the $F_y^{'}$ (-1.62e-4 and +1.68e-4) matched well with the predicted yield curvature value (±1.79e-4 in^{-1}).

A large increase in curvature occurred during the $\mu_{7.2,1}$ cycle, and the maximum values reached were +2.33e-3 and -2.37e-3 in^{-1}. Some instruments on the north and south faces were removed after the $\pm\mu_{7.2,1}$ cycle, making this the last cycle for which curvature could be calculated.

Strain Gage Histories and Profiles

An example strain gage history is shown in Figure 4.20. A small diagram in the top right corner shows the location of the BS3 strain gage, which is on the west

face, 19.4 inches from the base of the column. All strain gage histories are shown in the Appendix.

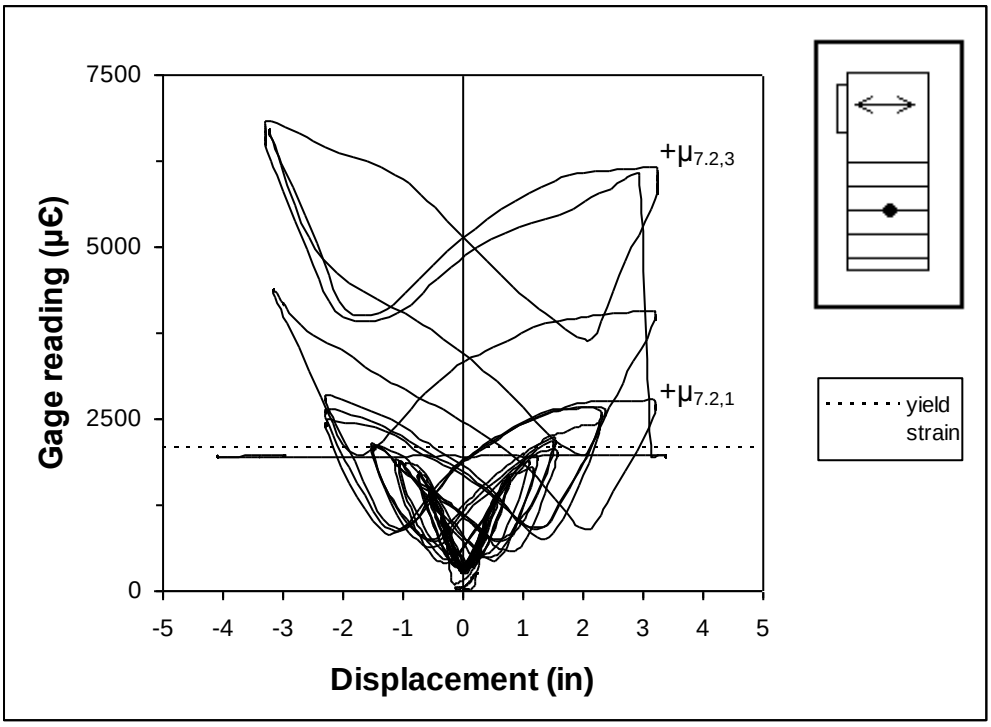

Figure 4.20 – NWD: BS3 strain gage history

The first strain in this stirrup occurs while loading to $+3F_y^{'}/4$, where a strain of 262 με was recorded. This cycle caused the formation of the first flexure-shear cracks. This particular stirrup began to yield during the $-\mu_{3.5,1}$ cycle. A maximum value of 6840 με was reached at the height of the $-\mu_{7.2,3}$ cycle. The specimen was being loaded to $+\mu_{7.2,4}$ when the gage stopped reading correctly.

The force-controlled and displacement-controlled cycle strain profiles for push direction loading are shown in Figures 4.21 and 4.22.

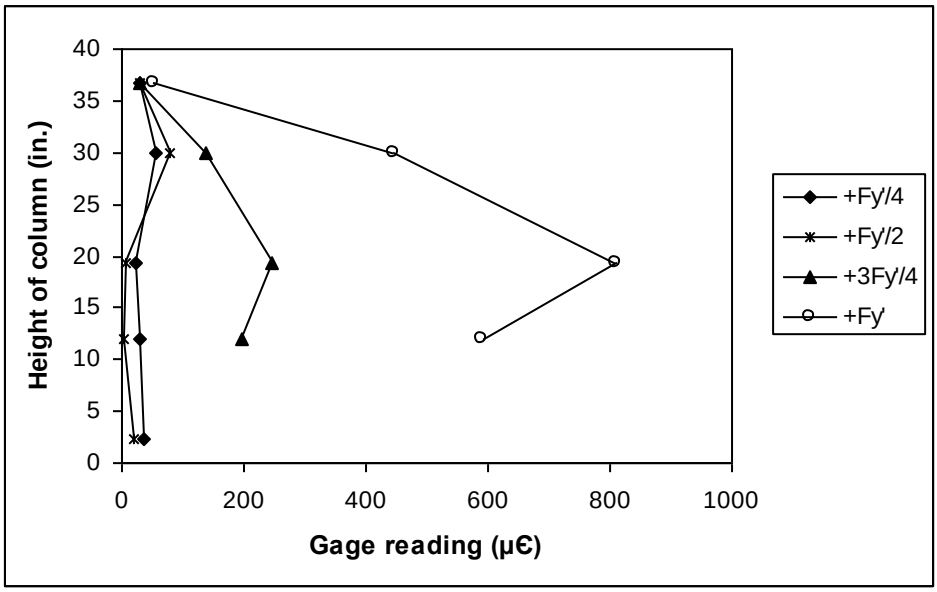

Figure 4.21 – NWD: West face strain profile for force-controlled cycles

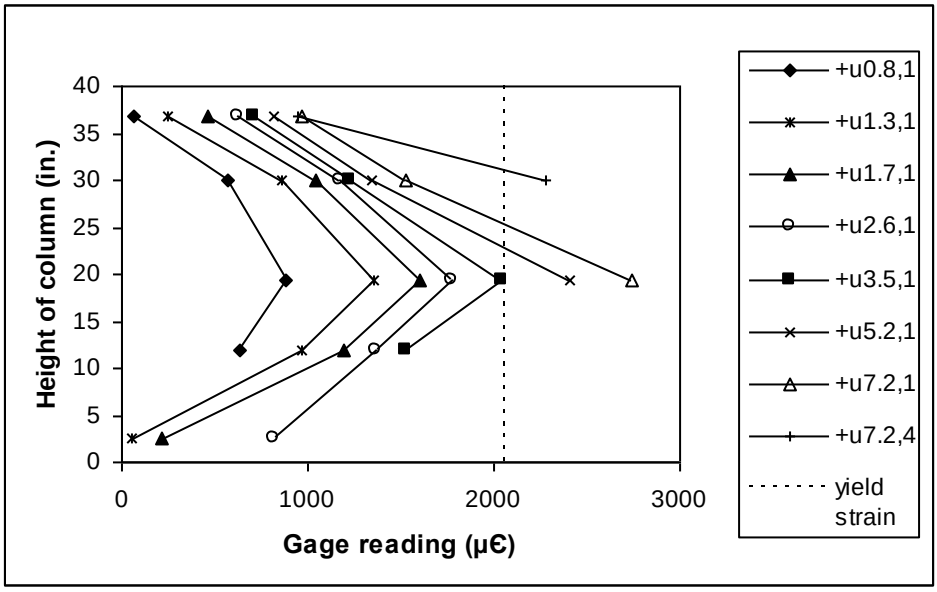

Figure 4.22 – NWD: West face strain profile for displacement-controlled cycles

The maximum strain for all cycles occurred at the central gage, 19.4 inches from the base of the column. Both profiles show symmetry about this gage. Some gages

stopped working correctly towards the end of the test, so their values are not shown here.

4.2 – Lightweight Clay Ductile Shear Failure Specimen (CLD)

The actual loading procedure for this test is shown in Figure 4.23.

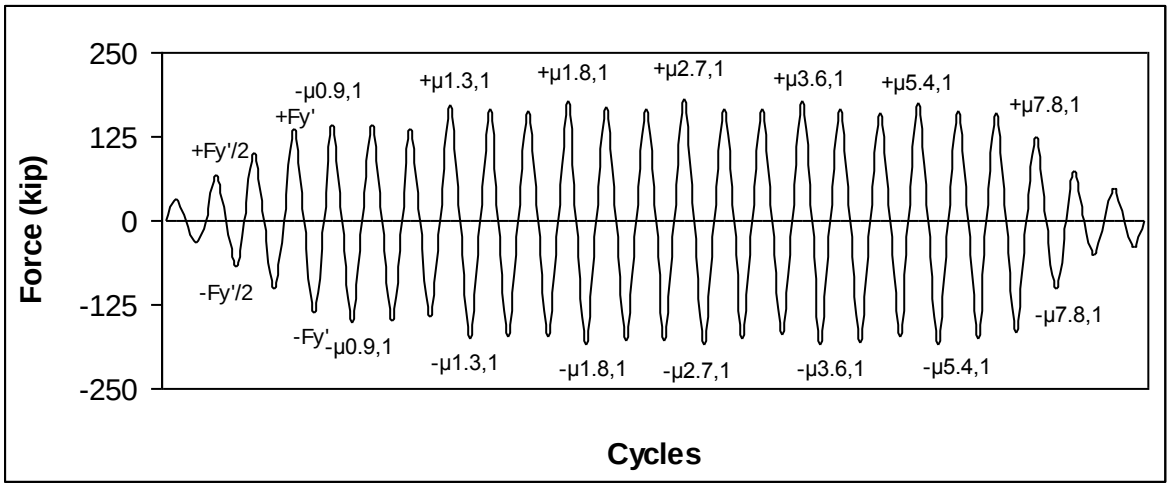

Figure 4.23 – CLD: Actual loading protocol

Force-controlled Cycles

The first flexural cracks appeared on the north and south faces during the $F_y^{'}/2$ cycle. Some cracks also appeared on the west face for the pull direction, but none were found on the east face (Figure 4.24).

Figure 4.24 – CLD: North face (left) and west face (right) at $\pm F_y^{'}/2$

During the $\pm 3F_y^{'}/4$ cycle, some cracking was found in the top half of the column. Also, flexural cracks on the east and west faces became flexure-shear cracks, and were spaced at four to seven inches. These cracks extended in length and became increasingly inclined for the $\pm F_y^{'}$ cycle (Figure 4.25). Additionally, flexure cracks spread on the north and south faces, and the first instance of vertical cracking occurred on the south face.

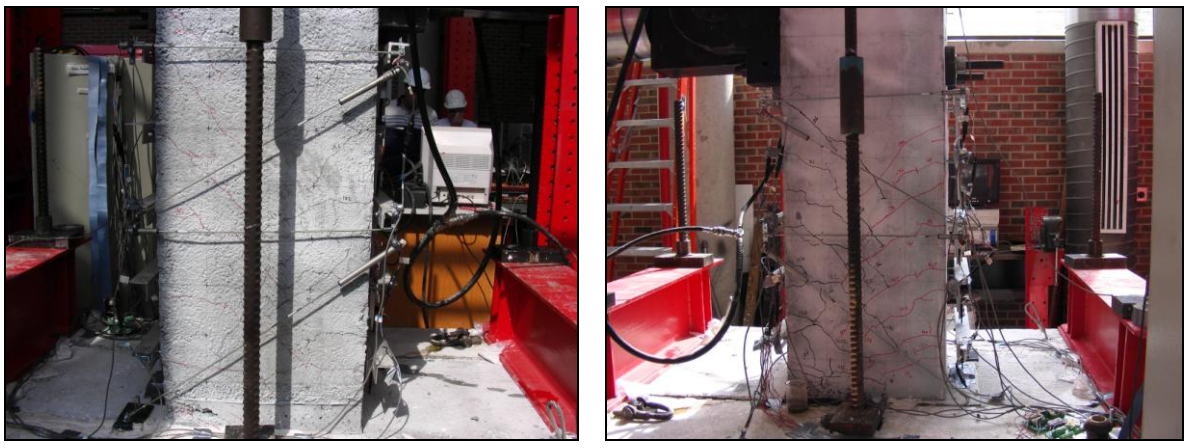

Figure 4.25 – CLD: East (left) and west (right) faces at $\pm F_y^{'}$

The top displacement reached during the + $F_y^{'}$ cycle was +0.38 inches, and for - $F_y^{'}$ was -0.34 inches.

Displacement-controlled Cycles

The first shear-only cracks appeared during the first $\mu_{0.9}$ cycle (0.43 in. top displacement). Some cracks were extended on the east and west faces, but no changes were recorded for the north and south face. The second and third cycles brought only a few extensions of existing cracks. The largest crack width for the third cycle was 0.009 in.

The $\pm\mu_{1.3,1}$ cycle brought on more extensions of the flexure-shear and the shear-only cracks, with no new cracks. A very small amount of spalling began on the south face of the specimen, and a few small cracks appeared on the north face (Figure 4.26, left).

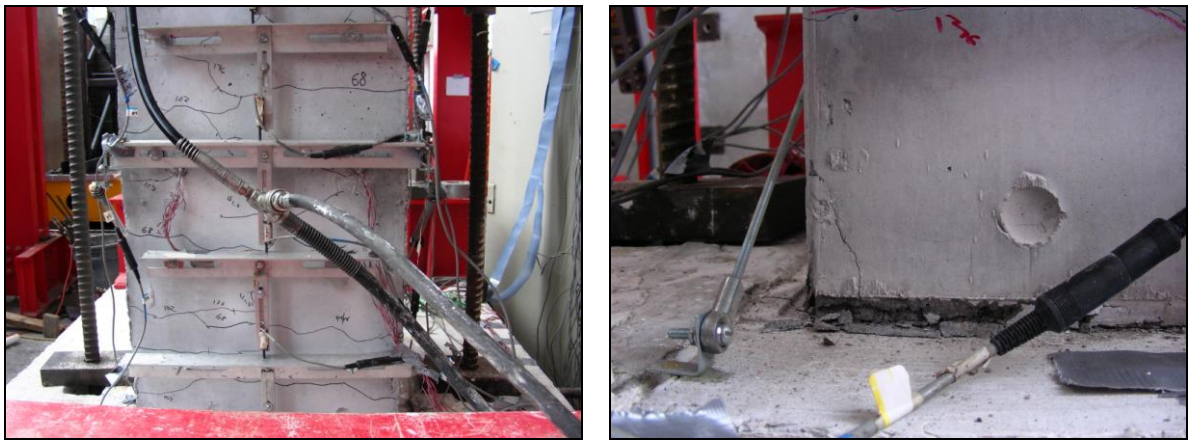

Figure 4.26 – CLD: North face at - $\mu_{1.3,1}$ (left) and south face at - $\mu_{1.3,3}$

By the third cycle, several cracks were extended on the east and west faces, while the north and south faces continued to show signs of spalling (Figure 4.26, right). A slight increase in crack width was observed, as the widest flexural crack recorded was 0.01 inches.

The $\pm\mu_{1.8,1}$ cycle caused no new cracks to form on the north and south faces, but crushing and spalling did progress. The east and west faces showed a few extensions, and crack widths increased to 0.013 inches. The second and third cycles caused few extensions and also progressed crushing and spalling.

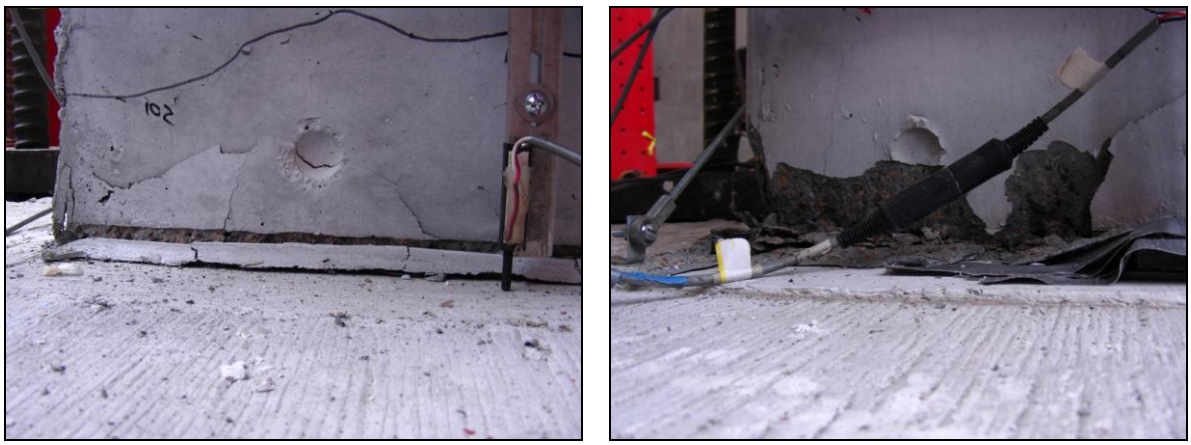

Figure 4.27 – CLD: North face (left) and south face (right) at - $\mu_{1.8,3}$

Several extensions occurred on the east and west faces during the $\pm\mu_{2.7,1}$ cycle, and the largest crack width was measured at 0.06 inches. Some extensions were made by the third cycle (Figure 4.28), and one new flexure crack formed in the lower half of the column on both north and south faces. Crushing can be seen in the bottom corners of the column.

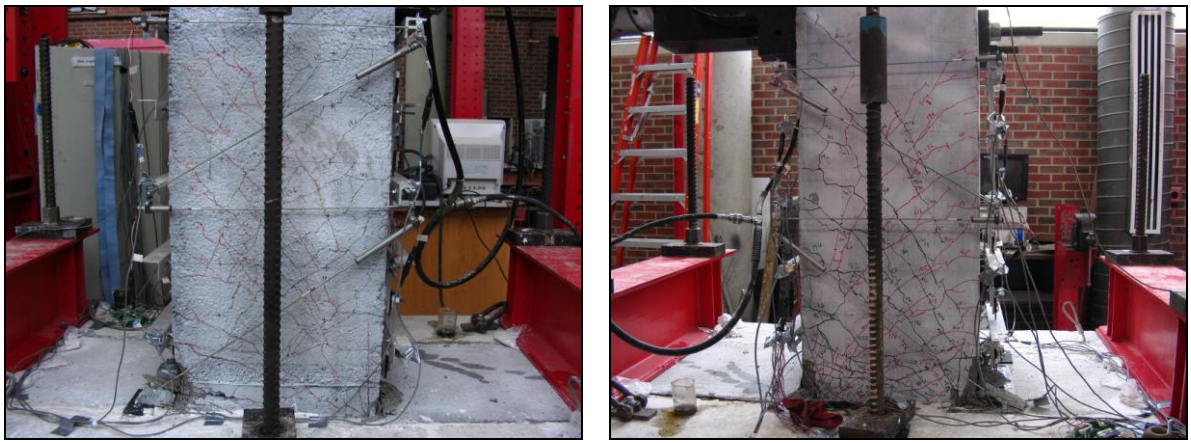

Figure 4.28 – CLD: East (left) and west (right) faces at - $\mu_{2.7,3}$

The $\mu_{2.7,1}$ cycle produced the highest load average between push and pull cycles (185 kips at 1.30 inches). However, the strength did not start to degrade significantly until the $\mu_{7.8}$ level. The three cycles of $\mu_{3.6}$ caused no new shear cracks and very few extensions.

For the $\mu_{5.4}$ cycle, crack widths were measured at up to 0.25 inches. Some extensions were found, and crushing became severe on all faces (Figure 4.29). The four instruments located at the bottom of the column on east and west faces became unreliable by the third cycle, due to the spalling off of the concrete to which the instrument angles were attached.

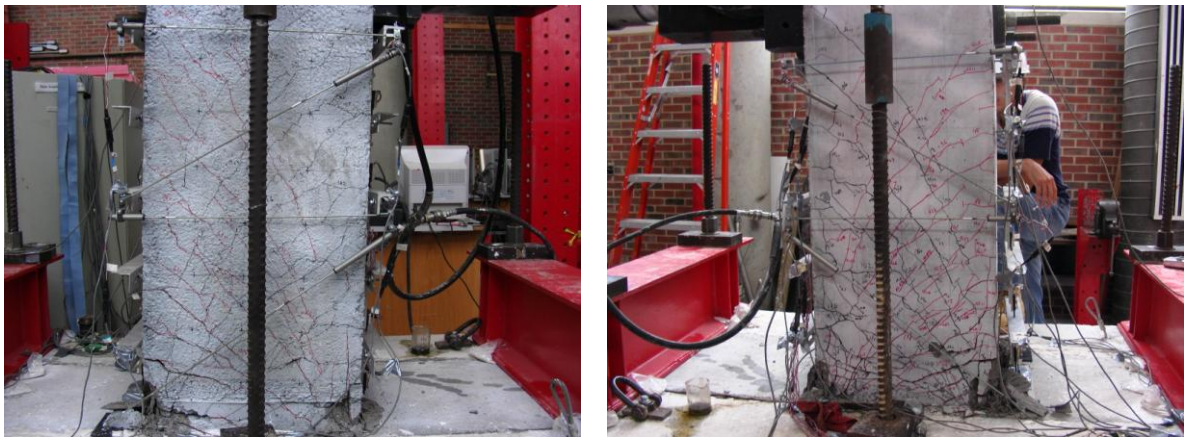

Figure 4.29 – CLD: East (left) and west (right) faces at - $\mu_{5.4,1}$

Some vertical cracks formed on the north and south faces throughout the $\mu_{5.4}$ cycles, and crushing and spalling continued.

Ductility levels $\mu_{1.8}$ to $\mu_{5.4}$ obtained similar load levels and similar degradation the three cycles. A large drop in strength was experienced for the $\mu_{7.8,1}$ cycle, where maximum loads reached were +137 and -106. These loads degraded to +53 and -41 by the third cycle, and the test was stopped here. Figures 4.30 - 4.34 show the deterioration of all faces of the specimen for the last few cycles of loading.

Figure 4.30 – CLD: East face at - $\mu_{5.4,3}$ (left), - $\mu_{7.8,1}$ (center), and - $\mu_{7.8,3}$ (right)

Figure 4.31 – CLD: West face at - $\mu_{5.4,3}$ (left), - $\mu_{7.8,1}$ (center), and - $\mu_{7.8,3}$ (right)

Figure 4.32 – CLD: West face long. bar buckling and stirrup detachment at - $\mu_{7.8,3}$

Two hook ends nearly detached from the longitudinal bar in Figure 4.32, due to the dilation of the column and buckling of the longitudinal bar.

Figure 4.33 – CLD: North face at - $\mu_{5.4,3}$ (left), - $\mu_{7.8,1}$ (center), and - $\mu_{7.8,3}$ (right)

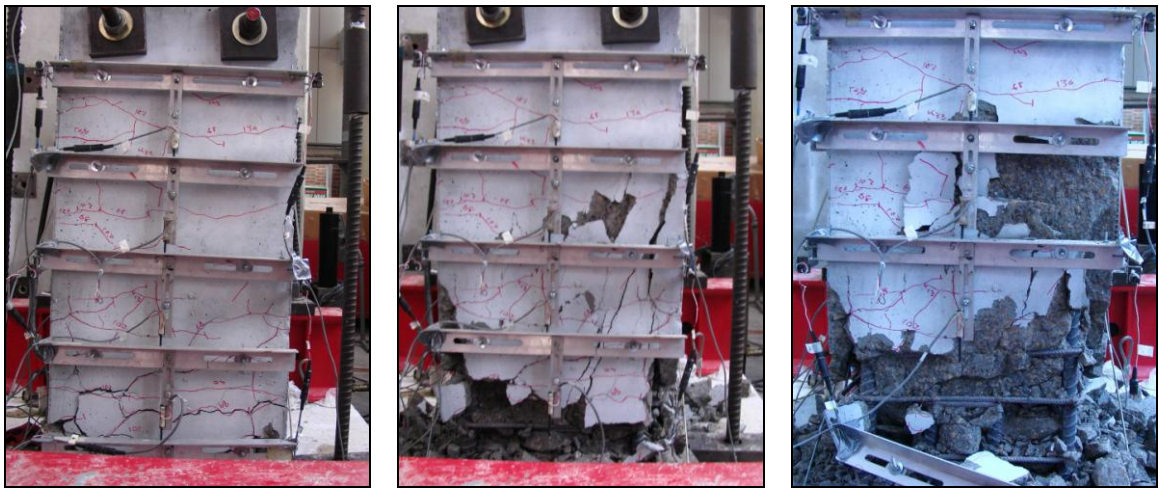

Figure 4.34 – CLD: South face at - $\mu_{5.4,3}$ (left), - $\mu_{7.8,1}$ (center), and - $\mu_{7.8,3}$ (right)

Figure 4.33, shows the progression of the vertical cracking on the north face. By the third cycle of $\mu_{7.8}$, much of the concrete cover spalled off of every face. Figure 4.34 shows the crack progression and severe spalling of the south face of the specimen. Also note the removal of instruments in order to prevent damage.

The inclination of the shear cracks that formed on the east and west faces were approximately 33°. The top displacement for this specimen was +4.07 for the $\mu_{7.8,3}$ cycle. The two string potentiometers recorded counterclockwise twisting in the specimen for all three cycles of $\mu_{7.8}$. This angle of twist was much greater in the push direction, where values of 2.5° to 2.9° were measured, while the highest twist measured for the pull direction was 0.63°.

Force-Displacement Response / Damping

The actual force-displacement response is shown below (Figure 4.35).

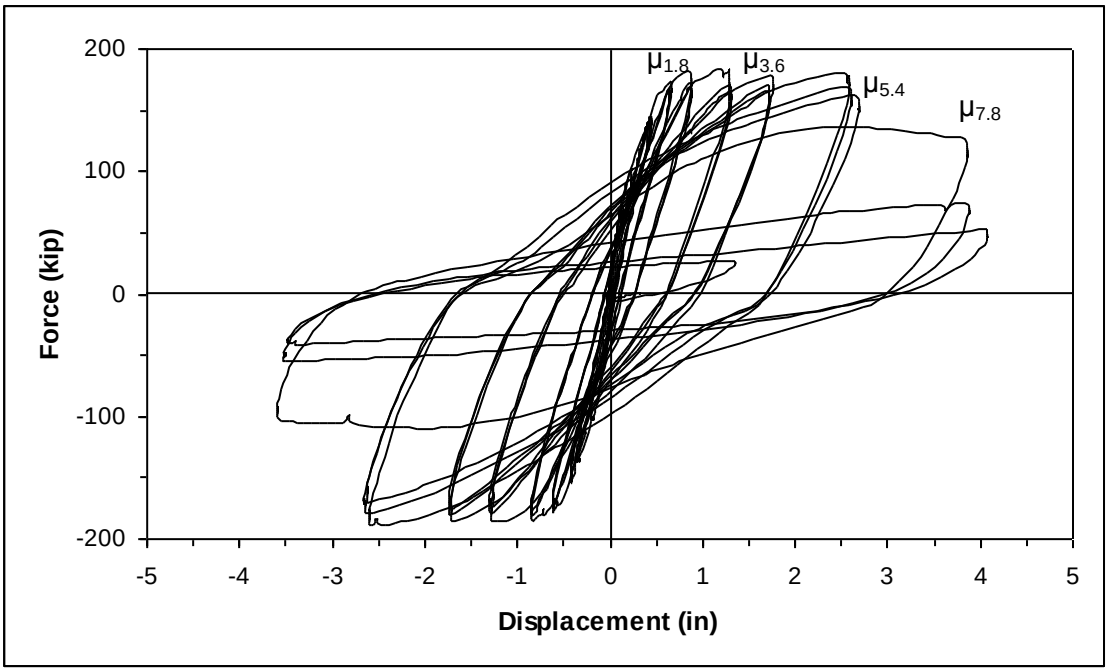

Figure 4.35 – CLD: Actual Force-Displacement Response

The maximum load remains high for cycles $\mu_{1.8}$ to $\mu_{5.4}$ for each set of cycles. Damping values of 23.8% and 27.9% were calculated for the $\mu_{5.4,1}$ and $\mu_{7.8,1}$ cycles, respectively.

Curvature Profiles

Curvature profiles are shown for this test (Figures 4.36 and 4.37). The predicted yield curvature is also plotted on each graph.

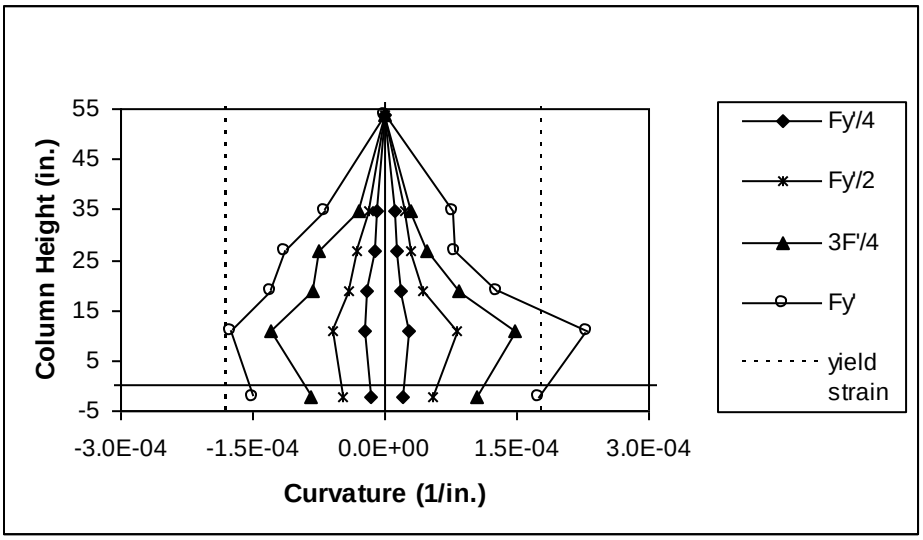

Figure 4.36 – CLD: Curvature profile for force-controlled cycles

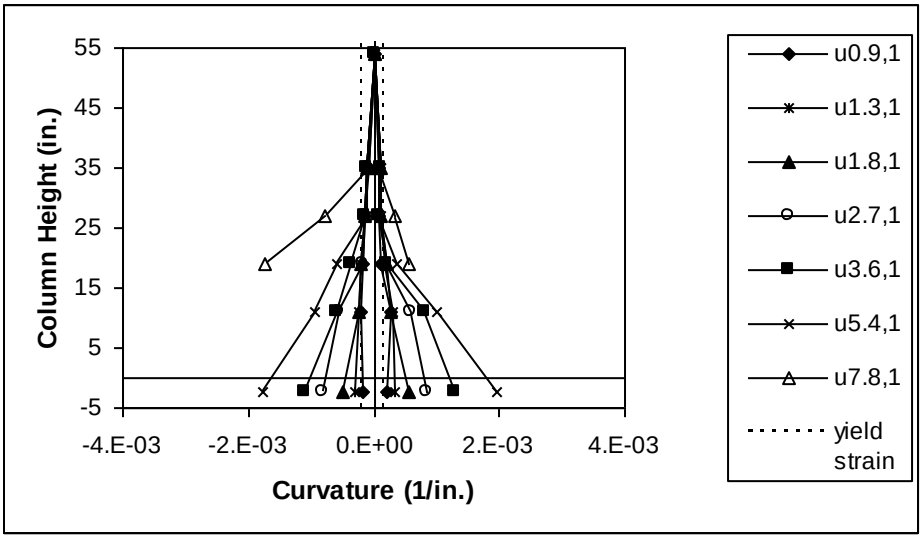

Figure 4.37 – CLD: Curvature profile for displacement-controlled cycles

For the force-controlled profile, the curvature increased with distance from the load, but decreased for the bottom cell in the footing. The calculated curvature values at

the center of the bottom cell for the F_y' cycle were -1.76e-4 and +2.29e-4 in^{-1}), so only the negative value matched well with the predicted yield curvature (±1.79e-4 in^{-1}.).

A large increase in curvature occurred during the $\mu_{7.8,1}$ cycle, however the bottom two cells were not included because of the removal of instruments. The maximum curvature values recorded were +1.95e-3 in^{-1} and -1.77e-3 in^{-1} for the $\pm\mu_{5.4,1}$ loading.

Strain Gage Histories and Profiles

One strain gage history is shown in Figure 4.38. The figure shows the location of the TS2 strain gage, located on the east face, 29.5 inches from the base of the column. All strain gage histories are given in the Appendix.

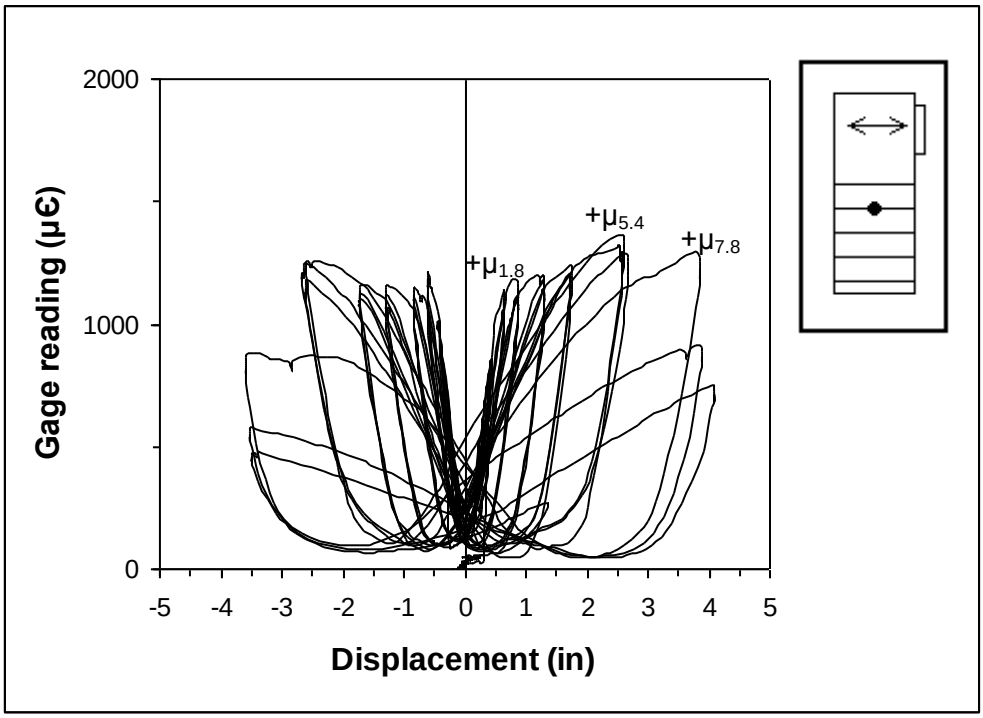

Figure 4.38 – CLD: TS2 strain gage history

Because the yield strain value of 2069 μЄ was never reached, this stirrup did not yield. The first significant strain in this stirrup occurs while loading to + $F_y^{'}$, where a strain of 648 μЄ was recorded. This coincides with the formation of several flexure-shear cracks. A maximum value of 1360 μЄ was reached during the + $\mu_{5.4,2}$ loading.

The strain profiles for push direction loading are shown in Figures 4.39 and 4.40.

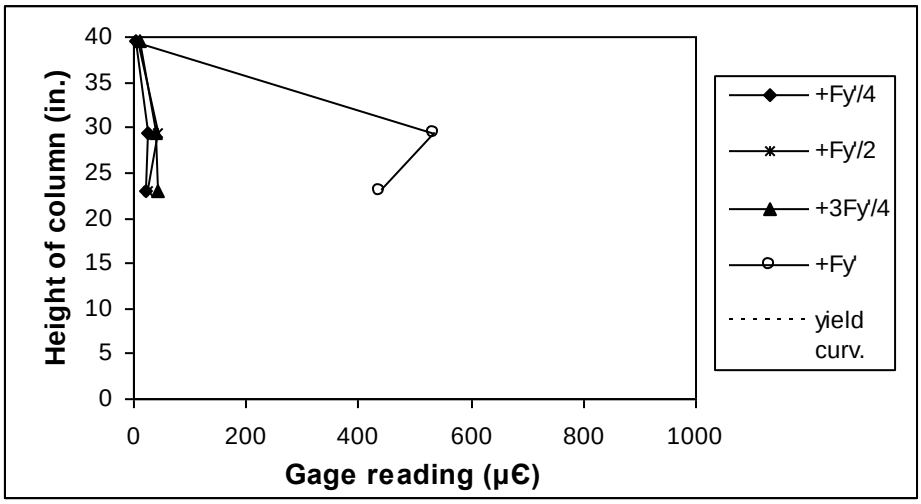

Figure 4.39 – CLD: East face strain profile for force-controlled cycles

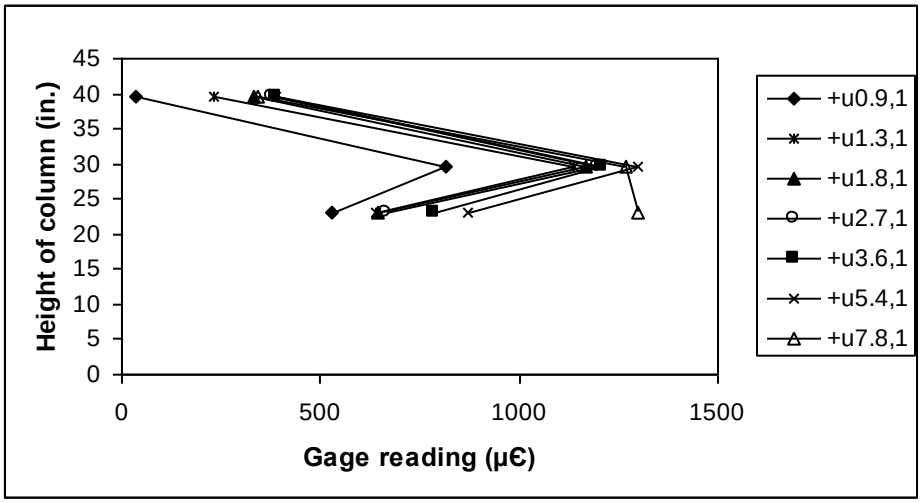

Figure 4.40 – CLD: East face strain profile for displacement-controlled cycles

The bottom two gages did not collect data for this test. Strain begins during the + $F_y^{'}$ loading, as shown in Figure 4.39. The maximum strain was found in the second gage from the top at 29.5 inches. The displacement-controlled profile shows a significant increase in strain for the + $\mu_{7.8,1}$ loading, but only at the central strain gage.

4.3 – Lightweight Shale Ductile Shear Failure Specimen (SHD)

The actual loading procedure for this test is shown in Figure 4.41. As shown, only one cycle of $\mu_{7.6.1}$ was conducted for this test because of a significant load drop.

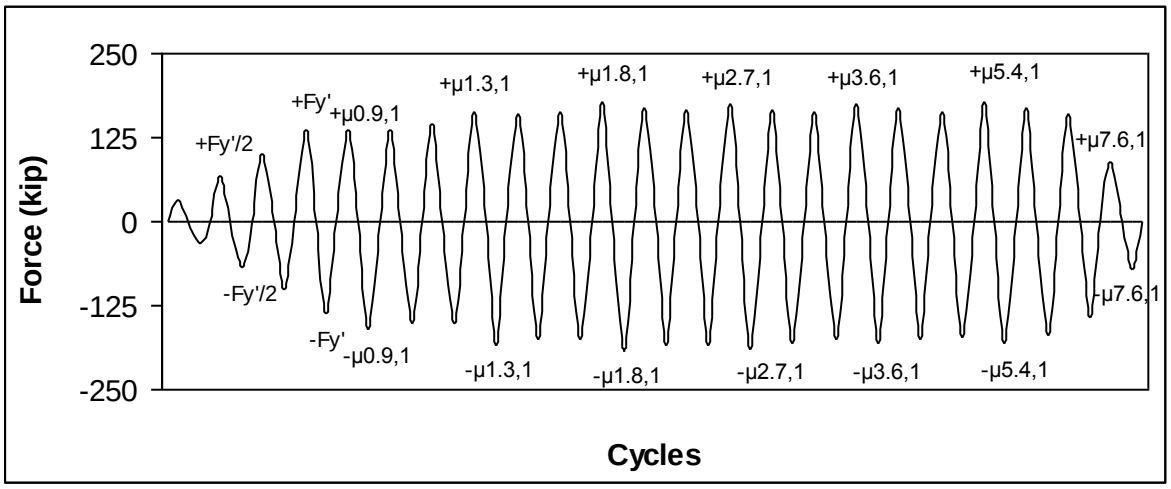

Figure 4.41 – SHD: Actual loading protocol

Force-controlled Cycles

Only a few flexure cracks were formed at the base of the column during the $F_y^{'}/2$ cycle. One of these cracks spread to the east and west faces. During the $\pm 3F_y^{'}/4$ cycle, several more flexure cracks were formed, and some became flexure-shear cracks (Figure 4.42).

Figure 4.42 – SHD: South face (left) and west face (right) at $\pm 3F_y^{'}/4$

Most of the cracks were extended during the $F_y^{'}$ cycle, and more flexure cracks were formed on the north and south faces. The top displacements reached for this cycle were +0.40 and -0.31 inches.

Displacement-controlled Cycles

Flexure-shear and shear-only cracks formed during the $\mu_{0.9,1}$ (±0.41 inches) cycle, and these cracks were extended during the second and third cycles. The north side showed no changes, while the south side developed new flexure cracks for the first and second cycles.

The $\pm \mu_{1.3,1}$ cycle brought on more extensions of the flexure-shear and the shear-only cracks, with a few new shear cracks. The largest flexure crack width measured was 0.02 inches. Some cracks were extended for the second and third cycles.

The $\mu_{1.8}$ cycles caused the first signs of crushing and spalling (Figure 4.43). Some cracks were extended and the largest shear crack was measured at 0.01 inches. The maximum recorded forces of +180 kips and -194 kips occurred during the first cycle of $\mu_{1.8}$, at displacements of ±0.82 inches.

Figure 4.43 – SHD: South face (left) and west face (right) at - $\mu_{1.8,3}$

Crack extensions and crushing continued for the three cycles of $\mu_{2.7}$. Cracks widened to 0.04 inches. Two vertical cracks were found on the south face by the end of the third cycle.

The third cycle of $\mu_{3.6}$ caused the formation of three vertical cracks on north face, and crushing worsened in the corners of the column (Figure 4.44).

Figure 4.44 – SHD: East (left) and west (right) faces at - $\mu_{3.6,3}$

Several extensions were formed for the $\mu_{5.4,1}$ cycle, while few new cracks formed on the north and south faces. Crushing continued for the second and third cycles. Some counterclockwise twisting occurred in the third cycle, and was measured at 0.42°. The progressive damage of the specimen for the last few cycles of loading is shown in Figures 4.45 – 4.48.

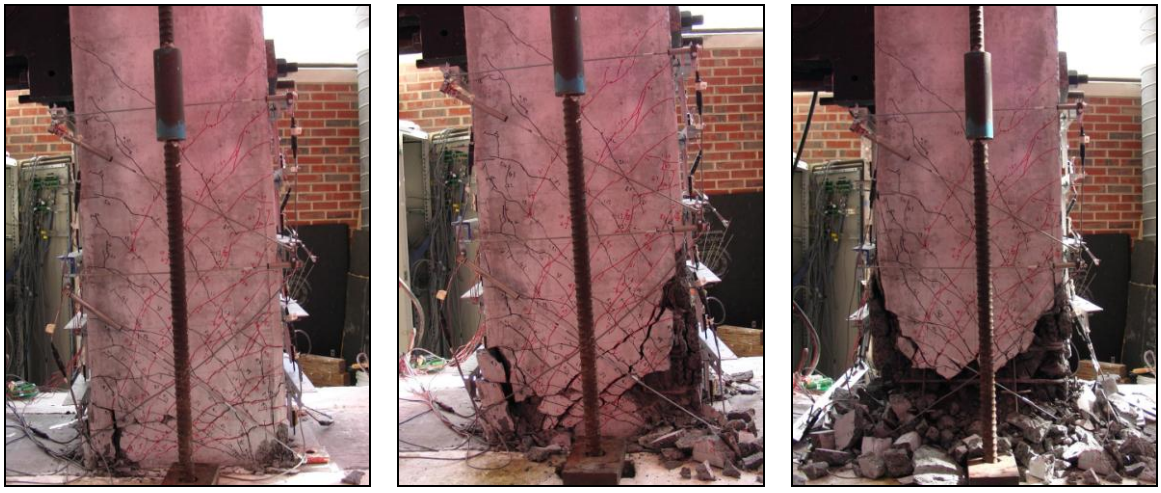

Figure 4.45 – SHD: West face at - $\mu_{5.4,1}$ (left), - $\mu_{5.4,3}$ (center), and - $\mu_{7.6,1}$ (right)

The column began to rapidly degrade during the $\mu_{5.4}$ cycles. The maximum cycle load dropped significantly from +182 and -186 kips in the $\mu_{5.4,1}$ cycle down to +95 and -70 kips in the $\mu_{7.6,1}$ cycle.

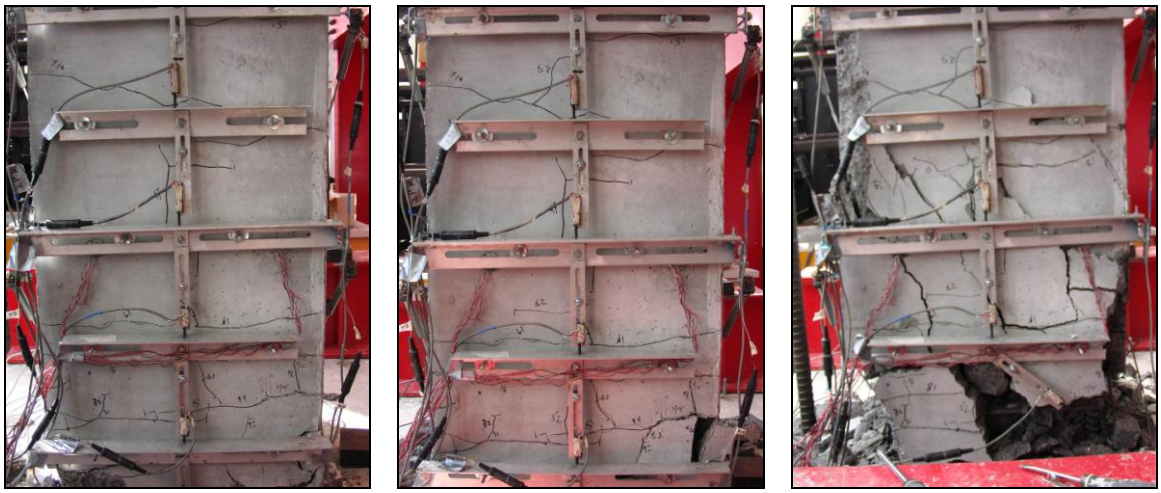

Figure 4.46 – SHD: North face at - $\mu_{5.4,1}$ (left), - $\mu_{5.4,3}$ (center), and - $\mu_{7.6,1}$ (right)

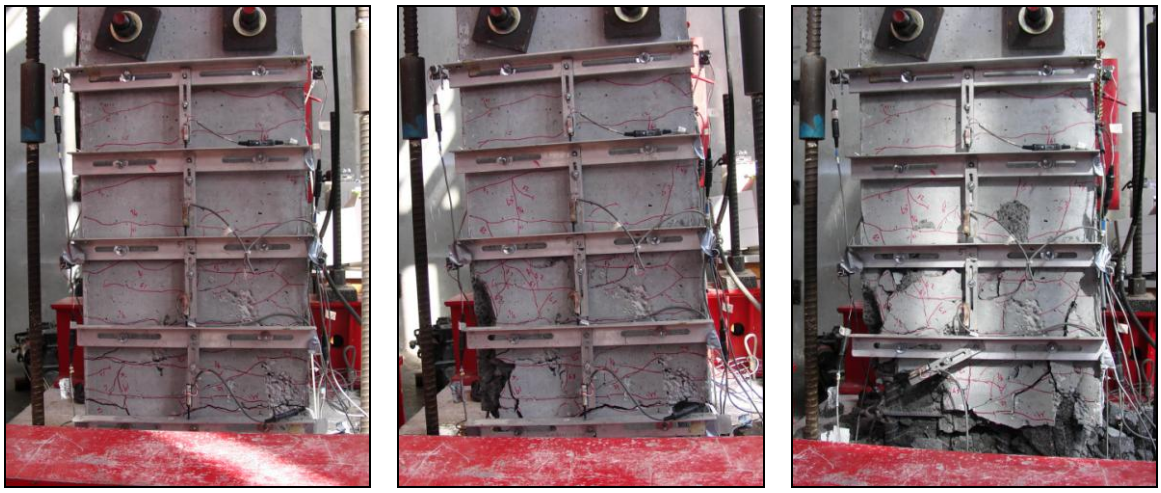

Figure 4.47 – SHD: South face at - $\mu_{5.4,1}$ (left), - $\mu_{5.4,3}$ (center), and - $\mu_{7.6,1}$ (right)

The north and south faces showed excessive spalling. The propagation of vertical cracking can be seen in Figure 4.47. Also shown is the removal of some instruments to prevent damage during the $\mu_{7.6,3}$ cycle. The twisting of the column continued in the $\mu_{7.6}$ cycle, when a maximum angle of rotation of 2.46° was measured.

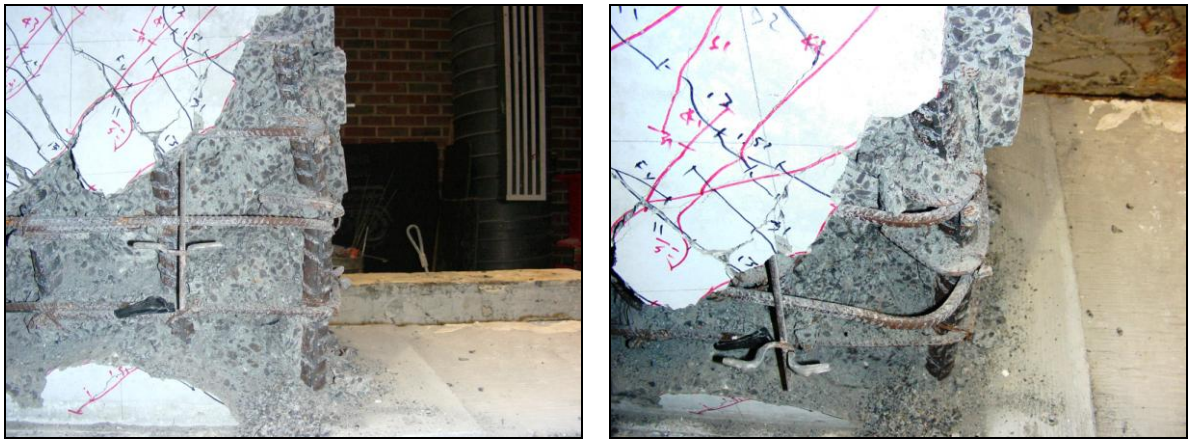

Figure 4.48 – SHD: West face long. bar buckling (left) and stirrup detachment (right) at - $\mu_{7.6,1}$

Longitudinal bars experienced bar buckling for this test, as shown in Figure 4.48. One transverse stirrup completely detached from the longitudinal bar.

The inclination of the shear cracks that formed on the east and west faces were approximately 35°. The top displacement for this specimen was +3.67 for the $\mu_{7.6,1}$ cycle.

Force-Displacement Response / Damping

The actual force-displacement response for this test is shown below (Figure 4.49).

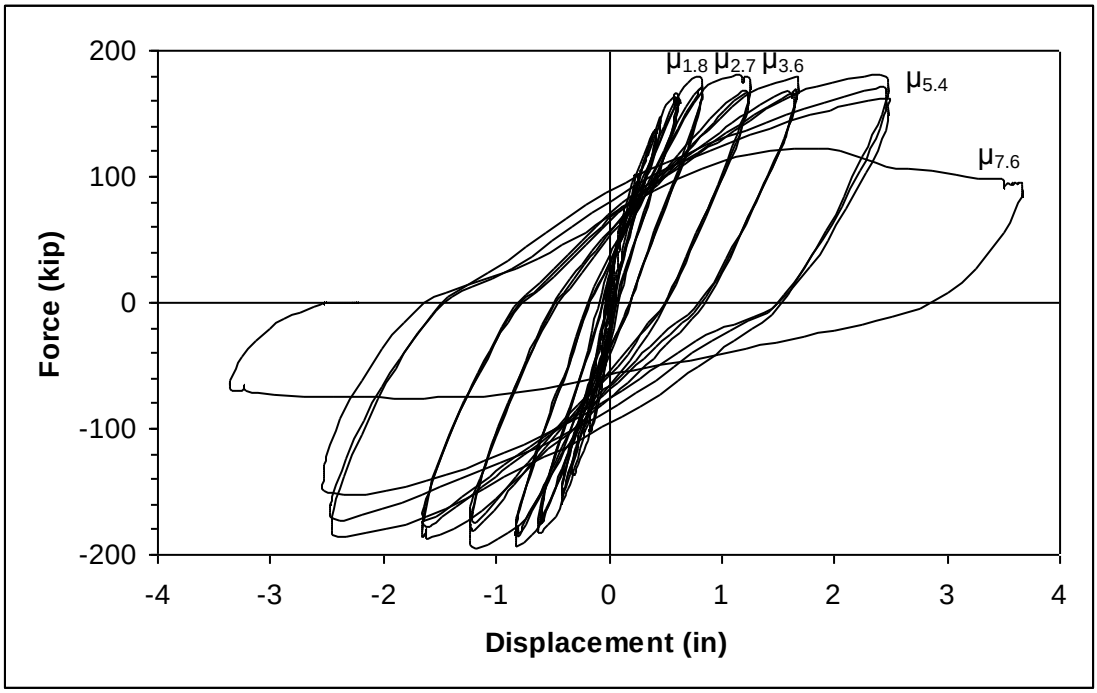

Figure 4.49 – SHD: Actual Force-Displacement Response

The maximum load remains high for cycles $\mu_{1.8}$ to $\mu_{5.4}$. Hysteretic damping values of 23.4% and 25.7% were calculated for the $\mu_{5.4,1}$ and $\mu_{7.6,1}$ cycles, respectively.

Curvature Profiles

Curvature profiles are shown for this test (Figures 4.50 and 4.51).

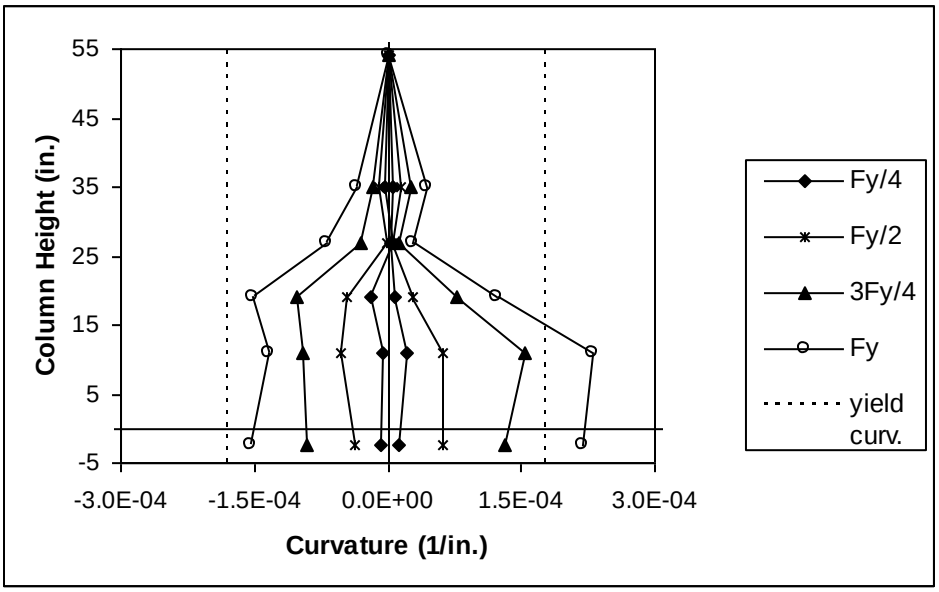

Figure 4.50 – SHD: Curvature profile for force-controlled cycles

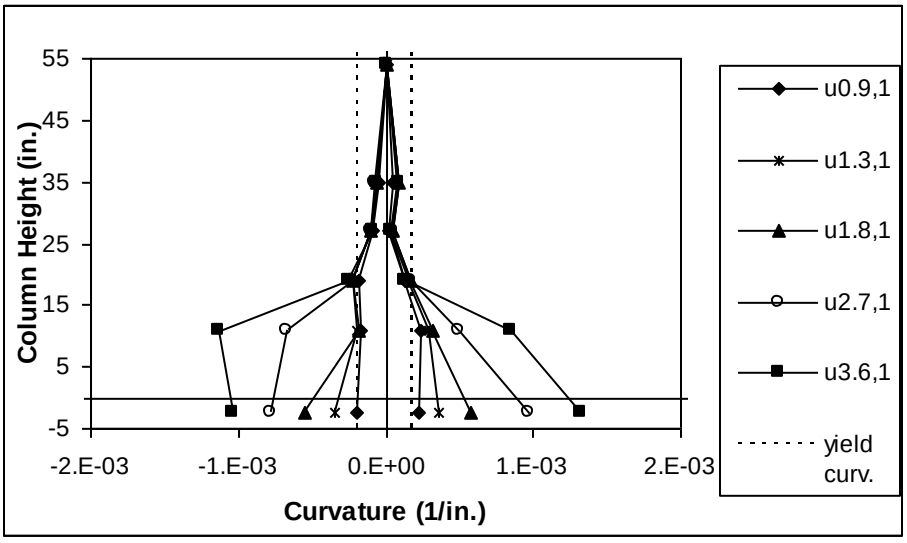

Figure 4.51 – SHD: Curvature profile for displacement-controlled cycles

The maximum calculated curvature values for the $F_y^{'}$ cycle were -1.55e-4 and +2.30e-4 in^{-1}). The instruments began to read incorrectly during the $\mu_{5.4,1}$ cycle, so

curvature calculations are not shown for this and later cycles. The maximum curvature values recorded were +1.32e-3 in^{-1} during the + $\mu_{3.6,1}$ loading and -1.13e-3 in^{-1} for the - $\mu_{3.6,1}$.

Strain Gage Histories and Profiles

An example gage history is shown in Figure 4.52. The figure shows the location of the BS3 strain $\mu_{3,1}$ gage, located on the east face, 20.5 inches from the base of the column. All strain gage histories are given in the Appendix.

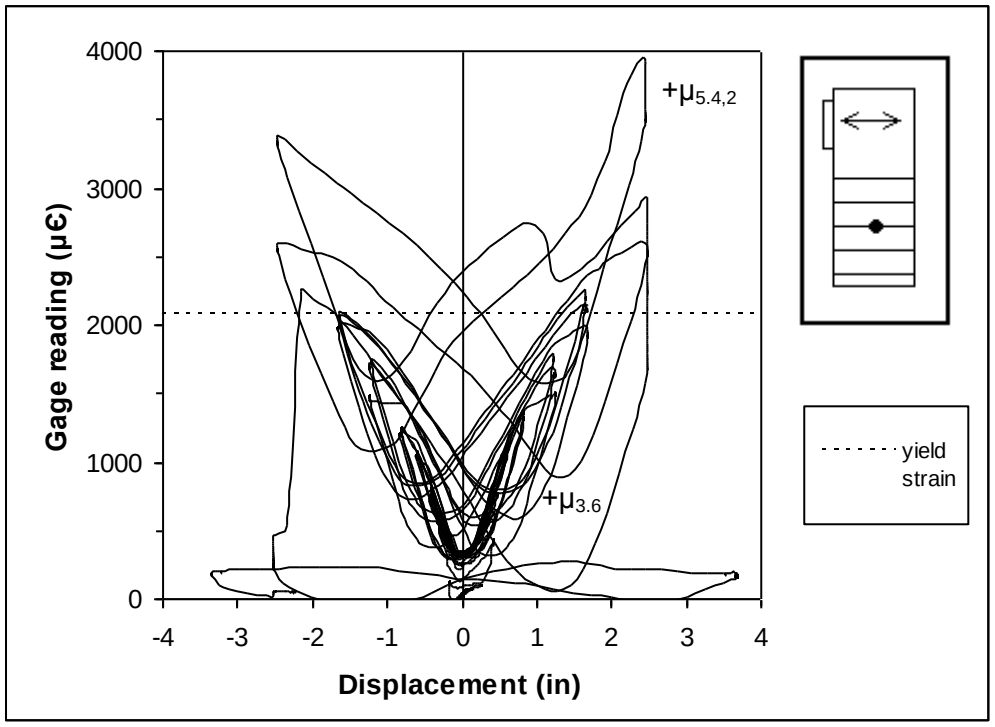

Figure 4.52 – SHD: BS3 strain gage history

The first significant strain in this stirrup occurred while loading to + $F_y^{'}$, where a strain of 437 μЄ was recorded. This coincides with the extension of several flexure-shear cracks. The stirrup began to yield during the + $\mu_{3.6,2}$ cycle loading. A maximum value of 3960 μЄ was reached during the + $\mu_{5.4,2}$ loading.

The strain profiles for push direction loading are shown in Figures 4.53 and 4.54.

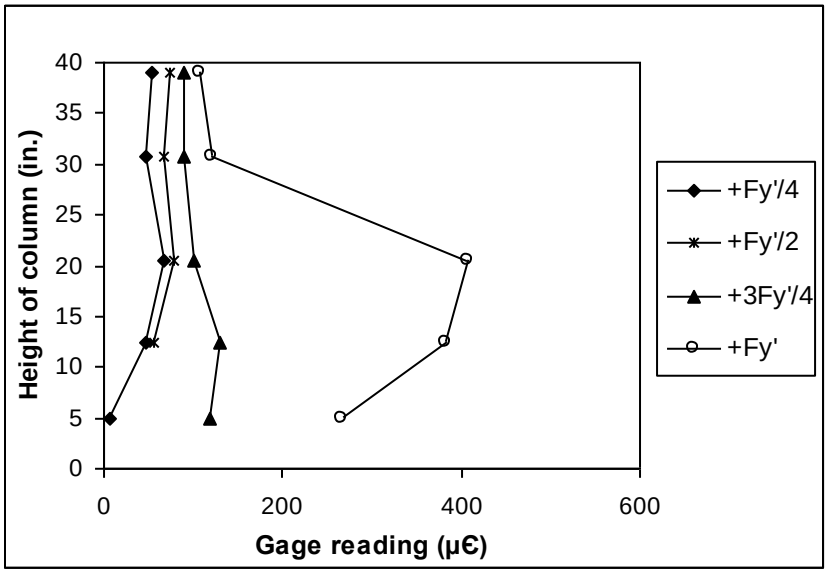

Figure 4.53 – SHD: West face strain profile for force-controlled cycles

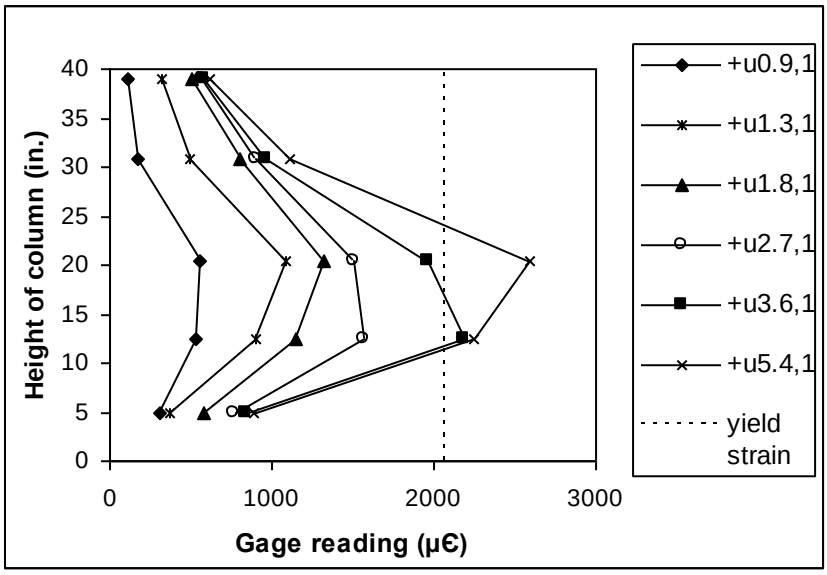

Figure 4.54 – SHD: West face strain profile for displacement-controlled cycles

Both profiles show the maximum strains occurring at two different points for different cycles, 20.5 and 12.5 inches above the base of the column. The displacement-controlled profile shows large increases in strain for the $+\mu_{3.6,1}$ and $+\mu_{5.4,1}$ cycles, only for the second and third gages from the bottom.

4.4 – Lightweight Slate Ductile Shear Failure Specimen (SLD)

The actual loading procedure is shown in Figure 4.55. As shown, the test was stopped after a significant load drop in the push cycle of $\mu_{6.9,3}$.

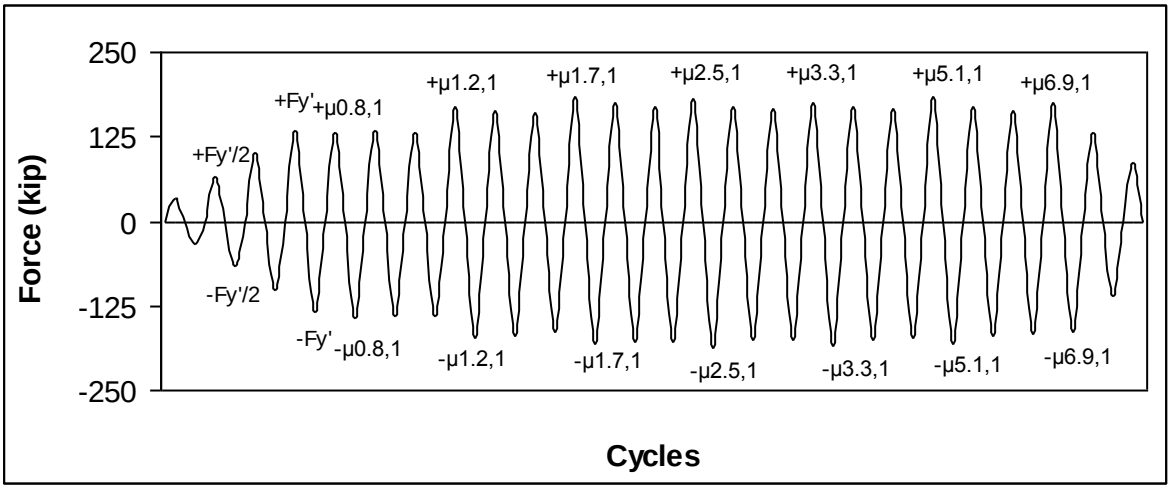

Figure 4.55 – SLD: Actual loading protocol

Force-controlled Cycles

The first flexure cracks formed on all faces during the $F_y^{'}/2$ cycle. These cracks remained mostly horizontal for this cycle. Also, two small vertical cracks were found on the south face. During the $\pm 3F_y^{'}/4$ cycle, these cracks spread throughout the height of the column, and most became flexure-shear cracks. One more crack formed on the south face. By the $F_y^{'}$ cycle, many cracks spread and some shear-only cracks were formed. The top displacements reached for this cycle were +0.40 and -0.35 inches.

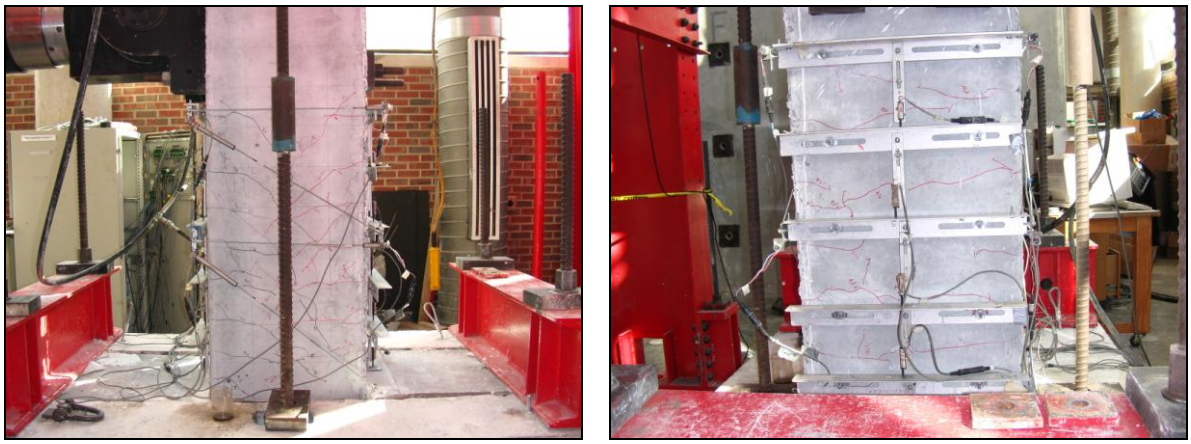

Figure 4.56 – SLD: West (left) and south faces (right) at $\pm F_y^{'}$

Displacement-controlled Cycles

Flexure-shear and shear cracks were extended during all cycles of $\mu_{0.8}$. Almost no changes were recorded for the north and south side faces. The $\mu_{1.2}$ cycles brought on more extensions of cracks and a few new flexure and shear-only cracks formed.

The first signs of spalling occurred during the $\mu_{1.7,3}$ cycle (Figure 4.57). Several cracks were extended and the largest shear crack was measured at 0.01 inches.

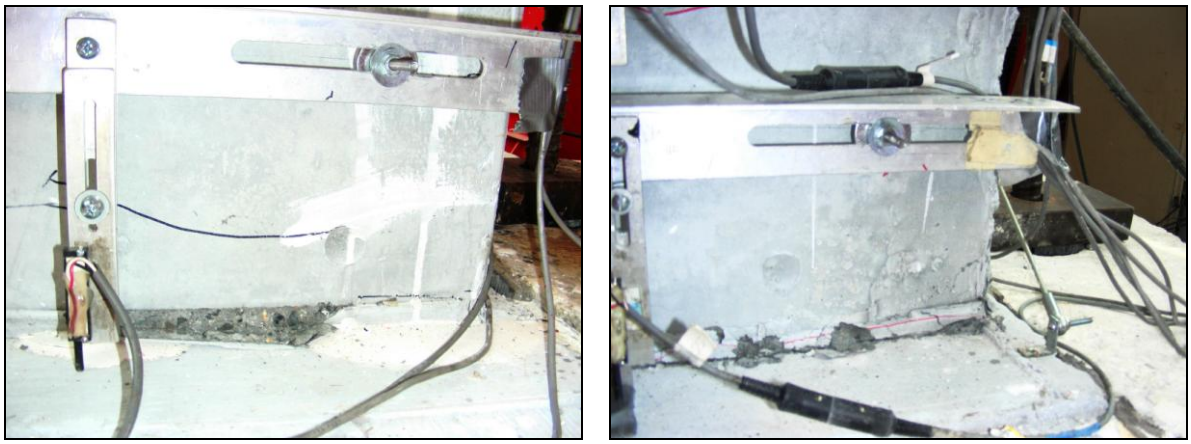

Figure 4.57 – SLD: North (left) and south faces (right) at - $\mu_{1.7,3}$

Crack extensions and crushing continued for the three cycles of $\mu_{2.5}$. Shear cracks widened to 0.025 inches. The maximum recorded forces of +188 kips and -189 kips occurred during the first cycle of $\mu_{2.5}$, at displacements of ±1.23 inches.

The $\mu_{3.3}$ and $\mu_{5.1}$ cycles were very similar. Both caused some extensions on the east and west faces. No new cracks appeared on the north or south faces, but crushing progressed. Crack widths increased to 0.06 inches by the first cycle of $\mu_{5.1}$. The progressive damage of the specimen for the last few cycles of loading is shown in Figures 4.58 – 4.60.

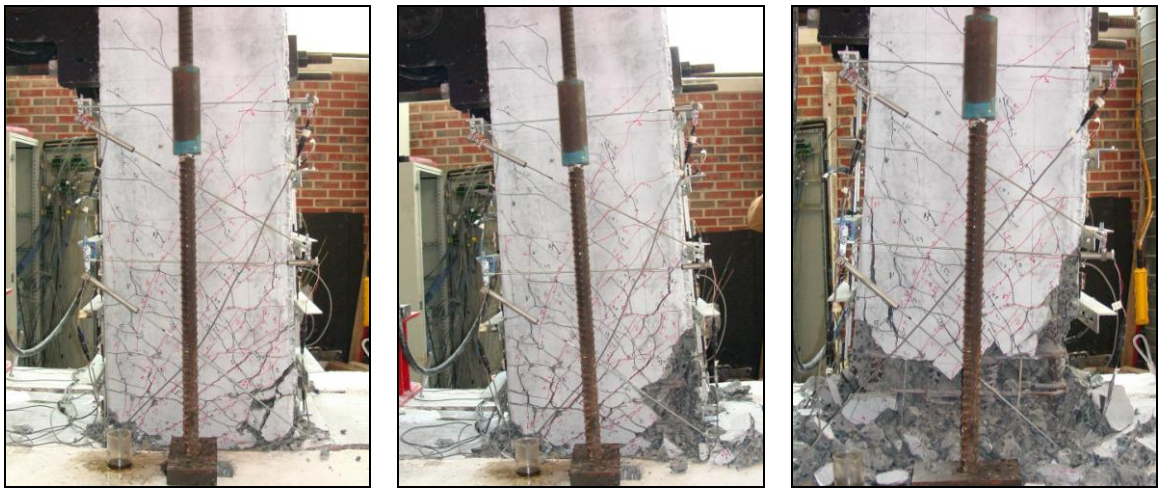

Figure 4.58 – SLD: West face at - $\mu_{5.1,3}$ (left), - $\mu_{6.9,1}$ (center), and + $\mu_{6.9,3}$ (right)

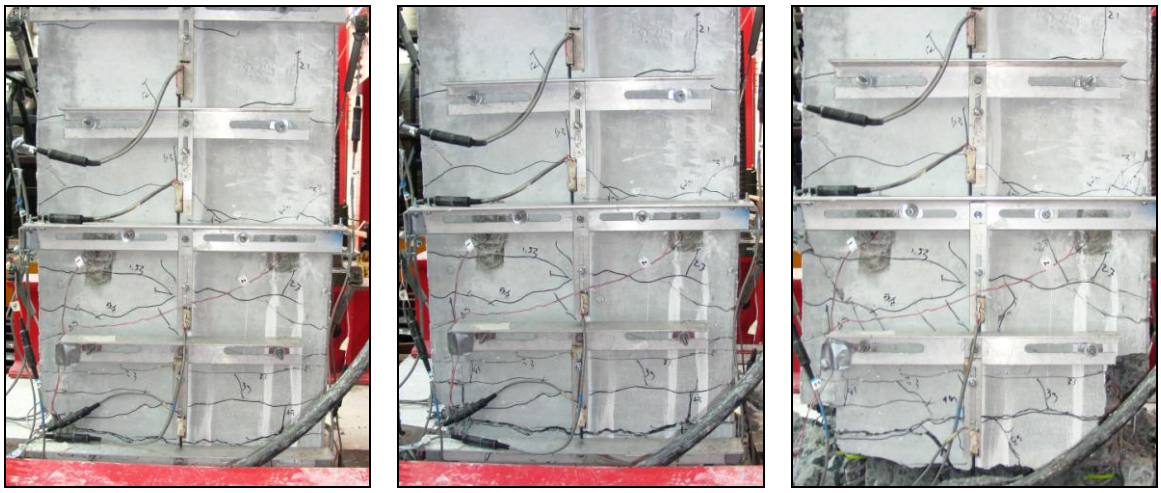

Figure 4.59 – SLD: North face at - $\mu_{5.1,3}$ (left), - $\mu_{6.9,1}$ (center), and + $\mu_{6.9,3}$ (right)

The maximum cycle load dropped from +176 kips in the + $\mu_{6.9,1}$ cycle down to +93 kips in the + $\mu_{6.9,3}$ cycle.

Figure 4.60 – SLD: West face long. bar buckling (left) and stirrup detachment (right) after + $\mu_{6.9,3}$

The twisting of the column began in the + $\mu_{6.9,2}$ cycle, where a rotation of 0.2° was measured. The maximum value of 2.39° occurred during the + $\mu_{6.9,3}$ cycle. Longitudinal bars experienced bar buckling for this test, as shown in Figure 4.60. One transverse stirrup nearly detached from a corner longitudinal bar.

The inclination of the shear cracks that formed on the east and west faces were approximately 34°. The top displacement for this specimen was +3.58 for the $\mu_{6.9,3}$ cycle.

Force-Displacement Response / Damping

The actual force-displacement response for this test is shown in Figure 4.61.

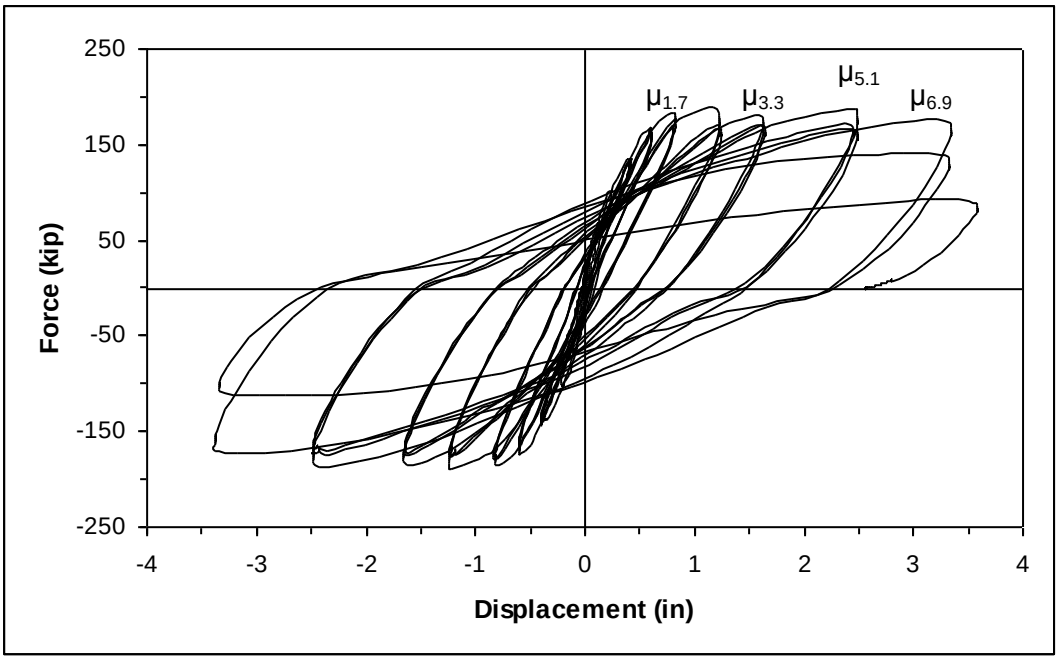

Figure 4.61 – SLD: Actual Force-Displacement Response

Damping values of 23.0% and 26.1% were calculated for the $\mu_{5.1,1}$ and $\mu_{6.9,1}$ cycles, respectively.

Curvature Profiles

Curvature profiles are shown in Figures 4.62 and 4.63.

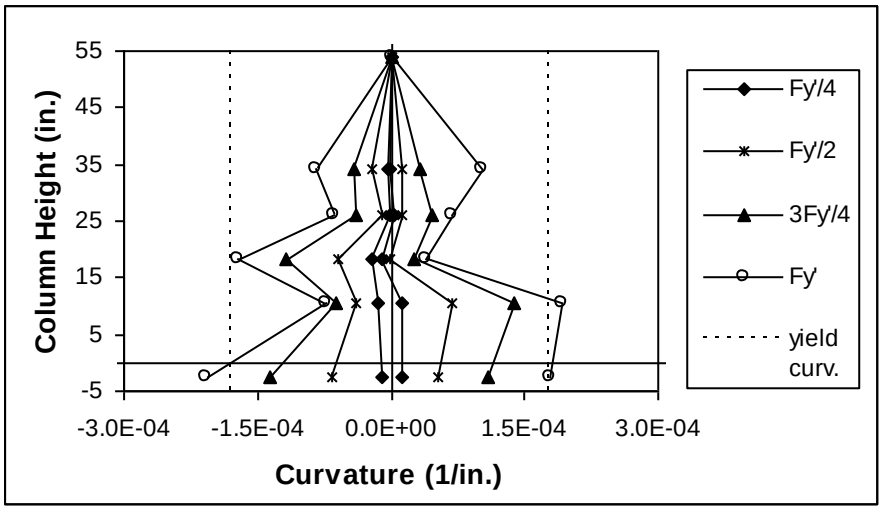

Figure 4.62 – SLD: Curvature profile for force-controlled cycles

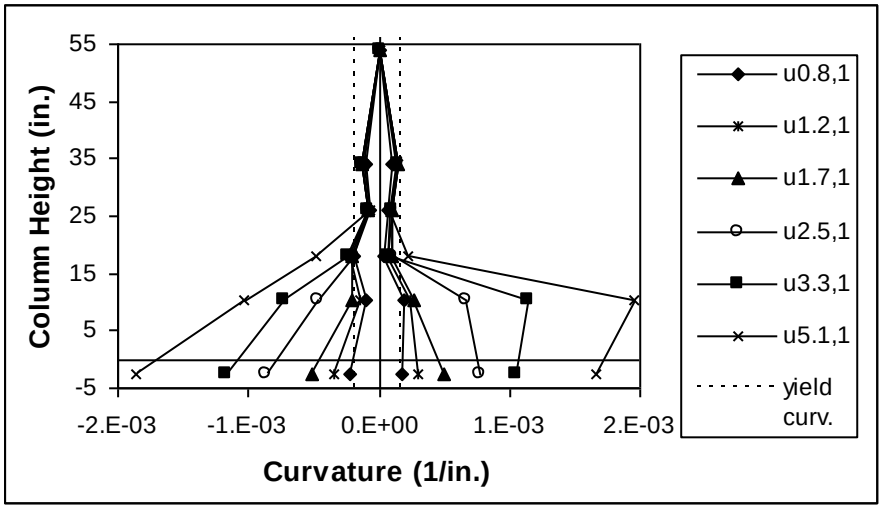

Figure 4.63 – SLD: Curvature profile for displacement-controlled cycles

The maximum calculated curvature values for the $F_y^{'}$ cycle were -2.07-4 and +1.92-4 in^{-1}). Some instruments were removed before the $\mu_{6.9,1}$ cycle, so this cycle is not shown on the curvature profile. The maximum curvature values recorded were +1.95e-3 in^{-1} and -1.86e-3 in^{-1} for the $\pm\mu_{5.1,1}$.

Strain Gage Histories

Only two strain gages collected data, and one located on the west face is shown in Figure 4.64. Both strain gage histories are given in the Appendix.

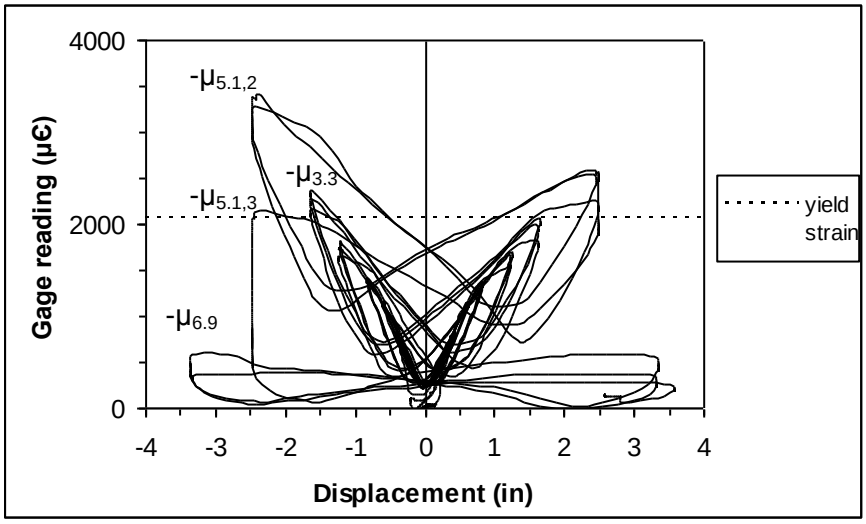

Figure 4.64 – SLD: West face strain gage history

The first significant strain of 364 μЄ in this stirrup occurred while loading to $+3F_y^{'}/4$. This is the cycle in which the first flexure-shear cracks appeared. The stirrup began to yield during the $-\mu_{3.3,1}$ cycle loading. A maximum value of 3420 μЄ was reached during the $-\mu_{5.1,2}$ loading. This gage stopped reading correctly while loading to $-\mu_{5.1,3}$. Since only two of ten gages recorded data, a strain profile was not generated for this test.

CHAPTER 5 – TEST COMPARISONS

This chapter will explain the findings of the research project by comparing the shear performance of lightweight aggregate to normal weight aggregate specimens, as well as quantifying any observed differences between normal-strength and high-strength concrete. Although shear performance is the main focus, other quantities including displacement capacity, strength degradation, and energy absorption are also compared, and force-displacement envelopes are shown and discussed.

5.1 – Displacement Capacity

Brittle Failure Test Specimens:

Force-displacement envelopes were created for both normal-strength and high-strength specimens, and results for brittle shear failure tests are shown below.

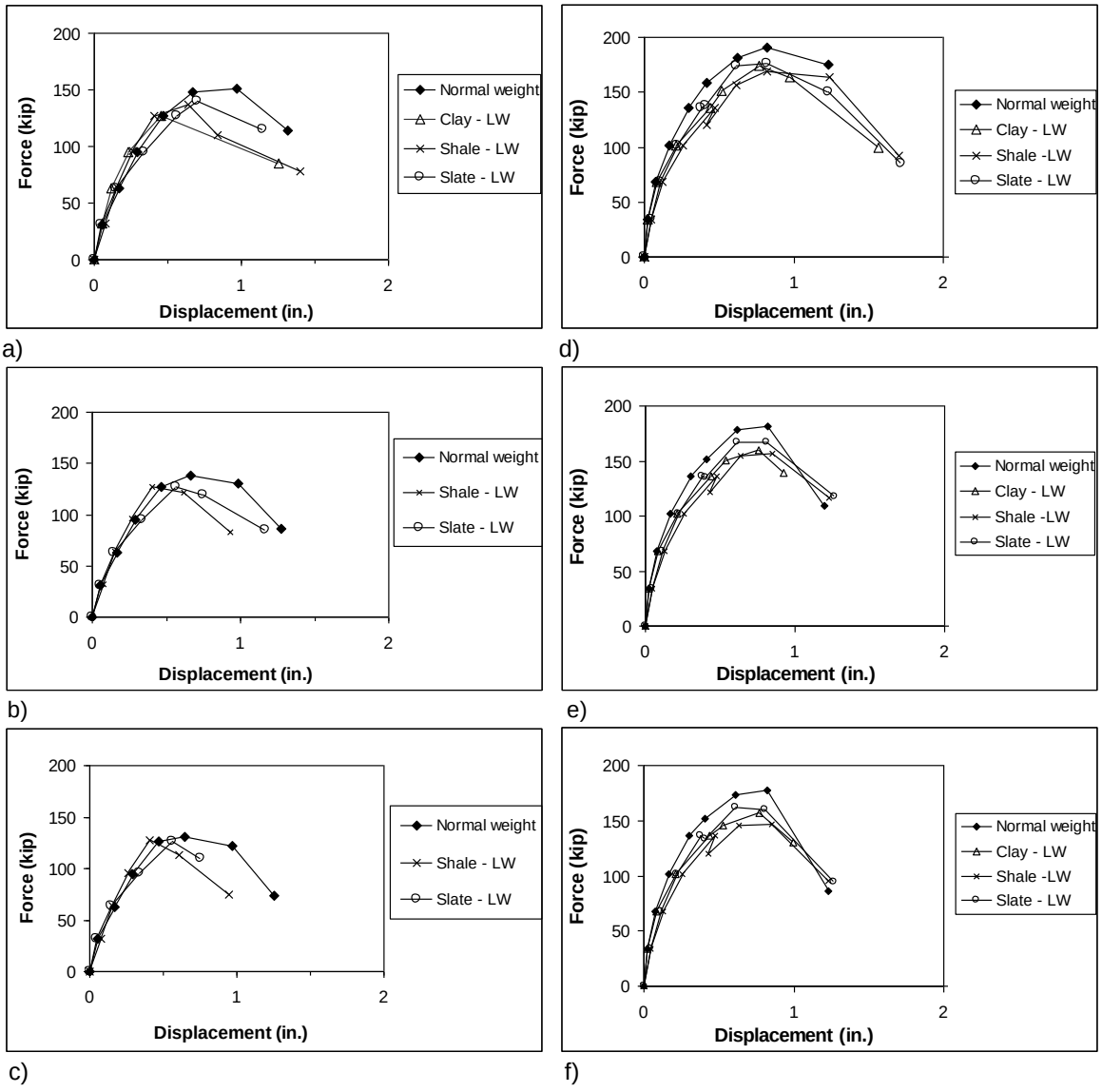

Figure 5.1 – Force-displacement envelopes for normal-strength (left, Robalino 2006) and high-strength (right) brittle test specimens, for first cycle of loading (a and d), second cycle (b and e), and third cycle (c and f)

In the case of the normal-strength specimens, the normal weight specimen was found to have a slightly higher displacement capacity than lightweight specimens because of the higher displacement at maximum load. However, a significant difference was not recorded. This is illustrated in Figure 5.1(a-c). Note data for the clay lightweight specimen was not collected for second and third cycles.

For high-strength brittle specimens, it is noted that the normal weight specimen had a larger concrete strength than lightweight specimens (Table 2.2), thus partly explaining the higher maximum force values shown in Figure 5.1(d-f). From these graphs, it does not appear that the normal weight specimen has a higher ductility capacity. This observation is confirmed upon examination of displacement values calculated at three points of interest: maximum load, 90% of maximum, and 80% of maximum. Instead of focusing only on maximum displacement, which was obtained at varying percentages of maximum load, the specimens can be compared at the same load levels. The results are shown in Table 5.1.

Table 5.1 – High-strength brittle specimens, displacement capacities for specific loads

High-strength		max load	90% max	80% max
NWB	Force (kip)	189	170	151
	Displ. (in)	0.83	0.90	0.96
	drift (%)	1.5	1.7	1.8
CLB	Force (kip)	176	158	141
	Displ. (in)	0.79	1.04	1.24
	drift (%)	1.5	1.9	2.3
SHB	Force (kip)	172	155	138
	Displ. (in)	0.83	1.25	1.35
	drift (%)	1.5	2.3	2.5
SLB	Force (kip)	173	156	138
	Displ. (in)	0.83	1.25	1.37
	drift (%)	1.5	2.3	2.5

The table indicates that the lightweight specimens averaged higher displacements than the normal weight specimen for loads that were 90% of the maximum load recorded during each respective test. The shale and slate specimens had the highest displacements at 80% of maximum load. From this table, it can also be concluded that levels of drift for normal weight concrete are attainable for lightweight concrete. The normal weight and all lightweight specimens achieved a level of 1.5% drift at maximum load. Generally, no significant difference in terms of displacement capacity has been found between normal weight and lightweight concrete for either normal- or high-strength specimens for low levels of displacement.

Ductile Failure Test Specimens:

Force-displacement envelopes for ductile shear failure specimens are shown in Figure 5.2.

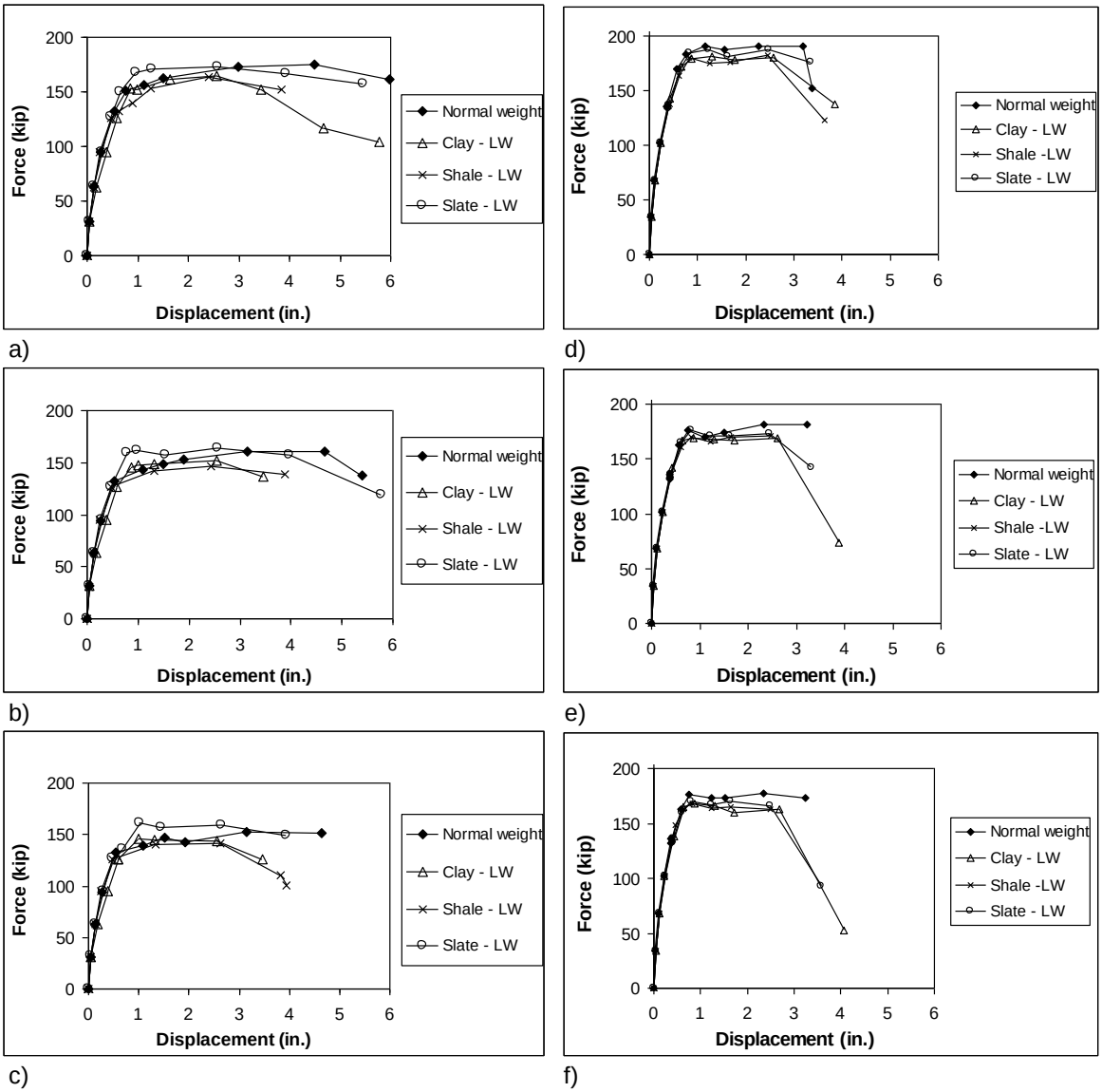

Figure 5.2 – Force-displacement envelopes for normal-strength (left, Robalino 2006) and high-strength (right) ductile test specimens, for first cycle of loading (a and d), second cycle (b and e), and third cycle (c and f)

Figure 5.2 (a-c) shows that the normal weight specimen has a similar displacement capacity compared with the lightweight specimens.

For high-strength ductile specimens, the normal weight specimen did exhibit higher loads at equal displacements, shown in Figure 5.2 (d-f). Table 5.2 shows displacement calculated at particular load values for the high-strength specimens.

Table 5.2 – High-strength ductile specimens, displacement capacities for specific loads

High-Strength		max load	90% max	80% max
NWD	Force (kip)	197	177	158
	Displ. (in)	2.28	3.25	3.34
	drift (%)	4.2	6.0	6.2
CLD	Force (kip)	185	167	148
	Displ. (in)	2.59	2.65	3.41
	drift (%)	4.8	4.9	6.3
SHD	Force (kip)	187	168	150
	Displ. (in)	0.83	2.47	2.74
	drift (%)	1.5	4.6	5.1
SLD	Force (kip)	189	170	151
	Displ. (in)	1.23	3.36	3.35
	drift (%)	2.3	6.2	6.2

It is shown that at 90% of maximum load, the normal weight specimen has obtained a higher displacement value than all the lightweight specimens, and the three lightweight specimens averaged just below the normal weight specimen displacement for a load of 80% of the maximum. The displacement values at maximum load for the shale and slate specimens are much lower than for the other two specimens. This is because the specimens experienced small load drops after maximum, but remained high until a large level of ductility was reached. This is discussed further in section 5.2. Drift levels for normal weight and lightweight specimen averaged to similar values. The ductile shale specimen obtained a somewhat lower percentage for each of the three points of interest.

No significant difference in terms of displacement capacity has been found between normal weight and lightweight concrete regardless of concrete strength.

5.2 – Strength Degradation

The strength of a column degrades over repeated cycles. Two columns may begin with equal strengths, but if one has a much higher rate of strength degradation, it will perform significantly worse in the event of an earthquake. Degradation is discussed in this section, and normal and lightweight concrete specimens are compared.

Brittle Failure Test Specimens:

Strength degradation calculations were not made in terms of percentages for the normal-strength specimens. This degradation can be seen in Figure 5.1 (a-c). The lightweight specimens were found to exhibit larger strength degradations and lower levels of ductility.

Strength degradation was quantified for high-strength tests in two ways. First, the percentage of strength loss was calculated with respect to the first cycle of loading. These levels were computed for second and third cycles of every ductility level. Second, percentage of strength loss with respect to the maximum load reached during the entire test was determined. Both are shown in tabular form (Tables 5.3-5.6). The maximum load is highlighted gray.

Table 5.3 – NWB: Strength degradation

HS-NWB				
ductility level	Force (kip)	cycle	% strength loss from 1st cycle	% strength loss from test max.
μ1	156	1	--	--
	149	2	5	--
	150	3	4	--
μ1.5	180	1	--	--
	176	2	3	--
	170	3	6	--
μ2	189	1	--	--
	178	2	6	6
	174	3	8	8
μ2.9	158	1	--	16
	108	2	32	43
	86	3	45	55

Table 5.4 – CLB: Strength degradation

HS-CLB				
ductility level	Force (kip)	cycle	% strength loss from 1st cycle	% strength loss from test max.
μ1	155	1	--	--
	154	2	1	--
	151	3	3	--
μ1.5	176	1	--	--
	163	2	7	7
	158	3	10	10
μ1.9	164	1	--	7
	142	2	13	19
	133	3	19	25
μ3	113	1	--	36

Table 5.5 – SHB: Strength degradation

HS-SHB				
ductility level	Force (kip)	cycle	% strength loss from 1st cycle	% strength loss from test max.
μ0.7	124	1	--	--
	127	2	--	--
	122	3	1	--
μ1.1	160	1	--	--
	157	2	2	--
	150	3	6	--
μ1.5	172	1	--	--
	157	2	9	9
	149	3	13	13
μ2.2	158	1	--	9
	113	2	29	35
	93	3	41	46
μ3	83	1	--	52

Table 5.6 – SLB: Strength degradation

HS-SLB				
ductility level	Force (kip)	cycle	% strength loss from 1st cycle	% strength loss from test max.
μ0.9	138	1	--	--
	135	2	3	--
	133	3	4	--
μ1.3	172	1	--	--
	166	2	4	--
	161	3	7	--
μ1.7	173	1	--	--
	162	2	7	7
	156	3	10	10
μ2.5	161	1	--	7
	111	2	31	36
	91	3	43	47
μ3.6	89	1	--	49

Before the maximum load was reached in each test, strength degradation varied between 1 and 7% with respect to the first cycle of loading. Normal and lightweight

specimens showed similar values up to this point. During the three cycles in which the maximum load occurred, slightly more degradation was experienced for the lightweight concrete, averaging 9%, compared to 7% for the normal weight specimen. Unlike the normal-strength specimens, the maximum load for the lightweight high-strength specimens occurred around the same displacement as the normal weight specimens. From Figure 5.1 (a-c), it can be seen that reductions in strengths occur at similar loads and displacements. For the high-strength brittle test specimens, strength degradation with respect to maximum load as well as during cycles of the same ductility level, occurred at similar rates for normal weight and lightweight concrete.

Ductile Failure Test Specimens:

For normal-strength specimens, strength degradation was more significant in lightweight concrete specimens. Like the brittle specimens, these started to lose strength at lower levels of deformation when compared to normal weight concrete. Referring back to Figure 5.2 (a-c), note how the normal weight specimen remains at high loads for high levels of ductility.

The strength degradation data for high-strength tests are shown in Tables 5.7-5.10. The maximum load for each test is highlighted gray, and the data before the maximum was reached has been omitted. Before this point, the percentage of strength degradation varied between 0 and 9%, with no difference between normal weight and lightweight tests.

Table 5.7 – NWD: Strength degradation after maximum load

HS-NWD				
ductility level	Force (kip)	cycle	% strength loss from 1st cycle	% strength loss from test max.
μ5.2	197	1	--	--
	184	2	6	6
	182	3	7	7
μ7.2	193	1	--	2
	183	2	5	7
	170	3	12	13
μ9.3	129	1	--	34

Table 5.8 – CLD: Strength degradation after maximum load

HS-CLD				
ductility level	Force (kip)	cycle	% strength loss from 1st cycle	% strength loss from test max.
μ5.4	185	1	--	--
	174	2	6	6
	167	3	10	10
μ7.8	124	1	--	33
	64	2	48	65
	47	3	62	75

Table 5.9 – SHD: Strength degradation after maximum load

HS-SHD				
ductility level	Force (kip)	cycle	% strength loss from 1st cycle	% strength loss from test max.
μ1.8	187	1	--	--
	178	2	5	5
	176	3	6	6
μ2.7	183	1	--	2
	174	2	5	7
	170	3	7	9
μ3.6	180	1	--	4
	174	2	3	7
	169	3	6	10
μ5.4	184	1	--	2
	172	2	7	8
	158	3	14	16
μ7.6	100	1	--	47

Table 5.10 – SLD: Strength degradation after maximum load

HS-SLD ductility level	Force (kip)	cycle	% strength loss from 1st cycle	% strength loss from test max.
μ2.5	189	1	--	--
	174	2	8	8
	172	3	9	9
μ3.3	184	1	--	3
	173	2	6	8
	171	3	7	9
μ5.1	188	1	--	0
	173	2	8	8
	168	3	11	11
μ6.9	175	1	--	7
	127	2	27	33
	93	3	47	51

During the three cycles in which the maximum load occurred, similar values were recorded for degradation of about 7%. All tests show rapid degradation during the last cycle. Figure 5.2 (d-f) shows strength degradation occurring earlier for lightweight specimens, particularly for the second and third cycles of loading for the last cycles. For the high-strength ductile test specimens, strength degradation occurred at slightly higher rates for lightweight concrete.

Lightweight concrete, regardless of strength, loses strength at a somewhat faster rate compared to normal weight concrete at high levels of ductility (μ_7 or greater). This effect is slightly reduced for higher strength concrete.

5.3 – Energy Absorption

Hysteretic damping calculations were made for all test specimens. The normal-strength tests obtained values between 12 and 14% for brittle tests, and 20 to 25% for ductile specimens. The high-strength results are shown in Tables 5.11 and 5.12, where maximum values were 12 to 15% and 25 to 28% for brittle and ductile specimens respectively.

Table 5.11 – Hysteretic damping calculations for high-strength brittle specimens

	Hysteretic Damping (%)			
Cycle	NWB	CLB	SHB	SLB
~μ1,1		6.93	6.12	6.16
~μ1.5,1		10.4	6.60	7.57
~μ2,1		10.8	8.80	9.80
~μ3,1	~14	14.7	13.3	14.7
~μ4,1			12.2	
		low	high	

Table 5.12 – Hysteretic damping calculations for high-strength ductile specimens

	Hysteretic Damping (%)			
Cycle	NWD	CLD	SHD	SLD
~μ1,1	7.09	5.41	4.93	4.76
~μ1.5,1	9.52	8.18	7.52	7.36
~μ2,1	10.5	11.5	9.93	9.77
~μ3,1	15.9	17.7	16.0	15.7
~μ4,1	17.7	19.5	18.6	17.6
~μ6,1	22.2	23.8	23.4	23.0
~μ8,1	25.8	27.9	25.7	26.1
		low	high	

All values were calculated at the first cycle of each ductility level. As noted in Chapter 3, an actual force-displacement response was not obtained for the normal weight brittle test specimen, and the value shown is an estimate. Also, since all

tests reached different levels of ductility, approximate levels are shown. Low and high values are highlighted. It can be seen that the clay specimen obtained the highest levels of damping for both brittle and ductile test sets, but all values were very similar. These values are also shown graphically in Figure 5.3

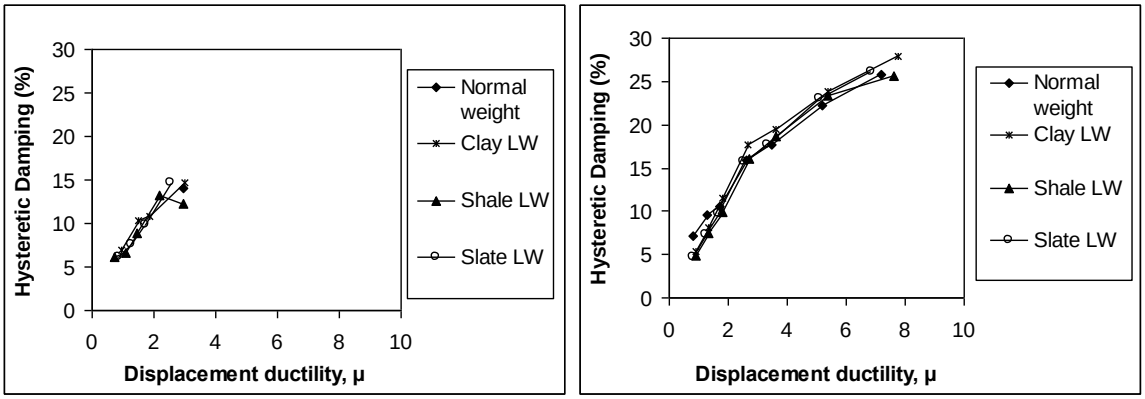

Figure 5.3 – Damping values for high-strength brittle (left) and ductile (right) test specimens

The two graphs are plotted on the same scale to show that very similar values of damping were obtained for brittle and ductile failure tests at low levels of ductility. Considering both normal- and high-strength test specimens, there is no significant difference between normal and lightweight concrete in terms energy absorption.

As mentioned in Chapter 3, the hysteretic damping calculations were made using the Jacobsen approach (Jacobsen 1960). Several assumptions are made by Jacobsen, particularly that the structure undergoes sinusoidal response, which is not accurate. Thus if actual hysteretic damping values are desired the values obtained from Jacobsen's approach must be corrected. Correction factors were applied to the values obtained using Jacobsen's approach in order to obtain hysteretic damping found from a time-history analysis. These factors can be found using Figure 5.4.

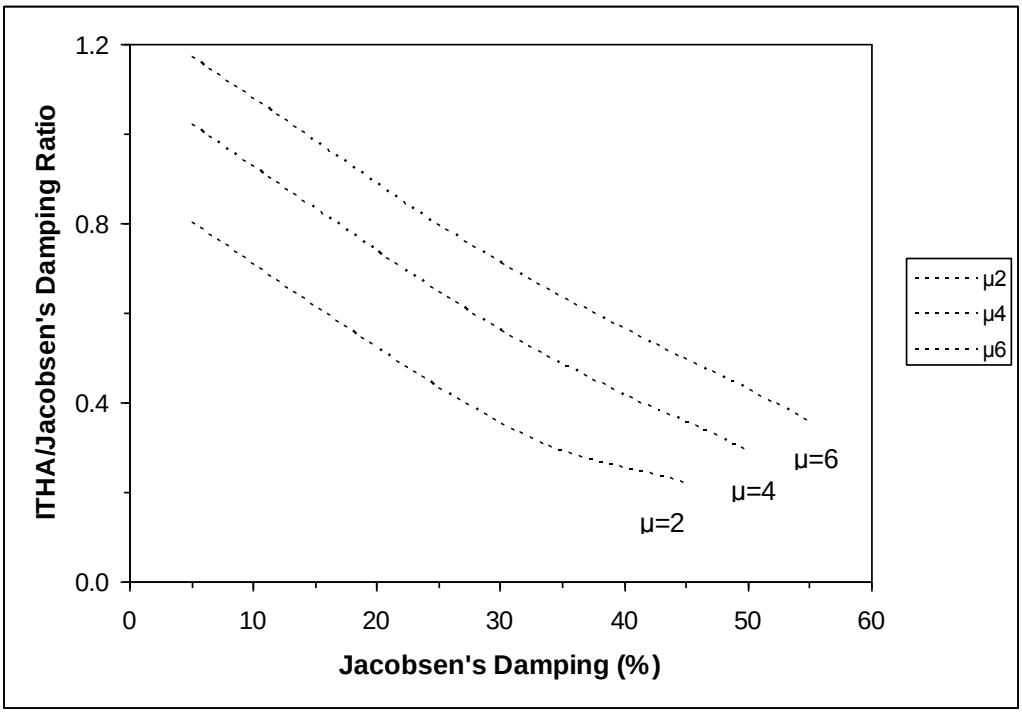

Figure 5.4 – Correction factors applied to Jacobsen Damping (Priestley et al. 2007)

The values found from this figure are multiplied by the damping values using Jacobsen's approach to obtain corrected values. Interpolations were made for ductility levels other than two, four, and six. A comparison of the amount of energy absorption for different concrete types was desired, but computing actual values of damping was necessary to compare with the damping model developed by Dwairi (Dwairi 2007). Figure 5.5 shows the damping values after applying correction factors.

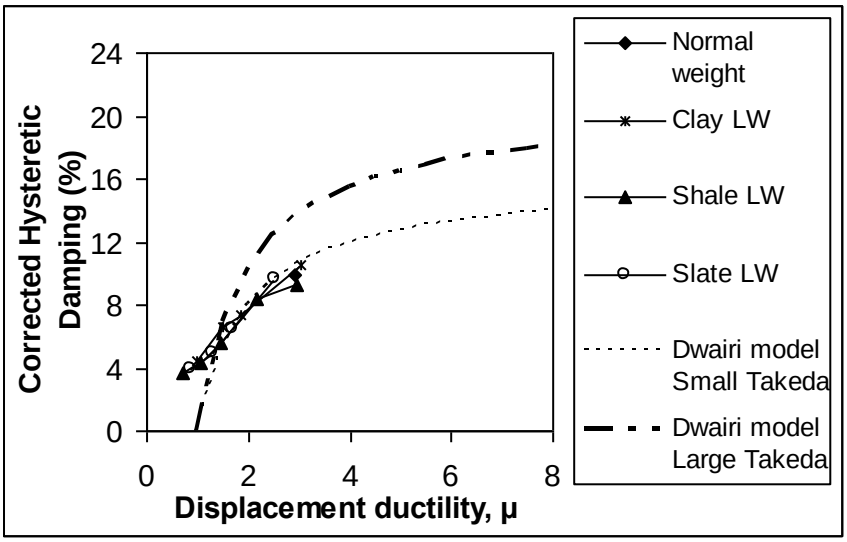

a)

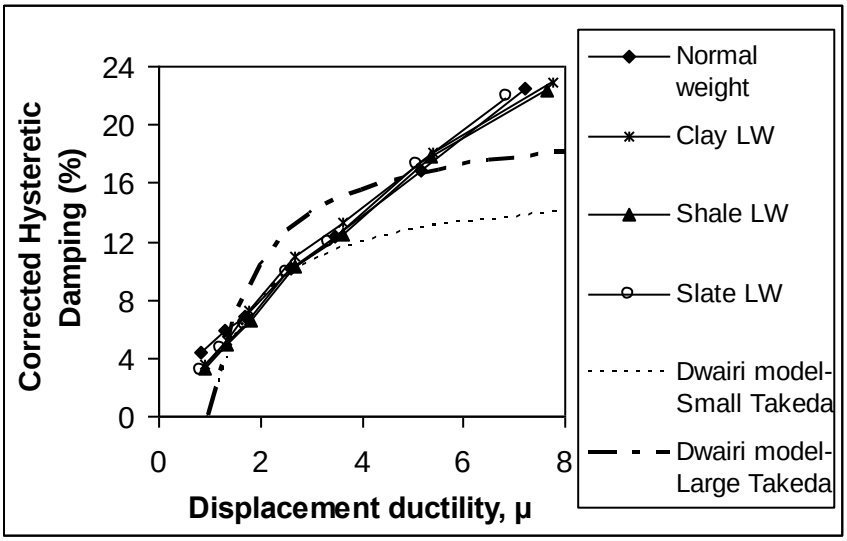

b)

Figure 5.5 – Corrected damping values plotted with Dwairi model for a) brittle and b) ductile tests

The Dwairi model equations chosen for this data set correspond to the Small Takeda and Large Takeda hysteretic systems (Takeda 1970), typically used for reinforced concrete columns and beams respectively. The equations for hysteretic damping are shown below.

$$\xi_{hyst} = 50\left(\frac{\mu - 1}{\pi\mu}\right) \qquad \text{Eq. 5.1}$$

$$\xi_{hyst} = 65\left(\frac{\mu - 1}{\pi\mu}\right) \qquad \text{Eq. 5.2}$$

Equation 5.1 is used with the Small Takeda hysteresis, while Equation 5.2 is used with the Large Takeda hysteresis. These equations are applicable for effective periods of one second or greater, which is the case for most structures. The Dwairi model shows good agreement using the Small Takeda hysteresis at low levels of ductility, but differs greatly beyond ductility level three. The loop shapes of the ductile specimens were more similar to the Large Takeda than the Small Takeda hysteresis, although the Large Takeda is intended for beams. Columns typically experience high axial loads when in service, while beams have relatively low axial loads. Since the axial load applied to the columns for this project was only a 5% axial load ratio, the corrected damping values are much higher than the Dwairi model using the Small Takeda hysteresis, and even higher than the model using the Large Takeda hysteresis beyond a ductility level of five.

Based on this set of tests, the Dwairi model may be used for predictions up to a ductility level of five. The Small Takeda hysteretic loop matched well with corrected damping values at low levels of ductility, but values were very inconsistent at high levels of ductility considering both the Small and Large Takeda loops.

5.4 – Shear Strength

Total shear strength vs. ductility plots for experimental and predicted values are shown in Figures 5.6 and 5.7. The values for V_n are simply the applied force at the top of the column.

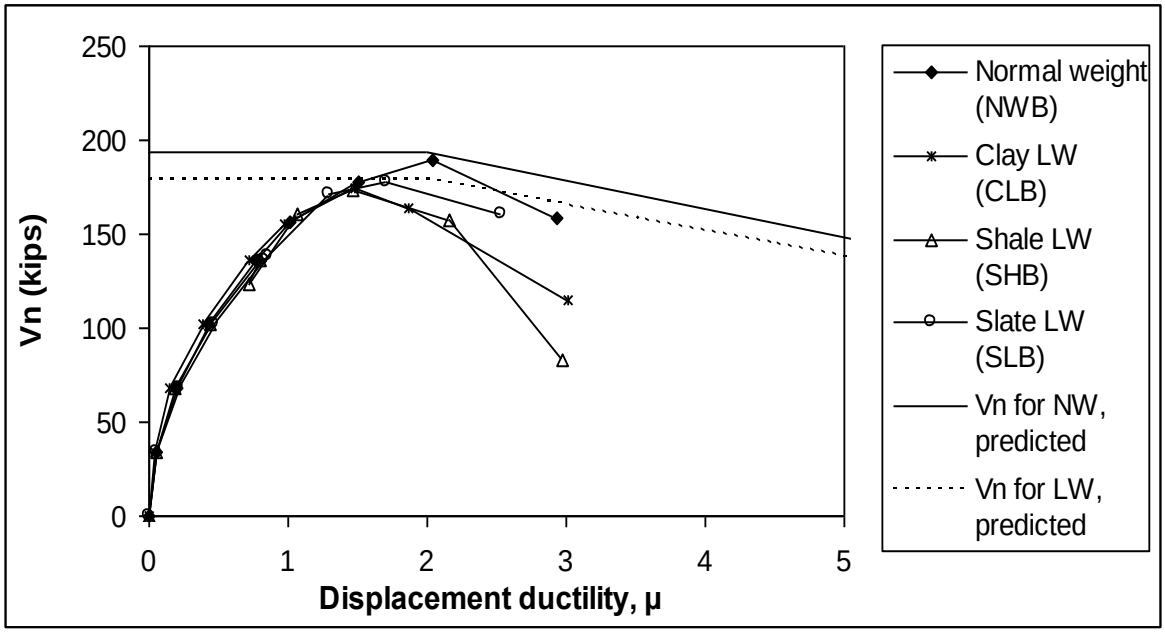

Figure 5.6 – V_n vs. ductility for high-strength brittle tests

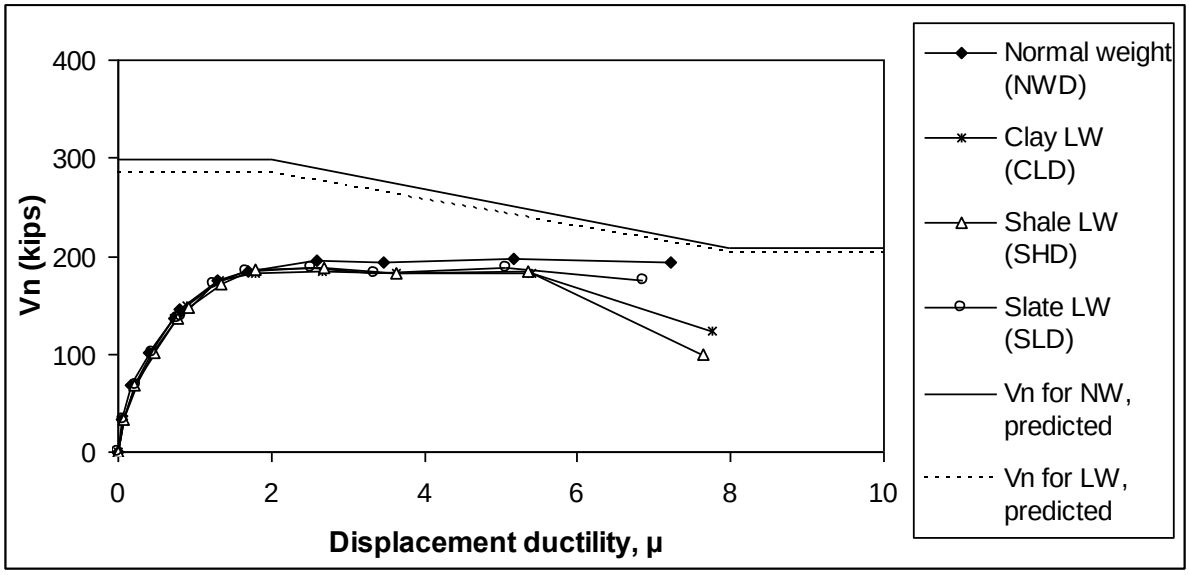

Figure 5.7 – V_n vs. ductility for high-strength ductile tests

Figure 5.6 shows that the normal weight specimen nearly reaches its predicted value, while the lightweight specimens fall somewhat short. Figure 5.7 implies that no shear failure occurred, consistent with test observations. However, significant shear deformation was recorded (Figure 7.9). The normal weight specimen obtained the highest load at high displacements, possibly indicating a higher shear strength. Again, the concrete strengths were different for all specimens, which directly affect values for V_c, the contribution of concrete to shear strength. In order to eliminate this as a factor, γ vs. μ plots were generated by back-calculating from V_c, which is determined by subtracting the steel truss and axial load contributions from the maximum lateral load V_n (Equation 2.1).

V_s, the contribution of the steel truss, can be calculated directly from strain gage data. This involves the conversion of maximum steel strains into stresses,

then into forces. These calculations were made at each force-controlled load point, and at the first cycle of each ductility level. The detailed process for this method is discussed in the Appendix. Of the four brittle tests, reliable strain gage data was only obtained for the shale lightweight specimen, so it is the only one shown on the graph below. This data was not collected for the normal weight brittle specimen as mentioned in section 3.1, and the slate and clay lightweight specimens had only two and three working strain gages, respectively.

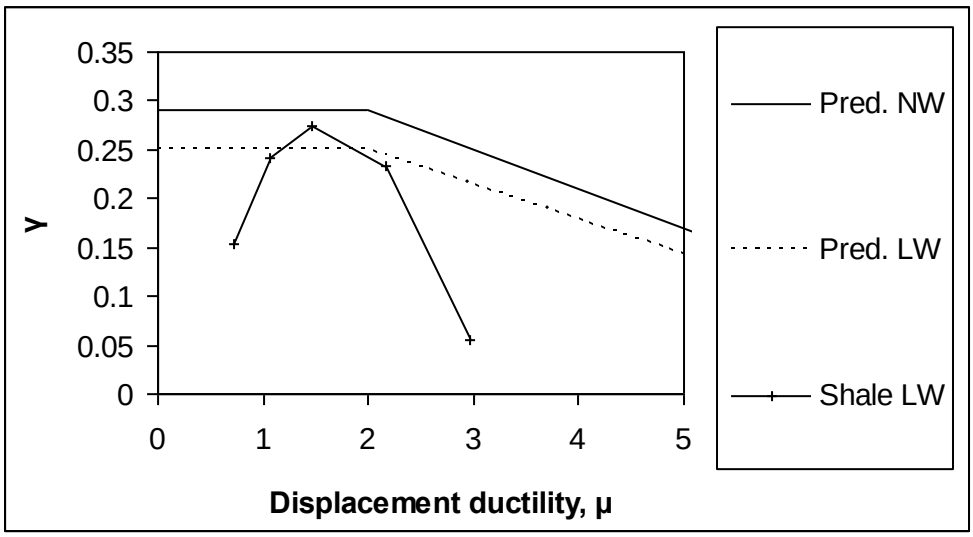

Figure 5.8 – Actual and predicted γ values for high-strength shale lightweight brittle test specimens

Figure 5.8 shows that the shale lightweight specimen exceeded the predicted value for lightweight concrete, and its maximum value for γ was 0.275.

The maximum recorded strain in the transverse steel was used to calculate V_s. Since only five strain gages were placed throughout the height of the column on each side, the stirrup with the maximum strain may not have been obtained even if the gages worked properly. Therefore, this method yields approximate results.

For the ductile tests, reliable strain gages were found for normal weight and shale specimens. Figure 5.9 shows γ vs. μ for the ductile tests.

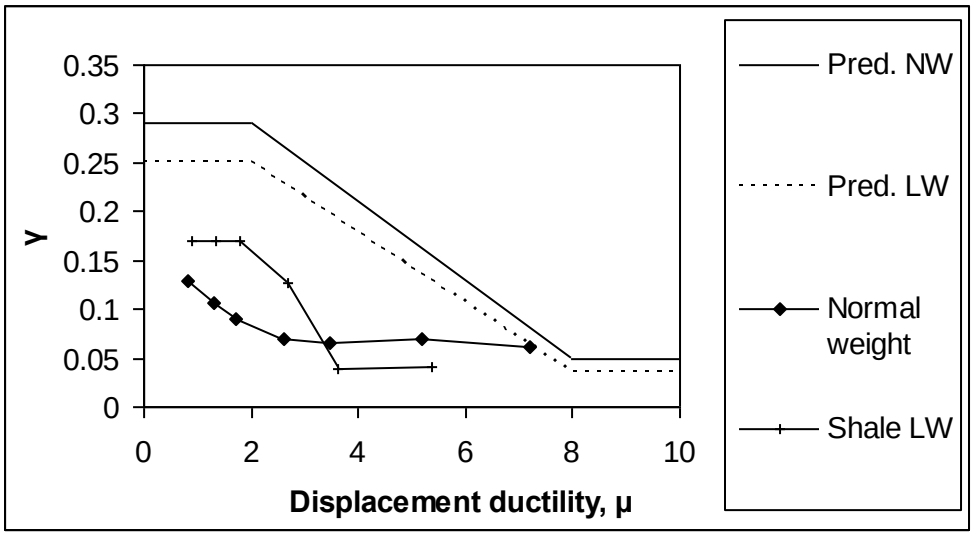

Figure 5.9 – Actual and predicted γ values for high-strength normal weight and shale lightweight ductile test specimens

At lower levels of ductility, the curves are not expected to match with the predicted values, because the shear demand was low for this portion of the test. The normal weight specimen curve nearly intersected with the high ductility plateau of the predicted normal weight shear capacity envelope. Although the shale specimen reached an ultimate ductility level of $\mu_{7.6}$, accurate data was not obtained beyond $\mu_{5.4}$. Even so, the γ value would not intersect with the predicted lightweight shear capacity envelope.

Because accurate strain gage data was not obtained for all tests, attempts are made to estimate strains in the steel based on other known data. Shear

deformation envelopes and deformation component graphs were obtained for all tests, excluding the normal weight brittle test, and are given in the Appendix. For the three tests with working strain gages, strain vs. shear deformation plots were generated (Figure 5.10). The goal was to find a trend between tests so that the behavior of tests for which strain gage data was unavailable could be estimated using the shear deformation envelopes (Figures 7.8 and 7.9).

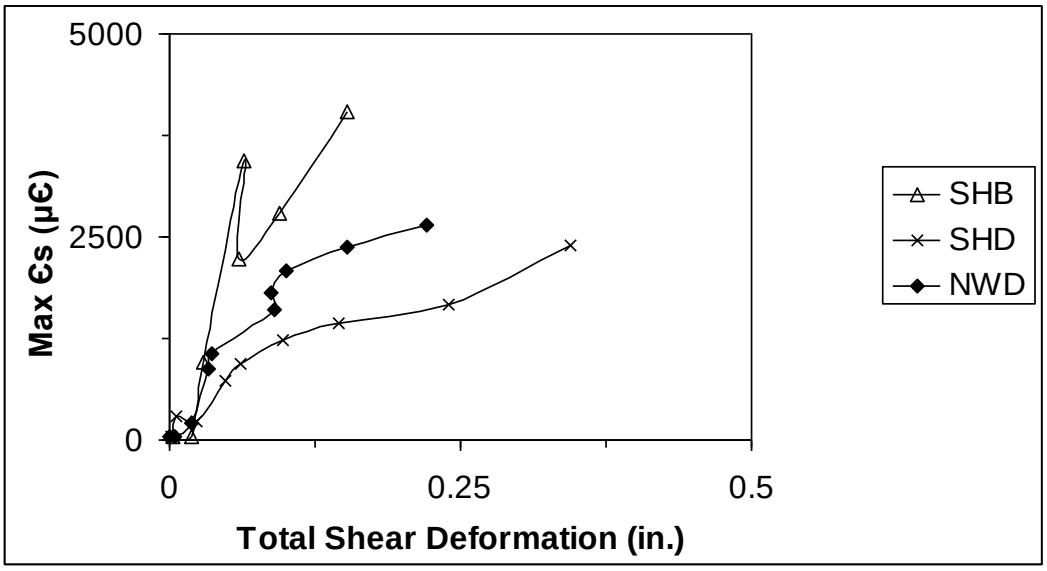

Figure 5.10 – Max strain vs. shear deformation for tests with working strain gages

This figure does not show the expected trend, as all three tests show significantly different results. Therefore, the strain could not be estimated in the remaining five tests. The shear deformation envelopes show that there is no significant difference between all test specimens. Figure 7.9 shows a large shear deformation for the clay ductile test, but this test simply had reliable external instrumentation for a longer period of time compared to other tests. An alteration to the Revised UCSD model

cannot be made on the basis of only two lightweight tests. Also, since there was no intersection between the shear force and the shear capacity envelope for the ductile tests, no recommendations are made involving the alteration of the high ductility level plateau for the Revised UCSD model for lightweight concrete.

For normal weight concrete, Robalino recommended a low ductility plateau level (μ = 0 to 1.5) of 0.175, a high ductility plateau level (μ = 5.7 to 10) of 0.25, and a linear transition in between for the γ value of the Revised UCSD model when using lightweight concrete as shown in Figure 5.11 (Robalino 2006).

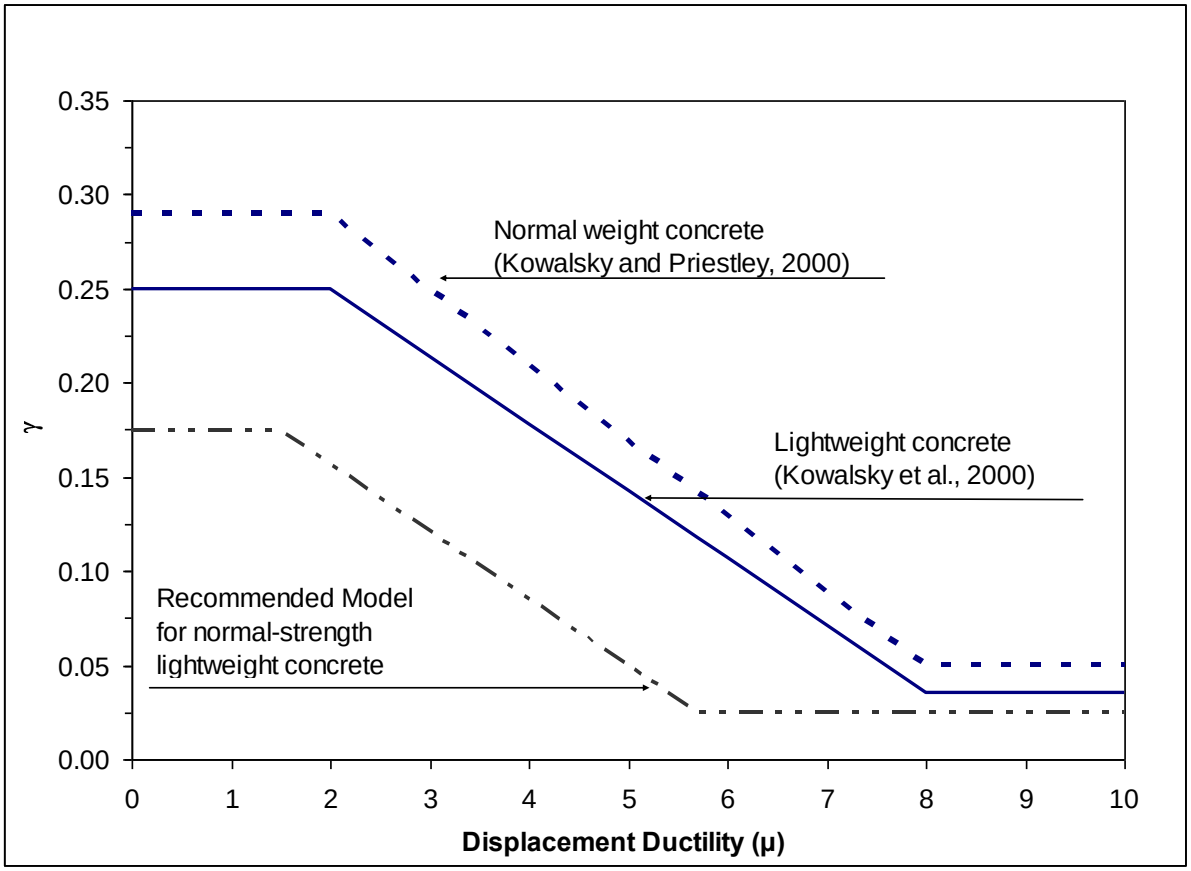

Figure 5.11 – Revised strength degradation analytical models for normal-strength concrete shear resisting mechanism (Robalino 2006)

5.5 – Miscellaneous Data

Other results from the research are discussed here. The following table shows at what cycle different types of cracks were formed. For the formation of flexure and shear cracks, in most cases, cracks appeared on lightweight specimens during an earlier cycle than normal weight specimens. Transverse steel was activated earlier, and this shows evidence of a weaker concrete component for lightweight concrete.

Table 5.13 – Miscellaneous data for high-strength specimens

	NWB	CLB	SHB	SLB
first flex. on N and S	Fy'/2	Fy'/2	Fy'/2	Fy'/2
first flex. on E and W	3Fy'/4	Fy'/2	Fy'/2	Fy'/2
first flex-shear cracks	Fy'	3Fy'/4	3Fy'/4	3Fy'/4
first shear-only cracks	μ1,1	Fy'	Fy'	Fy'
first crushing/spalling	μ 1.5,1	μ 1.9,1	μ 2,1	μ 1.5,1
max. strain location above base	--	21"	21.5"	--
max. curvature (1/in)	--	1.87E-03	5.07E-04	1.49E-03

	NWD	CLD	SHD	SLD
first flex. on N and S	Fy'/2	Fy'/2	Fy'/2	Fy'/2
first flex. on E and W	3Fy'/4	Fy'/2	Fy'/2	Fy'/2
first flex-shear cracks	3Fy'/4	3Fy'/4	3Fy'/4	3Fy'/4
first shear-only cracks	Fy'	μ 1,1	μ 1,1	Fy'
first crushing/spalling	μ 1.8,1	μ 1.5,1	μ 2,1	μ 2,3
max. strain location above base	19.4"	29.5"	20.5"	--
max. curvature (1/in)	2.37E-03	1.95E-03	1.32E-03	1.95E-03

Table 5.13 also shows where the maximum strain in transverse steel occurred relative to the base of the column. The average for the tests that obtained strain gage data was 22.4”, about a distance D (21”) from the support. The maximum curvature values for each test are shown. The normal weight ductile specimen achieved the highest value, due to its high value of ductility reached. The shale specimen showed the lowest curvature values in both brittle and ductile test specimens.

CHAPTER 6 – CONCLUSIONS AND RECOMMENDATIONS

In terms of displacement capacity, the normal weight specimen did exhibit higher loads at equal displacements when compared to lightweight specimens, but this difference was not significant for normal- nor high-strength concrete columns.

The strength of the concrete shear resisting mechanism degraded at a somewhat faster rate at higher levels of ductility (μ_7 or greater), for lightweight specimens compared to normal weight specimen. This was the case for both normal- and high-strength concrete, although high-strength showed a slower rate of degradation.

Considering both normal- and high-strength test specimens, there is no significant difference between the energy absorption of normal and lightweight concrete.

The formation of flexure and shear cracks occurred at an earlier cycle for lightweight specimens compared to normal weight. This caused the earlier activation of transverse steel, which gave the lightweight concrete a weaker concrete component of shear resistance.

It is recommended that the γ factor remain unchanged for the Revised UCSD model for lightweight concrete when using high-strength concrete, as shown in Figure 6.1.

Future research is needed in order to confirm the findings of this research.

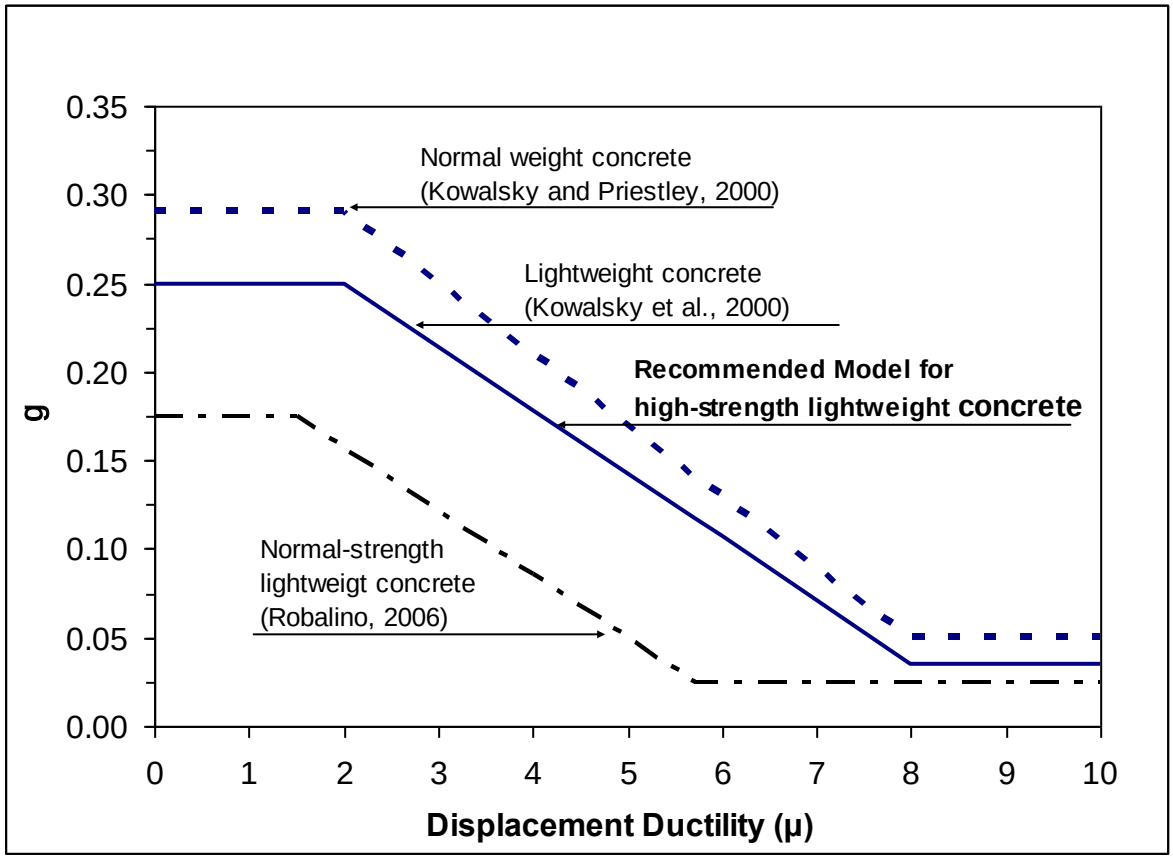

Figure 6.1 – Strength degradation analytical models for normal-strength and high-strength concrete shear resisting mechanisms

REFERENCES

ACI (American Concrete Institute). ACI 318-05 Building Code Requirements for Structural Concrete and Commentary (2005). (11.2.1.2, 21.2.4.2)

ACI Committee 445 and ACI Committee 441. "Deformation Capacity and Shear Strength of Reinforced Concrete Members Under Cyclic Loading." *ACI Special Publications Series* Vol. 236 (2006).

Bae, S., and Bayrak, O. "Seismic Performance of Full-Scale Reinforced Concrete Columns." *ACI Structural Journal* Vol. 105, No. 2 (2008): 123-33.

Dwairi, H.M. "Equivalent Damping in Support of Direct Displacement-Based Design." *Journal of Earthquake Engineering* Vol. 11, No.4 (2007): 512-30.

Expanded Shale, Clay and Slate Institute (ESCSI). "Expanded Shale, Clay & Slate: A World of Applications…Worldwide." (2006).

Ghosh, S.K., and Ahmad, S. "High-Strength Concrete for Seismic Applications." *ACI Concrete International* Vol. 28, No. 9 (2006): 47-49.

Jacobsen, L.S. "Damping in Composite Structures." *Proceedings, 2nd World Conference on Earthquake Engineering* Vol. 2 (1960): 1029-44.

Jennings P.C. “Engineering Features of the San Fernando Earthquake.” California Institute of Technology (1971).

Kowalsky, M.J., and Priestley, M.J.N. “Improved Analytical Model for Shear Strength of Circular Reinforced Concrete Columns in Seismic Regions.” *ACI Structural Journal* Vol. 97, No. 3 (2000): 388-96.

Kowalsky, M.J., Priestley, M.J.N., Seible, F. “Shear Behavior of Lightweight Concrete Columns Under Seismic Conditions.” University of California at San Diego, Report No. SSRP-95/10 (1995).

Kowalsky, M.J., Priestley, M.J.N., and Seible, F. “Shear and Flexural Behavior of Lightweight Concrete Bridge Columns in Seismic Regions.” *ACI Structural Journal* Vol. 96, No. 1 (1999): 136-48.

Kowalsky, M.J., Priestley, M.J.N., and Seible, F. “Dynamic Behavior of Lightweight Concrete Bridges.” *ACI Structural Journal* Vol. 97, No. 4: (2000): 602-18.

Montejo, L.A., and Kowalsky, M.J. “CUMBIA: Set of Codes for the Analysis of Reinforced Concrete Members.” Department of Civil, Construction, and Environmental Engineering, North Carolina State University. Technical Report No. IS-07-01 (2007).

Priestley, M.J.N., Verma, R., and Xiao, Y. "Seismic Shear Strength of Reinforced Concrete Columns." *ASCE Journal of Structural Engineering* Vol. 120, No. 8 (1994): 2310-29.

Priestley, M.J.N., Calvi, G.M., and Kowalsky, M.J. "Displacement-Based Seismic Design of Structures." IUSS Press, Pavia, Italy: (2007).

von Ramin, M., and Matamoros, A. B. "Shear Strength of Reinforced Concrete Members Subjected to Monotonic Loads." *ACI Structural Journal* Vol. 103, No. 1 (2006): 83-92.

Restrepo, J. I., Seible, F., Stephan, B., and Schoettler, M. J. "Seismic Testing of Bridge Columns Incorporating High-Performance Materials." *ACI Structural Journal* Vol. 103, No. 4 (2006): 496-504.

Robalino, Pablo. "Shear Performance of Reinforced Lightweight Concrete Square Columns in Seismic Regions." North Carolina State University, Master's Thesis URN: etd-08172006-154126 (2006).

Takeda, T., Sozen, M., and Nielsen, N. "Reinforced concrete response to simulated earthquakes," *ASCE Journal of Structural Engineering* Vol. 96, No. 12 (1970): 2557-73.

United States Geological Survey (USGS) Circular 1045. “Lessons Learned from the Loma Prieta, California, Earthquake of October 17, 1989.” Ed. Plafker, G. and Galloway, J. P. (1989): 31, 34.

Xiao, J., and Zhang, C. “Seismic Behavior of RC Columns with Circular, Square, and Diamond Sections.” *Construction and Building Materials* Vol. 22, No. 5 (2008): 801-810.

APPENDIX

Curvature Calculations

Curvature was calculated using data from the north and south face linear potentiometers.

$$\varphi = \frac{\theta}{G} \qquad \text{Eq. 7.1}$$

$$\theta = \frac{XN + XS}{d} \qquad \text{Eq. 7.2}$$

In Equation 7.1, φ is the curvature over the cell of interest, θ is the rotation, and G is the vertical gage length. Since five potentiometers were used on the north and south faces, curvature and rotation could be calculated for these five cells. In Equation 7.2, XN and XS are the absolute values of the displacements measured by the potentiometers on the north and south faces, respectively. The variable d is the horizontal distance between north and south potentiometers.

Strain Gage Method for Calculating the Steel Truss Component for Shear Resistance

From the strain gage data, the maximum strain was found for each force-controlled point and for the first cycle of each ductility level. The location of this strain represents the location of the weakest concrete component, thus the capacity of the concrete shear resisting mechanism. The stress was then calculated simply by multiplying strain by the modulus of elasticity (29000 ksi), and this value was limited by f_{ye}. V_s could then be calculated from the stress using Equation 7.3.

$$V_s = \frac{A_s f_s D}{s}$$ Eq. 7.3

The equation for V_S from the Revised UCSD model (Eq. 2.7) was not used for this particular application because θ could not be measured accurately for the stirrup at maximum strain, and the depth to the neutral axis varied for each cycle. Therefore the conservative Eq. 7.3 was chosen.

Shear Deformation Calculations and Graphs

The general method for calculating shear deformation used in this paper is from Kowalsky et al., 1995, however, some equations differ. The deformation in the vertical direction of a particular cell is labeled as FL.

$$FL = \frac{XN + XS}{2}$$ Eq. 7.4

$$\delta FL = FL\cos(\lambda)$$ Eq. 7.5

FL is simply the average of measurements taken by potentiometers on the north and south faces. δFL is the diagonal component of the vertical deformation, where λ is the angle from the vertical axis to the angled potentiometer measured in degrees. The east and west faces had very similar though not exact device placement, so λ was the average between the two faces.

The horizontal displacements are calculated in a similar manner.

$$EXE = \frac{XEB + XET}{2}$$ Eq. 7.6

$$EXW = \frac{XWB + XWT}{2}$$ Eq. 7.7

$$\delta EX = EX\cos(\lambda) \quad \text{Eq. 7.8}$$

XEB is the measured displacement on the east face at the base of the cell, XET is at the top of the cell, and XWB and XWT correspond to the west face. EX is the average of EXE and EXW. These types of deformation are due to bending and column dilation, so these components are subtracted from the total deformation to obtain shear deformation.

$$\delta S = \delta MS - \delta FL - \delta EX \quad \text{Eq. 7.9}$$

δS is the diagonal component of shear deformation, and δMS is the measured value from the potentiometer. This value was then translated into a horizontal component.

$$\Delta_s = \frac{\delta S}{\sin(\lambda)} \quad \text{Eq. 7.10}$$

Δ_s is computed for each cell. Each column had two cells on the east and west faces. For total shear deformation, all Δ_s values are added together. The predicted total shear deformation is an output from CUMBIA (Montejo and Kowalsky 2007) which uses an approach described in a reference material (Priestley et al. 2007).

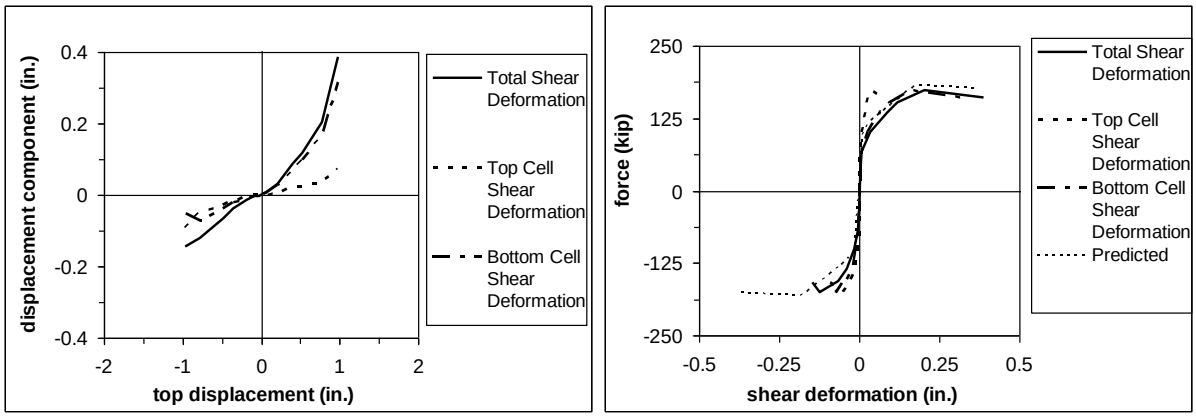

Figure 7.1 – Shear deformation by components (left) and shear deformation envelopes (right) for clay brittle specimen

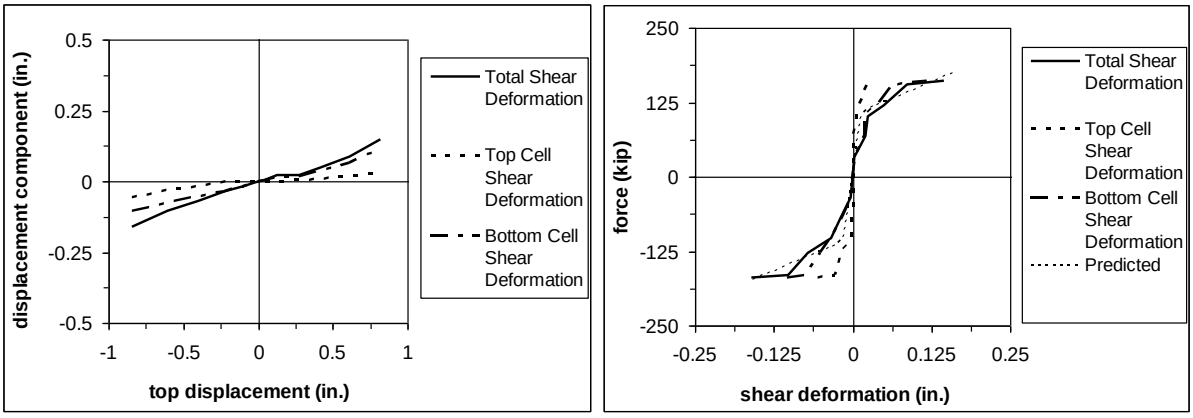

Figure 7.2 – Shear deformation by components (left) and shear deformation envelopes (right) for shale brittle specimen

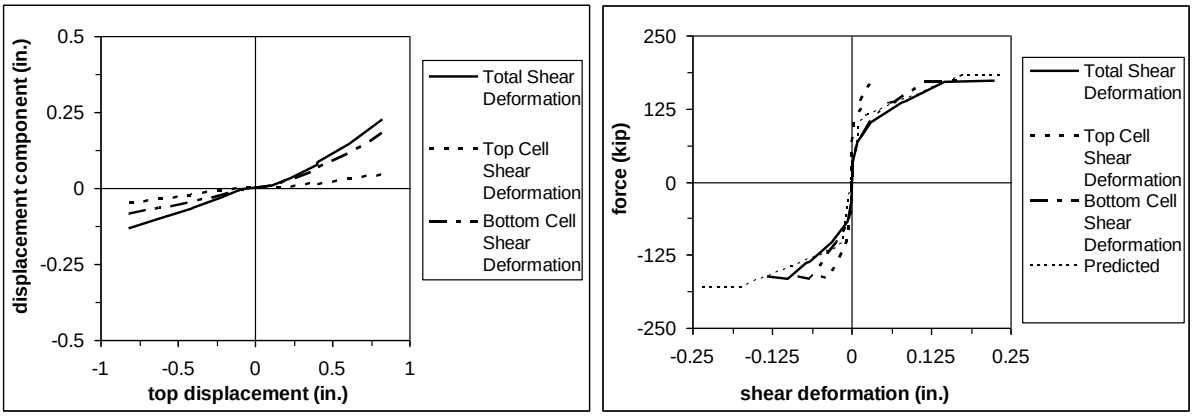

Figure 7.3 – Shear deformation by components (left) and shear deformation envelopes (right) for slate brittle specimen

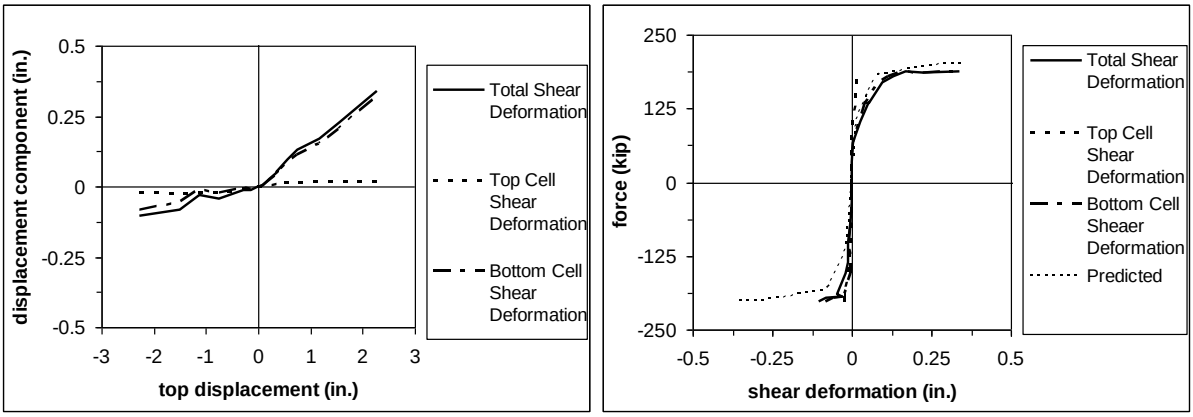

Figure 7.4 – Shear deformation by components (left) and shear deformation envelopes (right) for normal weight ductile specimen

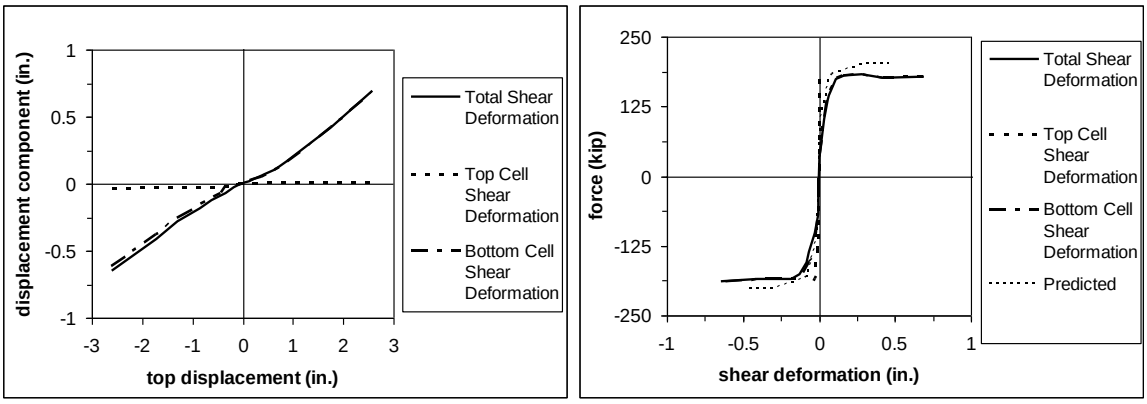

Figure 7.5 – Shear deformation by components (left) and shear deformation envelopes (right) for clay ductile specimen

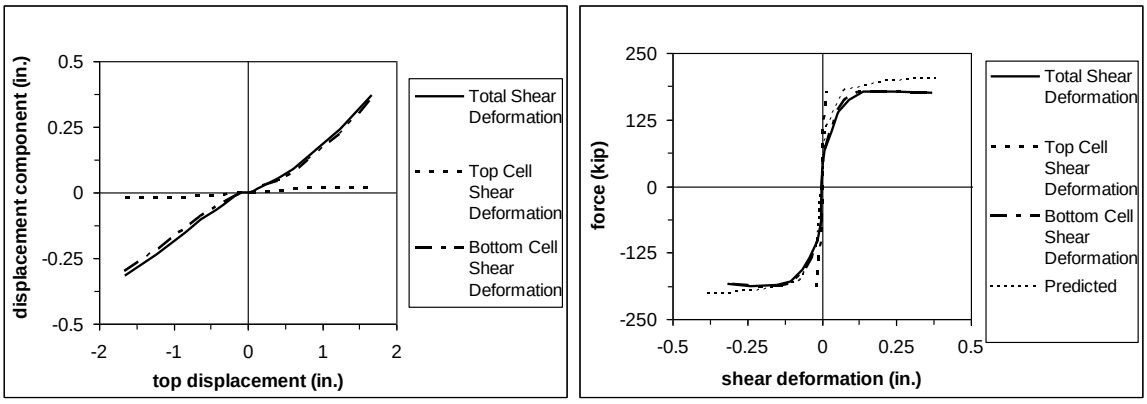

Figure 7.6 – Shear deformation by components (left) and shear deformation envelopes (right) for shale ductile specimen

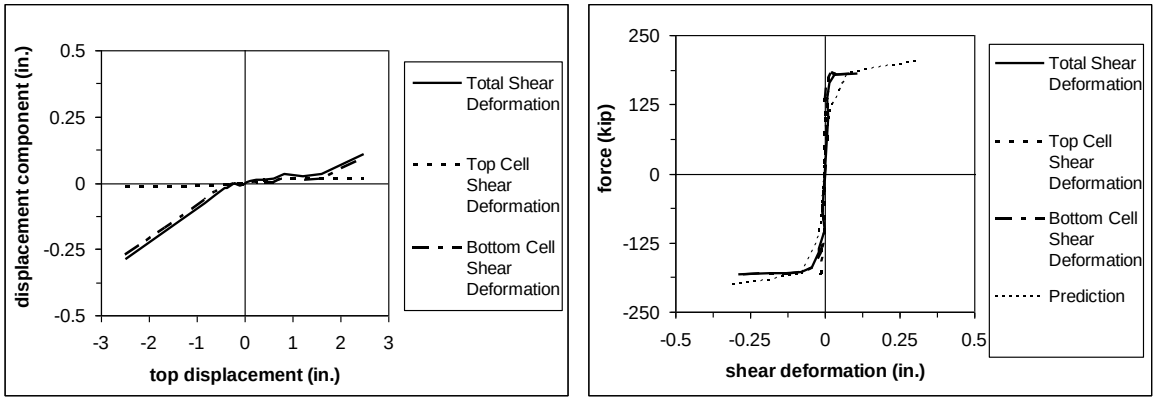

Figure 7.7 – Shear deformation by components (left) and shear deformation envelopes (right) for slate ductile specimen

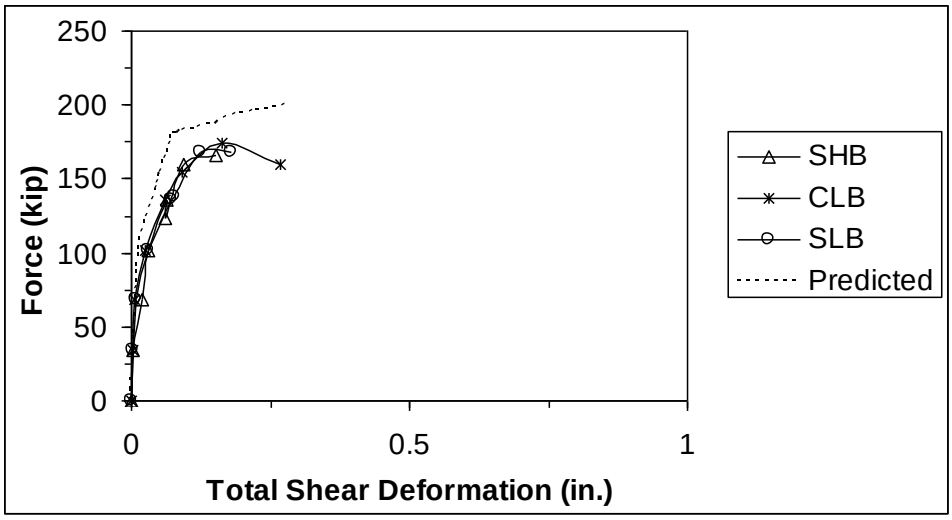

Figure 7.8 – Shear Deformation envelopes for all brittle tests

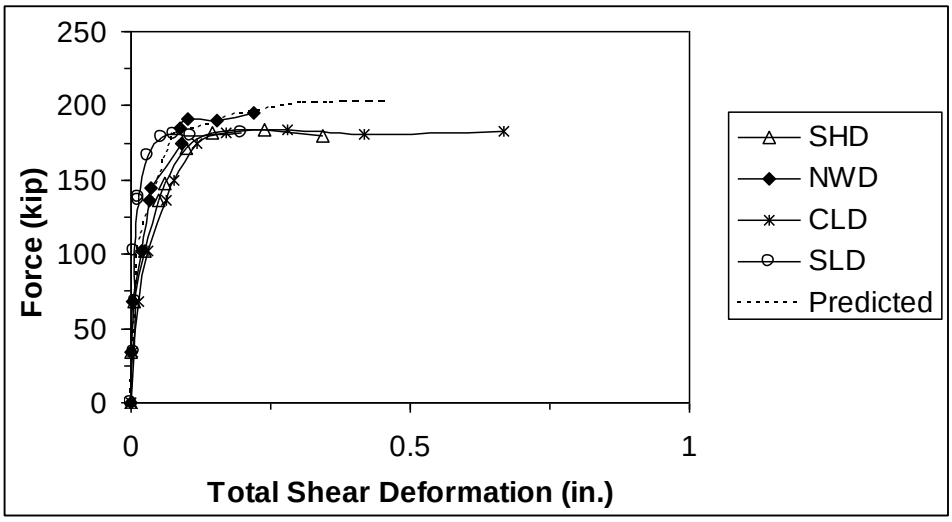

Figure 7.9 – Shear Deformation envelopes for all ductile tests

Flexural Deformation Calculations and Graphs

In order to calculate the total measured deformation of a column and compare it to the top displacement, flexural deformation is calculated. The flexural deformation of one cell is simply the rotation of the cell (θ_i) multiplied by the distance from the center of the cell to the top of the column (h_i). The sum of the deformation of the two cells is the total flexural deformation.

$$\theta_i = \frac{|XS_i| + |XN_i|}{D_i} \qquad \text{Eq, 7.11}$$

$$\delta f_i = \theta_i h_i \qquad \text{Eq. 7.12}$$

$$\Delta_f = \sum_i \delta f_i \qquad \text{Eq. 7.13}$$

D_i is the horizontal distance between potentiometers, δf_i is the flexural deformation of cell i, and Δ_f is the total flexural deformation.

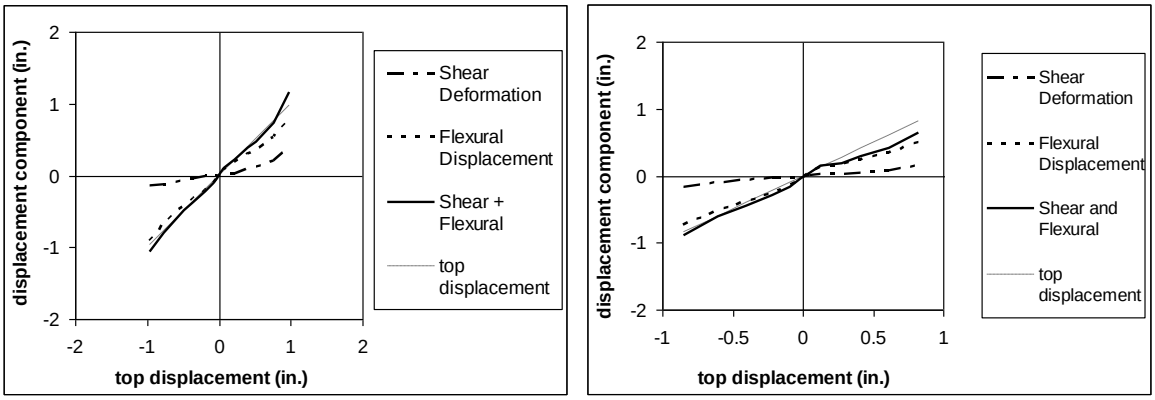

Figure 7.10 – Deformation components for clay (left) and shale (right) brittle specimens

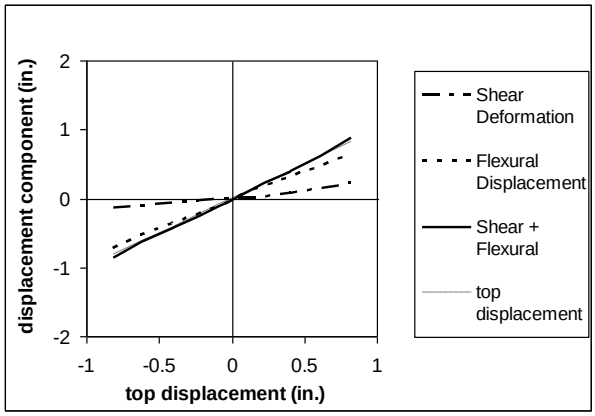

Figure 7.11 – Deformation components for slate brittle specimen

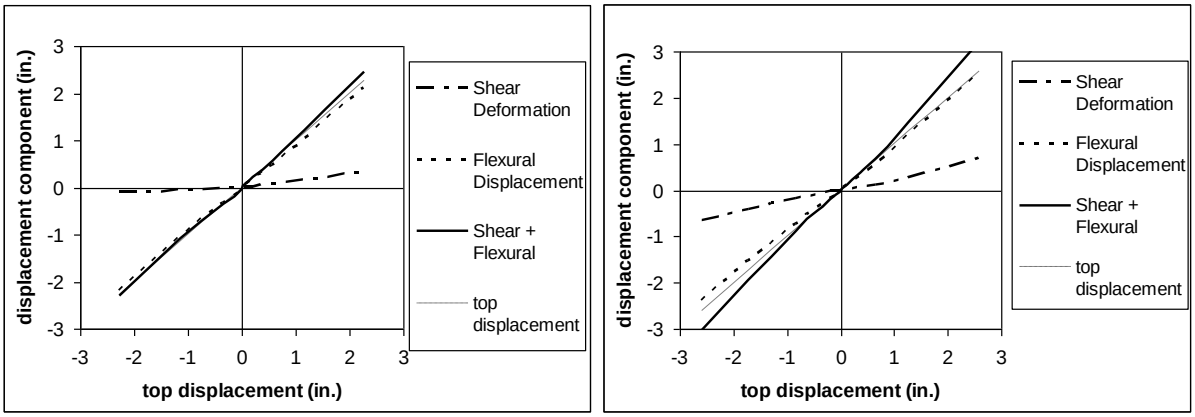

Figure 7.12 – Deformation components for normal weight (left) and clay (right) ductile specimens

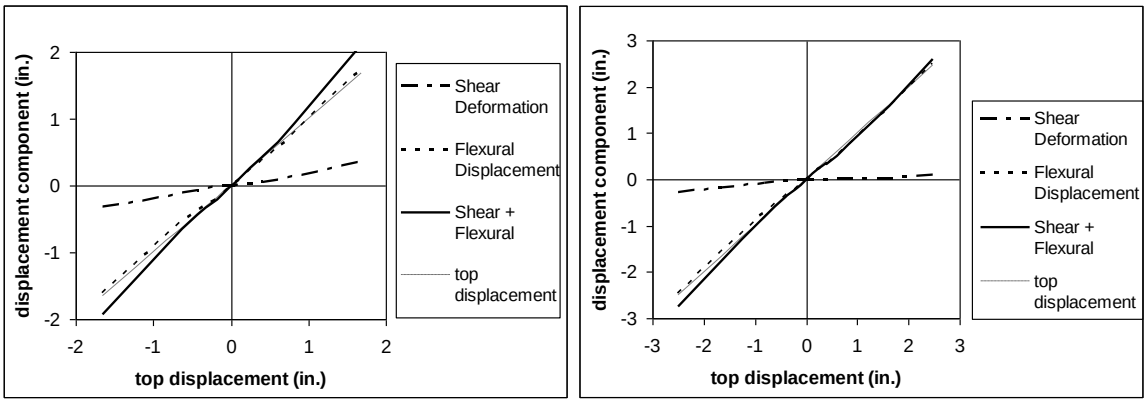

Figure 7.13 – Deformation components for shale (left) and slate (right) ductile specimens

Damping Calculations Using Jacobsen's Approach

Jacobsen found that the damping of a rigid perfectly plastic force-displacement response loop experienced a hysteretic damping value of about 2/π. Under this reasoning, the area of a particular loop (A_{loop}) could be divided by the area of a rigid perfectly plastic loop (A_{RPP}) with the same maximum force and displacement values. This number is multiplied by 2/π to obtain an approximate hysteretic damping value (Equation 7.14). For example, Figure 7.14 shows the hysteretic loop for the first cycle of $\mu_{5.4}$ for the high-strength shale ductile specimen.

$$\xi_{hyst} = \frac{2}{\pi}\frac{A_{loop}}{A_{RPP}} \qquad \text{Eq. 7.14}$$

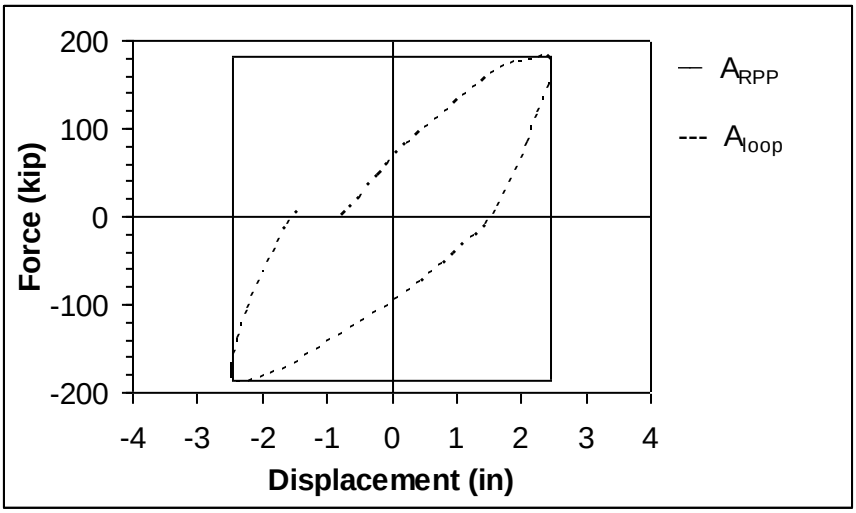

Figure 7.14 – Areas for use with Jacobsen's approach

One cycle was isolated from the data at points of zero load and the area of this loop was found with the use of a MATLAB function called 'polyarea'.

Strain Penetration Length Calculations

The curvature at the base of the column was calculated based on a strain penetration length. Since the strains in the longitudinal steel are not zero at the base of the column, a development length is calculated in order to determine the distance over which strain and rotation are taking place. This length is defined in the following manner (Priestley et al. 2007).

$$L_{SP} = 0.15 f_{ye} d_{bl} \qquad \text{Eq. 7.15}$$

The yield stress of the longitudinal bars (f_{ye}) was found through material tests to be 62.4 ksi and the diameter of the bars (d_{bl}) was 1.25 inches. Therefore the strain penetration length calculated for this research was 11.7 inches.

Equipment Specification

The data acquisition system used for this project was an Optim-Megadac. All instruments were aligned and calibrated before use. Data points were taken every two seconds for each test. The actuator model used was a 243.80T, which has a 440 kip capacity in the push direction, 300 kip capacity in the pull direction, and a maximum stroke of 40 inches.

General purpose strain gages from Vishay Micro-measurements were used. The model number was C2A with 120 Ω resistance and a gage factor of 2.075. Stirrups were sanded down to a smooth surface where 3/8 in. long strain gages were applied, and a coating was used to protect the strain gages before and during

concrete pours. Linear potentiometers with stroke capacities of 1, 1.5, 3, and 7 inches were used for each test.

Force-Displacement Responses

The force-displacement responses for all tests are shown here using the same scale for easy comparison.

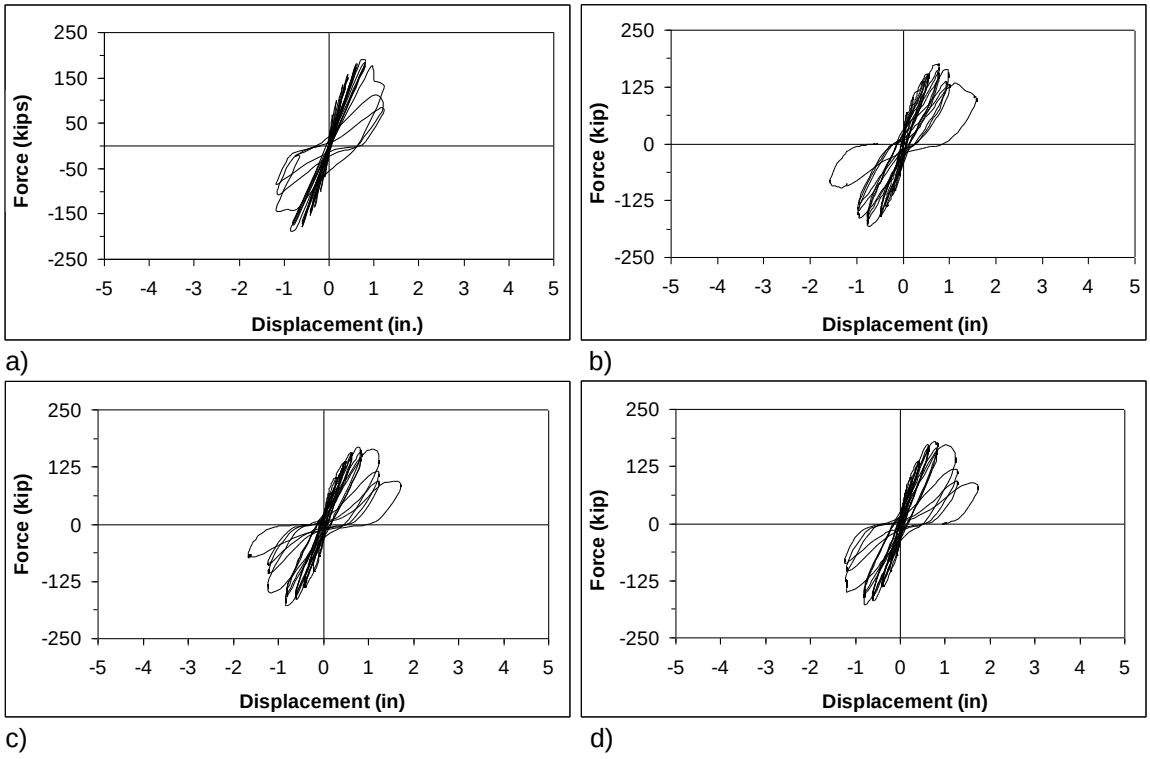

Figure 7.15 – Brittle test force-displacement responses – a) NWB, b) CLB, c) SHB, d) SLB

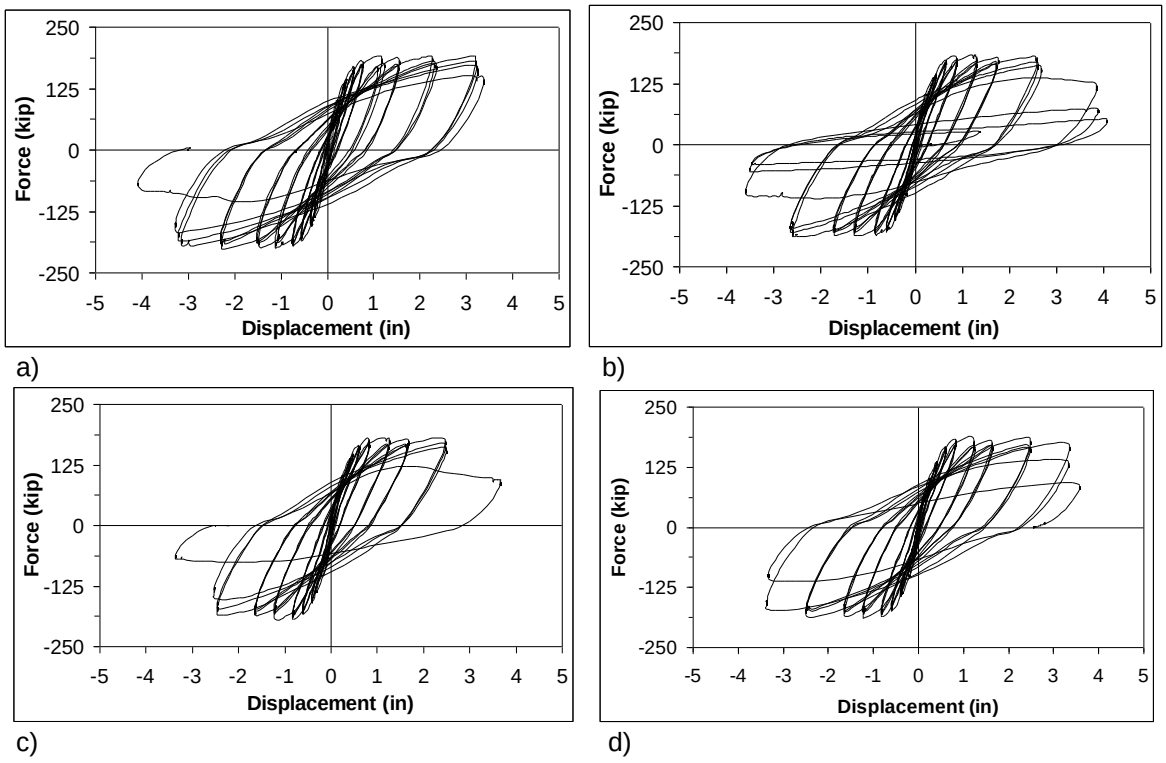

Figure 7.16 – Ductile test force-displacement responses – a) NWB, b) CLB, c) SHB, d) SLB

Working Strain Gage Histories

All working strain gage histories for the eight high-strength concrete tests are shown here. Strain gage data was not collected for the normal weight brittle failure specimen. Additionally, the two slate specimens had only two working gages each, and the exact location of these gages is not known because of the removal of identification labels.

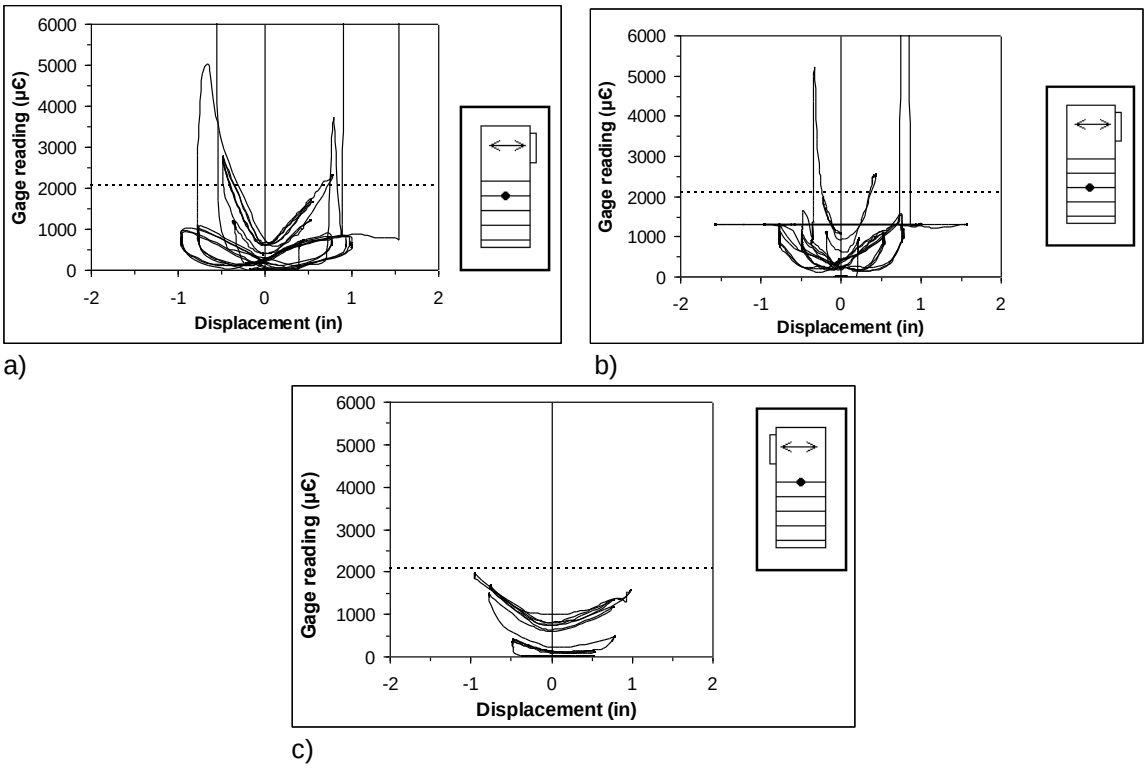

Figure 7.17 – CLB: Strain gage histories – a) TS2, b) TS3, c) BS1

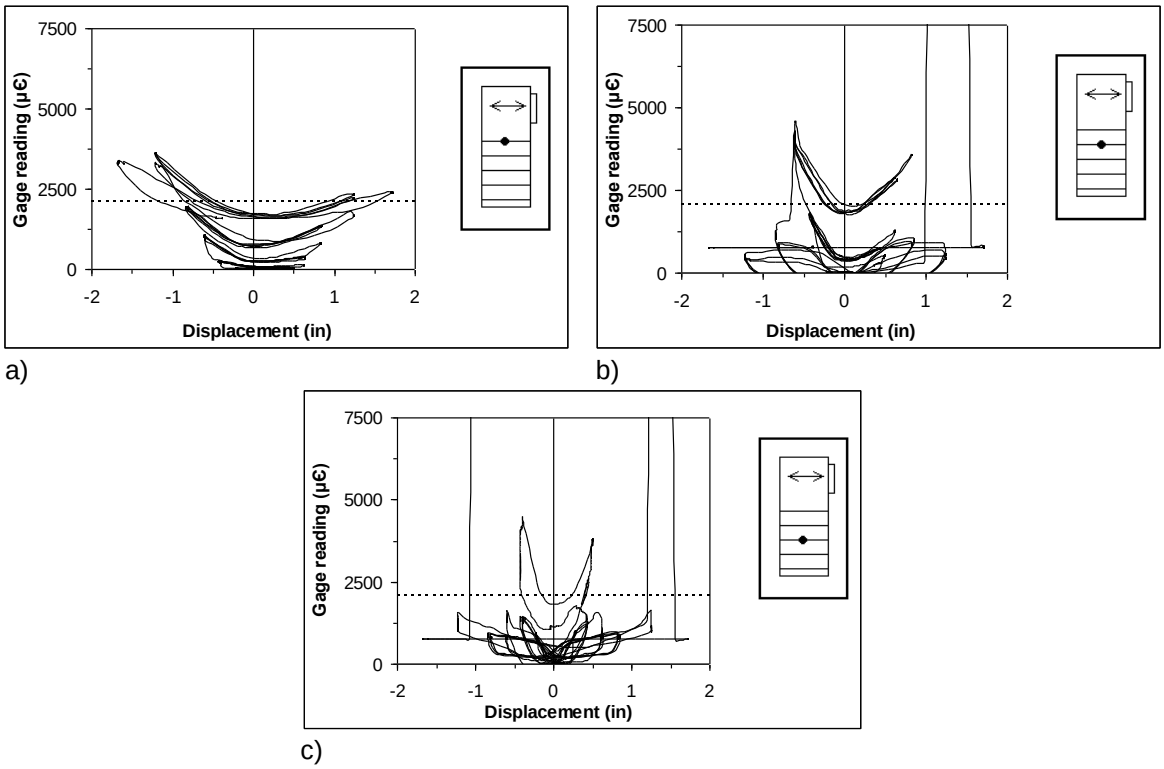

Figure 7.18 – SHB: East face strain gage histories – a) TS1, b) TS2, c) TS3

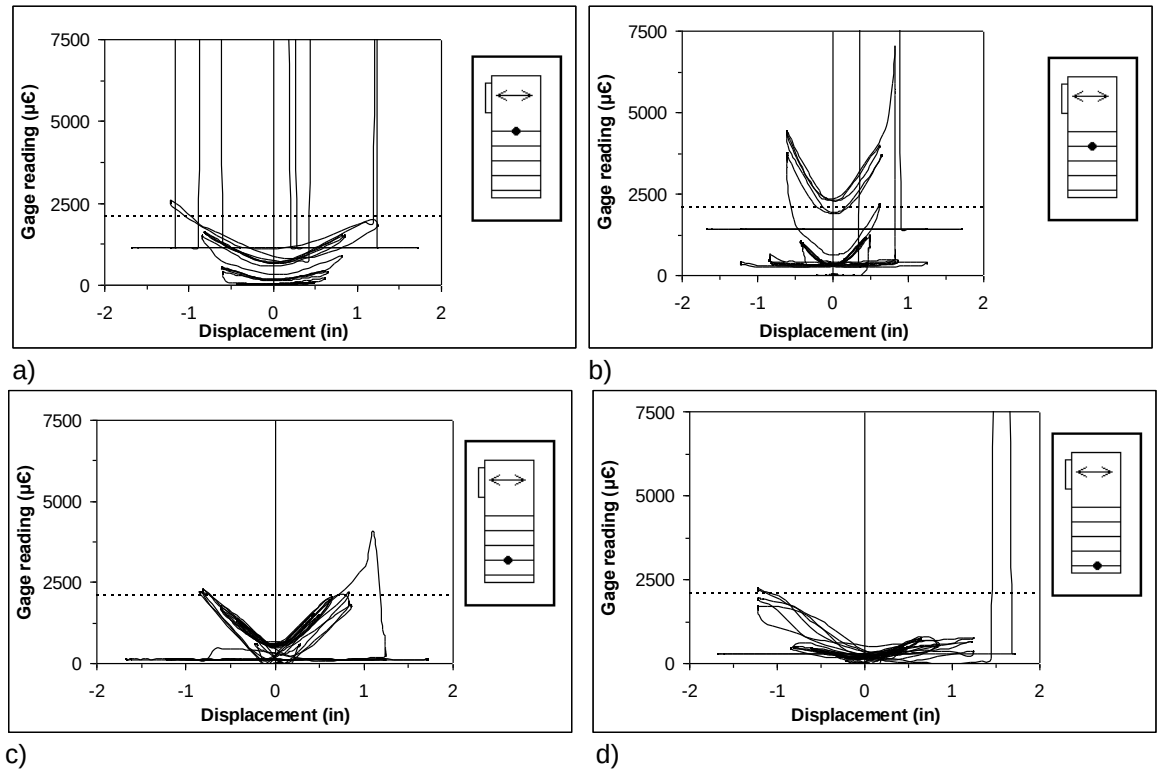

Figure 7.19 – SHB: West face strain gage histories – a) BS1), b) BS2, c) BS4 and d) BS5

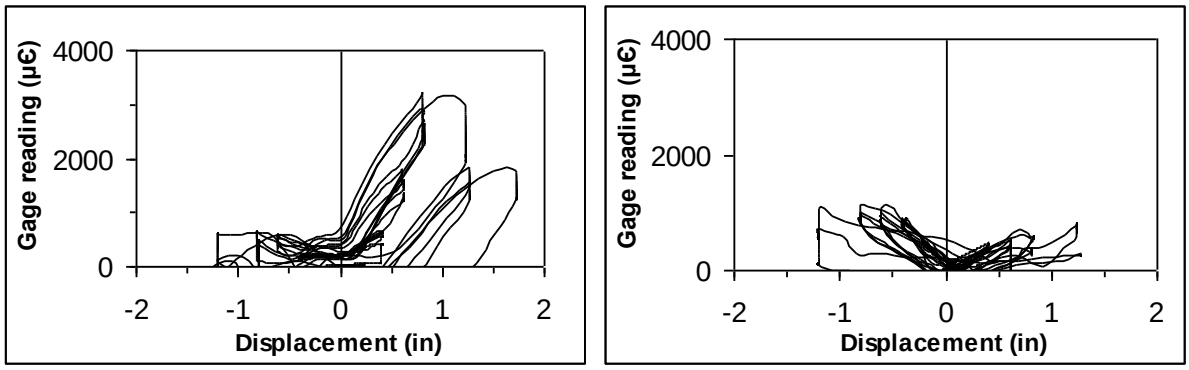

Figure 7.20 – SLB: East face strain gage histories

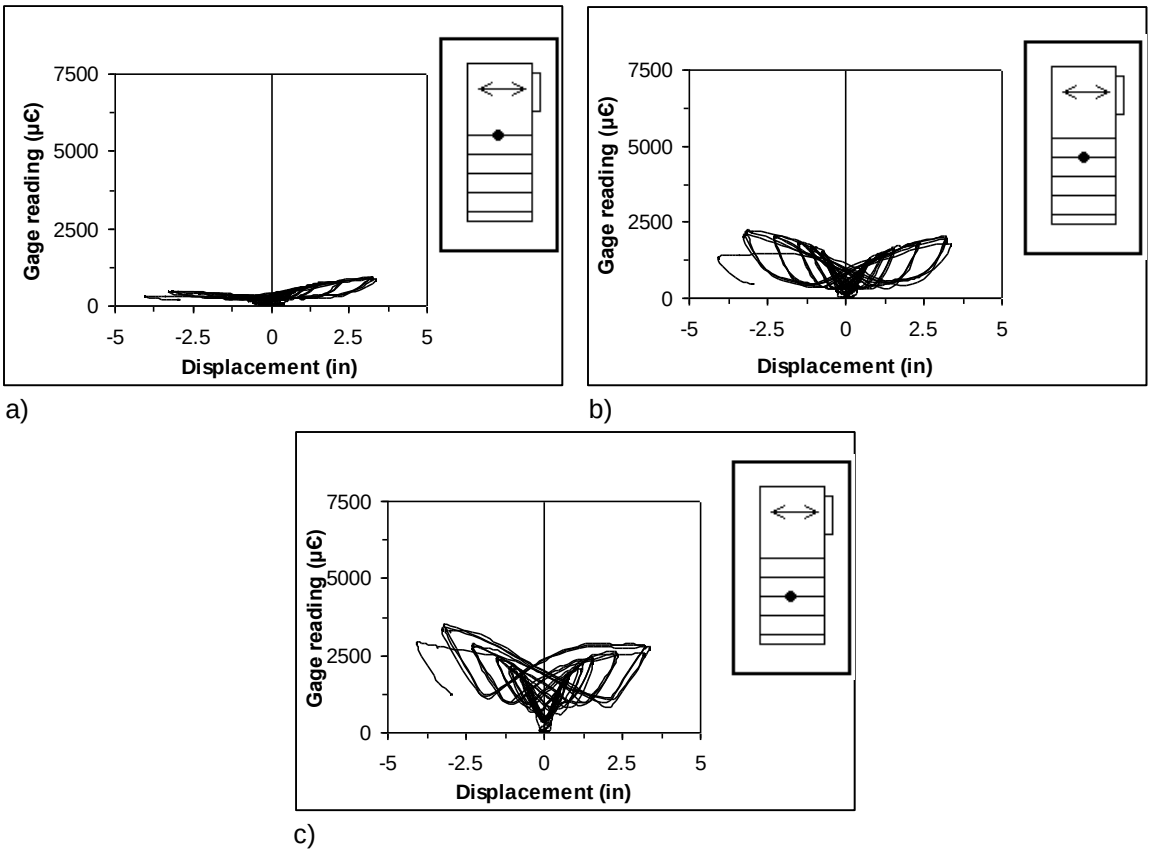

Figure 7.21 – NWD: East face strain gage histories – a) TS1, b) TS2, c) TS3

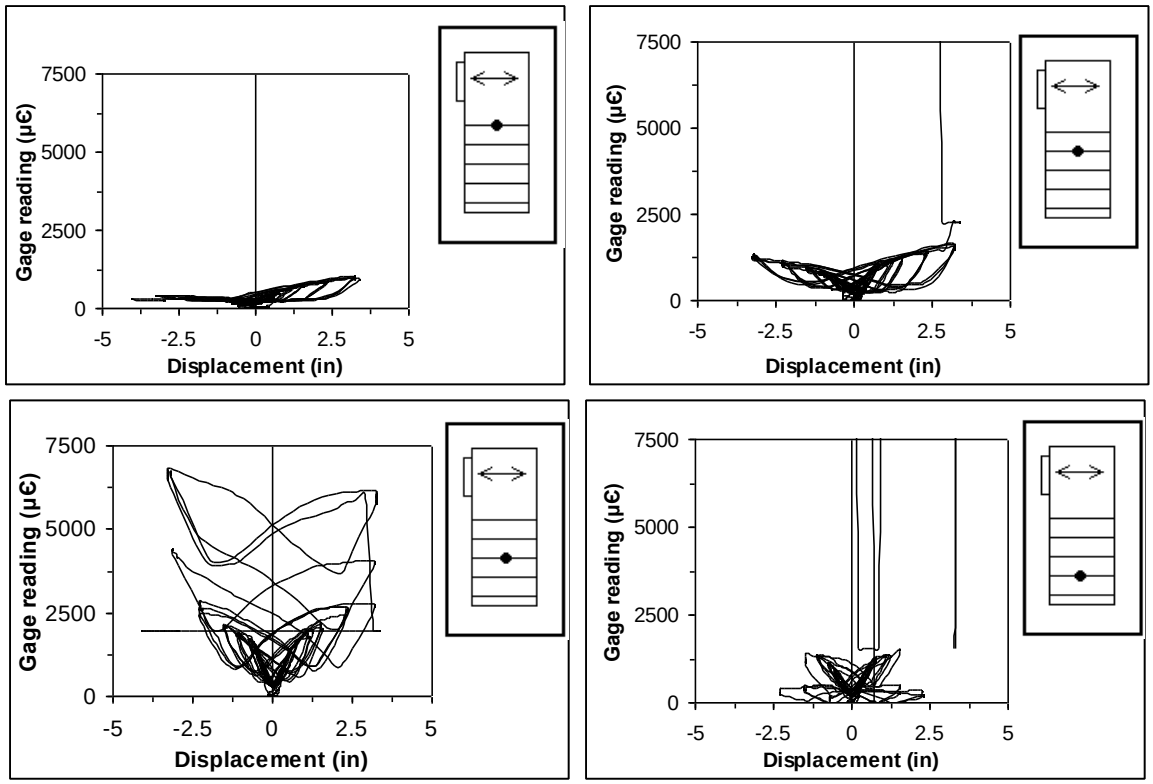

Figure 7.22 – NWD: West face strain gage histories – top left (BS1), top right (BS2), bottom left (BS3) and bottom right (BS4)

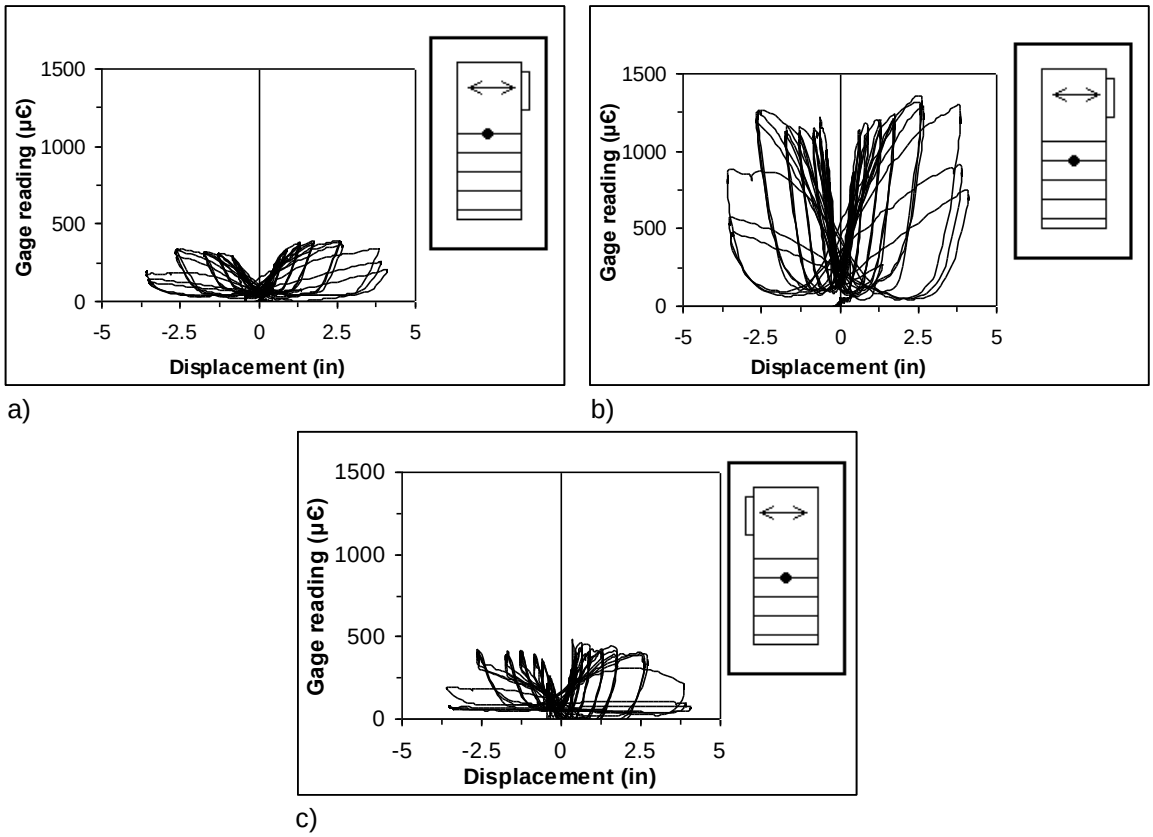

Figure 7.23 – CLD: Strain gage histories – a) TS1, b) TS2, c) BS2

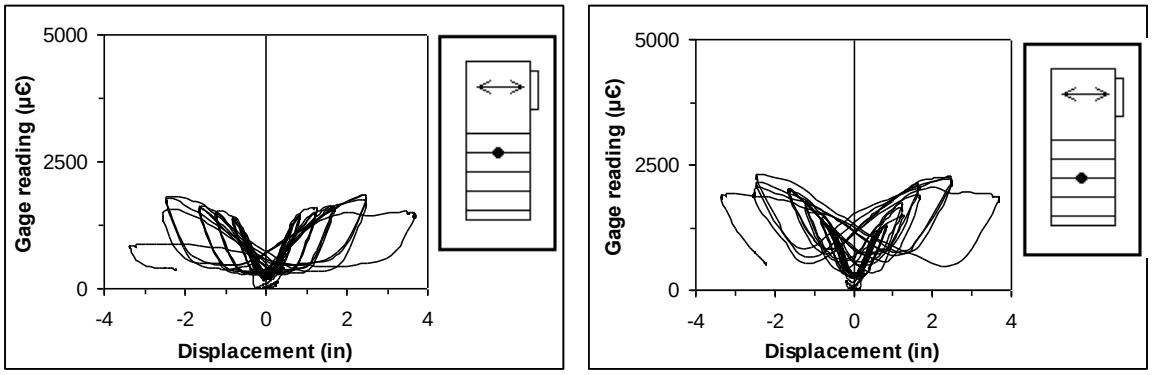

Figure 7.24 – SHD: East face strain gage histories – left (TS2), right (TS3)

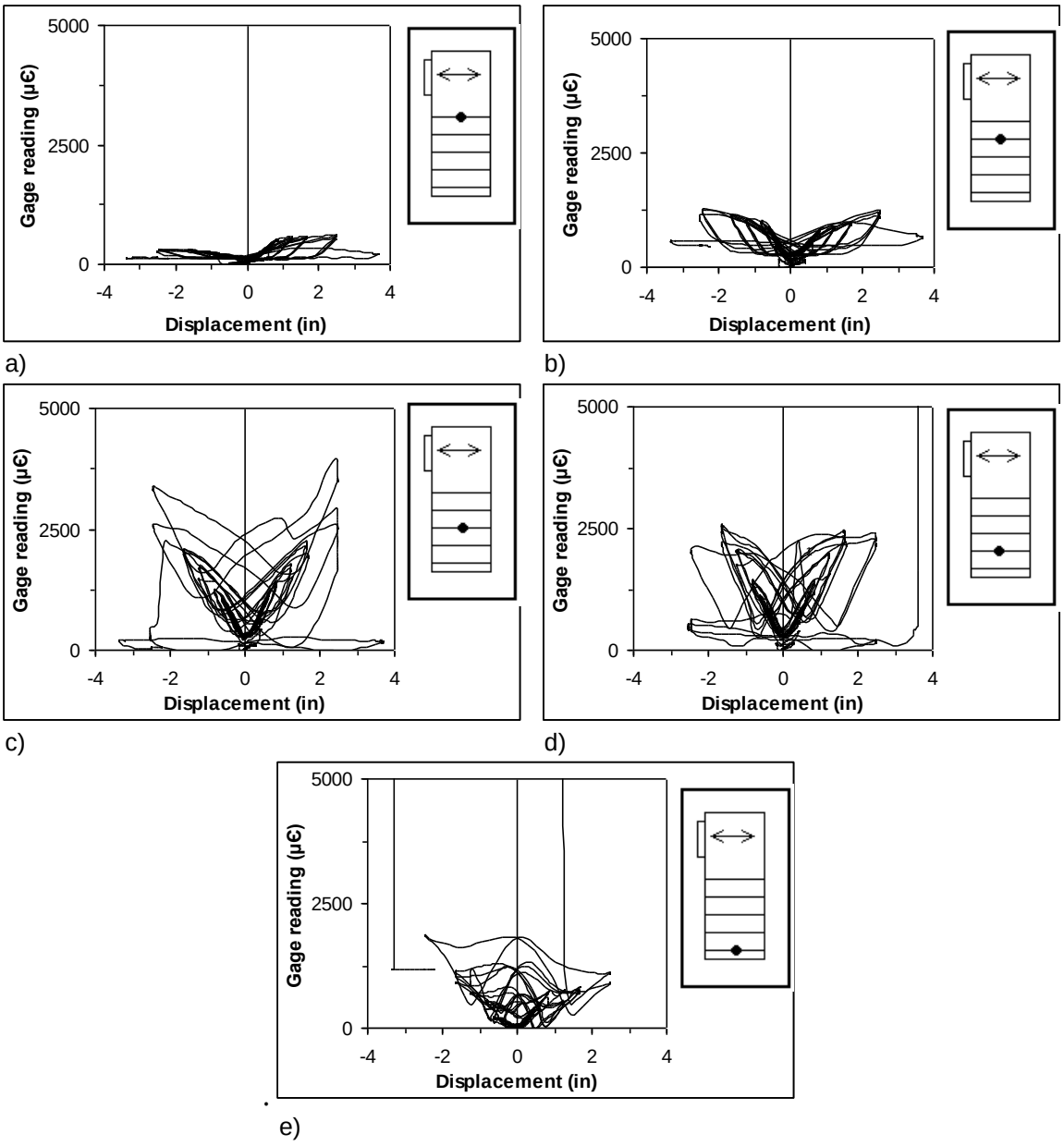

Figure 7.25 – SHD: West face strain gage histories – a) BS1, b) BS2, c) BS3, d) BS4, e) BS5

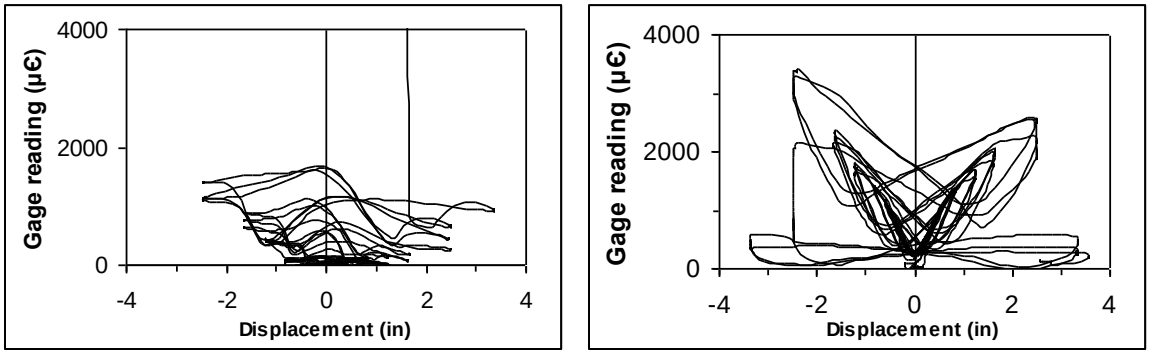

Figure 7.26 – SLD: Strain gage histories for east (left) and west (right) faces

Linear Potentiometer Histories

Linear potentiometers were used for all tests in order to calculate curvature and shear deformation. These instruments worked for all tests with the exception of the normal weight brittle test in which almost no data was collected. N1 corresponds to the linear potentiometer on the north face at the top position on the column, and N5 is at the bottom of the north face of the column. S,E, and W labels represent instruments on the south, east and west face respectively. The north and south face instruments had stroke capacities of 1 inch and 1.5 inches at different locations. The east and west faces each had two 3 inch horizontal and two 7 inch inclined potentiometers. These are labeled E1-E4 and W1-W4, where E1 is the top horizontal instrument, and E4 is the bottom inclined instrument. The configuration is shown in Figure 2.17.

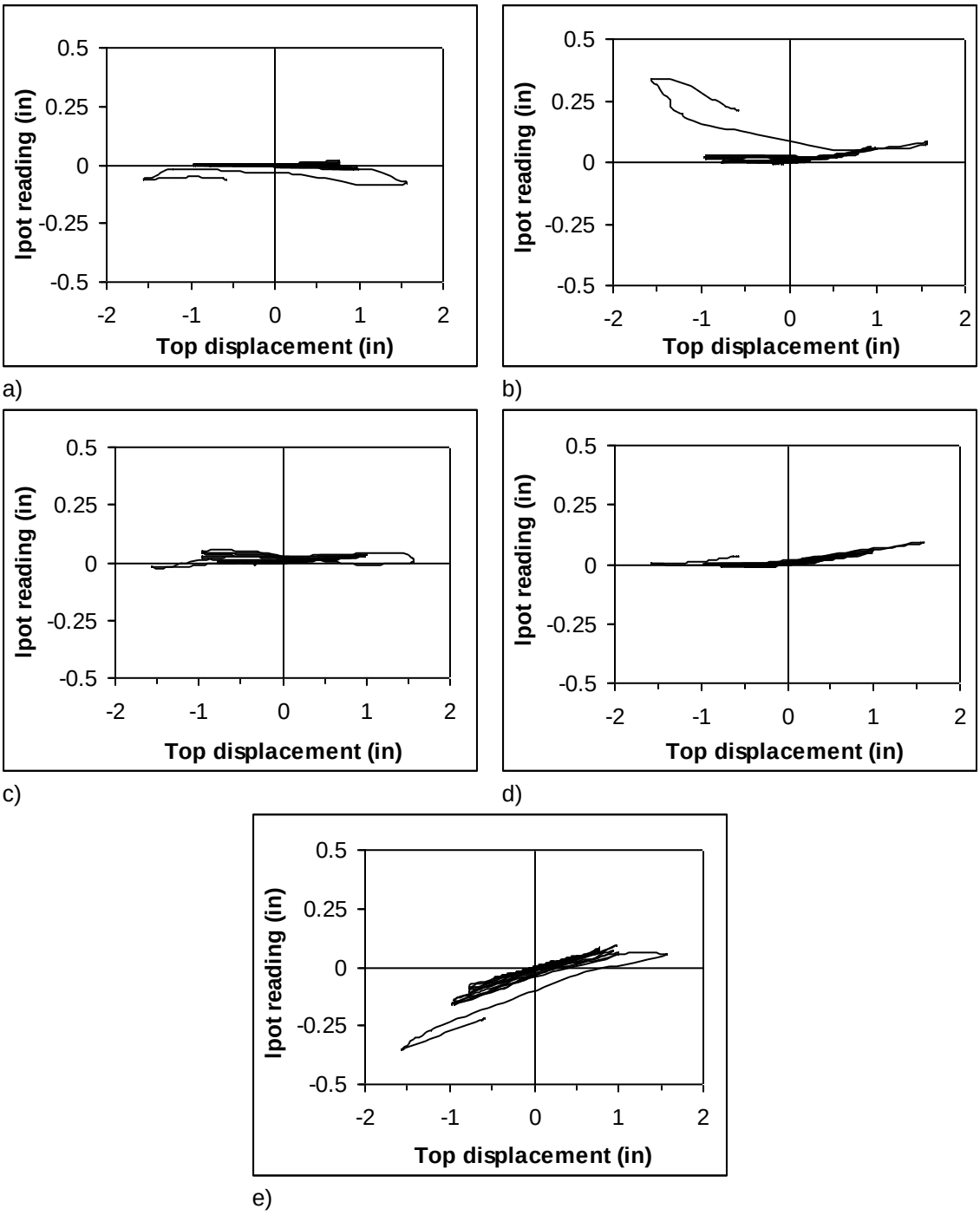

Figure 7.27 – CLB: North face linear potentiometer histories – a) N1, b) N2, c) N3, d) N4, e) N5

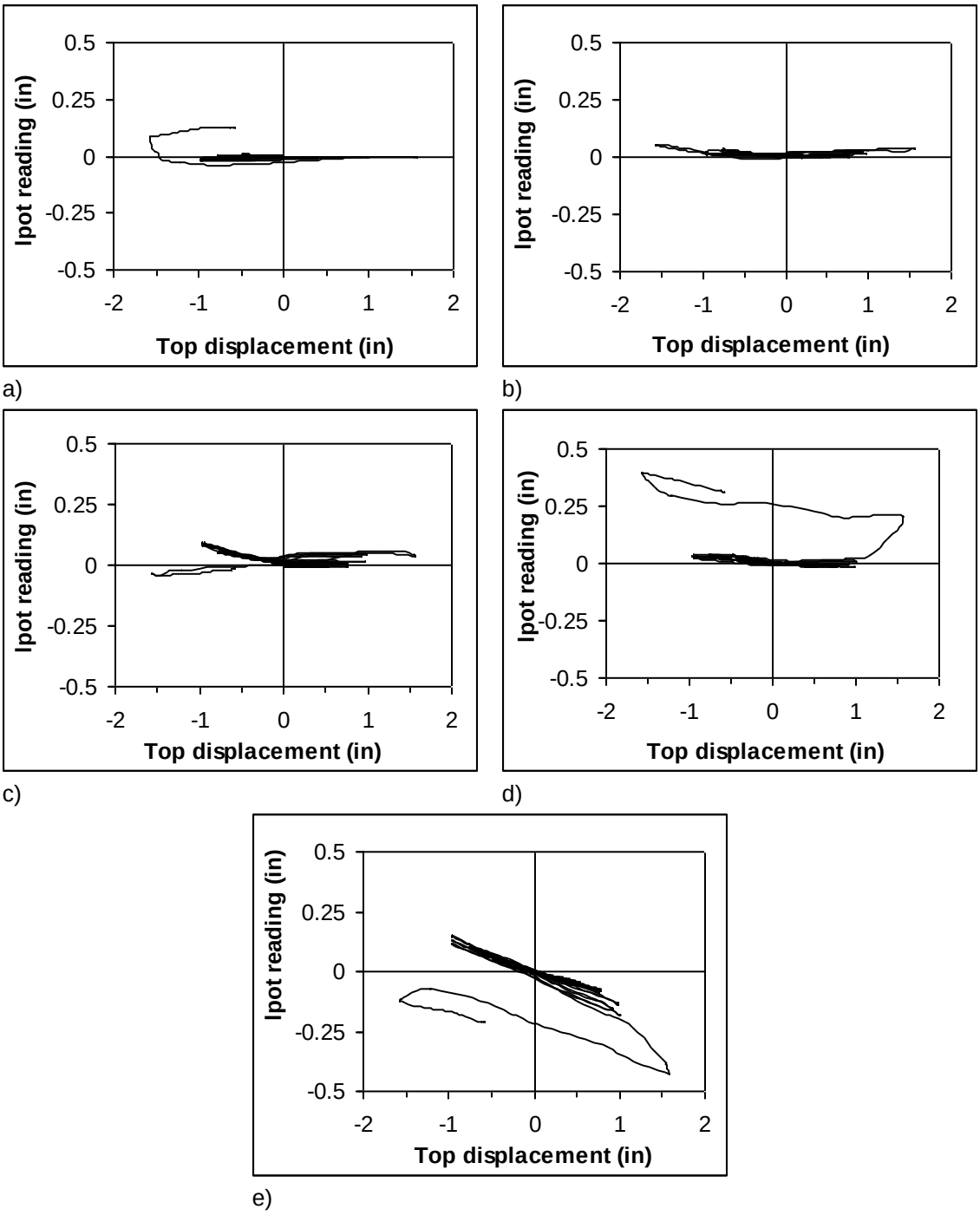

Figure 7.28 – CLB: South face linear potentiometer histories – a) S1, b) S2, c) S3, d) S4, e) S5

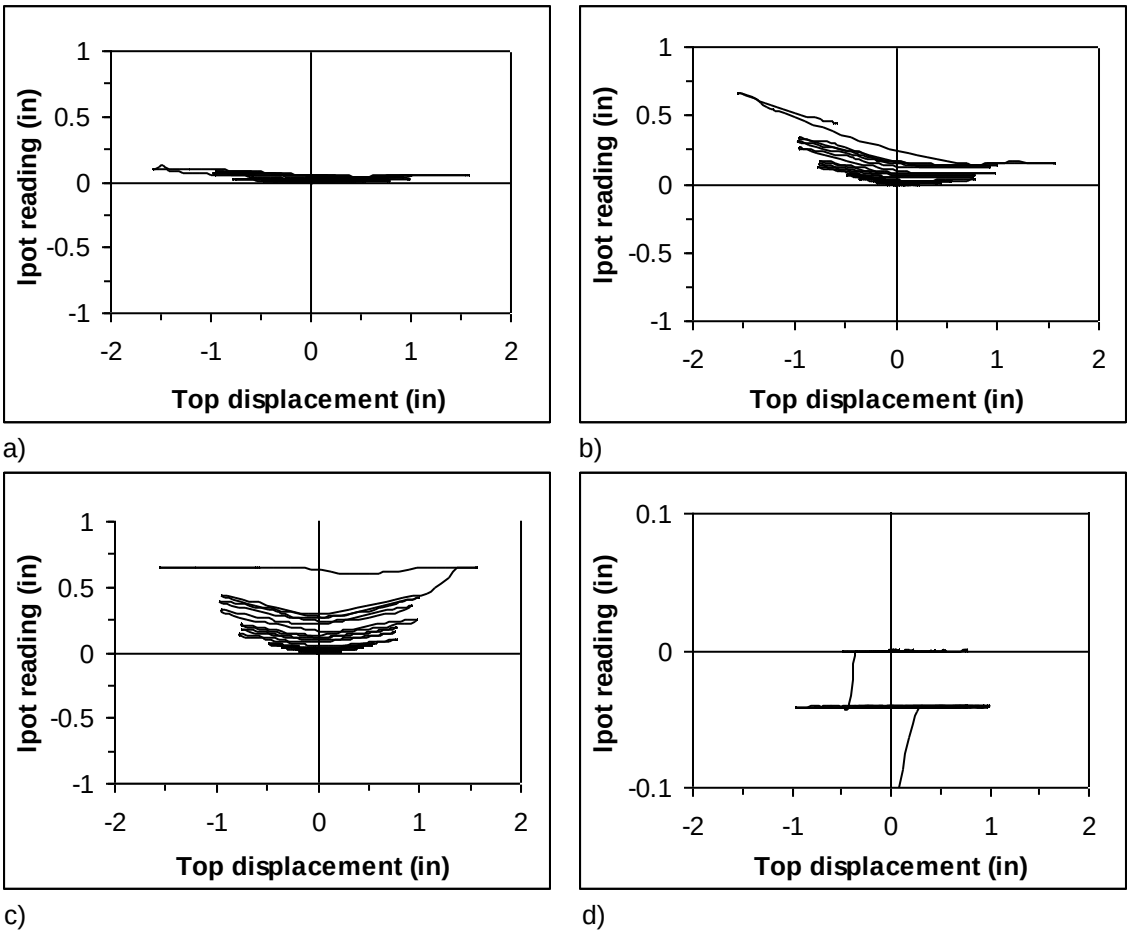

Figure 7.29 – CLB: East face linear potentiometer histories – a) E1, b) E2, c) E3, d) E4

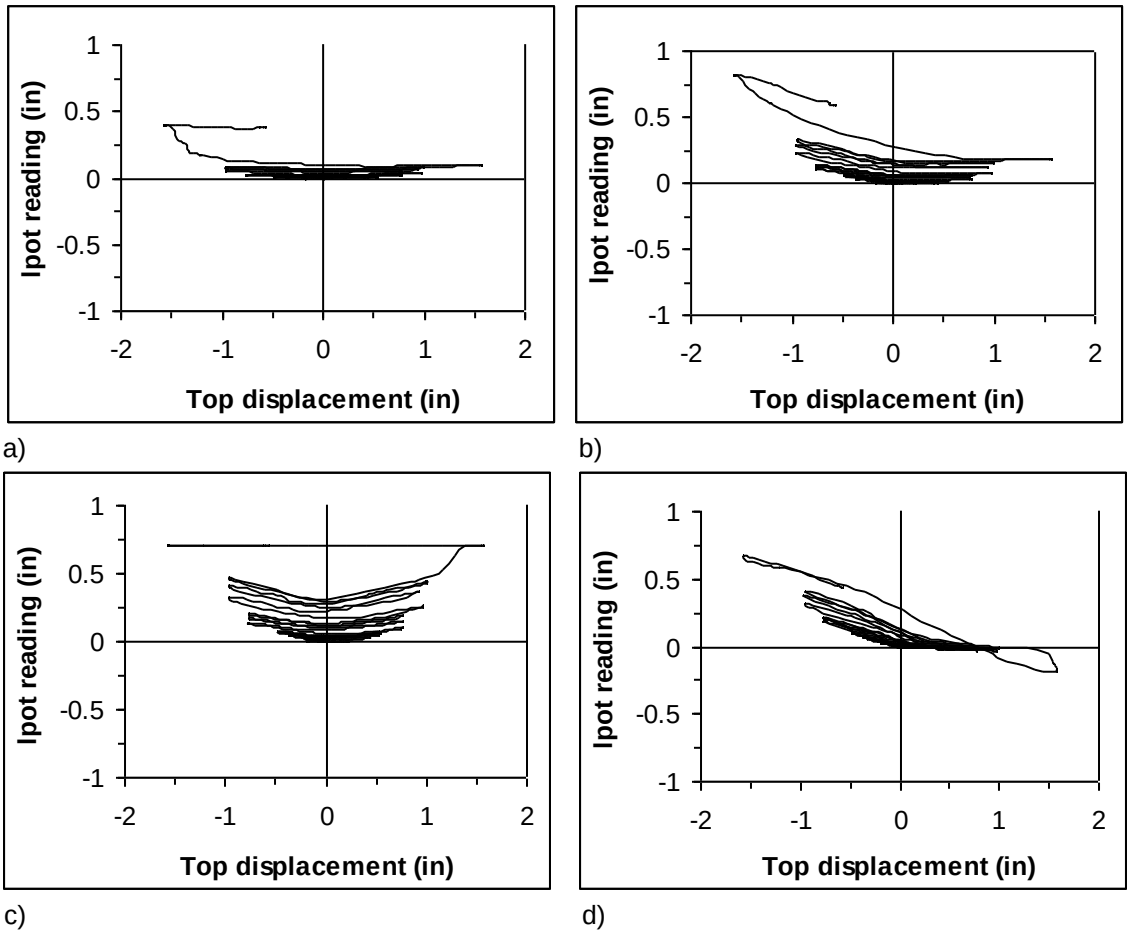

Figure 7.30 – CLB: West face linear potentiometer histories – a) W1, b) W2, c) W3, d) W4

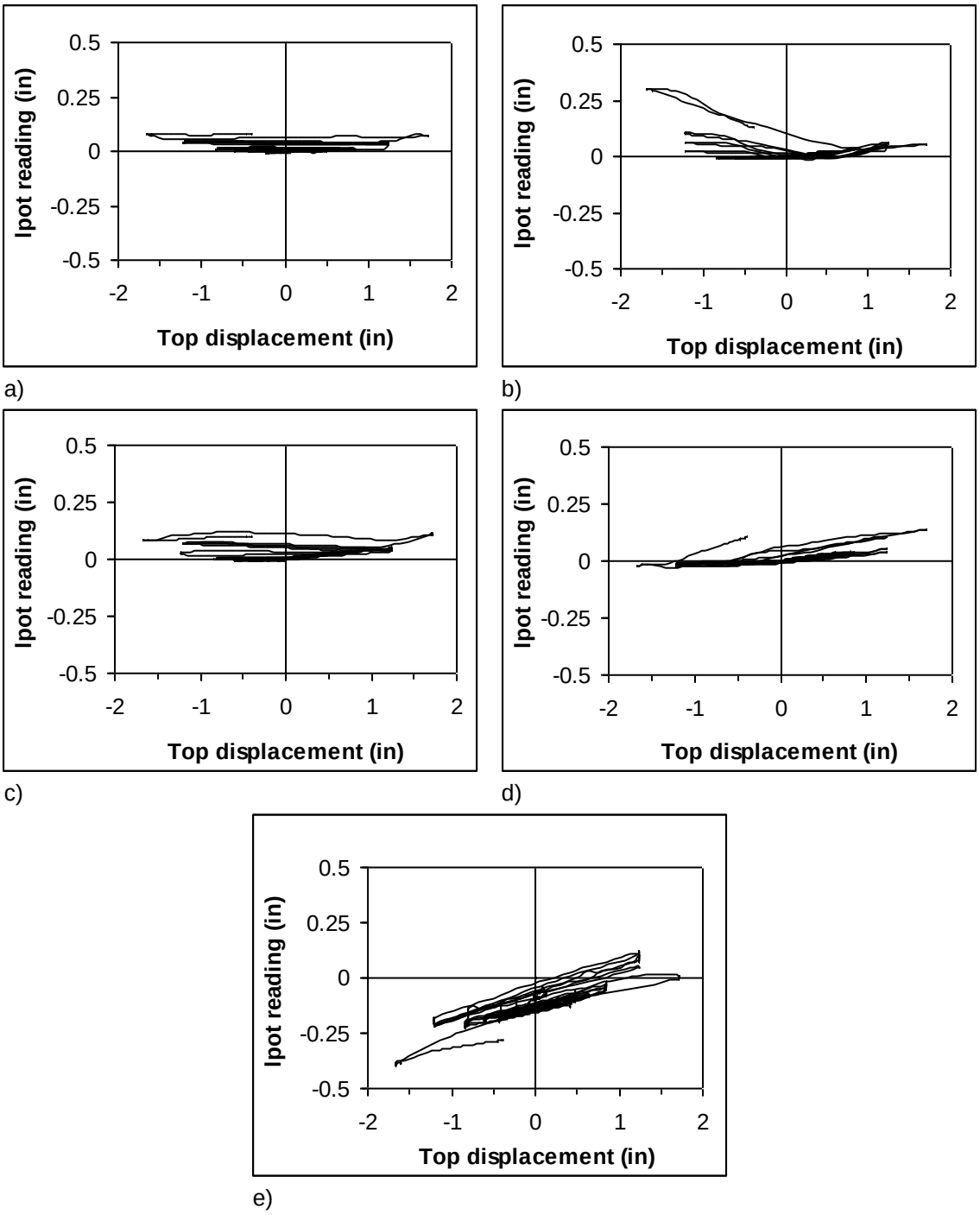

Figure 7.31 – SHB: North face linear potentiometer histories – a) N1, b) N2, c) N3, d) N4, e) N5

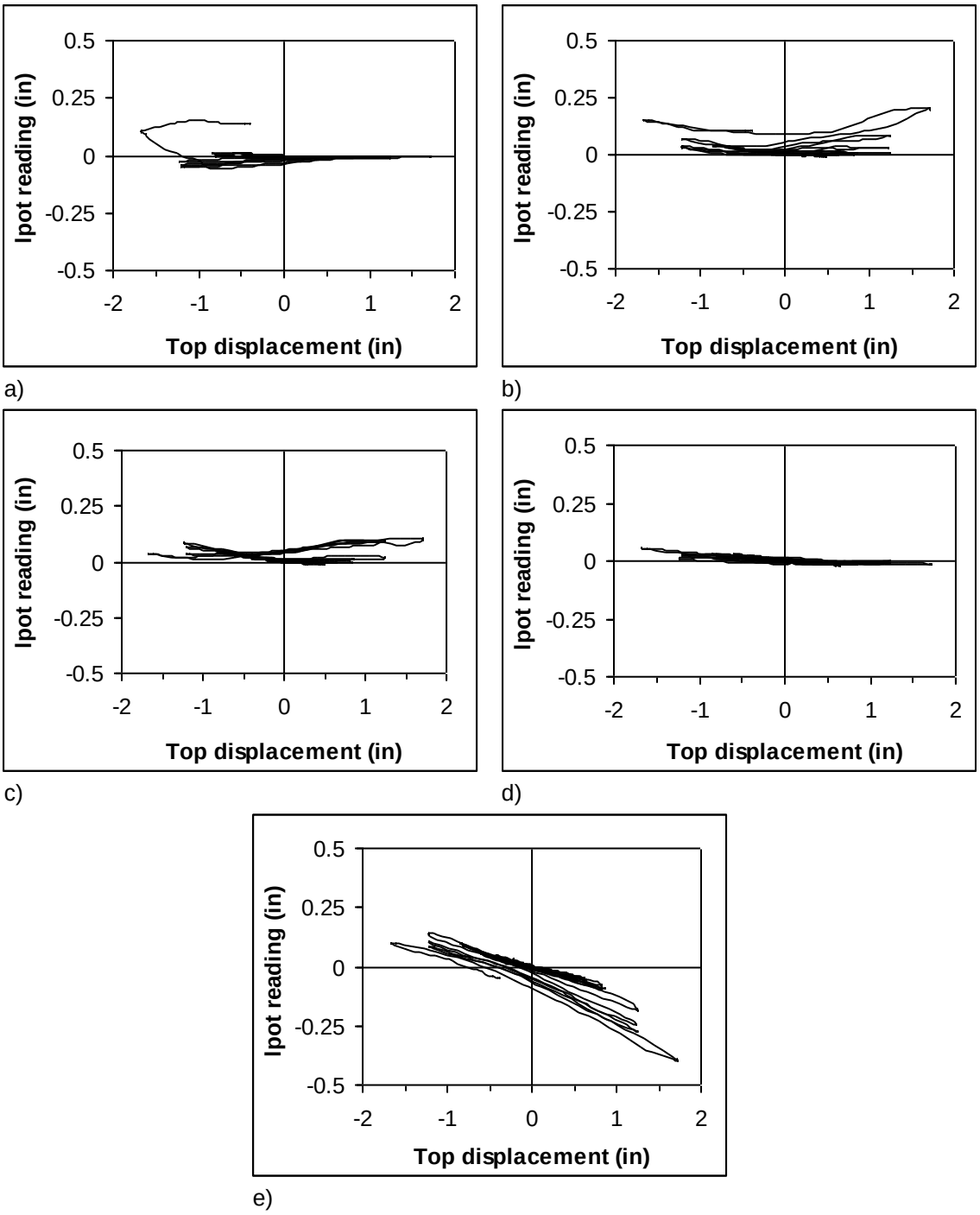

Figure 7.32 – SHB: South face linear potentiometer histories – a) S1, b) S2, c) S3, d) S4, e) S5

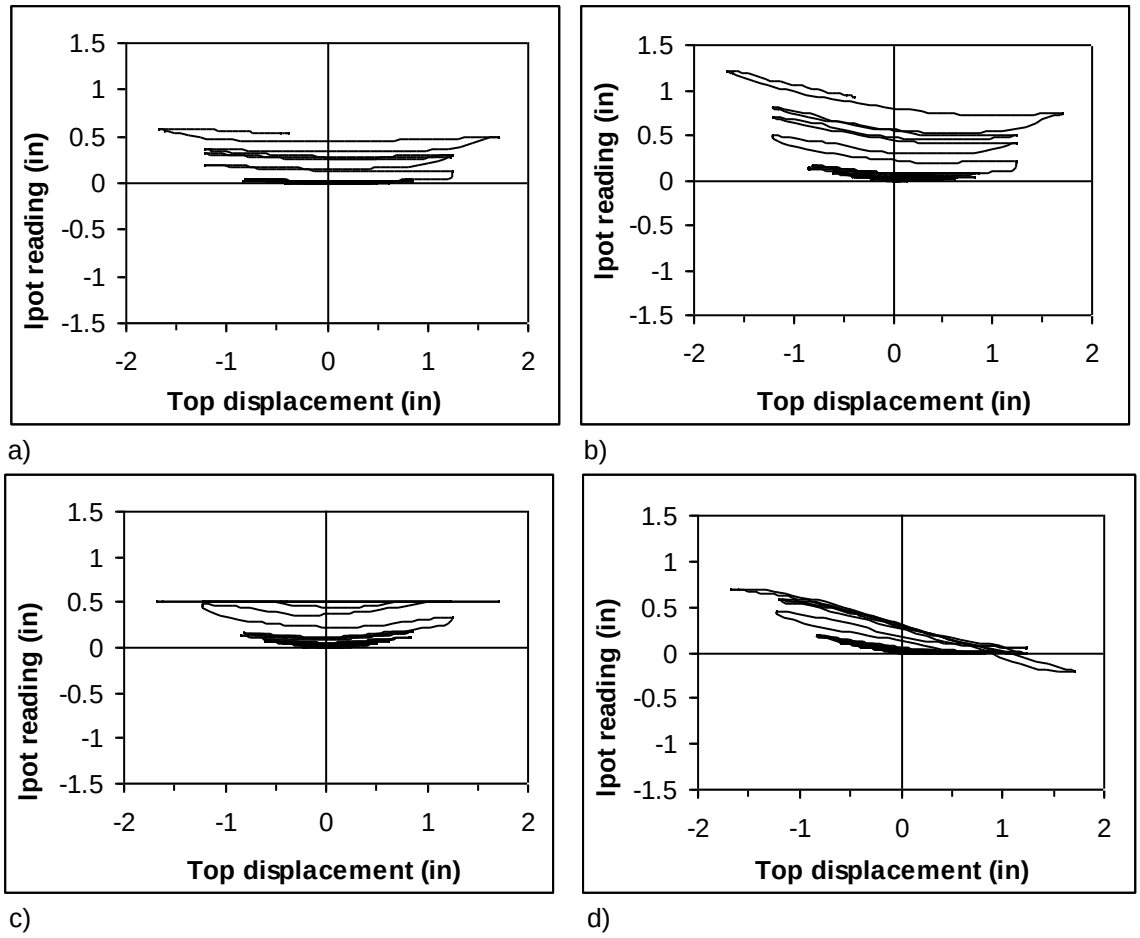

Figure 7.33 – SHB: East face linear potentiometer histories – a) E1, b) E2, c) E3, d) E4

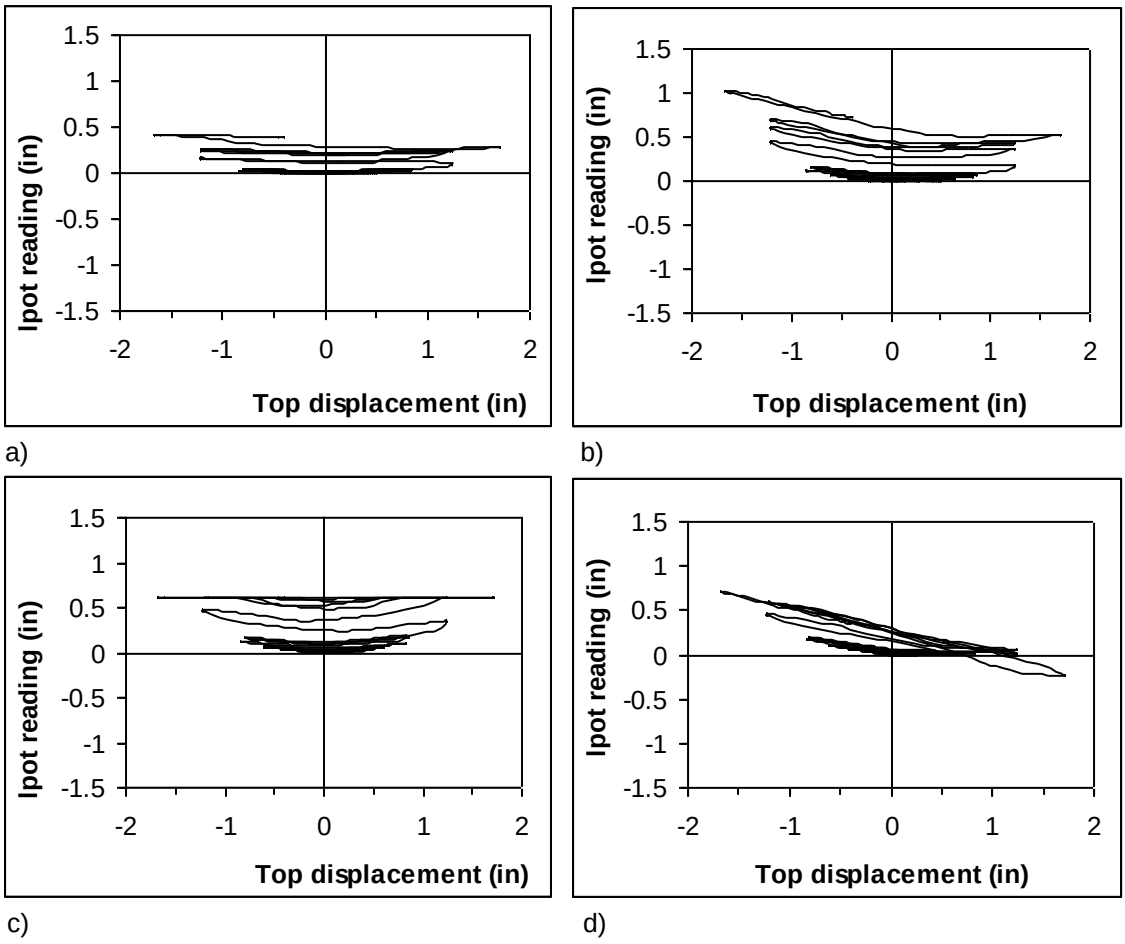

Figure 7.34 – SHB: West face linear potentiometer histories – a) W1, b) W2, c) W3, d) W4

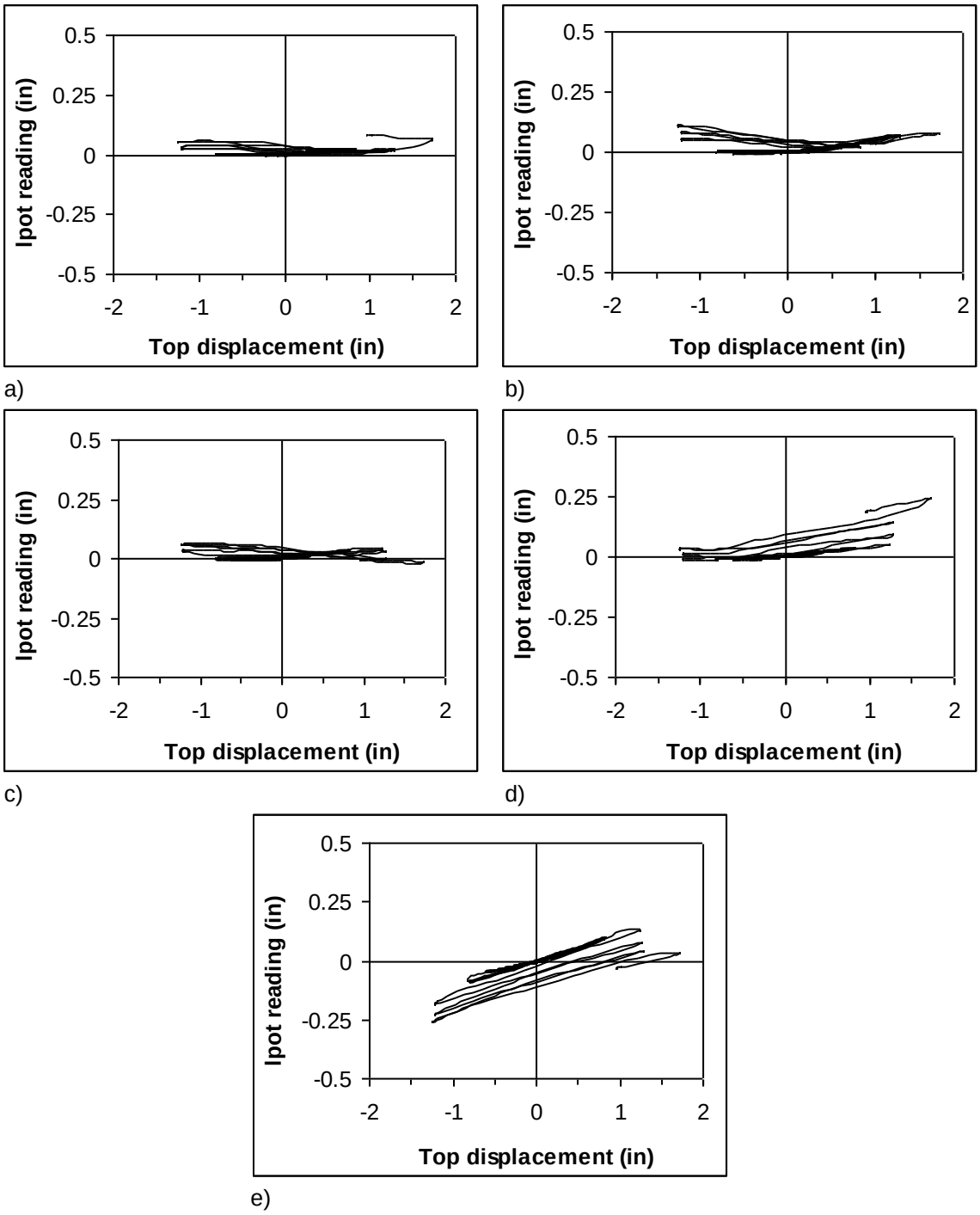

Figure 7.35 – SLB: North face linear potentiometer histories – a) N1, b) N2, c) N3, d) N4, e) N5

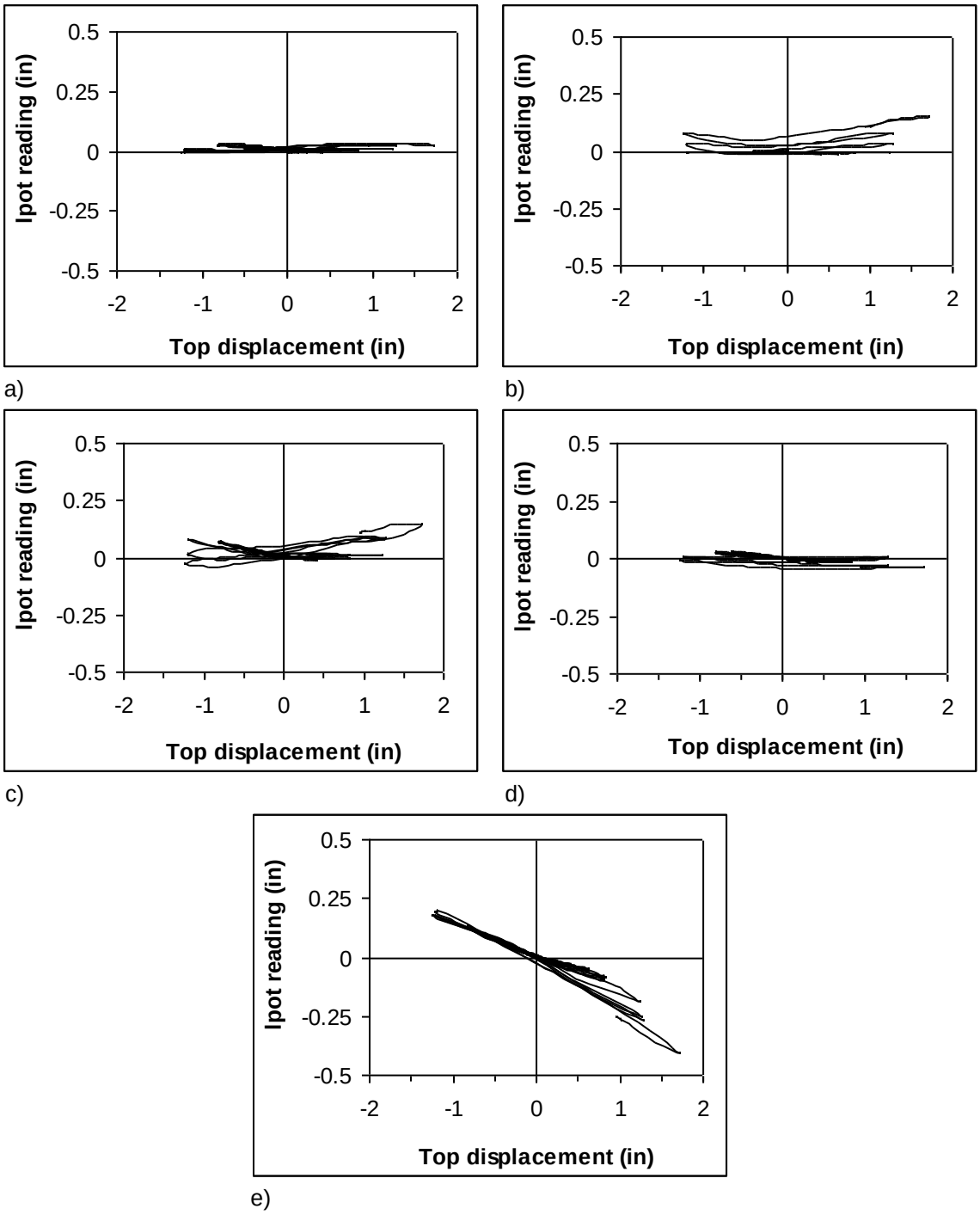

Figure 7.36 – SLB: South face linear potentiometer histories – a) S1, b) S2, c) S3, d) S4, e) S5

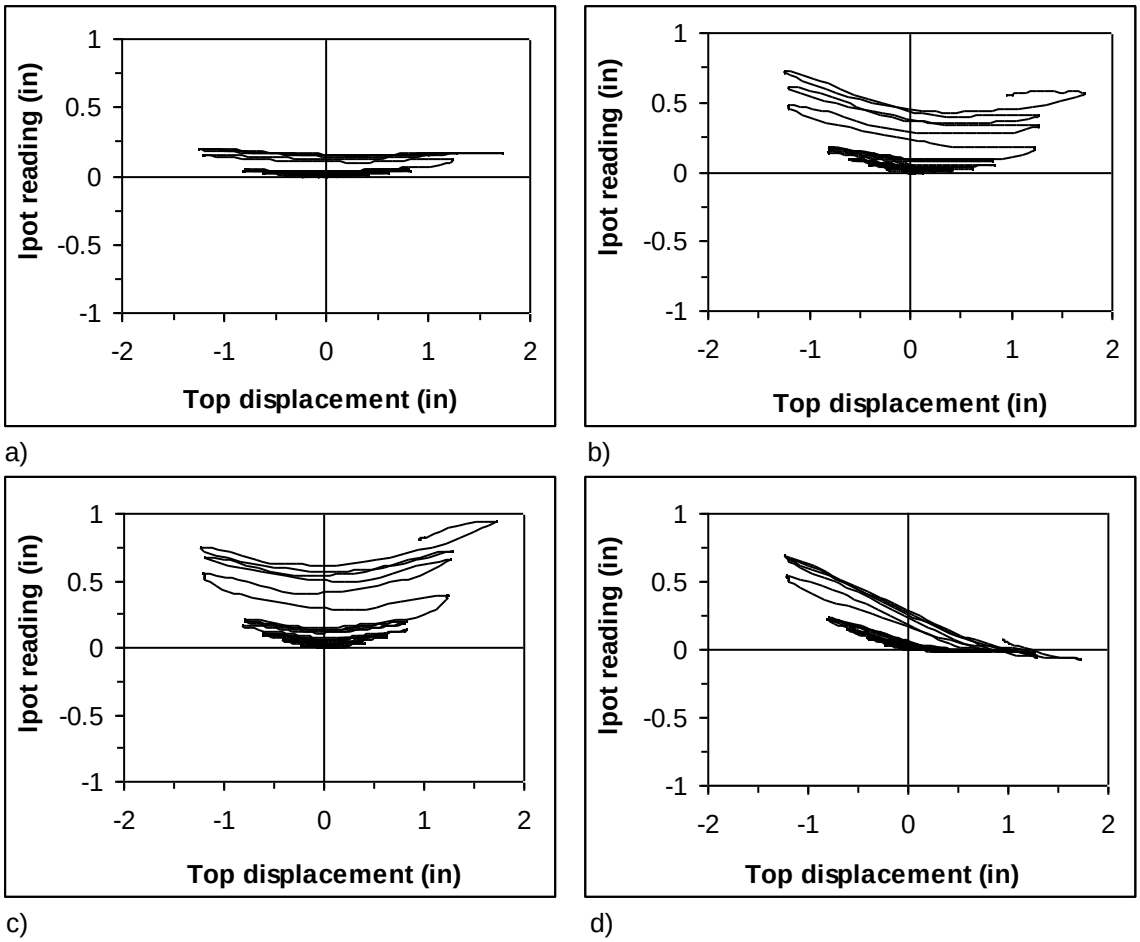

Figure 7.37 – SLB: East face linear potentiometer histories – a) E1, b) E2, c) E3, d) E4

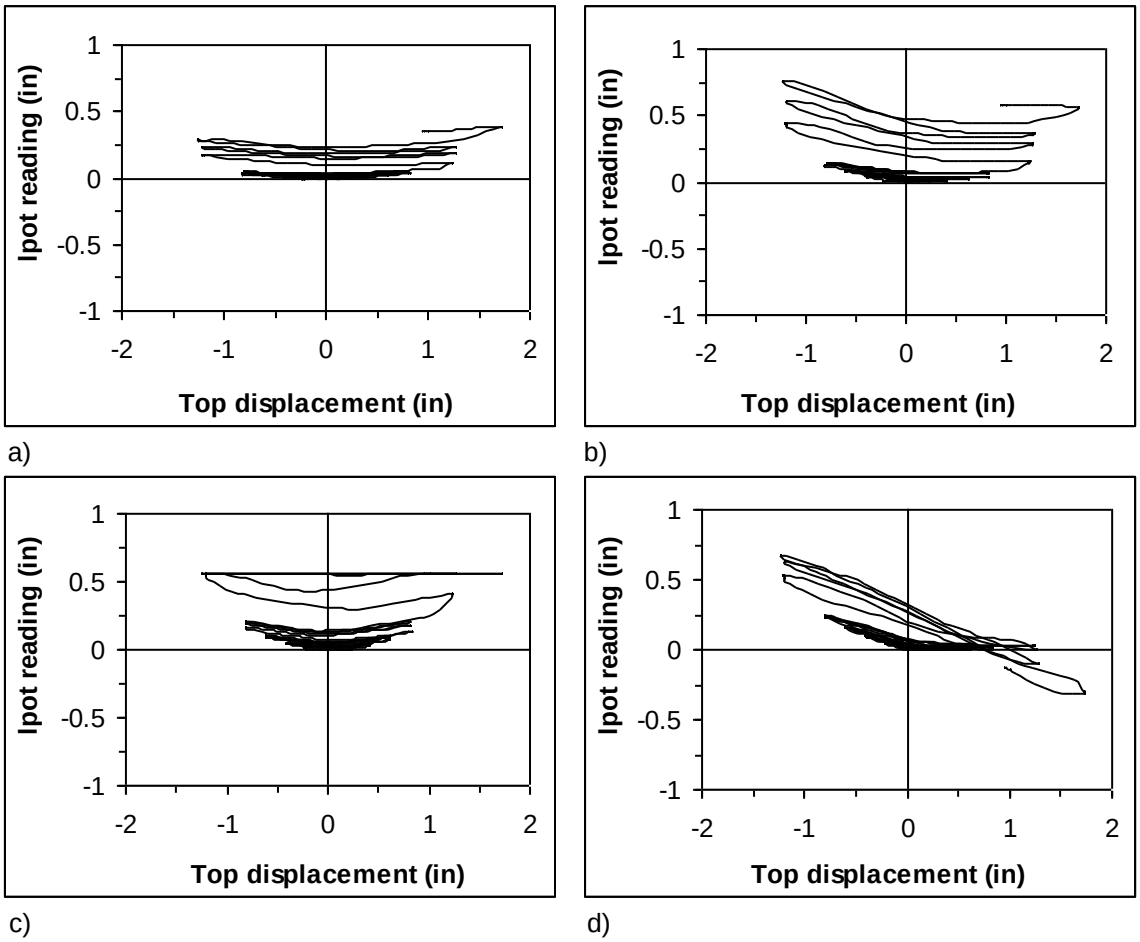

Figure 7.38 – SLB: West face linear potentiometer histories – a) W1, b) W2, c) W3, d) W4

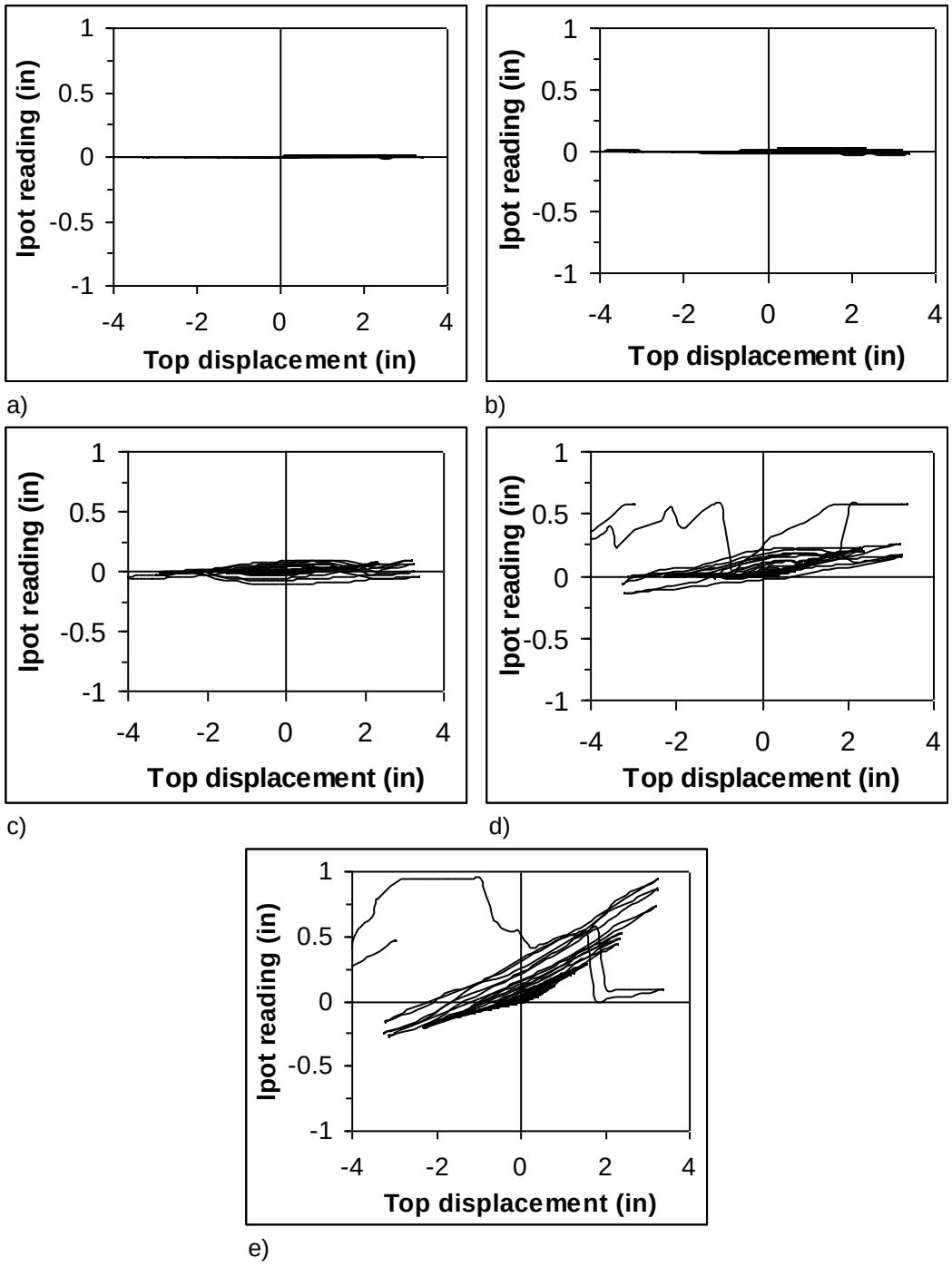

Figure 7.39 – NWD: North face linear potentiometer histories – a) N1, b) N2, c) N3, d) N4, e) N5

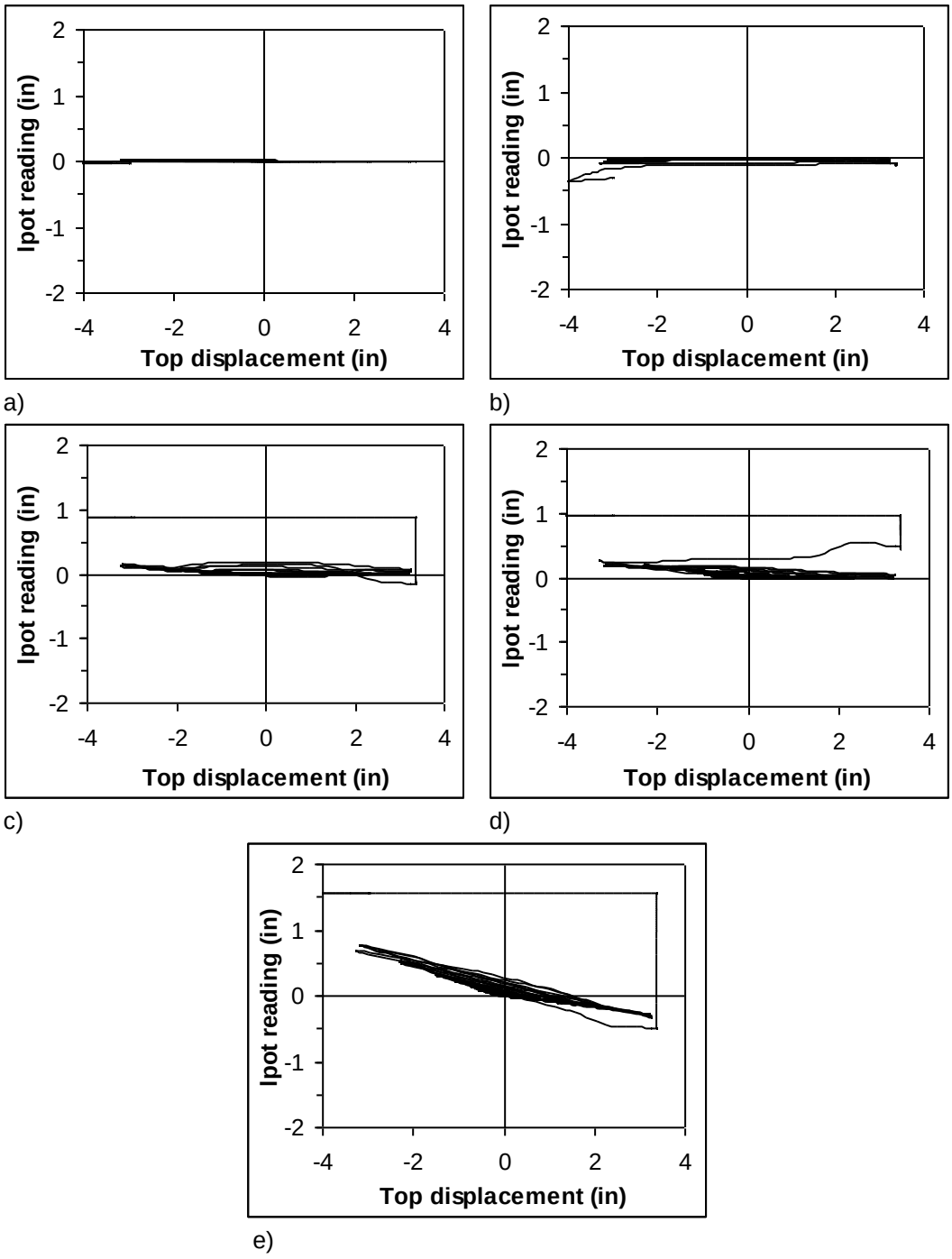

Figure 7.40 – NWD: South face linear potentiometer histories – a) S1, b) S2, c) S3, d) S4, e) S5

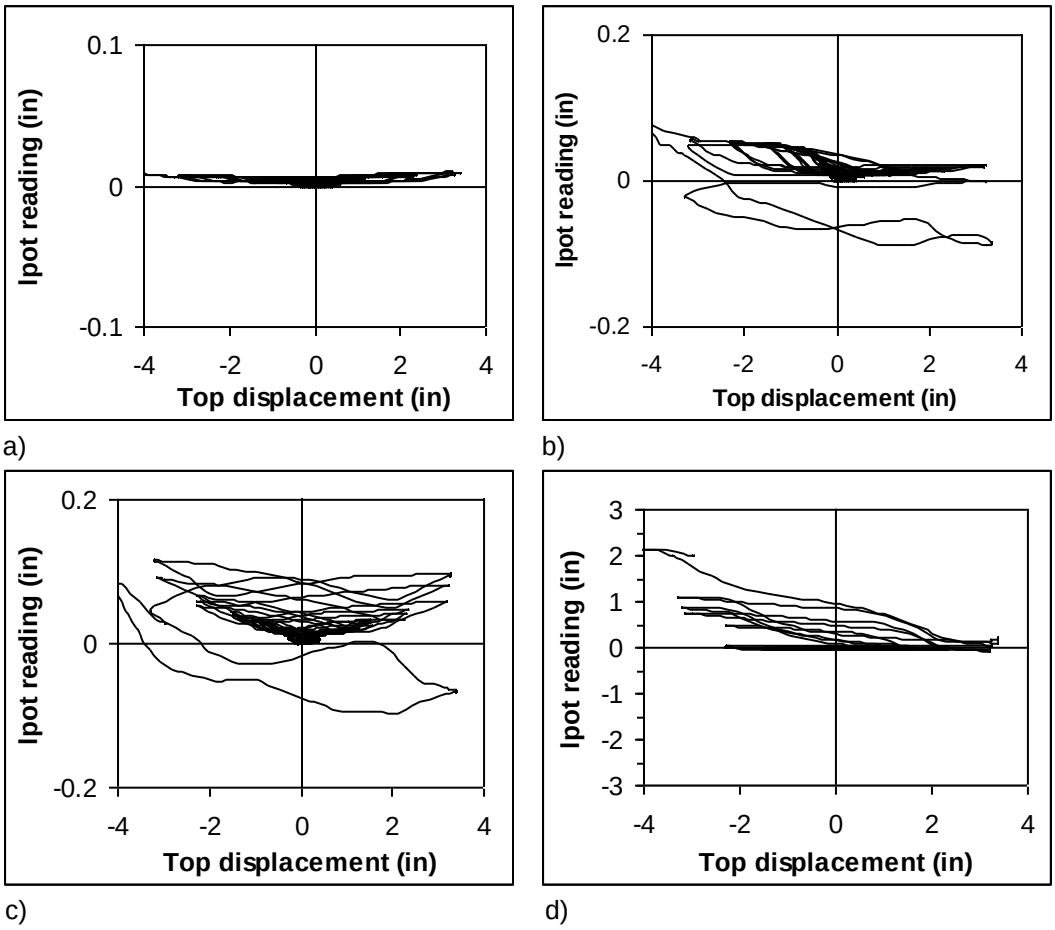

Figure 7.41 – NWD: East face linear potentiometer histories – a) E1, b) E2, c) E3, d) E4

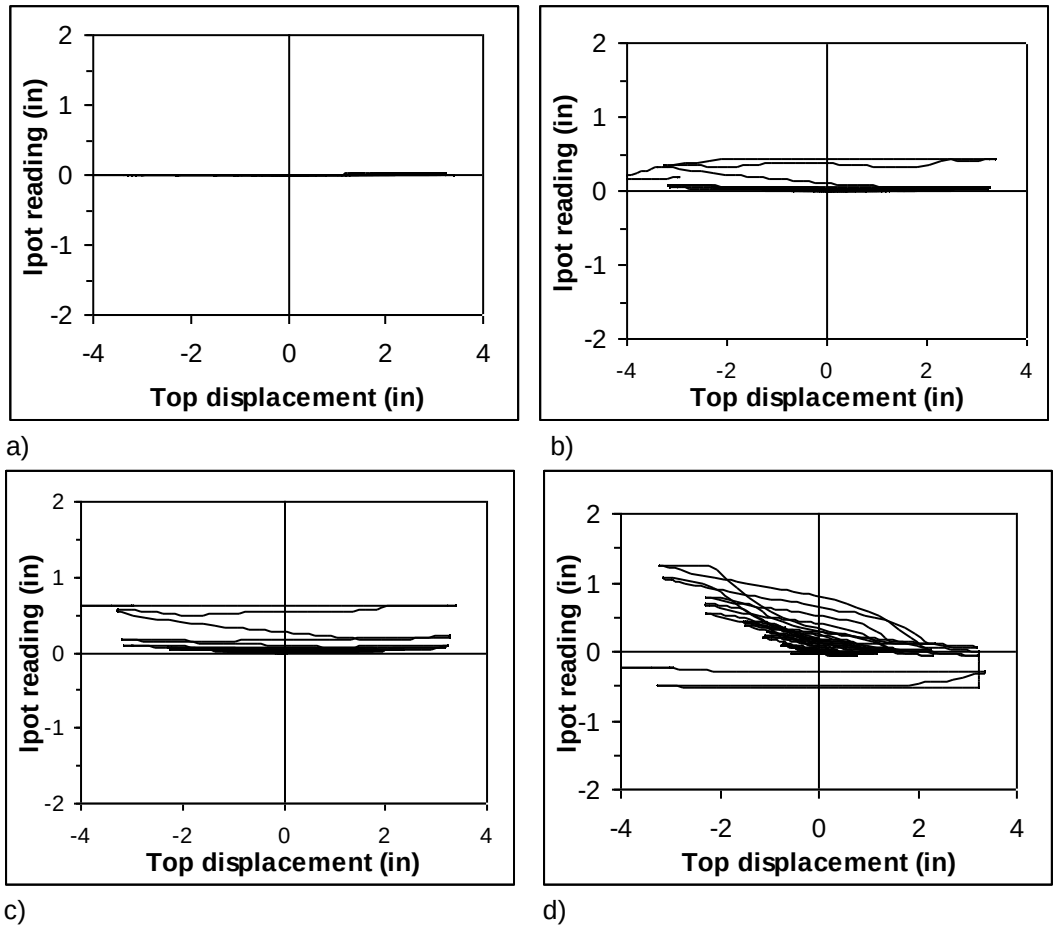

Figure 7.42 – NWD: West face linear potentiometer histories – a) W1, b) W2, c) W3, d) W4

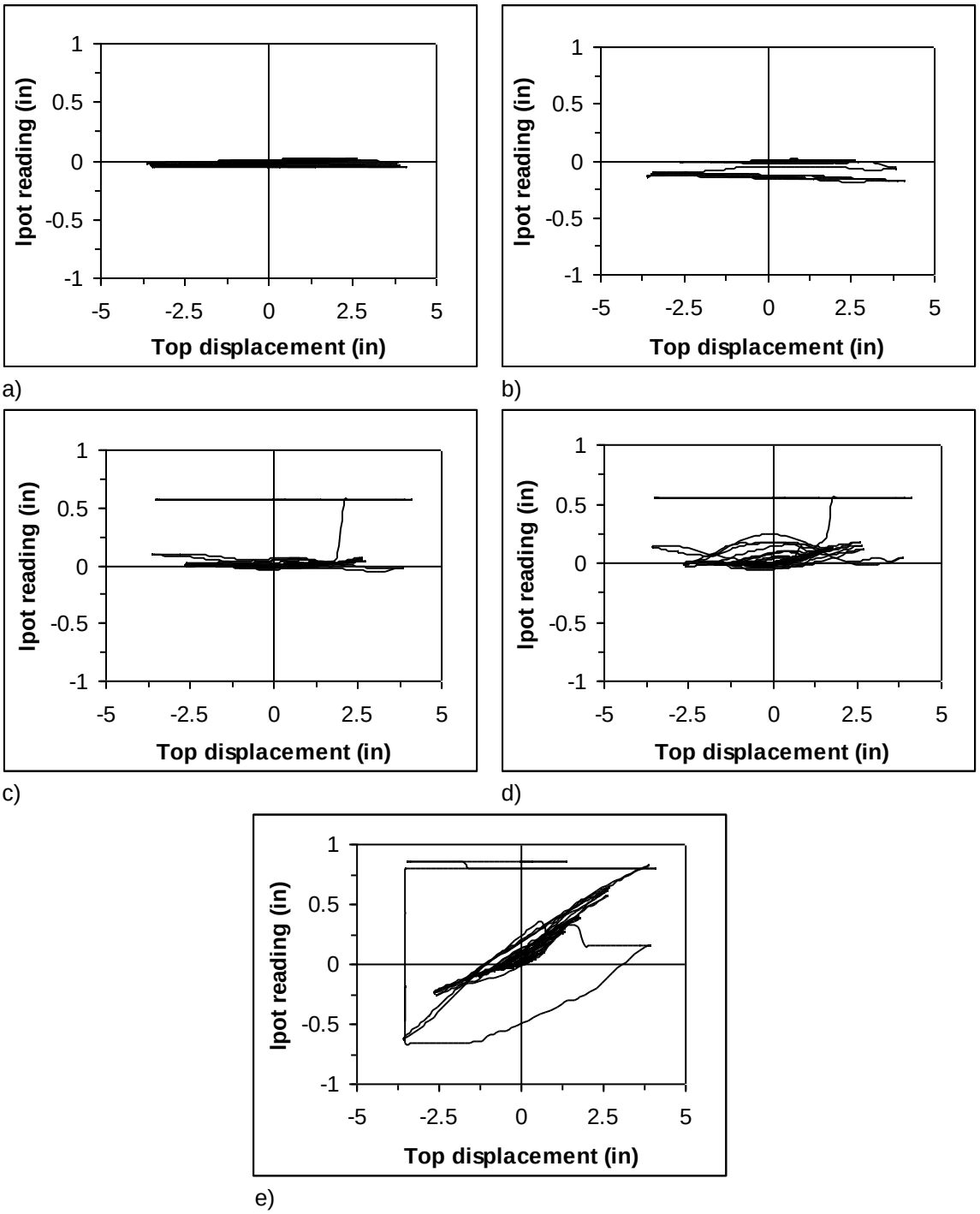

Figure 7.43 – CLD: North face linear potentiometer histories – a) N1, b) N2, c) N3, d) N4, e) N5

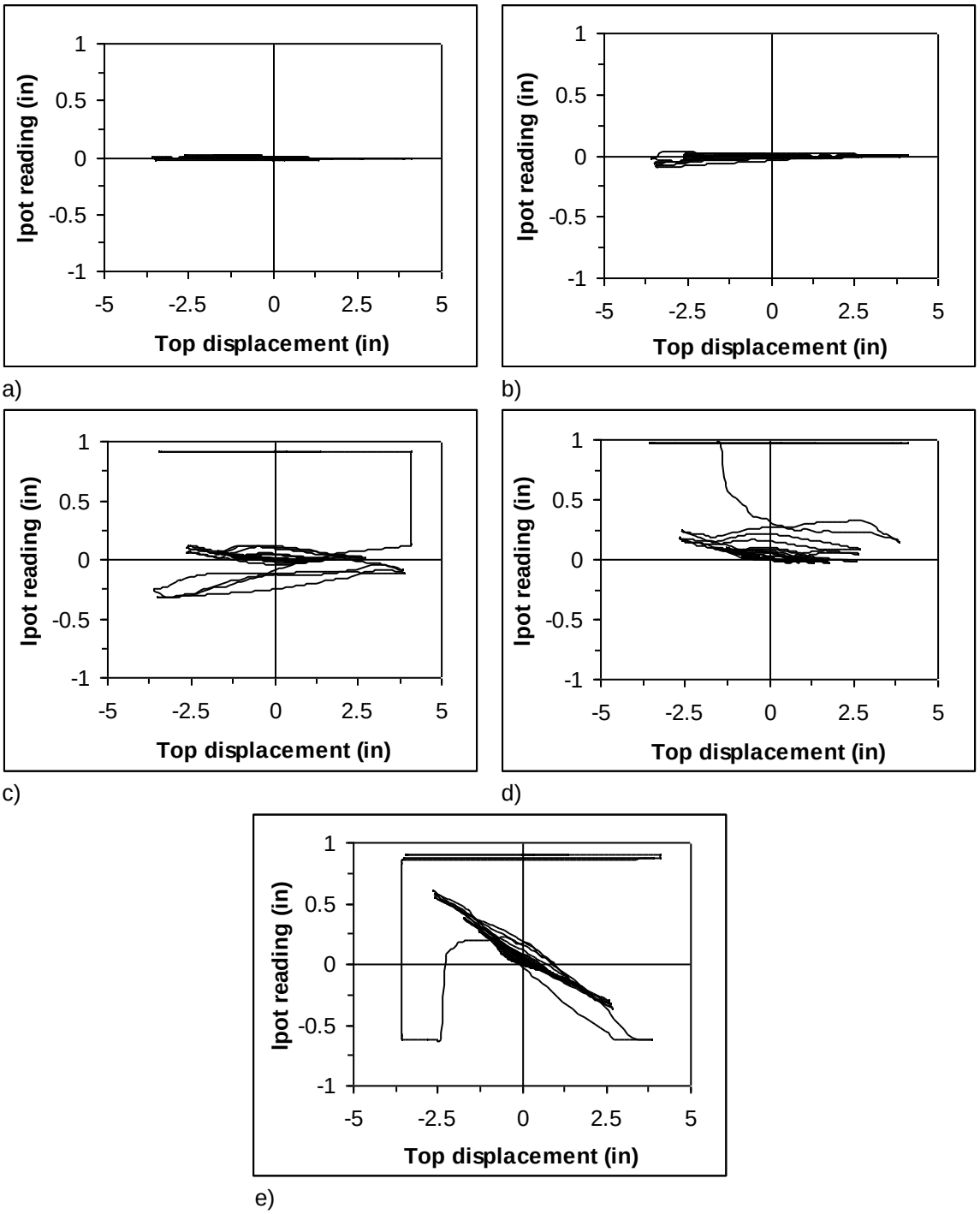

Figure 7.44 – CLD: South face linear potentiometer histories – a) S1, b) S2, c) S3, d) S4, e) S5

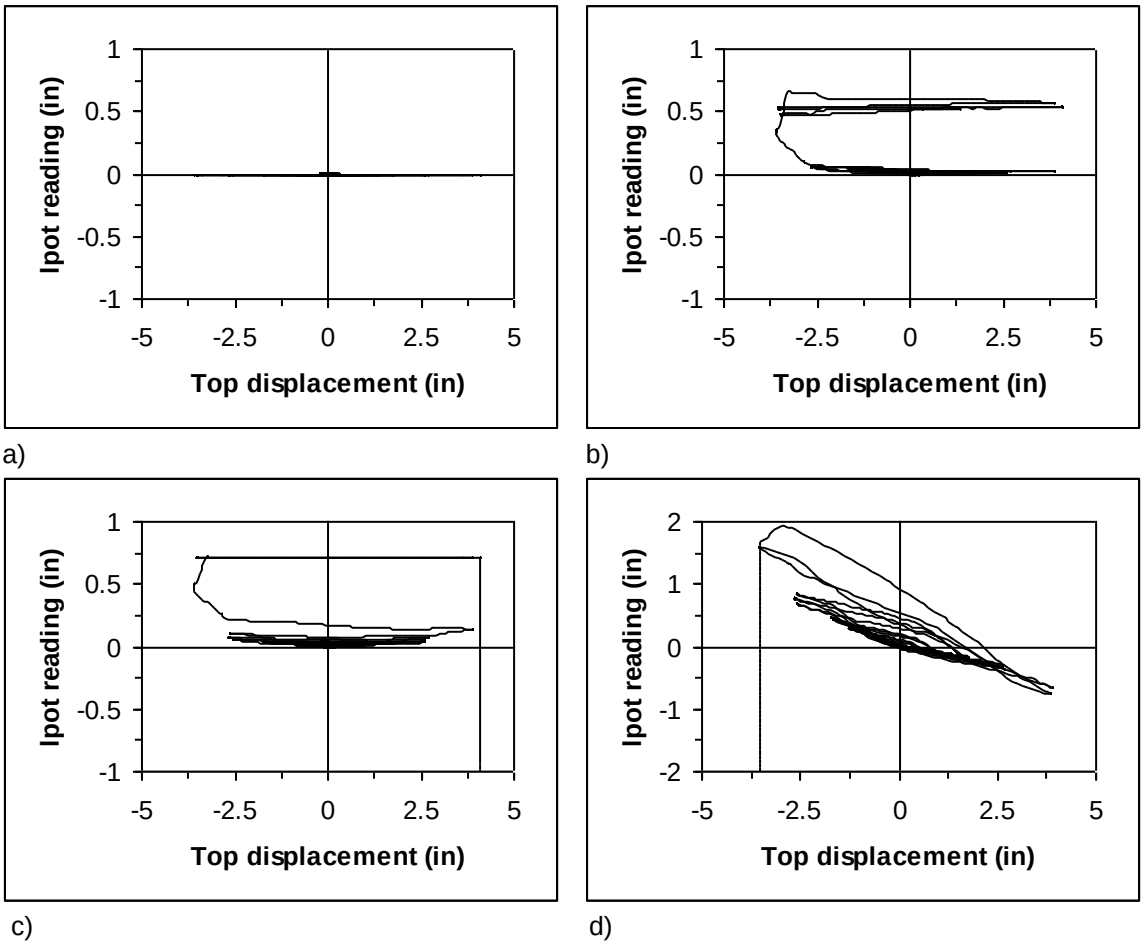

Figure 7.45 – CLD: East face linear potentiometer histories – a) E1, b) E2, c) E3, d) E4

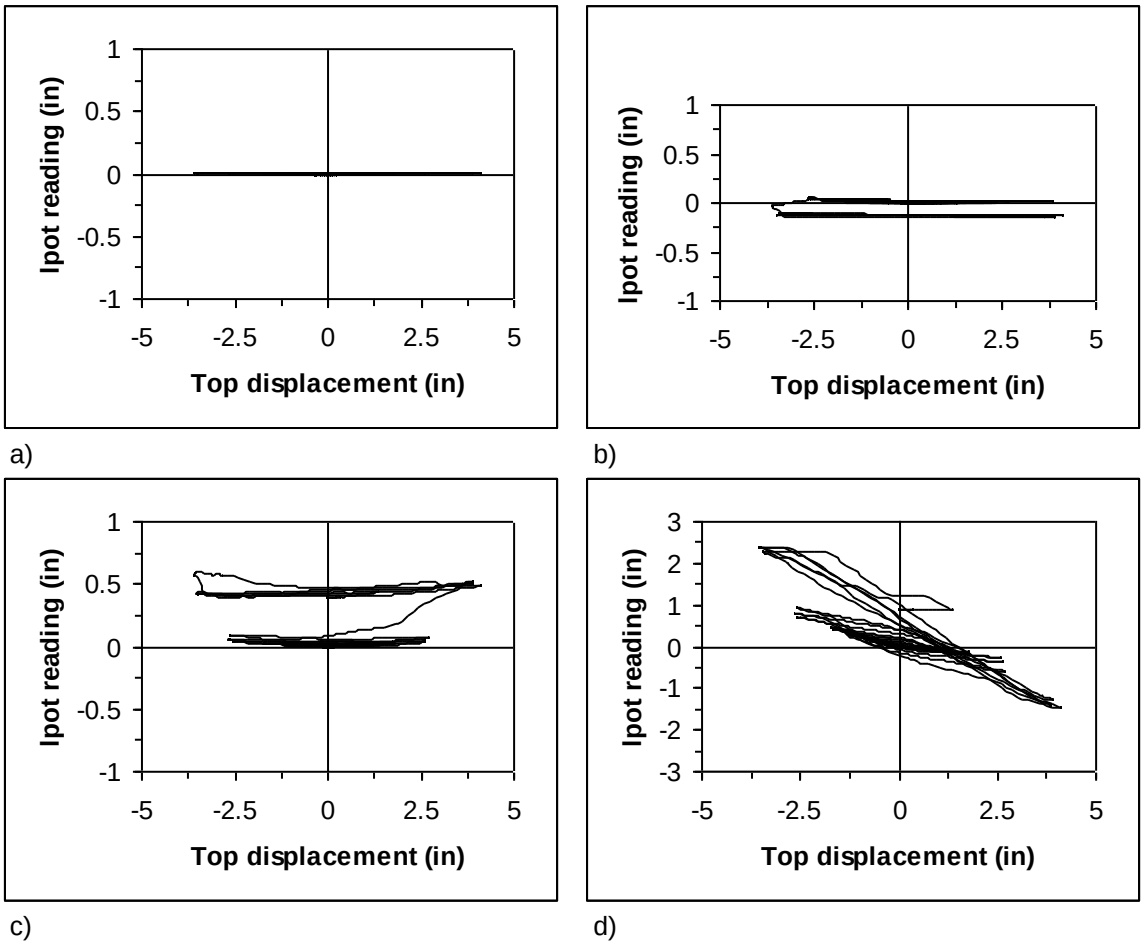

Figure 7.46 – CLD: West face linear potentiometer histories – a) W1, b) W2, c) W3, d) W4

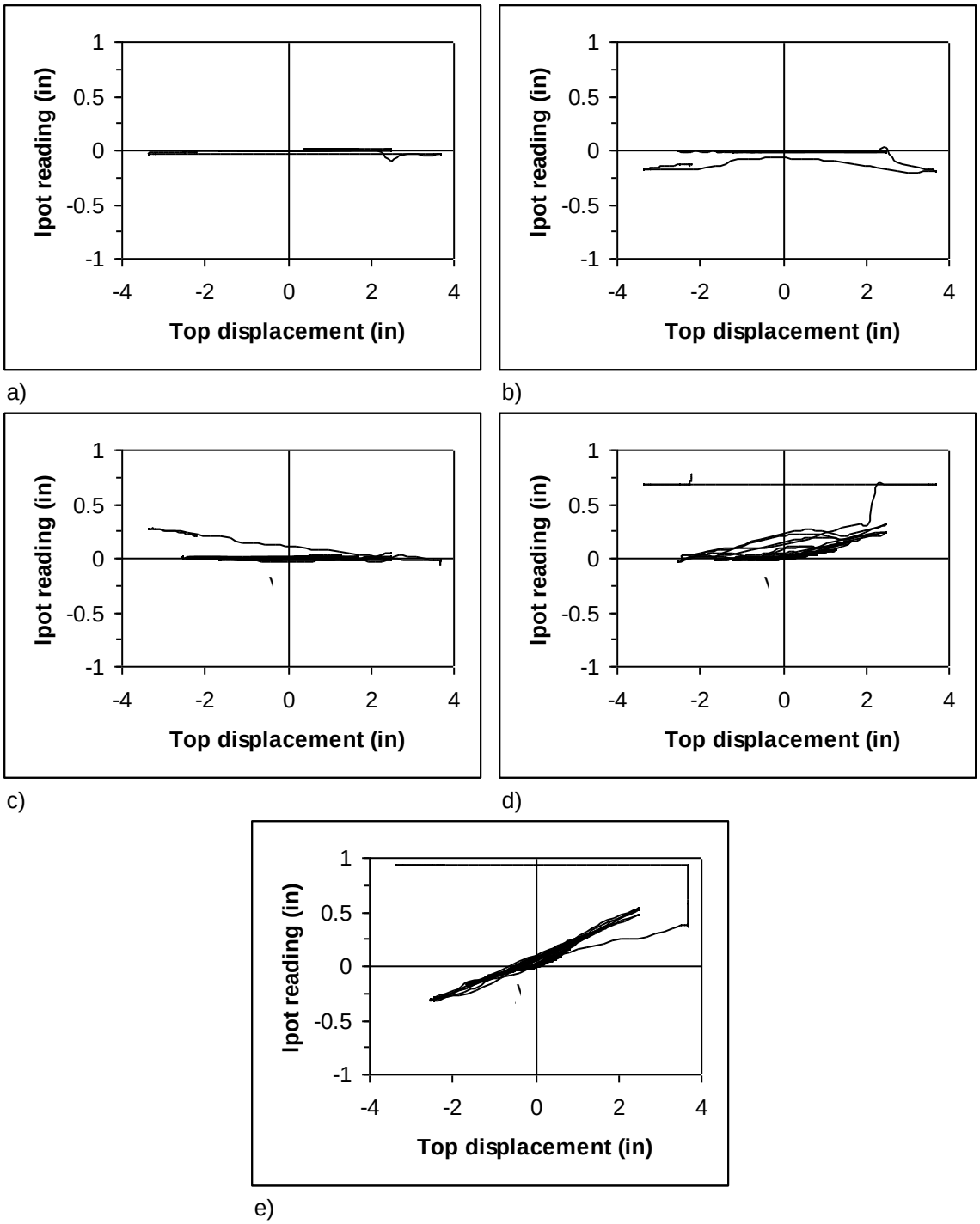

Figure 7.47 – SHD: North face linear potentiometer histories – a) N1, b) N2, c) N3, d) N4, e) N5

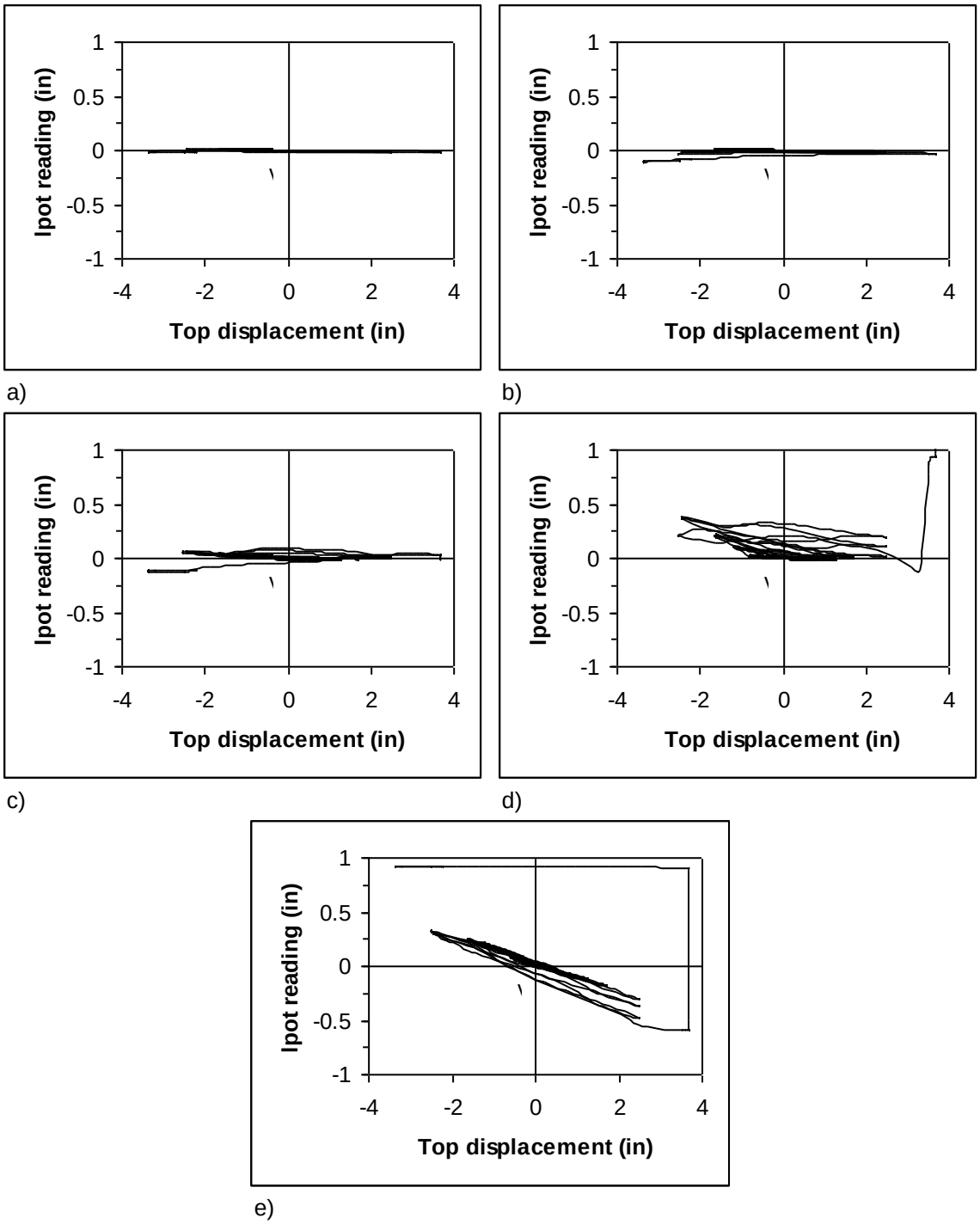

Figure 7.48 – SHD: South face linear potentiometer histories – a) S1, b) S2, c) S3, d) S4, e) S5

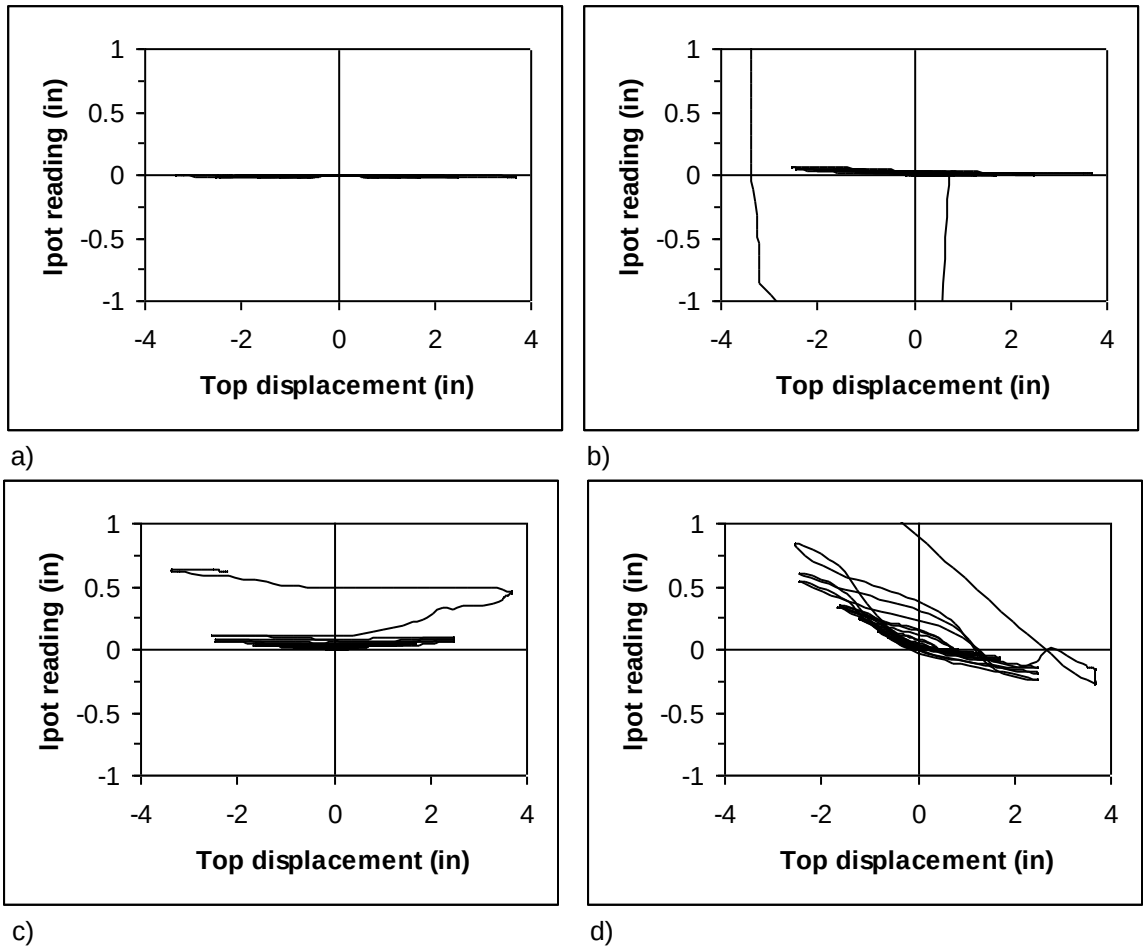

Figure 7.49 – SHD: East face linear potentiometer histories – a) E1, b) E2, c) E3, d) E4

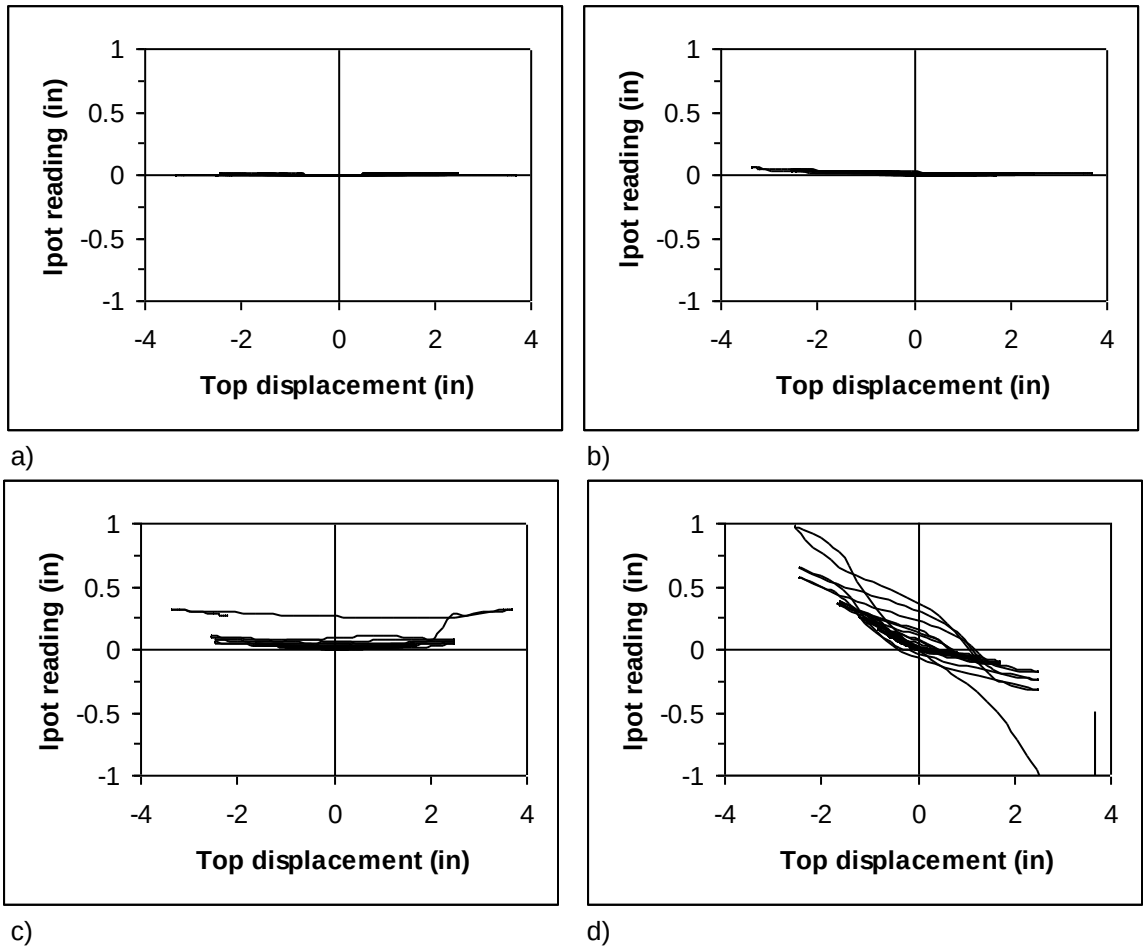

Figure 7.50 – SHD: West face linear potentiometer histories – a) W1, b) W2, c) W3, d) W4

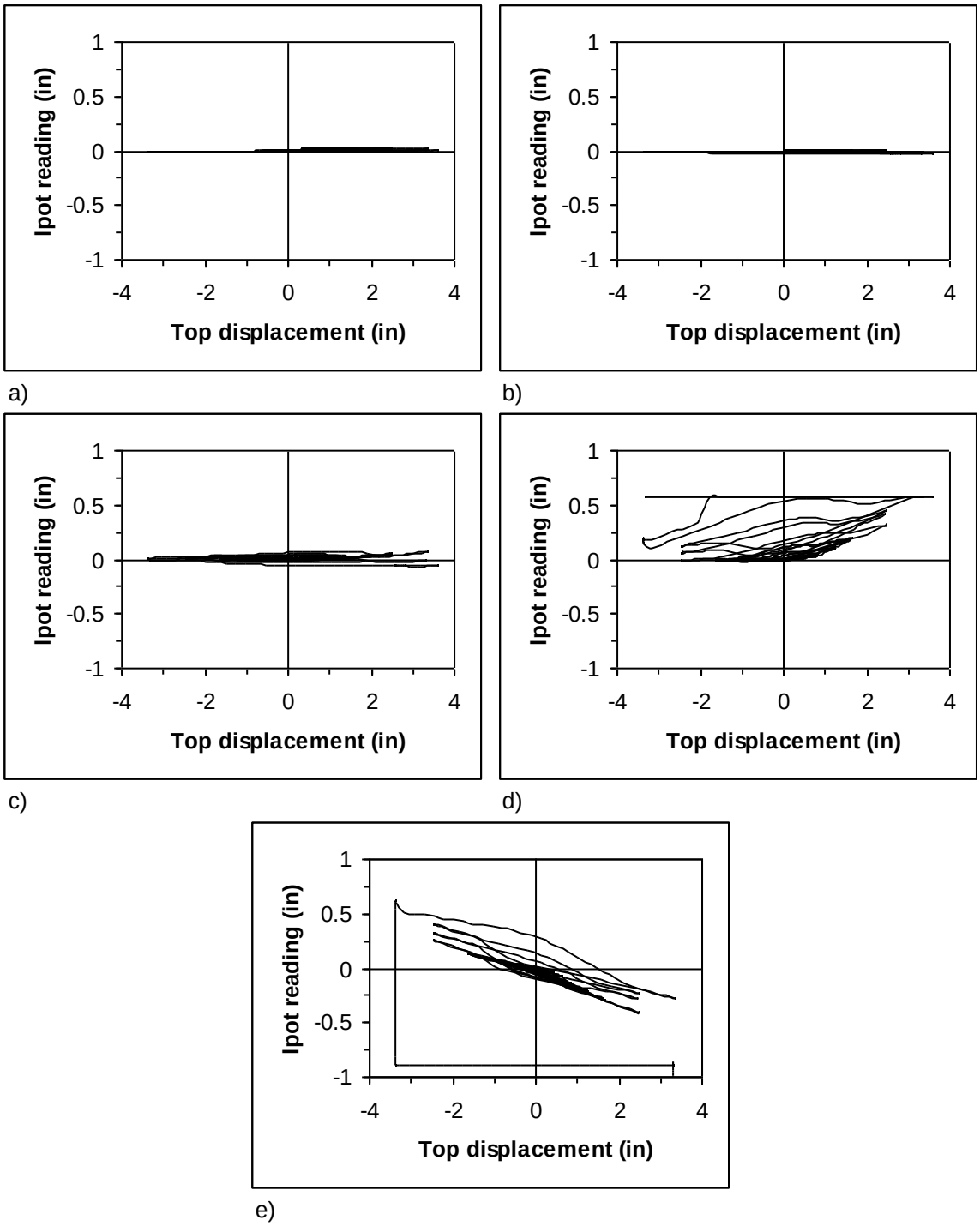

Figure 7.51 – SLD: North face linear potentiometer histories – a) N1, b) N2, c) N3, d) N4, e) N5

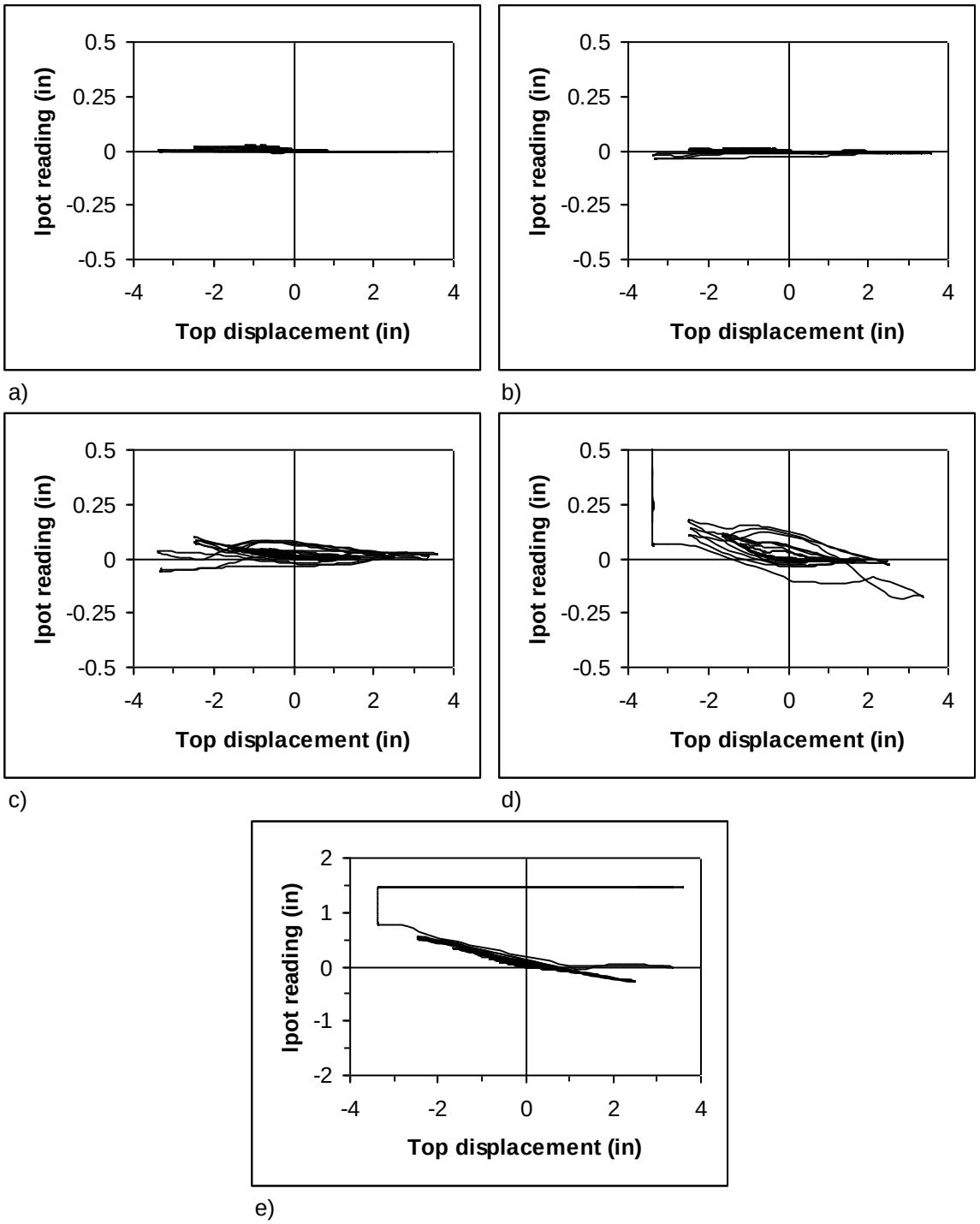

Figure 7.52 – SLD: South face linear potentiometer histories – a) S1, b) S2, c) S3, d) S4, e) S5

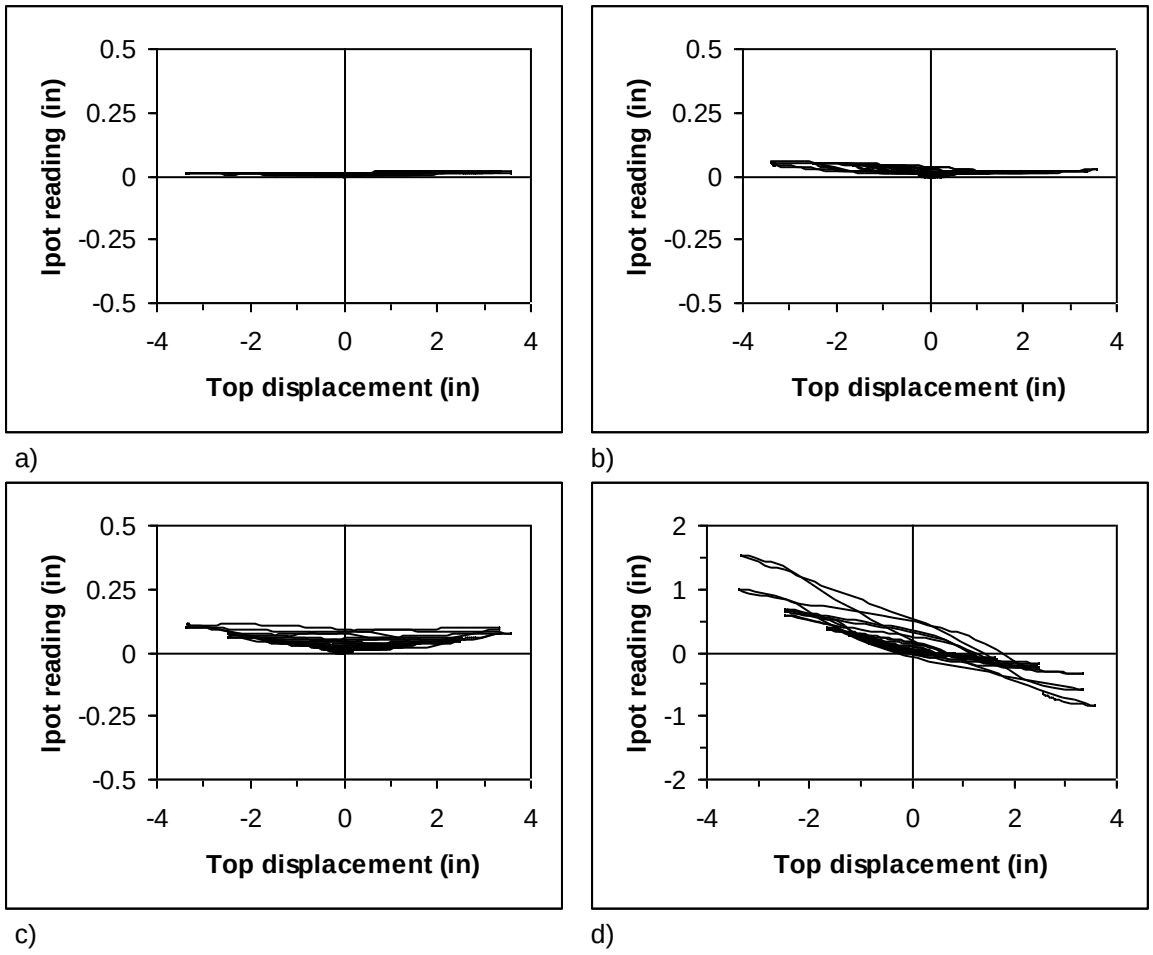

Figure 7.53 – SLD: East face linear potentiometer histories – a) E1, b) E2, c) E3, d) E4

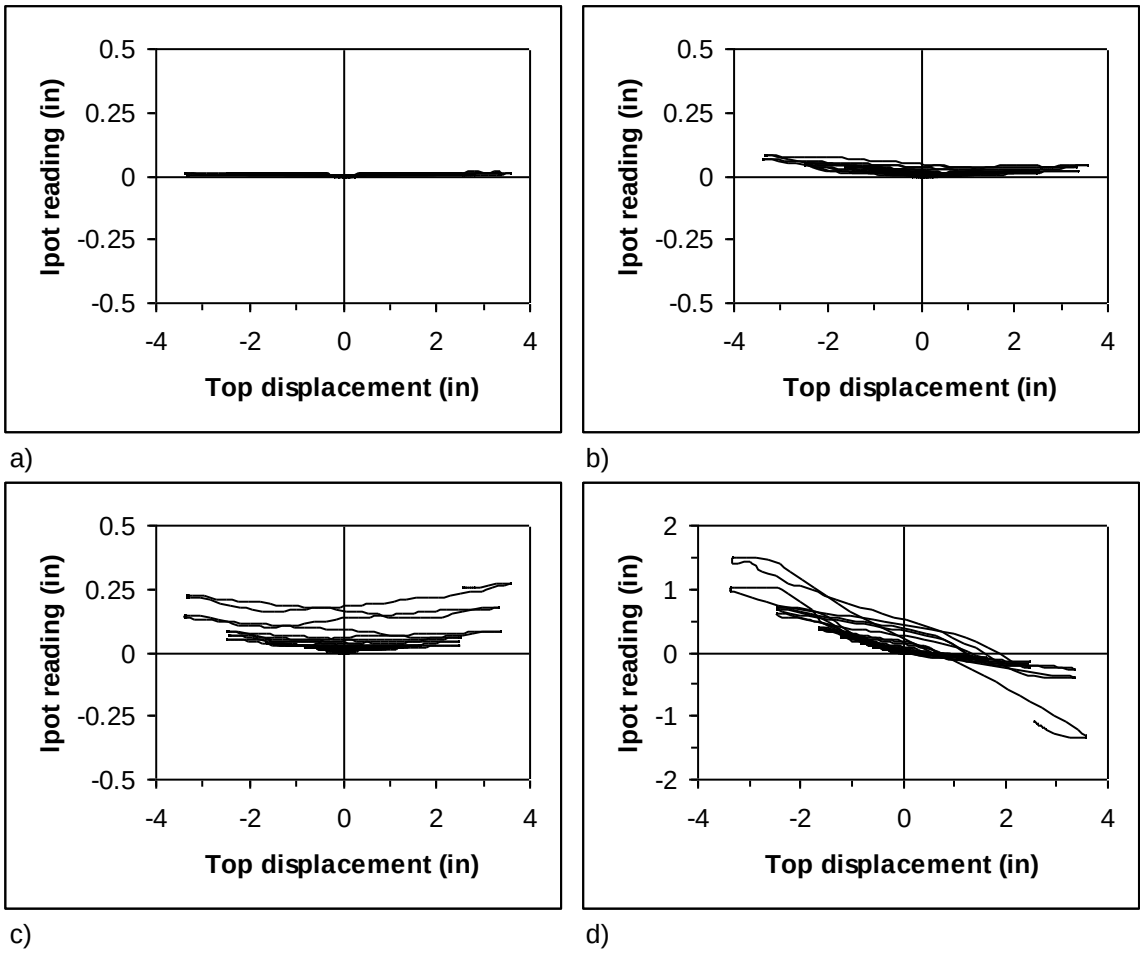

Figure 7.54 – SLD: West face linear potentiometer histories – a) W1, b) W2, c) W3, d) W4